2005
Annual Progress Report

HEAVY VEHICLE PROPULSION MATERIALS

Less dependence on foreign oil, and eventual transition to an emissions-free, petroleum-free vehicle

FREEDOMCAR AND VEHICLE TECHNOLOGIES PROGRAM

U.S. Department of Energy
Energy Efficiency and Renewable Energy
Bringing you a prosperous future where energy is clean, abundant, reliable, and affordable

FreedomCAR & Fuel Partnership

21st CENTURY TRUCK PARTNERSHIP

U.S. Department of Energy
Office of FreedomCAR and Vehicle Technologies
1000 Independence Avenue S.W.
Washington, DC 20585-0121

FY 2005

Progress Report for Heavy Vehicle Propulsion Materials

Energy Efficiency and Renewable Energy
Office of FreedomCAR and Vehicle Technologies
Advanced Materials Technologies

Edward Wall	**Program Manager, OFCVT**
Rogelio Sullivan	**Advanced Materials Technologies Team Leader**
James Eberhardt	**Technology Development Area Specialist**

May 2006

CONTENTS

1. INTRODUCTION 1

2. MATERIALS FOR FUEL SYSTEMS 5

A. Low-Cost, High-Toughness Ceramics 5

3. MATERIALS FOR EXHAUST AFTERTREATMENT 9

A. Materials for Exhaust Aftertreatment 9
B. Development of Materials Analysis Tools for Studying NO_x Adsorber Catalysts (CRADA No. ORNL-02-0659 with Cummins, Inc.) 17
C. Development of NO_x Sensors for Heavy Vehicle Applications 25
D. Ultra-High Resolution Electron Microscopy for Characterization of Catalyst Microstructures and Deactivation Mechanisms 31
E. Microstructural Changes in NO_x Trap Materials under Lean and Rich Conditions at High Temperatures 39
F. Aftertreatment Catalysts Materials Research 47
G. Catalysis by First Principles 49
H. Durability of Diesel Particulate Filters (CRADA with Cummins, Inc.) 61

4. MATERIALS FOR AIR HANDLING, HOT SECTION, AND STRUCTURAL COMPONENTS 69

A. High-Temperature Advanced Materials for Lightweight Valve Train Components 69
B. Engineered Surfaces for Diesel Engine Components 77
C. Cermet Composites for Wear Applications 87
D. Processing and Characterization of Structural and Functional Materials for Heavy-Vehicle Applications 89
E. NDE Development for Valve-Train Components for Diesel Engines 97
F. Durability of Diesel Engine Component Materials 103
G. Life Prediction of Diesel Engine Components 109
H. Low-Cost Manufacturing of Precision Diesel Engine Components 115
I. Cost-Effective Machining of Titanium Materials 123
J. Advanced Cast Austenitic Stainless Steels for High-Temperature Components 131
K. Viscoplastic Twinning in an Ultrafine $TiAl/Ti_3Al$ Laminate Composite 139
L. Ti-6Al-4V Billet Feedstock Manufacture and Evaluation 147
M. High-Density Infrared Surface Treatment of Materials for Heavy-Duty Vehicles 151
N. High-Temperature Aluminum Alloys 155
O. Application of Titanium Alloys for Heavy-Duty Vehicles 163
P. Mechanical Behavior of Ceramic Materials for Heavy-Duty Diesel Engines 169
Q. Powder Processing of Nanostructured Alloys Produced by Machining 179
R. Deformation Processes for the Next-Generation Ceramics 185
S. Development of Titanium Component Applications in Heavy-Duty Diesel Engines 191
T. High-Speed Machining of Titanium 199

5. TEST AND MATERIALS STANDARDS 207

A. Rolling Contact Fatigue 207
B. Implementing Agreement for a Programme of Research and Development on Advanced Materials for Transportation Applications 215
C. Mechanical Property Test Development 223
D. An Integrated Surface Modification of Engineering Materials for Heavy Vehicle Applications 231

Appendix A. ACRONYMS AND ABBREVIATIONS 237

1. INTRODUCTION

Heavy Vehicle Propulsion Materials

Advanced materials are an enabling technology for fuel-efficient heavy-vehicle truck engines. The Heavy Vehicle Propulsion Materials Project is organized around the following technology issues: fuel systems; exhaust aftertreatment; air handling, hot section, and structural components; and standards.

Materials for Fuel Systems

Currently, the fuel system represents a significant portion of the cost of a heavy-duty diesel engine. Enabling materials and cost-effective precision manufacturing processes are instrumental in developing improved fuel injection systems. In addition to new and improved materials, improved manufacturing and inspection methods for the injector components are being developed.

Manufacturing technology for nickel aluminide–titanium carbide cermet fuel system components continued this year in coordinated efforts at Oak Ridge National Laboratory (ORNL), CoorsTek, Inc., and Cummins, Inc. ORNL supplied a large pilot-scale batch of processed powder mixtures with alternate Ni_3Al precursors to CoorsTek (a parts supplier) for injection molding of test components and completed work with CoorsTek for scale-up of the manufacturing process. Sintered parts were supplied to Cummins Engine for rig testing of machined components.

A novel "pin-on-twin" scuffing test has been developed to evaluate fuel injector materials in diesel fuel and low-sulfur fuel environments in a simulated fuel system environment. It is in beneficial use for evaluating fuel system materials. The system is available to users of the High Temperature Materials Laboratory (HTML) at ORNL, as well as to the Propulsion Materials Program.

Materials for Exhaust Aftertreatment

The reduction of nitrogen oxides (NO_x) and particulate emissions is critically important to the Office of FreedomCAR and Vehicle Technologies (OFCVT) program and is highly materials dependent. The U.S. Department of Energy (DOE) goals for improved efficiency of heavy vehicles are greatly complicated by engine design and exhaust aftertreatment technologies designed to meet the mandatory U.S. Environmental Protection Agency (EPA) emission regulations for 2007 and 2010. Materials and systems research is being conducted to minimize the potentially negative effects of emission-reduction technologies on fuel economy and to result in cleaner and more efficient engines.

The durability of exhaust aftertreatment systems in heavy vehicles is a concern. A lifetime of at least 500,000 miles is expected, and a 1,000,000-mile lifetime is desired (compared with 100,000 miles for automobiles). Exposure of the aftertreatment systems to high temperatures, vibration, erosion, and chemical attack by species in the oil and fuel results in degradation of performance. The effects of exposure in service on the microstructure and microchemistry of the aftertreatment systems are being characterized, and this research may lead to the development of more durable systems. The development of advanced NO_x sensors is being pursued to facilitate optimal engine and aftertreatment control strategies.

Accomplishments this year included significant progress in a collaborative Ford–ORNL program intended to facilitate deployment of a NO_x trap for lean diesel or gasoline exhaust by (1) investigating materials issues related to deterioration of NO_x trap performance with aging as a result of thermal and sulfation-desulfation cycles and (2) investigating materials that are robust under the lean NO_x trap operating conditions. The latter objective includes the synthesis of new materials. Accomplishments of this effort include completing a study

of microstructural changes in a series of model catalysts during aging under lean and rich conditions at 500°C; beginning the updating of the ex-situ reactor to enable transmission electron microscopy (TEM) sampling under lean, rich, or stoichiometric conditions as well as lean-rich cycles; and equipping a new synthesis laboratory for the preparation of NO_x trap materials.

A new agreement was initiated entitled "Catalyst Materials by Design." The effort is led by a team that includes ORNL, the University of Notre Dame, and the University of California at Davis. The objective is to search for durable emissions catalysts by means of an integrated approach using computational modeling, synthesis and processing, characterization via high-resolution scanning TEM/TEM, and testing of catalyst materials. Computational modeling was carried out using density-functional-theory–based first-principles calculations. A series of platinum and rhenium (Re) nanoclusters, Re nanoclusters, and carbonylated Re clusters supported on commercial alumina were synthesized and characterized with respect to the size and chemistry of atomic clusters and the performance of the clusters in contact with carbon monoxide, NO_x, and hydrocarbons.

Research conducted at the High Temperature Materials Laboratory at ORNL is focused on the development and utilization of new capabilities and techniques for ultra-high-resolution scanning TEM/TEM to characterize the microstructures of catalytic materials of interest for reducing NO_x emissions in diesel and automotive exhaust systems. This research aims to relate the effects of reaction conditions on the changes in morphology of heavy metal species on "real" catalyst support materials, typically oxides. During this period, the morphologies of tri-rhenium carbonyl clusters on gamma-alumina support material were characterized at the atomic level to demonstrate for the first time the unambiguous imaging of clusters of known structure. Also, the nature of platinum catalyst structures on mixed-oxide support materials was characterized, including the imaging of platinum species dispersed as single atoms and in precrystalline clusters known as "rafts."

Exhaust aftertreatment materials projects are ongoing at both Caterpillar and Cummins. These projects are significant in that they represent a departure from an earlier culture in which the diesel engine companies relied heavily on catalyst manufacturers to provide the needed technologies and did not actively participate in the development of catalyst materials. These diesel engine manufacturers are actively collaborating with catalyst suppliers in the development of improved catalyst materials, and they are contributing to the development of a fundamental understanding of catalyst performance that is important to both suppliers and users of catalyst systems. In addition to the in-house efforts at Caterpillar and Cummins, Cummins and ORNL collaborated, through cooperative research and development agreements, in characterizing lab- and engine-tested catalysts via X-ray diffraction, spectroscopy, and microscopy. They also collaborated in characterizing diesel particulate filters and developing probabilistic design tools to predict the useful lifetimes of the filters.

Ford Motor Co. and ORNL are collaborating on the development of a NO_x sensor that can be used in systems for on-board remediation of diesel engine exhaust. The sensor should have an operating temperature of 600–700°C and be able to measure NO_x concentrations from 1 to 1500 ppm at oxygen levels from 5 to 20 vol %. Prototype sensing elements are fabricated by patterning electronically conductive and catalytic layers onto oxygen-ion–conducting substrates. The sensing elements are characterized for NO_x response, oxygen sensitivity, and response time. Accomplishments this year included developing sensing elements that display near "total NO_X" behavior and are stable in simulated long-term service.

Materials for Air Handling, Hot Section, and Structural Applications

Engine design strategies for meeting EPA emission requirements have resulted in the need for significantly higher turbocharger boost. The higher boost requirements result in higher heat of compression and greater thermal and fatigue loads on turbocharger components.

Caterpillar began a new project in 2003 to design and fabricate a cost-competitive diesel engine turbocharger, using lightweight titanium materials, that provides a reduction in both fuel consumption and transient emissions. Caterpillar has designed a series turbocharger for use on the C15 engine platform. This turbocharger consists of one turbo wheel and two compressor wheels that are attached to a single rotating drive shaft. This compact design will replace the two-turbocharger system that is presently installed in the C15 engine. Titanium aluminide will be used for the turbo wheel, and one of the compressor wheels will be made from a titanium alloy. The project was completed this year. Highlights include successfully developing joining technology for the rotor and shaft, evaluating the physical and mechanical properties of commercially available materials, and accessing the commercial viability of the advanced turbocharger.

Caterpillar and ORNL won a 2003 R&D 100 Award for the development of CF8C-Plus cast stainless steel. The new high-temperature stainless steel may have near-term applications in diesel engine exhaust manifolds and turbocharger housings. Highlights include demonstrating that CF8C-Plus cast stainless steel is far superior to SiMo cast iron at 600°C and above. CF8C-Plus also shows strength, creep resistance, and aging resistance benefits compared with other commercial cast stainless steels being considered for heavy-duty diesel turbocharger housings at 750°C. Significant progress has been made in commercializing the alloy: a 6700-lb gas-turbine end-cover was cast from CF8C-Plus at MetalTek. MetalTek has cast more than 30,000 lb for various applications.

Caterpillar, in collaboration with Argonne National Laboratory and ORNL, has a project to design and fabricate prototype engine valves from silicon nitride and TiAl materials that are 30% lighter than steel valves, provide a 200% increase in service lifetime, and potentially increase fuel efficiency in advanced engines by 10%. A probabilistic design approach was developed for the high-hardness valve materials. The friction welding of TiAl valve heads and Ti-6V-4Al valve stems was successfully optimized. The effects of surface finish on the performance of silicon nitride valves were evaluated, and the results indicated that valves with good surface finish performed well in bench tests.

This year, in preparation for an engine test to be conducted in FY 2006, test valves were procured and characterized for dimensional and surface properties and via laser-scattering for surface or sub-surface defects. In addition, an evaluation of the machinability of TiAl was initiated, along with a study of friction, wear, and corrosion of the alloy. A Caterpillar C15 ACERT™ engine was donated to the National Transportation Research Center for future component testing.

Caterpillar is also developing innovative approaches to thermal barrier and wear-resistant coatings for engines. Durability issues for thermal sprayed coatings, particularly thermal barrier coatings, remain the major technical challenge to their implementation in new engine designs. New approaches to coating design and fabrication are being developed to aid in overcoming this technical hurdle. A highlight from this year is the coating of pistons for a homogeneous charge compression ignition system with amorphous steel for single-cylinder engine testing.

The feasibility of reducing the weight of a heavy-duty engine by substituting a lighter material for the cast iron engine block and cylinder head was evaluated by ORNL and Ricardo, Inc. Finite element analysis was used to compute the stresses, temperatures, and fatigue safety factors of a 5.9-L diesel engine, run at the maximum design power, for three lightweight casting alloy systems: titanium, aluminum, and magnesium. The analysis indicated the feasibility of simple material substitutions in all cases, with the exception that the titanium alloy cylinder head will require inserts to reduce the temperature in the valve bridge area. Reducing the weight of the entire engine by up to 33% for the magnesium alloy and 20% for the aluminum alloy, and up-rating the power of the engine by 50% while reducing the weight by 15% for the titanium alloy, were predicted to be feasible.

Efforts in cost-effective manufacturing were carried out by ORNL, the University of Michigan, and Purdue University. Technology for machining difficult materials, such as titanium alloys, was developed in the ORNL/University of Michigan collaboration. ORNL characterized the grinding characteristics of TiC/Ni_3Al matrix cermets that are promising candidates for diesel engine fuel injector plungers and wear parts, and investigated the possibility of using cermets as cutting tool materials for high-speed titanium machining. The University of Michigan and ORNL participated in a consortium of manufacturers led by Third Wave Systems, Inc., to develop finite-element-analysis–based machining modeling software and to acquire new machining process modeling capabilities. Purdue University is investigating the consolidation of low-cost machining chips to produce nanocrystalline components with high strength and hardness.

Materials and Testing Standards

OFCVT has an International Energy Agency "Implementing Agreement for a Programme of Research and Development on Advanced Materials for Transportation Applications." Accomplishments this year include the development by NIST of a new design principle for surface texture design to enable friction reduction under boundary lubrication conditions.

NIST also leads a project to develop standard testing methods for advanced materials, primarily ceramics. During this year, NIST revised, refined, and improved several current ASTM and ISO standards.

The rolling contact fatigue (RCF) effort is led by ORNL. Its objectives include the characterization of the RCF performance of ceramics and tribological coatings; determination of the effects of subsurface damage, microstructure, material properties, and contact stress on RCF performance; and correlation of RCF performance measured by different internationally-used RCF test techniques. Highlights this year include completion of a summary report on RCF test methods and result interpretations used in Germany, Japan, United Kingdom, and the United States and the
development of a method to evaluate and discriminate the elastic properties of ball bearings in situ using resonance ultrasound spectroscopy.

Rogelio Sullivan
Team Leader, Materials Technologies
Office of FreedomCAR and Vehicle Technologies
Energy Efficiency and Renewable Energy

James J. Eberhardt
Technology Development Area Specialist
And Chief Scientist
Office of FreedomCAR and Vehicle Technologies
Energy Efficiency and Renewable Energy

2. MATERIALS FOR FUEL SYSTEMS

A. Low-Cost, High-Toughness Ceramics

T. N. Tiegs, F. C. Montgomery, and J. O. Kiggans
Oak Ridge National Laboratory
P.O. Box 2008, MS-6087
Oak Ridge, TN 37831-6087
(865) 574-5173; fax: (865) 574-4357; e-mail: tiegstn@ornl.gov

DOE Technology Development Area Specialist: James J. Eberhardt
(202) 586-9837; fax: (202) 586-1600; e-mail: james.eberhardt@ee.doe.gov
ORNL Technical Advisor: D. Ray Johnson
(865) 576-6832; fax: (865) 574-6098; e-mail: johnsondr@ornl.gov

---

Contractor: Oak Ridge National Laboratory, Oak Ridge, Tennessee
Prime Contract No: DE-AC05-00OR22725

Objectives

- Demonstrate that significant improvement in the reliability of structural ceramics for advanced diesel engine applications could be attained if the critical fracture toughness (K_{Ic}) were increased without strength degradation.
- Confirm that cost is a major factor in determining the applicability of new materials in engine components.
- Develop high-toughness materials that are also low cost.

Approach

- Show that TiC-Ni_3Al composites have a combination of superior physical properties and mechanical behavior using conventional powder processing methods.
- Develop TiC-based composites with 40–60 vol % Ni_3Al because they have expansion characteristics very close to those for steel.
- Collaborate development effort with CoorsTek, Inc., and Cummins Engine on processing scale-up and engine testing.
- Determine initial mechanical properties of ceramic-particulate-reinforced TiAl composites and make assessment of application in heavy vehicle systems.

Accomplishments

- Supplied large pilot-scale batch of processed powder mixtures with alternate Ni_3Al precursors to CoorsTek for injection molding of test components.
- Completed work with CoorsTek, Inc., (a parts supplier) for scale-up of the processing and to supply them with pilot plant scale quantities of powder mixtures for injection molding trials.
- Supplied sintered parts produced in conjunction with CoorsTek to Cummins Engine Co. for rig testing of machined components.

Future Direction

- End the project with the transfer of the TiC-Ni_3Al cermet technology to industry.

Introduction

TiC-Ni_3Al composites are under development for application in diesel engines because of desirable physical and mechanical properties. For these applications, the Ni_3Al volume contents are on the order of 30 to 50 vol % to match the thermal expansion of steel. Typically, flexural strengths greater than 1000 MPa up to 800°C and fracture toughnesses higher than 15 MPa $\sqrt{m}$ are obtained for the composites. The composites are densified by liquid phase sintering, and most of the early work used gas-atomized Ni_3Al particles with fine TiC powders. Later work was done using nickel and NiAl powders (along with the TiC) to form Ni_3Al by an in situ reaction during sintering. Over the last few years the in-situ reaction process was developed significantly because it produced high mechanical properties and developed a fine TiC grain size. The finer grain sizes were favored because of better wear resistance.

The fabrication techniques and equipment employed in production are very similar to those for the fabrication of WC-Co hard metals, and thus, the processing costs are well established. However, when the economics of producing the TiC-Ni_3Al composites was examined, a significant cost was associated with the use of the NiAl precursor powder (about 55% of the total raw material cost). Because the costs of the starting raw materials can be a significant fraction of the total cost of a component, alternative materials for fabricating the cermets are of interest. Part of the reason for the high cost of the NiAl is that it is produced only as a specialty powder at the present time. The development effort is being done in collaboration with CoorsTek, Inc.

Results

Alternate Precursors for Ni_3Al Formation

All previous work used a combination of nickel and NiAl for an in-situ reaction to form the Ni_3Al. A new NiAl commercial source has been identified and powder procured. Characterization of the powder by x-ray diffraction indicated that it was stoiciometric and had a pattern identical to earlier material from a different supplier. Particle size analysis showed the mean particle size was ~9.8 µm, which was similar to the previous material. However, the size distribution was broader than the earlier NiAl.

A large batch (3 kg) of TiC-50 vol % Ni_3Al powder was processed with the new NiAl powder and shipped to CoorTek for injection molding (IM) trials. Test parts were fabricated and shipped back to Oak Ridge National Laboratory (ORNL). Initial sintering results indicated the densification behavior was similar to the earlier composites, but slightly less: 6.05 g/cm^3 vs 6.11 g/cm^3.

Based on those results, new IM tooling was designed and fabricated at CoorsTek. Several large batches (>15 kg total) of TiC-50 vol % Ni_3Al powder were milled, homogeneously mixed, and shipped to CoorsTek. Parts with the new tooling have been IM and returned to ORNL. The specimens are currently awaiting sintering when the furnace is repaired.

While the initial sintering results indicated the densification behavior was similar to the earlier composites, flexural strength measurements revealed a rather low strength in comparison to the previous material from a different NiAl manufacturer. The comparison was 945 ± 150 MPa for the earlier materials and 600 ± 37 MPa for the newest batch. Scanning electron microscopy (SEM) examination of a fracture surface showed numerous agglomerates ≤100 µm in size. Energy dispersive x-ray analysis (EDAX) indicated they were NiAl particles. Evidently the new batch of NiAl powder contained larger particles (even though the powder was listed as <44 µm).

A modified milling procedure was instituted with the NiAl, and particle size analysis indicated all particles were <10 µm. Sintering of test parts with the modified powder was improved, and densities of ~6.11 g/cm^3 were obtained. This density is equal or better than the previous high-strength materials. A test batch (~3 kg) of powder with the modified milling procedure has been sent to CoorsTek for IM. Parts and test MOR bars have been sintered at ORNL and returned to CoorsTek for testing. Sintering behavior of these injection molded materials was similar to previous cermets, and the microstructure showed no unusual defects. Consequently, a large batch (>12 kg total) was fabricated and sent to CoorsTek for IM of test parts.

Assessment of Ceramic-Particulate-Reinforced TiAl Composites

TiAl offers significant improvements in weight-to-strength ratios compared to most advanced alloys. Such materials could have applications in heavy vehicle propulsion systems. Ceramic-metal composites that utilize TiAl as the bonding phase potentially could show increased fracture strength, higher elastic modulus, better creep resistance, and higher wear resistance than the base alloy. An exploratory study was initiated to fabricate ceramic-particulate-reinforced TiAl composites and determine the mechanical properties. Initial samples were fabricated by hot-pressing to readily obtain high-density specimens suitable for testing. An assessment was made to determine if the mechanical properties are suitable for further development for heavy vehicle applications.

Several compositions were fabricated including: TiC-50 vol % TiAl, TiN-50 vol % TiAl, and TiC-67 vol % TiAl. The TiAl was an alloy with the composition, Ti-48 Al-2 Cr-2 Nb, which has been shown to have excellent properties. The powder mixtures were made using similar methods to those used for the TiC-Ni_3Al cermets. Hot-pressing produced samples with closed porosity and densities of 94–95% theoretical density. Microstructural examination revealed good wetting and distribution of the TiC and TiAl particles. No obvious core-rim structure (like those observed with TiC-Ni_3Al cermets) was observed. However, the TiC did appear to have reacted with the TiAl to produce a reaction zone surrounding remnant TiC particles. EDAX showed these zones to contain Ti, Al, Nb, Cr, and C. X-ray diffraction (XRD) results indicated the formation of Ti_3AlC_2, which confirmed a reaction occurred between the TiAl and the TiC.

In contrast to the TiC, the TiAl did not appear to have wet the TiN particles very well. A reaction between the TiAl and the TiN was also evident, and EDAX indicated a metallic phase of Ti-Al-Nb-Cr and a second phase of Ti-Al-N. XRD showed the formation of $AlTi_2N$, indicating a reaction between the starting components. Indent hardness determinations showed the hardness was lower than similar ceramic particle volume loadings in Ni_3Al-based cermets. For example, the hardness of the TiC-50 vol % TiAl, TiN-50 vol % TiAl, and TiC-67 vol % TiAl composites was 4.0–4.6 GPa, 5.7–5.8 GPa, and 4.2–4.3 GPa, respectively. For comparable TiC-50 vol % Ni_3Al cermets, the hardness values would be >8 GPa.

Because of the reactions between the TiAl alloy and the TiC or TiN reinforcements, the prospects for sintering materials and obtaining good mechanical properties is not encouraging. However, other ceramic particles, such as TiB_2, ZrB_2, HfB_2, and Al_2O_3, should be compatible in the TiAl alloy matrix and provide reinforcement.

Conclusions

Pilot-scale batches of TiC-Ni_3Al composite mixtures with alternate Ni_3Al precursors were produced and supplied to CoorsTek for IM of test components. The prospects for sintering TiAl-based materials and obtaining good mechanical properties is not encouraging. However, other ceramic particles, such as TiB_2, ZrB_2, HfB_2, and Al_2O_3, should be compatible in the TiAl alloy matrix and provide reinforcement.

Presentations and Publications

T. N. Tiegs, "Aluminide Bonded Ceramic Composites," at the American Ceramic Society Conference on Advanced Ceramics and Composites, Cocoa Beach, Florida, January 23–27, 2005.

T. N. Tiegs, F. C. Montgomery, P. A. Menchhofer, and P. F. Becher, "Aluminide Bonded Ceramic Composites," to be published in *Ceram. Eng. Sci. Proc., Am. Ceram. Soc.*, Westerville, Ohio (2005).

T. N. Tiegs, "High Toughness Materials—TiC-Ni_3Al Cermets," at the Heavy Vehicles Materials Peer Review, Oak Ridge, Tennessee, September 13–15, 2005.

3. MATERIALS FOR EXHAUST AFTERTREATMENT

A. Materials for Exhaust Aftertreatment

Corey Shannon, Herbert DaCosta, Julie Faas, Matt Stefanick, Svetlana Zemskova, Christie Ragle, Ronald Silver, Paul Park, and Craig Habeger
Caterpillar, Inc.
P.O. Box 1875
Peoria, IL 61656
(309) 578-4065; fax (309) 578-2953; e-mail: park_paul_w@cat.com

DOE Technology Development Area Specialist: James J. Eberhardt
(202) 586-9837; fax: (202) 586-1600; e-mail: james.eberhardt@ee.doe.gov
ORNL Technical Advisor: D. Ray Johnson
(865) 576-6832; fax: (865) 574-6098; e-mail: johnsondr@ornl.gov

---

Contractor: Oak Ridge National Laboratory, Oak Ridge, Tennessee
Contract No.: DE-AC05-00OR22725
Subcontractor: Caterpillar, Inc., Peoria, Illinois

Objectives

- Develop advanced materials applied for diesel engine aftertreatment systems that will comply with future emission regulations.
- Assess impact of phosphorus on oxidation, lean-NO_x, NO_x adsorber (LNT) and urea-SCR (selective catalytic reduction) catalysts.
- Identify diesel particulate filter (DPF) substrate materials that have high durability and filtration efficiency with minimum impact on engine efficiency.

Approach

- Assess impact of phosphorous on aftertreatment systems by comparing fresh and aged catalyst performance using a fuel burner and a bench test system.
- LNT: Evaluate phosphorus impact on NO oxidation, NO_x storage and reduction functions.
- Urea-SCR: Evaluate phosphorus impact on zeolite and vanadia based catalysts using temperature and NH_3/NO_x ratio sweeps.
- Oxidation catalyst: Develop a correlation between bench and field in terms of deactivation mechanisms.
- Use previously developed test protocol to evaluate filtration efficiency and pressure drop of catalyzed and uncatalyzed DPF samples from various suppliers.

Accomplishments

- Completed lean-NO_x project (unfinished tasks carried over from last year).
  - Sulfur impacts on catalytic performance more severely than phosphorus.
  - Paraffins contributed lean-NO_x catalysis; however, benzene and mono-cyclo-paraffin were not active reductants, whereas aromatics and dicyclo-paraffin inhibited the catalytic reaction.

- Identified the cause of LNT deactivation due to phosphorus exposure.
  - NO_x storage capacity function was affected first and more severely than NO oxidation and NO_x reduction.
  - Phosphorus impacted the NO_x storage function more at low NO_x slip than at high NO_x slip conditions.
  - A model was used to estimate the impact of phosphorus deactivation on fuel penalty for the LNT.
- Identified the cause of vanadia- and zeolite-based SCR catalysts deactivation due to phosphorus exposure.
  - Phosphorus similarly impacted both NH_3 and NO conversions.
  - Zeolite catalyst showed higher phosphorus tolerance initially, but both catalysts had similar deactivation after extended exposure.
  - Speculate that phosphorus blocked NH_3 adsorption sites, which prevented NO reduction.
- Found that phosphorus impacted LNTs more than SCRs, but presented a challenge for both catalyst technologies.
- Identified a promising DPF substrate material with filtration efficiency larger than 95% and pressure drop significantly lower than conventional cordierite material.

Future Direction

- Capture intellectual property and identify a partner for commercialization (lean-NO_x project).
- Assess impact of combination of phosphorus, sulfur, and thermal deactivation on oxicat, LNT, and SCR catalysts.
- Explore mitigation strategies for phosphorus, sulfur, and thermal deactivation phenomena.
- Evaluate the effect of thermal deactivation on filtration efficiency of new DPF substrate materials.

Introduction

The objective of this project is to develop and evaluate materials that will be utilized in aftertreatment systems for diesel engine applications to comply with future government emission regulations. The materials include catalysts for NO_x abatement and filtration media for particulate matter control. This year's focus is on the determination of the effect of phosphorus deactivation on the performance of LNTs, SCR catalysts and oxidation catalysts, and on identifying diesel particulate filter (DPF) substrate materials that have high durability and filtration efficiency with minimum impact on engine efficiency.

Approach

Catalyst Deactivation

The study was focused on identifying the impact of phosphorus exposure on catalyst formulations by testing the performance of fresh and aged catalysts. The aged catalysts were prepared by exposing to phosphorus in a diesel fuel burner using a diesel fuel doped with tricresyl phosphate that mimicked the effect of phosphorus from combusted lube oil. Using x-ray florescence (XRF), we analyzed the amount of phosphorus adsorbed as a result of this exposure.

PM Trap

A developed test protocol was used to evaluate filtration efficiency and pressure drop of catalyzed and uncatalyzed DPF samples from various suppliers. In order to test DPF core samples that are supplied in sizes larger than 1 in. × 3 in., we designed and built a new chemical reactor with the capability to hold samples up to 2 in. × 6 in.

Results

Catalyst Deactivation

Lean-NO_x Catalyst Durability: Durability studies using sulfur and phosphorus aging have been performed on the Lean-NO_x catalyst developed from the previous study. Phosphorus was introduced to the sample using a diesel fuel burner burning phosphorus-blended zero-sulfur fuel, and the NO_x reduction performance was tested after each exposure increment. NO_x reduction of the catalyst maintained more than 40% NO_x conversion after reaching 30,000 h engine-equivalent (C15 engine)

phosphorus exposure (Figure 1). Phosphorus content of the aged samples was quantified using XRF.

Sulfur was introduced by SO_2 exposure directly using a bench test system, monitoring the NO_x reduction performance as a function of time-on-stream with SO_2. Sulfur content of the exposed samples has been quantified using a LECO CS-200 Carbon/Sulfur Determinator. NO_x reduction performance of the catalyst was reduced to ~30% NO_x reduction after 100-h engine-equivalent (C15 engine) sulfur exposure.

The negative impact of sulfur exposure was more pronounced than that of phosphorus exposure, both in magnitude and rate of degradation. Understanding the effects of sulfur and phosphorus provided insight into the development of catalyst materials and led to mitigation options best suited for the intended environment.

Lean-NO_x Catalyst Sensitivity to Diesel Fuel Components: A reductant study over the selected combination catalyst has demonstrated much lower activity when diesel fuel was used as a reductant compared to the desired reductant (example: dodecane). The influence of diesel fuel components on NO_x reduction performance has been investigated using a bench test system to determine the source of the activity loss (test condition: 500 ppm NO_x, 3000 ppm liquid hydrocarbons as C_1, 7% H_2O, 9% O_2, 50 ppm propene, 500 ppm CO, and 8% CO_2 with 35,000 h^{-1} space velocity). Mixtures were prepared such as 80% of dodecane and 20% of various organic hydrocarbons, including paraffin, isoparaffin, aromatic, diaromatic, and combinations thereof. Isoparaffins (max. 74% NO_x reduction) showed NO_x reduction performance at a similar level to dodecane (77%) (Figure 2). Monoaromatics and variations on

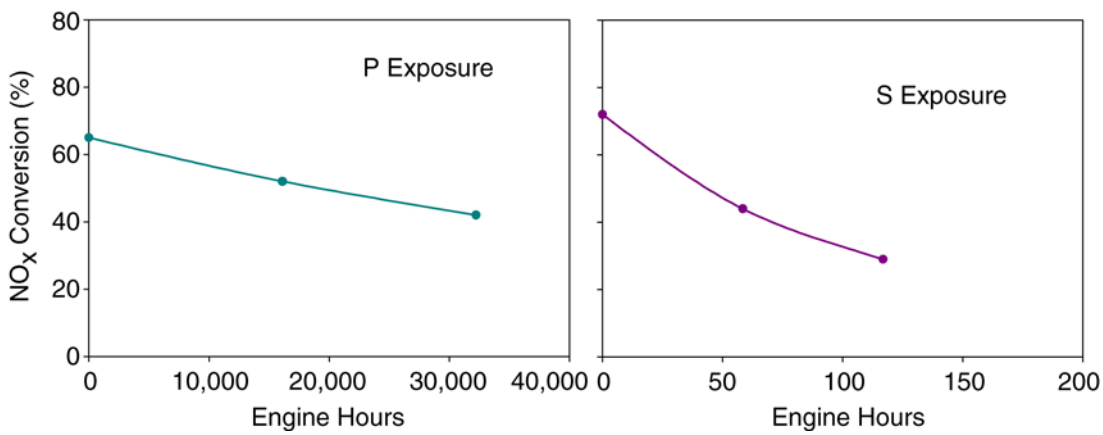

Figure 1. The effect of phosphorus and sulfur on the developed lean-NO_x catalyst performance based on C15 Caterpillar engine equivalent hours exposure.

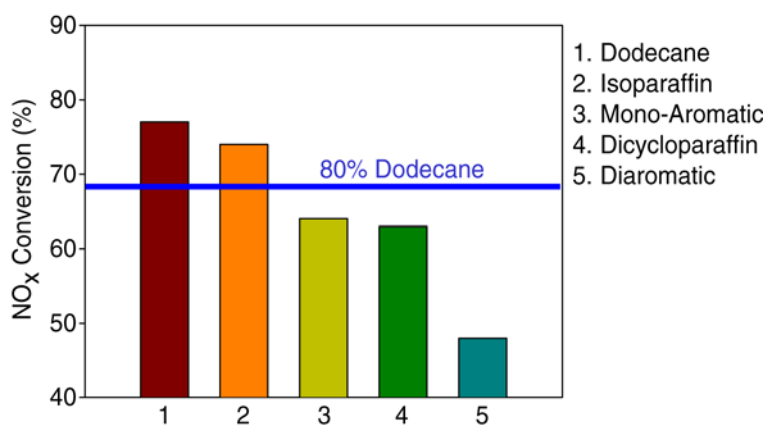

Figure 2. The effect of diesel component on lean-NO_x catalyst performance (20% of diesel components mixed with dodecane).

paraffins had a neutral effect on the NO_x reduction performance. Among the types of reductants tested, diaromatics strongly hindered the performance of the combination catalyst (48%), also shifting the operation temperature to a higher temperature range. Understanding the effects of fuel components provided insight into the development of catalyst materials as well as a fuel processor to obtain the proper reductant from diesel fuel to supply to the catalyst for maximum performance.

NO_x Adsorber Catalyst Durability: A series of model LNTs were prepared by coating 400-cpsi cordierite monolith cores with γ-Al_2O_3 washcoat. The cores were then dipped in cerium acetate solution, dried, then calcined at 550ºC for 5 h to give a loading of 20 wt % CeO_2. The process was repeated with a barium acetate solution to give a loading of 11 wt % BaO, and then with platinum/rhenium nitrate solution, resulting in a loading of 5 wt % platinum and 0.6 wt % rhenium. The finished catalysts were reduced in 5% H_2 at 350ºC for 2 h. The finished catalysts were tested for NO_x conversion using a laboratory reactor with 1-in. diameter by 3-in.-long catalyst cores at a space velocity of 55,000 h^{-1}. Each sample was degreened at 275ºC for 20 min in a reducing gas (2.5% H_2, 2.5% CO, 5% CO_2, 5% H_2O, balanced with N_2), then switched to an oxidizing mix (12% O_2, 5% CO_2, 5% H_2O, balanced with N_2). The 200-ppm NO_x (10% NO_2) was added to load the samples with NO_x. After saturating the samples with NO_x at 275ºC, the LNTs were ramped to 425ºC in the oxidizing mix without the NO_x, regenerated in the reducing gas, and reloaded with NO_x. After determining the initial performance of the model LNT, the sample was exposed to 3.6 g/L of phosphorus using a diesel fuel burner with phosphorus-doped fuel at 250ºC. The aged sample was then reanalyzed for NO_x conversion in the lab reactor. The aging process was repeated to increase phosphorus exposure to 10 g/L.

The NO oxidation to NO_2, NO_x storage, and NO_x reduction function of the NO_x adsorbers was tested after loading with 3.6 and 10 g/L phosphorus, with and without a blank monolith in front as a phosphorus getter. Results indicate that phosphorus degrades LNTs. The NO oxidation function was not affected by the exposure of 3.6 g/L phosphorus; however, the NO to NO_2 conversion dropped from 45% to about 35% after exposure to 10 g/L phosphorus.

In contrast to the relatively stable NO oxidation to NO_2 function, a significant impact was observed on the catalyst NO_x storage capacity even on exposure to 3.6 g/L of phosphorus. Figure 3 shows that at 20% NO slip, the moles of NO_x stored per mole of available barium in the LNT dropped by 65%. Furthermore at a constant storage capacity of 0.05 moles NO_x/mole barium, the NO_x slip increased from 6% on a fresh LNT to 30% after 3.6 g/L phosphorous, and to 90% after exposure to 10 g/L phosphorous.

The reduction of NO to N_2 under the rich condition was negatively affected by the loss of NO_x storage capacity. Figure 4 shows the NO_x storage capacity at 80% slip of a series of fresh LNTs

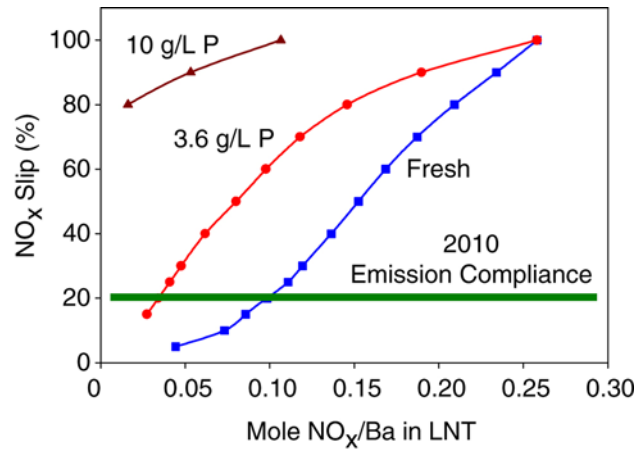

Figure 3. The effect of phosphorus exposure on LNT NO_x storage for three different phosphorus exposures.

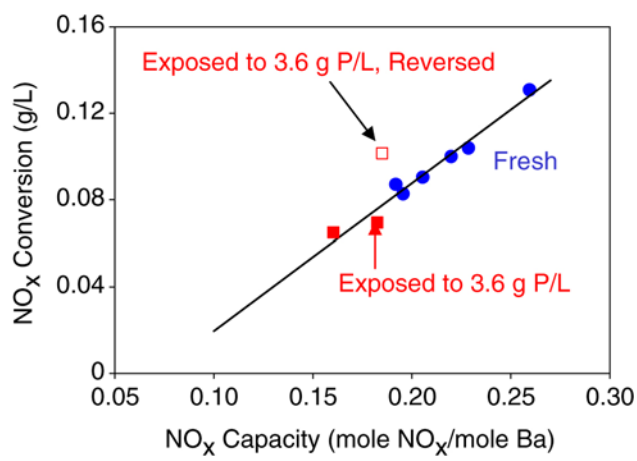

Figure 4. The effect of phosphorus exposure on LNT reduction of NO_x in a rich gas stream.

plotted against the amount of NO_x conversion. A straight line was fit to the data with a correlation coefficient of 0.968. Exposing the catalysts to 3.6 g/L phosphorus reduced the storage capacity and thus decreased the NO_x reduction. However, testing the LNTs in the opposite direction from which they were exposed to phosphorus revealed a significant boost in NO_x conversion from 0.0695 to 0.1014 g/L. When the LNT cores are exposed to phosphorus, the phosphorus tends to deposit in a nonuniform profile with the greatest amount of phosphorus in the front of the core and less phosphorus in the rear. Any NO_x introduced to the front of this aged sample cannot be adsorbed until it gets far enough into the core where phosphorus is not blocking the adsorption sites. Upon switching to rich gas, the front section of the aged LNT has no NO_x to release, and thus no reduction occurs. If NO_x containing gas is introduced at the rear of the core, NO_x begins storing immediately inside the new entrance of the sample because of the low phosphorus part of the sample. In this case, when the system is swept by rich gas, the upstream section of the LNT has stored NO_x to release, and the rhenium in the downstream (high phosphorus part of the sample) can reduce the NO_x to N_2. Thus the rhenium in the LNT appears to remain active for NO reduction even if no NOx is stored due to the phosphorus-blocking adsorption sites.

Results from this first phase of study show that phosphorus deactivation may become a significant source of deactivation as durability requirements become increasingly stringent. For LNTs, the NO_x storage capacity function is affected first and most strongly.

SCR Catalyst durability: Zeolite- and vanadia-based SCR catalysts were provided by a catalyst supplier. The samples were degreened according to the company's recommended procedure prior to testing. Both sets of samples were evaluated using a temperature ramp from 100 to 550°C in lean conditions at an NH_3/NO_x ratio of 1.11. After determining the initial activity of the SCR catalysts, samples were exposed to 3.6 g/L of phosphorus using the previously described diesel fuel burner with phosphorus-doped fuel at 250°C. The aged sample was then re-analyzed for NO_x conversion in the lab reactor. The aging process was repeated to increase phosphorus exposure to 10 g/L. Figure 5 shows the results over the fresh and 3.6-g/L phosphorus-exposed vanadia-based samples.

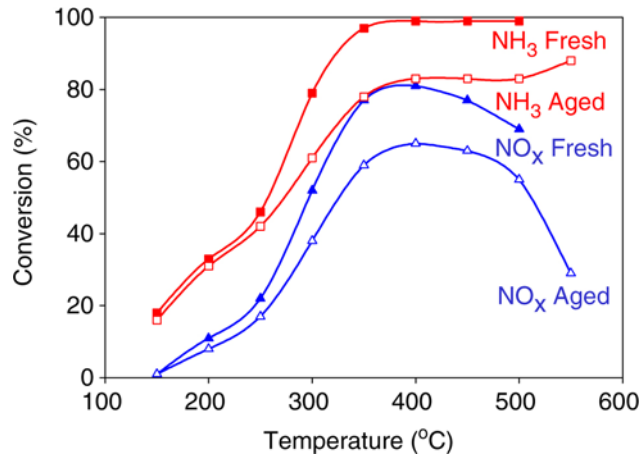

Figure 5. The effect of 3.6-g/L phosphorus exposure on NH_3 and NO_x conversion over vanadia SCR.

The results shown in Figure 5 indicate the vanadia-based SCR catalyst is strongly impacted by 3.6-g/L phosphorus exposure, especially at temperatures above 300°C. Both NO_x and NH_3 conversions are impacted, and to the same degree. As the temperature is increased above 450°C, the NH_3 oxidation reaction becomes significant over this catalyst, and thus the NO_x conversion decreases due to ammonia reacting to become NO. In other results (not shown), the rate of ammonia oxidation appears to increase relative to the rate of the SCR reaction with phosphorus exposure. As the phosphorus begins to block active sites, the first sites lost will be those involving adjacent pairs of vanadia for NO_x reduction, and the other vanadia sites will be available for a longer period of phosphorus exposure. Since the SCR reaction requires two adjacent vanadia sites and ammonia oxidation only requires one site, this could explain the observed effect on relative rates (NH_3 oxidation vs NO_x reduction).

The same tests were run with the zeolite-based SCR. Figure 6 shows the results over the fresh and 3.6-g/L phosphorus exposed zeolite-based catalysts. Compared to Figure 5, the zeolite appears to be less affected by this level of phosphorus than the vanadia catalyst. The effect of phosphorus seems to be relatively constant across a range of temperatures in this case. Both the NO_x and NH_3 conversions are affected to a similar degree. Unlike the vanadia sample, the zeolite catalyst does not show a significant drop in NO_x conversion at temperatures above 450°C due to ammonia oxidation.

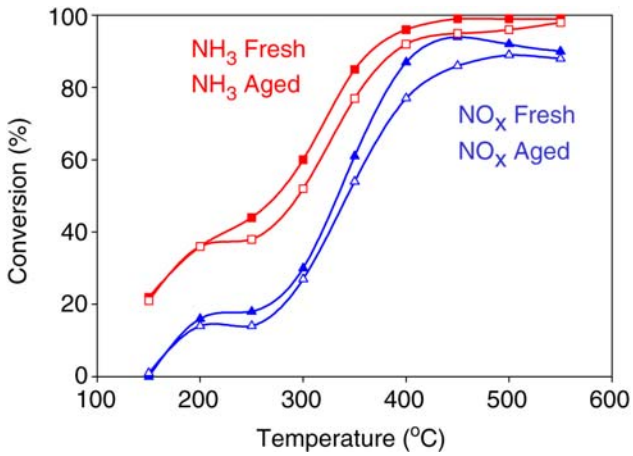

Figure 6. The effect of 3.6-g/L phosphorus exposure on NH_3 and NO_x conversion over zeolite SCR.

The results from tests of fresh and aged samples of both types were then compared using an Arrhenius type plot assuming pseudo first-order kinetics. The results in Figure 7 show that similar kinetics for the SCR reaction occur on both catalyst types.

Below 400°C, the impact of phosphorus on the reaction rate is lower because a significant portion of the SCR reaction takes place in the bulk, where the phosphorus does not penetrate. At temperatures above 400°C more and more of the reaction relatively occurs on the top surface of the catalyst, which is also where most of the phosphorus is deposited.

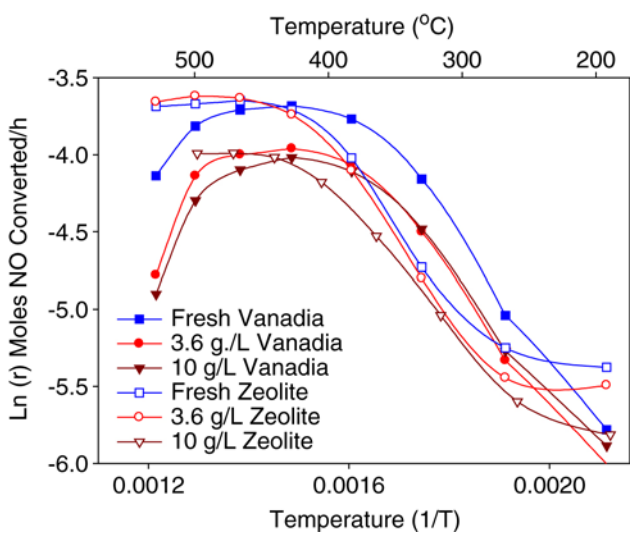

Figure 7. Kinetics of the SCR reaction over fresh and aged catalysts.

The differences between fresh and aged curves of the same type formulation are typical of what is observed when a physical blockage of active sites leads to activity loss. Results over the vanadia sample show that it loses significant activity on exposure to 3.6 g/L phosphorus, but it shows a smaller decline as the exposure is increased to 10 g/L. In contrast, the zeolite is not affected significantly by exposure to 3.6 g /L phosphorus, but the activity significantly decreases as the exposure increases to 10 g/L. Interestingly, increasing the temperature after phosphorus exposure seems to help the zeolite sample regain some of its activity but hurts the vanadia sample, possibly due to increased ammonia oxidation over the latter.

Phosphorus Adsorption

The amount of phosphorus that each type of formulation adsorbed after being exposed to 10 g/L phosphorus was determined by XRF. Results are shown in Figure 8.

The total amount of phosphorus adsorbed did not differ significantly from one catalyst type to the other, and the total amount adsorbed was about 15% of the phosphorus to which the sample was exposed. Similar deposition profiles were also determined for all the types of NO_x reduction catalysts tested. Out of the total amount of phosphorus that was adsorbed by a sample, most of it (65%) adsorbed on the front third of the core, 25% was adsorbed by the middle third, and 10% or less was adsorbed by the bottom third of the sample.

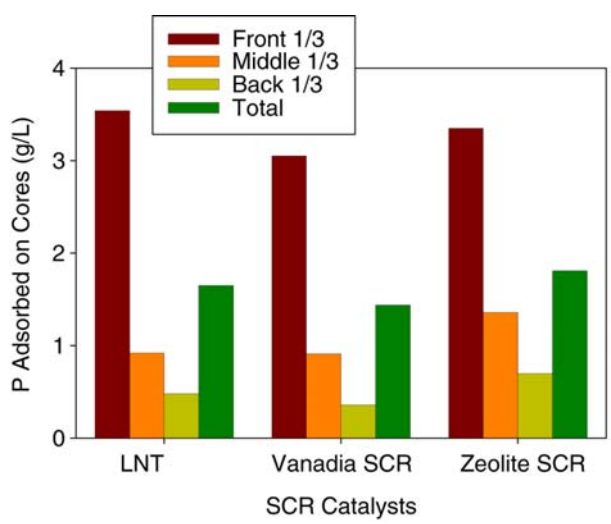

Figure 8. XRF analysis of phosphorus adsorption on NO_x reduction technologies.

PM Trap

Various catalyzed and uncatalyzed DPF materials were obtained from suppliers to screen filtration efficiency and backpressure. Filtration efficiency was determined using a Scanning Mobility Particle Sizer (SMPS), and backpressure was measured using a pressure transducer.

Figure 9 shows the filtration efficiencies of both the new DPF substrate and cordierite. Both graphs are averages of several fresh uncatalyzed DPF samples. The data shows that the filtration efficiencies of both materials are greater than 95%.

Figure 10 shows the results of pressure drop as a function of particulate loading time. The arrows notes backpressure measurements bypassing the DPF samples. The measurements were taken before and after loading the sample with particulate matter to account for variations as a function of particulates produced by the fuel burner. The data show that the new DPF substrate yields substantially lower pressure drop during particulate-loading than Cordierite and for the new material substrate.

Figure 11 shows filtration efficiency of the new DPF substrate material. The filtration efficiency of the catalyzed samples maintain above 98% throughout the particulate-loading process.

To examine the effect of catalyst coating on the pressure drop of the new substrate material, the pressure drop was measured over both catalyzed and uncatalyzed samples (Figure 12). Uncatalyzed sample shows lower pressure drop within 20 min of the test; however, the pressure drop significantly increases as a function of particulate loading time. The catalyzed sample shows opposite pressure drop

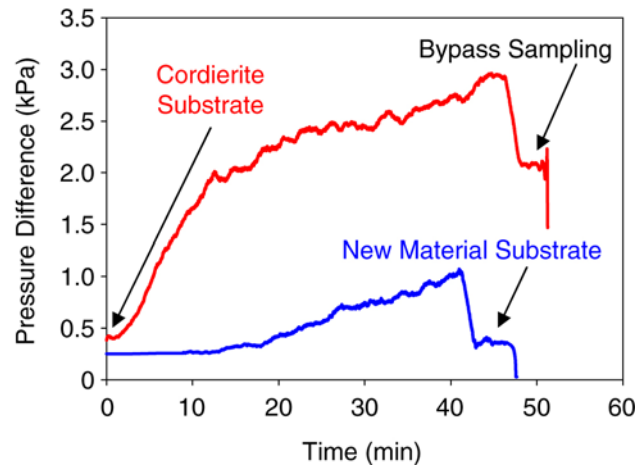

Figure 10. Pressure drop as a function of particulate-loading time for both Cordierite and for the new material substrate.

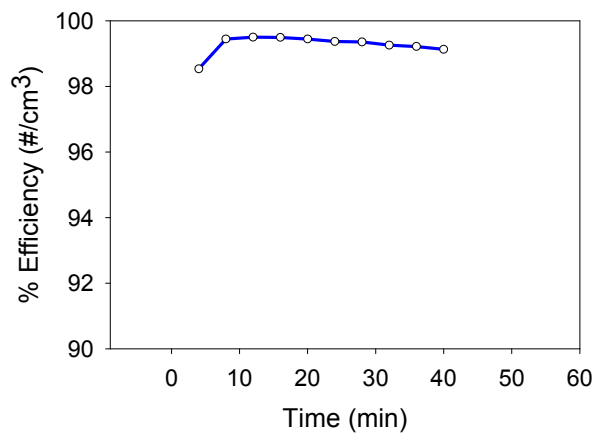

Figure 11. Filtration efficiency of the new catalyzed DPF substrate material.

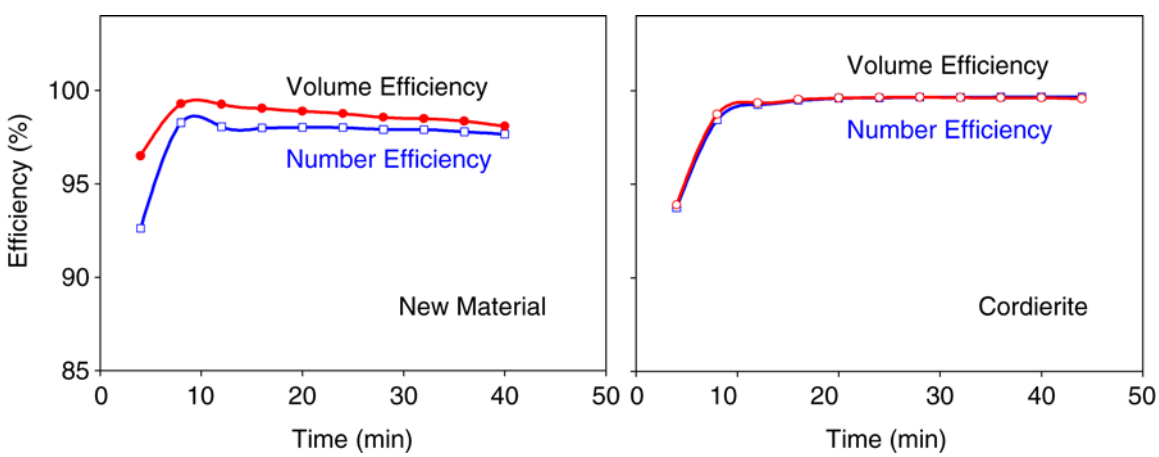

Figure 9. Filtration efficiency of fresh uncatalyzed samples of the new material and of cordierite (average of several samples).

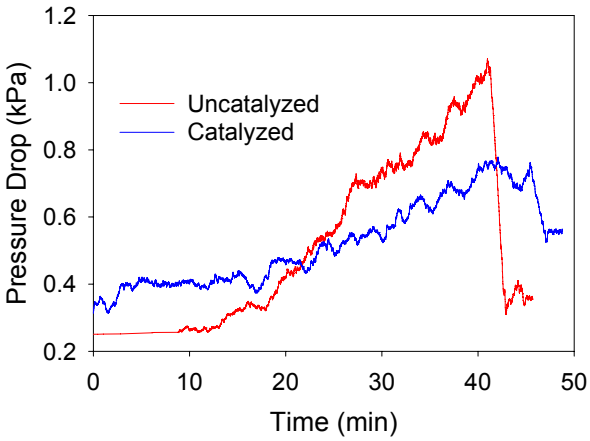

Figure 12. Pressure drop for catalyzed and uncatalyzed fresh samples of the new material substrate.

profile. The sample yields higher backpressure in the early stages of particulate loading, but the pressure drop rate decreases in the late stages of particulate loading possibly because the coated catalyst enhances regenerating soot collected in the sample.

Conclusions

Lean-NO_x Catalyst

The project was completed with the assessments of catalyst durability and diesel fuel component effect on the developed catalyst formulation. The catalyst is relatively durable to phosphorus deactivation but vulnerable to sulfur deactivation. The mitigation plan was developed to minimize the sulfur deactivation. The technology is ready to transfer to an organization specialized in retrofit applications.

Catalyst Durability

Results from the catalyst deactivation study showed that phosphorus exposure by itself can lead to loss of catalyst activity. The loss of activity appears to be tied to a physical blockage of surface active sites by the phosphorus compound. Most of the phosphorus adsorbs on the inlet side of the catalyst, whereas the adsorbed phosphorus concentration is lower at the outlet. For LNTs, the phosphorus blocks the adsorption of NO_2 on storage sites. For SCR, the phosphorus prevents NH_3 from adsorbing. The impact of phosphorus is greater on LNT activity than it is for SCR, but the resulting loss of activity can lead to a loss of fuel economy in both cases.

PM Trap

A promising material was identified that provides filtration efficiency larger than 95% with low pressure drop. In addition, catalyst coating did not present adverse effect on pressure drop.

Publications and Presentations

R. G. Silver, M. Stefanick, and A. Alletag, "Impact of Phosphorus on NO_x Aftertreatment Catalysts," poster presentation at 2005 DEER meeting, Chicago, Illinois (2005).

R. G. Silver, M. Stefanick, J. M. Faas, and S. Zemskova, "Impact of Phosphorus Exposure on Lean NO_x Trap Performance," presented at the 19th Annual Meeting of the North American Catalysis Society, Philadelphia (2005).

P. Park and C. Boyer, "Effect of SO_2 on the Activity over Ag/γ-Al_2O_3 Catalysts for NO_x Reduction in Lean Conditions," presented at the 19th Annual Meeting of the North American Catalysis Society, Philadelphia (2005).

P. Park and C. Boyer, "Effect of SO_2 on the Activity over Ag/γ-Al_2O_3 Catalysts for NO_x Reduction in Lean Conditions," *Appl. Catal. B.*, **59**, 27–34, 2005.

B. Development of Materials Analysis Tools for Studying NO_x Adsorber Catalysts (CRADA No. ORNL-02-0659 with Cummins, Inc.)

Thomas Watkins, Larry Allard, Doug Blom, Michael Lance, and Harry Meyer
Oak Ridge National Laboratory
P.O. Box 2008
Oak Ridge, TN 37831-6064
(865) 574-2046; fax: (865) 574-3940; e-mail: watkinstr@ornl.gov

DOE Technology Development Area Specialist: James J. Eberhardt
(202) 586-9837; fax: (202) 586-1600; e-mail: james.eberhardt@ee.doe.gov
ORNL Technical Advisor: D. Ray Johnson
(865) 576-6832; fax: (865) 574-6098; e-mail: johnsondr@ornl.gov

---

Contractor: Oak Ridge National Laboratory, Oak Ridge, Tennessee
Contract No.: DE-AC05-00OR22725

Objective

- Produce a quantitative understanding of the processing and in-service effects on NO_x adsorber catalyst technology leading to an exhaust aftertreatment system with improved catalyst performance capable of meeting the 2007 emission requirements.

Approach

- Characterize lab-engine tested samples with X-ray diffraction (XRD), spectroscopy, and microscopy.
- Correlate findings with Cummins data and experience.

Accomplishments

- Evaluated gradient formation on a macro scale of active elements on a catalyst as a function of catalyst history and operating conditions.
- Supported continued characterizations of new materials from various stages of the catalyst's life cycle.
- Begun determination of the soot and ash distribution as a function of macroscopic position within the NSR catalyst support brick.

Future Direction

- Evaluation of thermal degradation of a NO_x stoichiometric ratio (NSR) catalyst as a function of macroscopic position within the catalyst support brick.
- Continue the determination of the soot and ash distribution as a function of macroscopic position within the NSR catalyst support brick.

Introduction

To meet the 2007 emission requirements for diesel exhaust, aftertreatment in diesel engines may be necessary. The technology necessary for 2007 will need to integrate aftertreatment with engine control systems. Currently, no commercial off-the-shelf technologies are available to meet these standards. Consequently, Cummins, Inc. is working to understand the basic science necessary to

effectively utilize these catalyst systems. Oak Ridge National Laboratory (ORNL) is assisting with the materials characterization effort.

Base metal oxides (BMOs) are major components in current SO_x and NO_x adsorbers that Cummins seeks to use in NO_x adsorber catalyst systems. The function of these adsorbers is to collect oxysulfur (SO_x) and surface nitrite/nitrate (NO_x) species. These species are to be released from these surface sites during regeneration, where the adsorber BMO is either heated to some critical temperature or exposed to a reducing or reactant atmosphere. Sulfur poisoning of adsorber catalysts is a major problem that must be resolved for BMO-based emission reduction technologies to become commercially viable.

Approach

In general, the crystal structure, morphology, phase distribution, particle size, and surface species of catalytically active materials supplied by Cummins will be characterized using XRD, Raman spectroscopy, and electron microscopy. These materials will come from all stages of the catalyst's life cycle: raw materials, as-calcined, sulfated, regenerated, etc. Both ORNL and Cummins personnel have participated in this work.

Samples

Briefly, Cummins provided various series of "core" samples taken from cordierite "bricks" containing platinum, γ-alumina and $BaCO_3$ or platinum and γ-alumina. The general features of each series will be given below in the text as needed. The brick/core samples consisted of a series with varied amounts of platinum loading, a sample that had lost performance after numerous desulfations, and a sample loaded with sulfur.

Results

The following is a summary of the work from October 2004 to September 2005.

X-ray

X-ray diffraction (XRD) was employed to understand the crystalline nature of the samples. For the unfamiliar, the following analogy can be applied: As a fingerprint identifies a person, so a diffraction pattern identifies a crystalline material.

A model system was analyzed and consisted of platinum particles dispersed on a γ-alumina (Al_2O_3) on a cordierite ($Mg_2Al_4Si_5O_{18}$, the core/brick material) substrate. This series of samples were "redoxed pulsed" to remove nitrogen from the oxidation catalyst. Here, redox pulsing entails going from a rich/reducing fuel mixture to a lean/oxidizing fuel mixture and back. Samples A, B, C and D were designated the baseline, 6 h at 350°C, 6 hours at 350°C-low volume, and 6 h at 450°C, respectively. The conditions for sample D were regarded as the most severe and would be the most likely to cause Pt crystallite growth. Figure 1 compares the XRD pattern of sample D to the as-received γ-alumina powder. The powder has a high surface area, and the very broad peaks of the powder indicate a small crystallite size, 3 nm. A crystallite is a region of coherent diffraction and can be thought of as a subgrain, which is a very small perfect crystal. The narrower alumina peaks of sample D, indicate that the crystallite size has increased and that the surface area has likely decreased. Figure 2 shows that the γ-alumina has transformed to θ-alumina and indicates that sample has experienced temperatures in the 727 to 1027°C range.[1] Note the platinum and θ-alumina superimpose. Figure 3(a) shows the experimental set-up used to collect platinum crystallite information as a function of macroscopic length along the sample. As was inferred above, the x-ray crystallite size is related to the x-ray peak broadening. Typically, the size of a crystallite is smaller than the grain size of a material as observed on the scanning electron microscopy (SEM). Significant contributions to x-ray peak broadening occur when the crystallite size is less than 100 nm. The lower bound is approximately 2 nm. Figure 3 shows the crystallite size data for samples A, B, C, and D. The crystallite size did not vary systematically along the length. As will be shown later, the size does not agree with that found in the microscopy section. This is likely due to the aforementioned peak superposition. Thus, the crystallite sizes given may more accurately reflect the size of the θ-alumina.

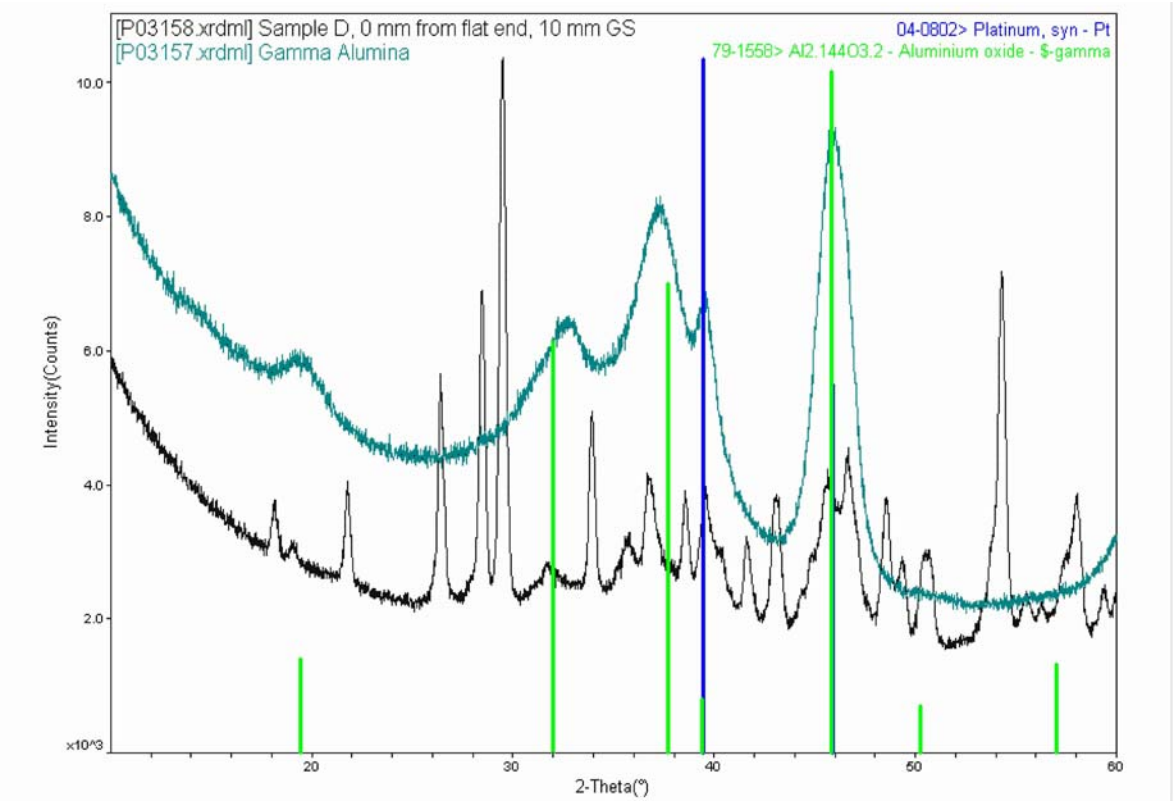

Figure 1. The diffraction patterns for the as-received γ-alumina powder and sample D (redox pulsed for 6 h at 450°C).

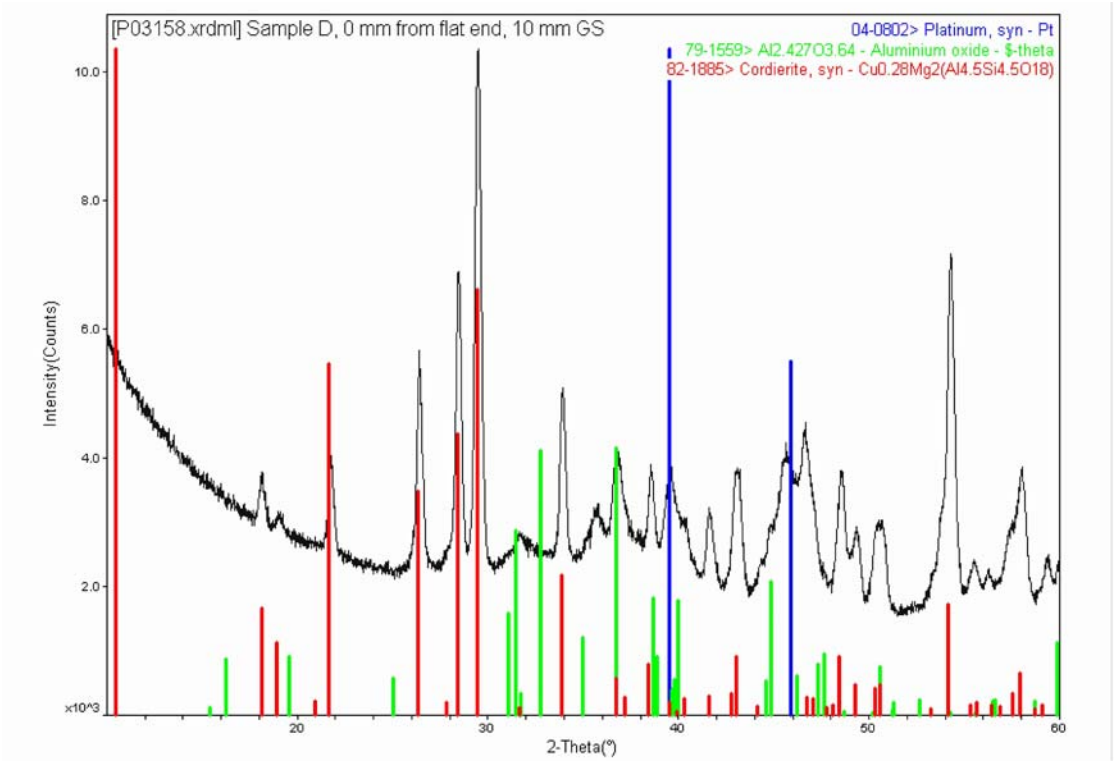

Figure 2. The diffraction pattern for sample D (redox pulsed for 6 h at 450°C).

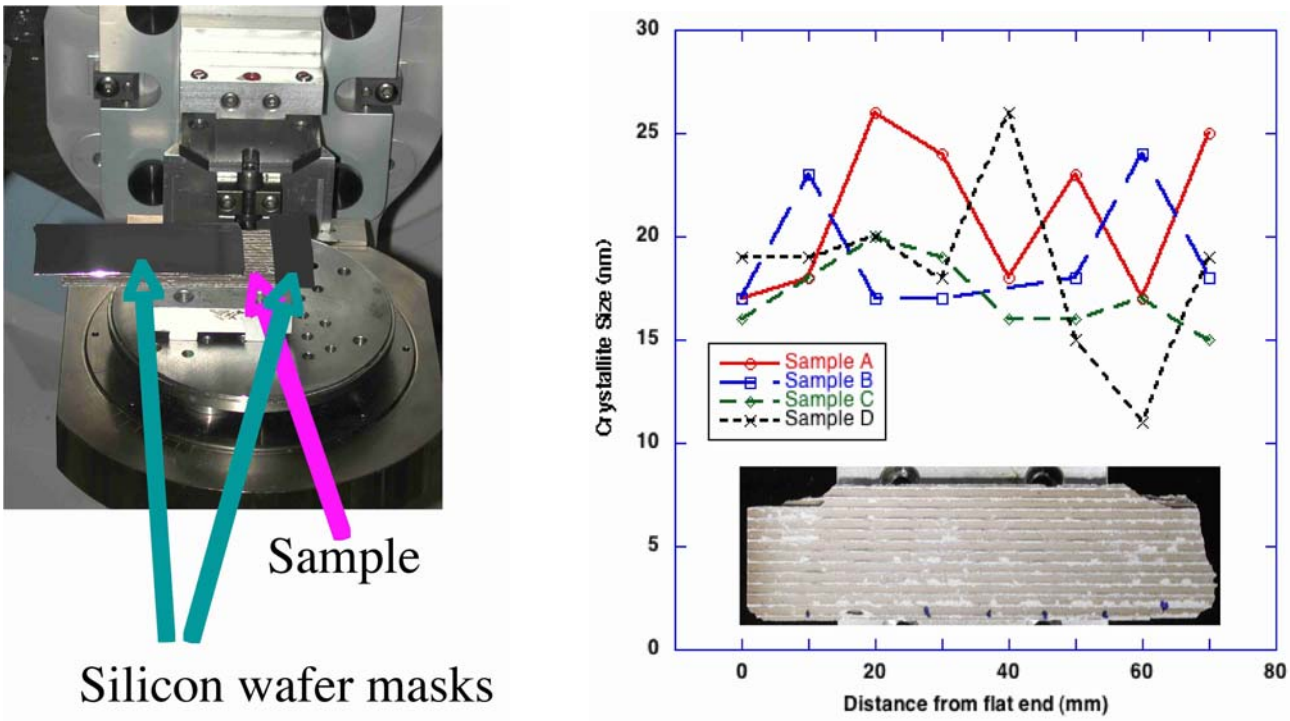

(a) (b)

Figure 3. (a) Silicon wafer masks allow measurement of data every 10 mm. (b) Platinum/alumina crystallite size as a function of length along the sample.

Raman Spectroscopy

Raman spectroscopy measures the characteristic vibrational energy levels of molecules and crystals and so is very sensitive to any changes in bonding, stoichiometry, and phase/symmetry.

Soot oxidation has been a critical issue for regeneration of diesel particulate filters (DPFs). The design of the regeneration strategy and the durability requirement for DPFs depend on an understanding of soot burning. Raman spectroscopy has been used to monitor surface configuration changes. Under thermal aging, engine soot undergoes a transformation from a mostly amorphous carbon structure into more orderly polyaromatic structures, which exhibit resistance toward oxidation. Certain neutralization products, such as thio-phosphorous and phosphorous derivatives, can also alter the thermal behavior of soot through interactions between ash- and soot-adsorbed species. The incomplete regeneration can be attributed to a buildup of a physical barrier that prevents oxygen and/or NO_2 from diffusing effectively onto the carbon surface.

Raman spectroscopy offers a unique way to characterize the long-range interactions and the order-disorder effects on carbonaceous materials. Both the first and the second-order features can be seen with Raman. Pristine graphite crystals show two first-order Raman features located at 42 and 1578 cm^{-1}. The 1578 cm^{-1} band, with a full width at half-maximum bandwidth of 16 cm^{-1} (see Figure 4), is referred to as the graphitic band (G). Grinding the graphite crystal generates an additional band at 1335 cm^{-1}, which can be assigned as the disordered band (D). Additional grinding gives an increase in the intensity and bandwidth of the disordered band. The appearance of the disordered band can be attributed to the disorder relaxation where the wave-vector selection rules are broken by lattice discontinuities and structural defects.

The Raman spectra of the fresh and the artificially matured samples of A1C are shown in Figure 4. After heating at 950°C, additional bands begin to show around 680 ~ 1000 cm^{-1}, which can be assigned to metal oxides. When samples are heated at high temperatures, spectral interference

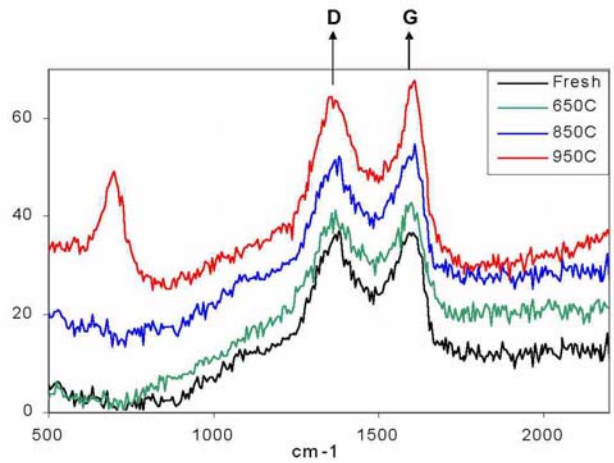

Figure 4. Raman spectra of A1C engine soot aged at various temperatures.

from ash components with the carbon bands begins to become pronounced. As the maturation temperature is increased, the graphitic band becomes sharper, and the intensity is enhanced. The transition frequency of the disordered band is also shifted to a slightly lower frequency. Similar trends are also seen in other samples. All these spectral trends suggest a structural change of the sample during thermal maturation.

The frequency ratios of the graphitic to disorder peak ($R = f_G/f_D$) measured for all three samples are plotted in Figure 5. All three samples follow a general trend with an increase of R with the maturation temperature. The increase of R for soot maturation is from 0.37 (<650°C) to 0.48 (>850°C). The change shows little statistical significance at temperatures

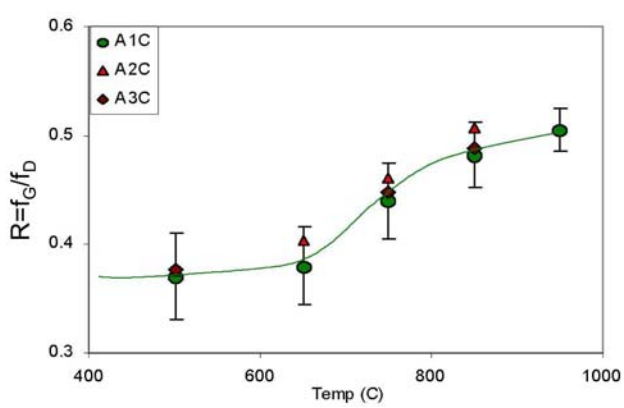

Figure 5. The correlation between Raman band ratio ($R = f_G/f_D$) and temperature.

below 700°C. Above 750°C, a rapid enhancement is observed, and the curve levels off beyond 850°C. The major change seems to occur around 700°C. This temperature is consistent with most young coal samples where their maturation scale changes dramatically under artificial pyrolysis around 700°C. This result shows that Raman spectroscopy can be used to monitor the degree of long-range order in soot samples, which is a key parameter in determining the regeneration processing of DPFs. More research is planned to better understand the kinetics of soot burning and DPF aging.

Microscopy

Scanning transmission electron microscopy (STEM) and electron probe microanalysis (EPMA) techniques were used to continue characterization of the microstructure of NO_x trap catalysts and oxidation catalysts. In the previous report, the microstructure and chemistry of samples from Reactor II (platinum loading ~2 wt %) at different positions along the reactor were studied, and the changes in morphology of platinum particles as well as the distribution of elements such as the trapping component within the washcoat were elucidated. Subsequently, a variety of both NO_x trap catalysts and oxidation catalysts were examined to quantify the precious metal particle size distributions both as a function of aging as well as macroscopic position in the reactor. In addition, the location and structure of the BMO trapping component of the NO_x trap systems were determined. Some example results and main conclusions from the microscopy experiments are given below.

The platinum particles of a fresh Pt/Ba/γ-alumina model catalyst sample were examined. The sample had a target loading of 1.6 g/in.^{3} and was exposed to 500°C in its preparation. The majority of platinum particles were observed to be between 1 and 2 nm in size, as can be seen in Figure 6. The HA-ADF STEM image has bright contrast for heavy elements, while lighter elements appear darker. The particles were too fine for quantification via image processing. "Spectral imaging" is an advanced technique for elemental analysis in electron beam instruments whereby a full EDS spectrum from 0–20 keV is collected at every individual pixel location. The collected data can be manipulated off-line to generate 1-dimensional and

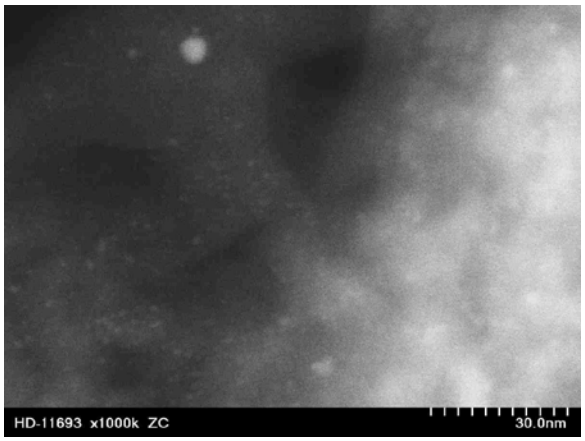

Figure 6. HA-ADF (Z-contrast) STEM image of platinum particles on alumina washcoat in sample PBA1. The majority of the particles are 1–2 nm in diameter in this micrograph.

2-dimensional elemental line scans and maps. Figure 7 shows both the HA-ADF STEM image and an extracted barium X-ray map for the sample. The X-ray map conclusively shows the spatial distribution of the barium-containing phase in this sample, and comparison with the high angle-annular dark field (HA-ADF) image allows for the identification of barium containing areas relative to the morphology and brightness seen in the HA-ADF image. Samples containing Pt/BMO/γ-alumina were also examined. Spectral imaging identified the trapping component as BMO-based. As seen in Figure 8, the BMO phase is widely distributed but not as easily identified from just the HA-ADF images.

Unlike previous specimens, sample D (see X-ray section above) came as a much longer core

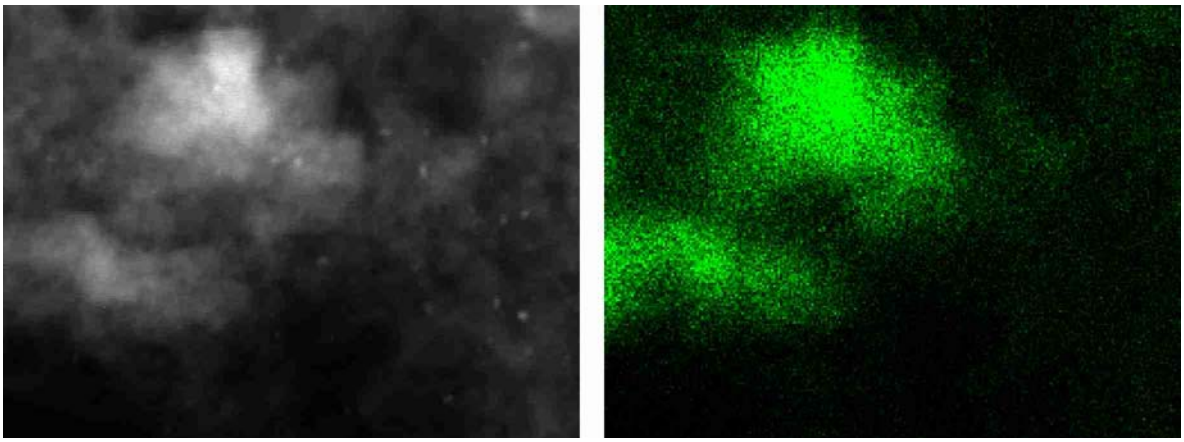

Figure 7. (a) HA-ADF STEM image. (b) Barium X-ray map extracted from spectral image. Barium containing phase corresponds to the large bright area in (a).

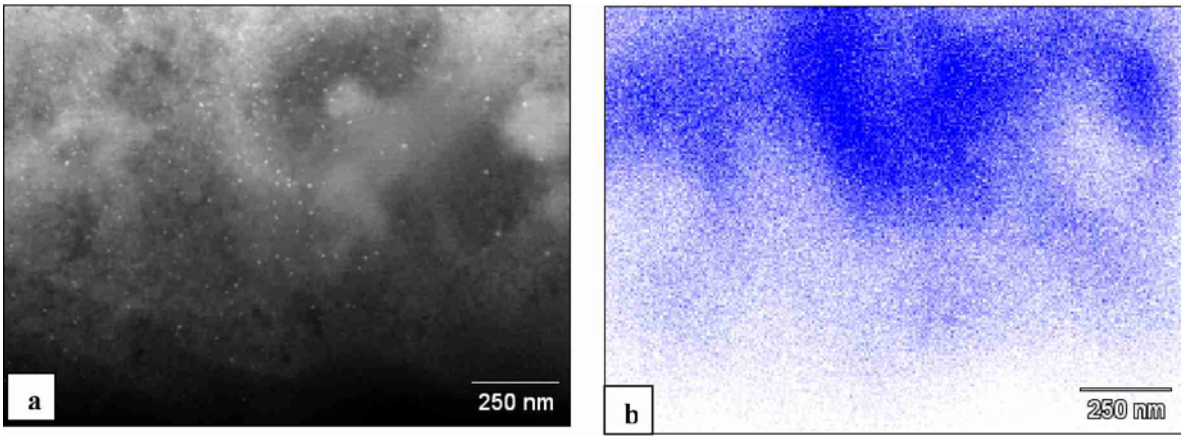

Figure 8. (a) HA-ADF STEM image. (b) BMO X-ray map. There has been some uncompensated shift between the reference image and the map. The BMO phase is widely distributed, but not easily identified in the HA-ADF image alone (a).

with the request to analyze the platinum particle size distribution down the length of the monolith. Sample D1 was taken near the smooth/flat upstream face of the monolith [see left side of inset in Figure 3(b)] and was closer to the engine. Sample D2 was from an area 7 cm away along the length of the monolith, near the rough/jagged side. Figure 9 shows the comparison of the platinum particle size distributions for samples D1 and D2. Sample D1 exhibits a very typical Gaussian distribution of particle sizes, while sample D2 has a bimodal distribution with both a population of small catalyst parti cles and large catalyst particles. For 757 particles in D1, the median and mean particle sizes were 6.82 and 6.76 nm, respectively. For 1125 particles in D2, the median and mean particle sizes were 5.87 and 5.48 nm, respectively. The higher temperatures that the platinum particles at location D1 experienced appear to have coarsened the particle slightly.

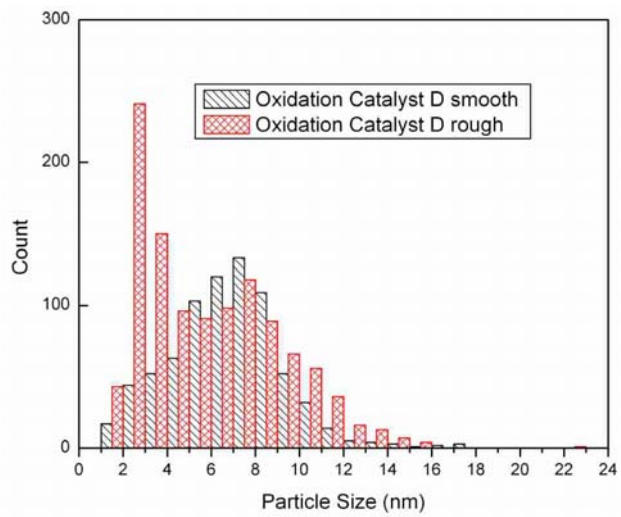

Figure 9. Comparison of platinum particle size distributions from two different areas on the same monolith. Each distribution is based on ten images each.

References

1. R-S. Zhou and R. L. Snyder, "Structures and Transformation Mechanisms of the η, γ and θ Transition Aluminas," *Acta Cryst*., **B47**, 617–30 (1991).

Presentations and Publications

T. R. Watkins, L. Allard, D. Blom, M. J. Lance, H. Meyer, L. Walker, C. Narula, R. D. England, B. Epling, H. Fang, and T. Yonushonis, "Development of Materials Analysis Tools for Studying NO_x Adsorber Catalysts," [Revised] presented at 11th Diesel Engine Emission Reduction (DEER) Conference, Chicago, Illinois, August 24, 2005.

T. R. Watkins, L. Allard, D. Blom, M. J. Lance, C. Narula, H. Meyer, R. D. England, H. Fang, T. Yonushonis, and H. Hess, "Catalyst Characterization, CRADA No. ORNL-02-0659 with Cummins, Inc.," presented at the Heavy Vehicle Materials Program Review, Oak Ridge National Laboratory, Oak Ridge, Tennessee, September 14, 2005.

H. L. Fang, M. J. Lance, and G. S. Painter, "Raman Characterization of Pt-support Interactions on Metal Oxides," in preparation.

C. Development of NO_x Sensors for Heavy Vehicle Applications

Timothy R. Armstrong, David L. West, Fred C. Montgomery, Jaco H. Visser, and David J. Kubinski**
Oak Ridge National Laboratory
P.O. Box 2008, Mail Stop 6186
Oak Ridge, TN 37831-6186
(865) 574-7996; fax: (865) 241-0112; e-mail: armstrongt@ornl.gov

**Scientific Research Laboratory, Ford Motor Co.*

DOE Technology Development Area Specialist: James J. Eberhardt
(202) 586-9837; fax: (202) 586-1600; e-mail: james.eberhardt@ee.doe.gov
ORNL Technical Advisor: D. Ray Johnson
(865) 576-6832; fax: (865) 574-6098; e-mail: johnsondr@ornl.gov

Contractor: Oak Ridge National Laboratory, Oak Ridge, Tennessee
Prime DOE Contract No.: DE-AC05-00OR22725
Subcontractor: Ford Motor Company, Detroit, Michigan

Objectives

- Develop NO_x sensors for remediation and monitoring of diesel engines.
- Develop sensors that have an operating temperature of 500–700°C and are able to measure NO_x concentrations from ~10–1500 ppm at oxygen levels from 5 to 20 vol %.
- Ensure that sensors are selective for either NO or NO_2, or able to measure "total NO_x" ([NO] + [NO_2]) since "NO_x" refers to mixtures of NO and NO_2.

Approach

- Fabricate prototype sensing elements by screen printing electrode layers onto oxygen-ion conducting [typically yttria stabilized zirconia (YSZ)] substrates.
- Operated elements either in a "non-Nernstian" mode (where the output is a voltage) or under direct current electrical bias.
- Characterize sensor in bench setting and in NG engine exhaust for NO_x sensor response, sensitivity to varying [O_2], and recovery/response kinetics.
- Develop breadboard based sensor for exhaust gas sensing.

Accomplishments

- Developed sensing elements displaying near "total NO_x" behavior and stable in simulated long-term service.
- Developed sensing elements that are capable of repeatedly detecting [NO_x] in the range of ~10 ppm and can operate at temperatures as high as 750°C with ±1 ppm sensitivity.
- Developed novel techniques for applying electrical stimulus to combat drift of the sensor background output.

Future Direction

- Evaluate the stability and performance of these sensing elements in real exhaust streams to quantify and correct for drift.
- Characterize the cross-sensitivity to other species (e.g., CO) that may be present in real exhaust streams.
- Clarify both the sensing mechanism and the cause(s) for sensor drift.

Introduction

The primary pollutants (excluding the greenhouse gas CO_2) from the combustion of low-sulfur fuels are CO, hydrocarbons (HC), and oxides of nitrogen ("NO_x," a mixture of NO and NO_2). Spark-ignited, direct-injection (SIDI) auto and truck engines employ a three-way catalyst (TWC) that can remove all three of these pollutants. However, the TWC is only effective over a narrow range of [O_2] in the exhaust, losing its effectiveness for NO_x removal at high partial pressures of O_2. This means that the currently employed TWC is not effective for NO_x remediation of the exhaust from compression-ignited (diesel) engines, as these are O_2-rich (typically 5–20 vol % O_2).

In this current absence of a "lean-NO_x" catalyst, three technologies are proposed to meet the challenge of NO_x remediation of diesel exhausts: "Lean-NO_x" traps (LNTs), selective catalytic reduction (SCR) with hydrocarbons, and SCR with urea. All of these technologies will require on-board NO_x sensors, to control trap regeneration (LNT) or reagent injection (SCR).

In this project we are developing NO_x sensing elements that can be used in diesel engine exhausts. The *minimum* requirement for this application is an operating temperature of 500–700ºC and the ability to measure 1–1500 ppm NO_x. It should be emphasized that "NO_x" refers to mixtures of NO and NO_2; therefore, full NO_x characterization of the exhaust may require two of the following three concentrations to be measured: [NO], [NO_2], [NO_x] (= [NO] + [NO_2]). This project is a cooperative research and development agreement with Ford Motor Company.

Approach

The approach selected is to build a sensing platform on yttria-stabilized zirconia (YSZ). YSZ, an oxygen-ion conducting material, is currently widely used in [O_2] sensors for gasoline engines. This approach is not original, because two NO_x sensors based on YSZ are near commercialization and have been proven by the engine manufacturers association not to be adequate to measure NO_x less than 50 ppm. In addition, both are relatively complex with multicavity constructions. This construction is required because in the first design[2] preliminary O_2 removal from the sampled exhaust is required before the NO_x is measured amperometrically. In the second design[3] the sampled exhaust passes over a conversion electrode in order to convert the NO_x into NO_2 before measurement in the sensing cavity.

The lion's share of work to date has focused on the sensing *element* portion of the sensor. This is the portion of the sensor that responds to the presence of NO_x. The reason for adopting this approach is that the working characteristics of the sensing element will dictate many aspects of sensor design (operating temperature, need for catalytic overlayers, etc.).

To fabricate sensing elements, electrodes are screen-printed and fired onto YSZ substrates (Figure 1). These elements are then tested for NO_x response using a furnace to simulate elevated temperature service and a commercial gas mixing unit to deliver blends of N_2, O_2, NO_x (either NO or NO_2), and other species as required.

Results

Much of the work on this project has been devoted to all-oxide "total NO_x" sensing elements. These sensing elements, a sample of which is depicted in Figure 1, consist of compositionally identical oxide electrodes on a YSZ substrate. These sensing elements are attractive because the use of a single electrode material will reduce production cost, and more importantly, their "total NO_x" (similar response to NO and NO_2) sensing behavior

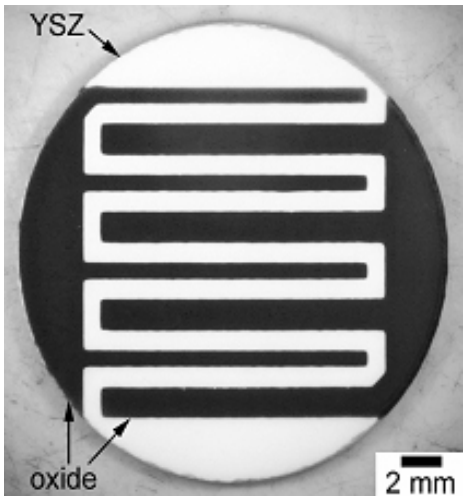

Figure 1. Prototype sensing element.

would enable measurement of [NO_x], regardless of the [NO]:[NO_2] ratio in the exhaust gas. This obviates the necessity to perform any NO_x conversion of the type described in Ref. 3.

Several electrode compositions have been evaluated in order to develop a composition with large NO_x response magnitudes. The best of these, when operated at 600ºC and 7 vol % O_2, had responses to 77 ppm NO and NO_2 of –37%* and –40%, respectively. However, long-term (>200-h) lab-scale testing of this composition revealed that it was unstable in exhaust conditions, and thus the development of new compositions, stable in exhaust conditions, has been carried out.

The NO_x sensing performance of two promising new compositions is shown in Figure 2. It can be seen that the NO_x responses are similar in magnitude over the concentration range 20–190 ppm, and efforts are ongoing to narrow the response between [NO] and [NO_2].

Figure 3 shows X-ray diffraction patterns from extensively tested sensing elements made with old electrode composition and the new composition. The new composition is clearly more stable as shown by the lack of decomposition products.

The data in Figure 2 were collected at 600ºC. It may be desirable to operate the sensing element at higher temperatures, both in order to improve the response/recovery time and prevent condensation on the sensing element. The higher temperature NO

*This is the change in measured voltage when NO_x is present.

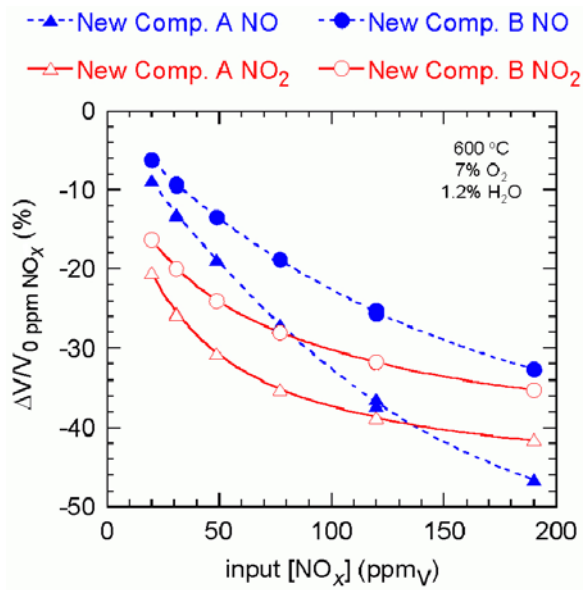

Figure 2. NO_x responses of two new electrode compositions.

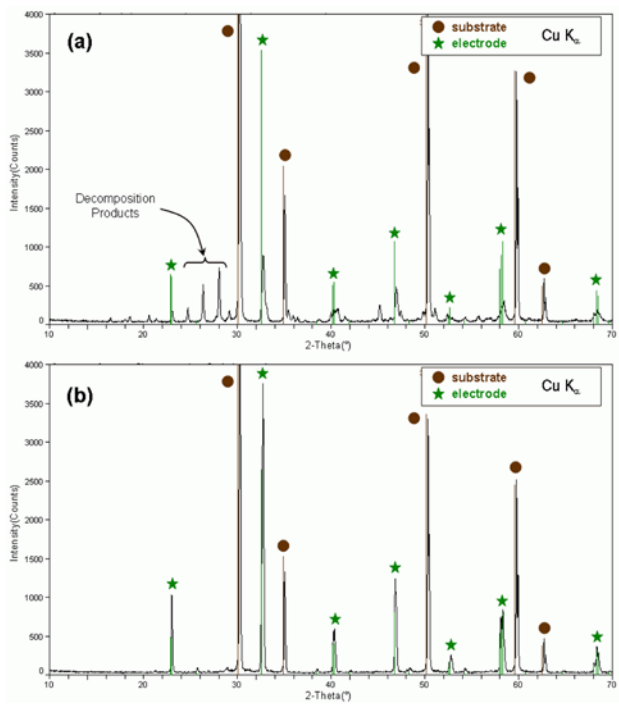

Figure 3. X-ray diffraction patterns of used elements made with (a) original and (b) new compositions.

sensing performance of these sensing elements is illustrated in Figure 4, which shows sensing element performance at 750ºC. Two aspects of the sensing performance in Figure 4 differ from that observed in Figure 2. First, the magnitude of the changes due to

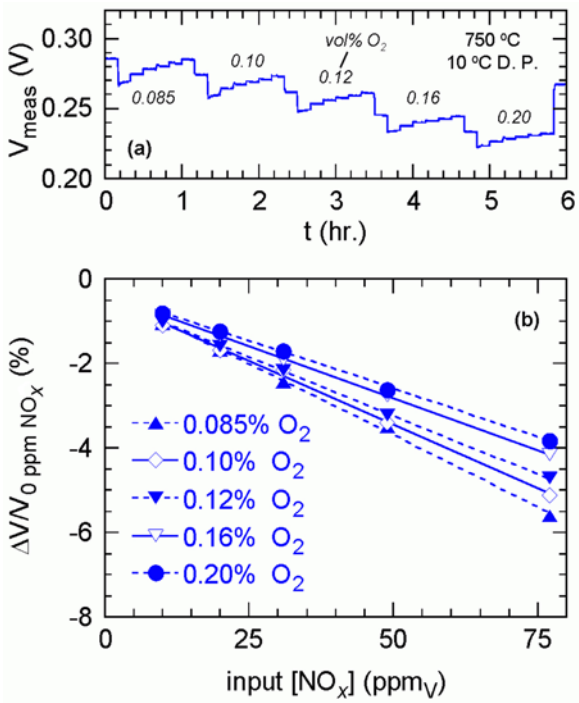

Figure 4. Sensing performance at 750°C. In (a) [NO] is stepped through the sequence 0, 77, 49. 31, 20, 10, 0 ppm at the indicated [O_2]. Computed changes in voltage are shown in (b).

NO are much smaller. Second, the dependence of the response on [NO] is linear. Note also that the response decreases with increasing [O_2]. This means that operation at these temperatures will most likely require lowering of the [O_2] in the sampled exhaust (by means of a pumping cell).

These sensing elements are electrochemical in nature, and electrochemical sensing elements are prone to drift. Drift is frequently observed because electrochemical sensors usually rely on charge transfer at interfaces, and these interfaces will age with use of the sensor.

Sample drift behavior observed with these sensing elements is illustrated in Figure 5. Shown there are the element responses to identical programmed changes in [NO] and [O_2] after 0, 10, and 70 h of continuous operation. The background resistance of the element is monotonically increasing, but the responses to the gas concentration changes are repeatable.

To combat this drift, we have been investigating alternate methods of applying an electrical stimulus to the sensing element. One such example is shown in Figure 6.

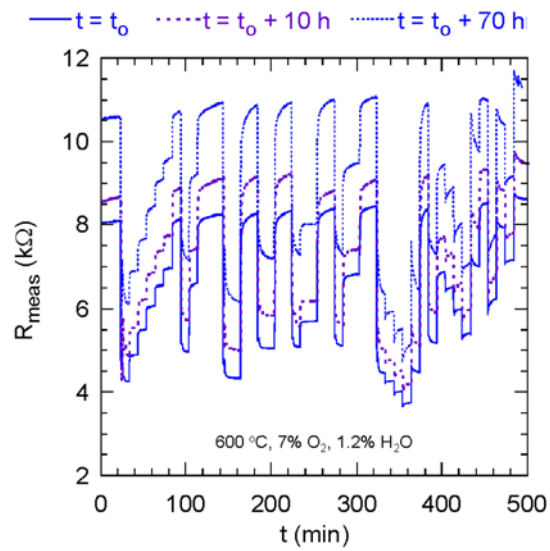

Figure 5. Response to identical changes in [NO] and [O_2] after 0, 10, and 70 h of continuous operation.

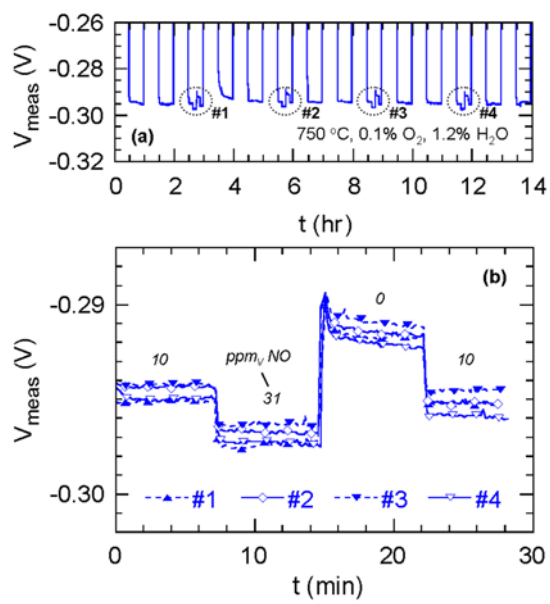

Figure 6. Element performance with alternating application of positive and negative electrical stimulus.

The electrical stimulus was alternated between positive and negative values (only the negative values are shown in Figure 6). During every third negative excursion, the [NO] concentration was varied systematically as indicated in Figure 6. Operated in this manner, the sensing element is capable of repeatedly detecting [NO] changes on the order of 10 ppm over more than 10 h of continuous

operation. These are thought to be the demands that monitoring of a lean NO_x trap would place on a NO_x sensor.

Conclusions

Sensing elements capable of "total NO_x" sensing behavior are under development. During the course of this project the following accomplishments have been achieved:

- Sensing elements displaying near "total NO_x" behavior and stable in simulated long-term service have been developed.
- NO sensing elements have been demonstrated.
- Sensing elements are capable of repeatedly detecting [NO_x] in the range of ~10 ppm and can operate at temperatures as high as 750°C with ±1 ppm sensitivity.
- Sensing elements stable for more than 1000 h in oxygen and steam containing environments have been developed.

The challenges ahead are fourfold: (1) the stability and sensitivity of these elements must be examined in real exhaust streams, (2) the cross-sensitivity to other species that may be present in the exhaust must be characterized, (3) techniques for combating drift must be introduced and optimized, and (4) the sensing mechanism of these elements needs to be elucidated.

This last item is important as ease of fabrication and cost may dictate changes in materials or geometry during the incorporation of these elements into sensors suitable for any engine application. Understanding of the sensing mechanism will be critical in predicting how such changes might affect the sensor performance.

References

1. K. B. J. Schnelle and C. A. Brown, "NO_x control," in *Air pollution control technology handbook*, CRC Press, 2001, pp. 241–255.
2. N. Kato, H. Kurachi, and Y. Hamada, "Thick film ZrO_2 sensor for the measurement of low NO_x concentration," SAE Technical Paper 980170, 1998.
3. A. Kunimoto, M. Hasei, Y. Yan, Y. Gao, T. Ono, and Y. Nakanouchi, "New total-NO_x sensor based on mixed potential for automobiles," SAE Technical Paper 1999-01-1280, 1999.

Patents

F. C. Montgomery, D. L. West, T. R. Armstrong, and L. C. Maxey, "NO_x Sensing Devices Having Conductive Oxide Electrodes," *ORNL Docket 1348C*.

Presentations and Publications

1. D. L. West, F. C. Montgomery, and T. R. Armstrong, "Total NO_x sensing elements with compositionally identical oxide electrodes," accepted by *Journal of the Electrochemical Society*, September 2005.
2. D. L. West, F. C. Montgomery, and T. R. Armstrong, "NO-selective NO_x sensing elements for combustion exhausts," accepted by *Sensors and Actuators B*, February 2005.
3. D. L. West,* F. C. Montgomery, and T. R. Armstrong, "All-oxide "total NO_x" sensing elements," *207th Meeting of the Electrochemical Society*, 2005.
4. D. L. West, F. C. Montgomery, and T. R. Armstrong, "DC electrical-biased, all-oxide NO_x sensing elements for use at 873 K," *29th International Cocoa Beach Conference on Advanced Ceramics and Composites*, 2005.
5. D. L. West, F. C. Montgomery, and T. R. Armstrong, "High-T NO_x sensing elements using conductive oxides and Pt," *Proceedings of ICEF: Engines for Mobile, Marine, Rail, Power Generation and Stationary Applications*, 2004.

D. Ultra-High Resolution Electron Microscopy for Characterization of Catalyst Microstructures and Deactivation Mechanisms

*L. F. Allard, D. A. Blom, D. W. Coffey, C. K. Narula, and M. A. O'Keefe**
Oak Ridge National Laboratory
P.O. Box 2008, MS-6064
Oak Ridge, TN 37831-6064

**Materials Sciences Division, Lawrence Berkeley National Laboratory, Berkeley, CA 94720*

DOE Technology Development Area Specialist: James J. Eberhardt
(202) 586-9837; fax: (202) 586-1600; e-mail: james.eberhardt@ee.doe.gov
ORNL Technical Advisor: D. Ray Johnson
(865) 576-6832; fax: (865) 574-6098; e-mail: johnsondr@ornl.gov

Contractor: Oak Ridge National Laboratory, Oak Ridge, Tennessee
Contract No.: DE-AC05-00OR22725

Objectives

- Develop and utilize new capabilities and techniques for ultra-high resolution transmission electron microscopy (UHR-TEM) to characterize the microstructures of catalytic materials of interest for reduction of NO_X emissions in diesel and automotive exhaust systems.
- Relate the effects of reaction conditions on the changes in morphology of heavy metal species on "real" catalyst support materials (typically oxides).
- Develop capability to experimentally study the effects of experimental reaction treatments on TEM samples of NO_X trap catalyst materials before and after reactions, using the High-Temperature Materials Laboratory (HTML) "ex-situ" catalyst reactor with a specimen holder designed for use in the aberration-corrected electron microscope (ACEM).

Approach

- Utilize Oak Ridge National Laboratory ACEM to characterize for the first time the atomic morphology of heavy-metal species such as platinum and rhenium on oxide support materials via techniques of annular dark-field (ADF) or "Z-contrast" imaging.
- Utilize dedicated scanning transmission electron microscope (STEM) instrument and techniques of spectrum imaging to characterize the structure and chemistry of a series of lean NO_X trap (LNT) and diesel particulate NO_X reduction (DPNR) filter samples being studied by Ford Research Laboratory colleagues.

Accomplishments

- Characterized the morphologies of tri-rhenium carbonyl clusters on gamma-alumina support material, at the atomic level to demonstrate for the first time the unambiguous imaging of clusters of known structure.
- Characterized the nature of platinum catalyst structures on mixed-oxide support materials, including the imaging of platinum species dispersed as single atoms and in precrystalline clusters known as "rafts."
- Performed initial analysis of the structures of several manufacturers' NO_X trap and DPNR filter materials, in the as-manufactured condition and after an initial "de-greening" process.

- Demonstrated the potential for the Z-contrast atomic imaging process to allow determination of the precise shapes of nanoparticles and clusters.
- Developed and fabricated a new specimen rod and modifications to the HTML ex-situ reactor system to permit catalyst reaction studies using the ACEM.

Future Direction

- Focus on the use of the ACEM to characterize the location of sulfur species on NO_X reduction catalyst materials, to enable characterization of the mechanisms of sulfur poisoning of these materials. This will involve not only imaging of the catalysts at the single-atom level, but also the use of the electron spectroscopy capabilities on the ACEM to obtain chemical information at the atomic level.
- Continue to work on the critical problem of determination of precise shapes of catalyst nanoparticles to determine the most important characteristics for control of catalytic performance.
- Extend new imaging and spectroscopy techniques to include studies of bi-metallic catalyst particles (e.g., gold-palladium).

Technical Progress

Imaging of ultrafine atomic clusters of heavy metals on low atomic number supports is expected to be significantly enhanced with the advent of research on the new aberration-corrected STEM/TEM electron microscope (JEOL 2200FS-AC "ACEM"). In this report, we illustrate the potential for imaging atomic species down to the single atom level, with samples of platinum on thin carbon films, platinum on and rhenium on alumina. The latter samples are part of a specimen suite comprising primarily tri-rhenium carbonyl clusters on gamma alumina, provided by Prof. B. C. Gates and students at UCalDavis. Details of the changes in cluster morphology related to decarbonylation experiments in an ex-situ reactor system will be reported by Narula, Moses, and Allard in a separate quarterly. Platinum on carbon samples were prepared by sputter deposition from a platinum target using argon ions, in our ion-sputtering unit. The ultra-thin carbon films were prepared by controlled evaporation of carbon onto NaCl substrates, then floating films (nominally 10Å to 15Å thick) on water, and picking the thin films up on holey carbon support films. The thin carbon is essentially not imaged in the ADF imaging mode of the ACEM, allowing only platinum atoms and clusters to be revealed in bright contrast.

The platinum on carbon experiment was conducted using two specimens. One sample was prepared using dual-gun sputtering for 20 s under standard beam energy conditions. The second sample was prepared using identical beam conditions, but only a single gun, giving nominally one-half the amount of platinum species on the carbon film surface. The ACEM was adjusted to achieve a fully corrected electron probe, using an illuminating aperture that calculated to produce a beam diameter of just about 1 Å.

Platinum/carbon imaging results: Figures 1 and 2 show the ADF images of the 1-gun and 2-gun depositions, respectively. Single atoms and "rafts" of atoms having 2–3 layers are seen in both samples. It is clear that there is a direct correlation between the deposition parameters and the relative amounts of platinum observed on the respective samples. Also note that these images were acquired prior to achieving fully stable operation on the instrument, and also while using a nonideal aperture size in the probe-forming lens system, so that no better than 1-Å resolution was expected. The line profile shown over a single platinum atom (raw data) indicates just over 1Å in diameter, as expected. The impressive result from this experiment is that we expect to be able to image single atoms of a heavy element with a resolution significantly lower than the expected 0.7-Å ultimate resolution of the microscope. A second observation (not illustrated here) is that the atoms and clusters are mobile on the surface of the carbon film and continually change position between successive image acquisitions. This phenomenon is not unexpected and has been observed in other sample types observed to date, including the rhenium on alumina samples described below. It is important to be able to (eventually) determine the relationship between images recorded at highest resolution on

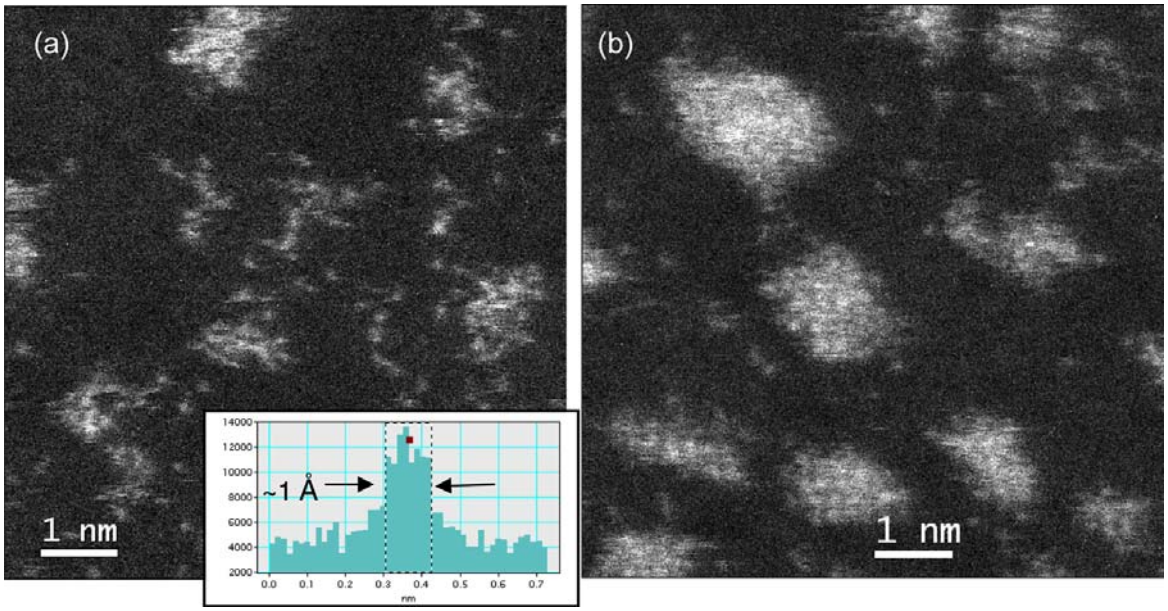

Figure 1. (a) Platinum sputtered onto thin carbon film, showing single atoms, clusters, and "rafts." (b) A second sputter coating of a carbon film with platinum, accumulating about double the total platinum relative to the first coating. Rafts are larger and fewer clusters are present, but no discrete crysallinity is evident even in the larger rafts.

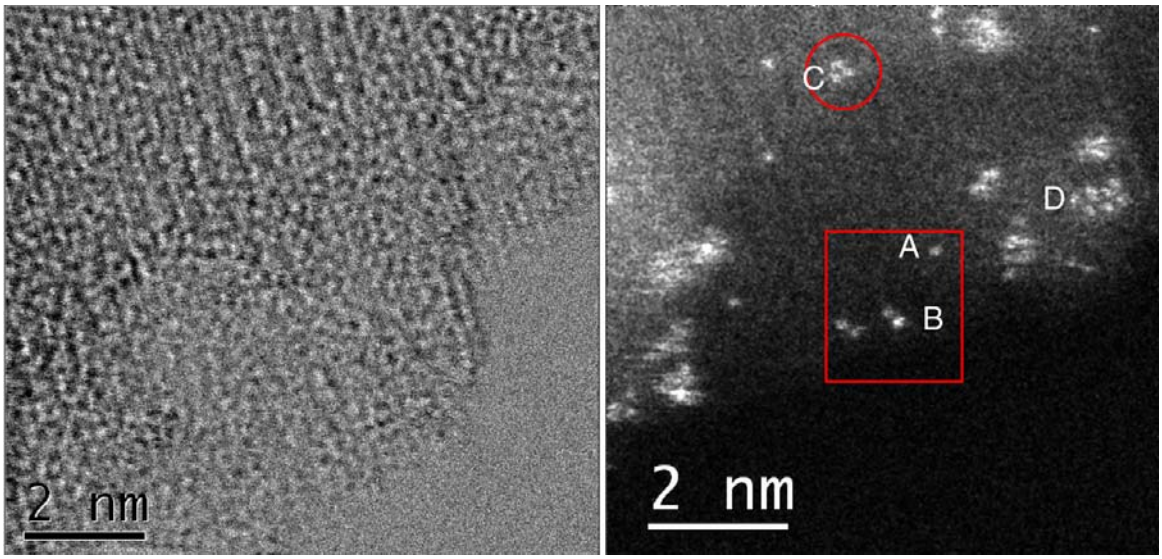

Figure 2. (a) BF image of thin plate of g-Al_2O_3, decorated with rhenium atoms. The phase contrast from the alumina obscures unambiguous determination of location of rhenium species. (b) Same area in ADF image, showing rhenium species in bright contrast. Single atom at A, apparent dimmer at B, clear trimer at C, small raft of atoms at D.

the ACEM and the original distribution of atoms and clusters on as-prepared catalyst specimens. Correlation of imaged morphologies with results from other measurement techniques, again as being done in the work with UCalDavis, may prove the most valuable for providing a reliable quantification of cluster morphologies and distributions.

Rhenium/g-Al_2O_3 imaging results: Figure 2 is a bright-field (BF) STEM image of a thin γ-Al_2O_3 flake, showing high phase contrast and an inability

to unambiguously distinguish the precise location of rhenium atoms and tri-rhenium clusters. The ADF image of the exact same sample area is shown in Figure 3, where the rhenium species are clearly seen in bright contrast. These images were also acquired with a probe diameter of about 1 Å. A single atom (A), an apparent dimer (B) and a tri-rhenium cluster (C) are seen (the raw digital images were smoothed using a 3 × 3 filter). Interestingly, one atom of the "dimer" is brighter in contrast than the other; an intensity profile (Figure 4) shows double the intensity in the bright atom, which is consistent with the intensity which would result from two atoms, one above the other, in the trimer arrangement shown in the cartoon. It is therefore likely that the dimer is actually a trimer seen precisely on edge, a configuration possible if the trimer were attached to a ledge on the alumina support just a few Ångströms in height. The trimer at C shows equal intensity for the individual atoms and is therefore a classical tri-rhenium cluster. The atom-atom spacing in trimer C is slightly different than the spacings in a nearby cluster D (2.0 Å vs 2.3 Å), suggesting that the rhenium atoms (perhaps still carbonylated) are influenced by the crystallography of the γ-alumina crystal lattice. Direct observations of atoms and clusters such as illustrated here, made possible by the new generation of aberration-corrected electron microscopes, and coupled with molecular simulations, offer the potential for a deeper understanding of the changes in morphology of heavy metal species in catalyst systems with aging treatments.

Characterization of fine particle morphology: The direct relationship in the ADF image between number of atoms in a column and the intensity of the column was shown clearly in the example of the tri-rhenium cluster on edge above. In our FY 2004 annual report we also demonstrated this effect for an ideal TEM image of a platinum cube-octahedron. Here we show a bright-field (BF) image of a 7-nm gold particle supported on a 10-nm-thick amorphous carbon film, processed to extract the so-called "exit surface wave" image, at a resolution in the 1-Å range. The problem with the BF images is that the

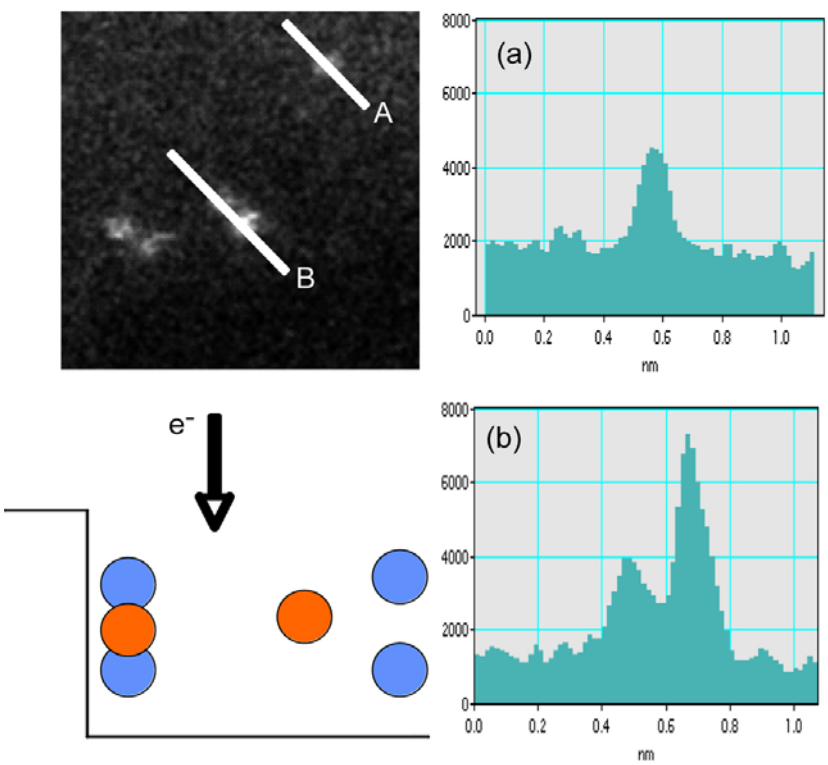

Figure 3. Analysis of the dimer at B shows one "atom" is twice the intensity of the adjacent, where the adjacent atom intensity profile is precisely the height of the single atom at A. This suggests the dimer is actually a trimer tethered to a ledge in the alumina surface and is oriented edge-on to the electron beam, as indicated by the cartoon.

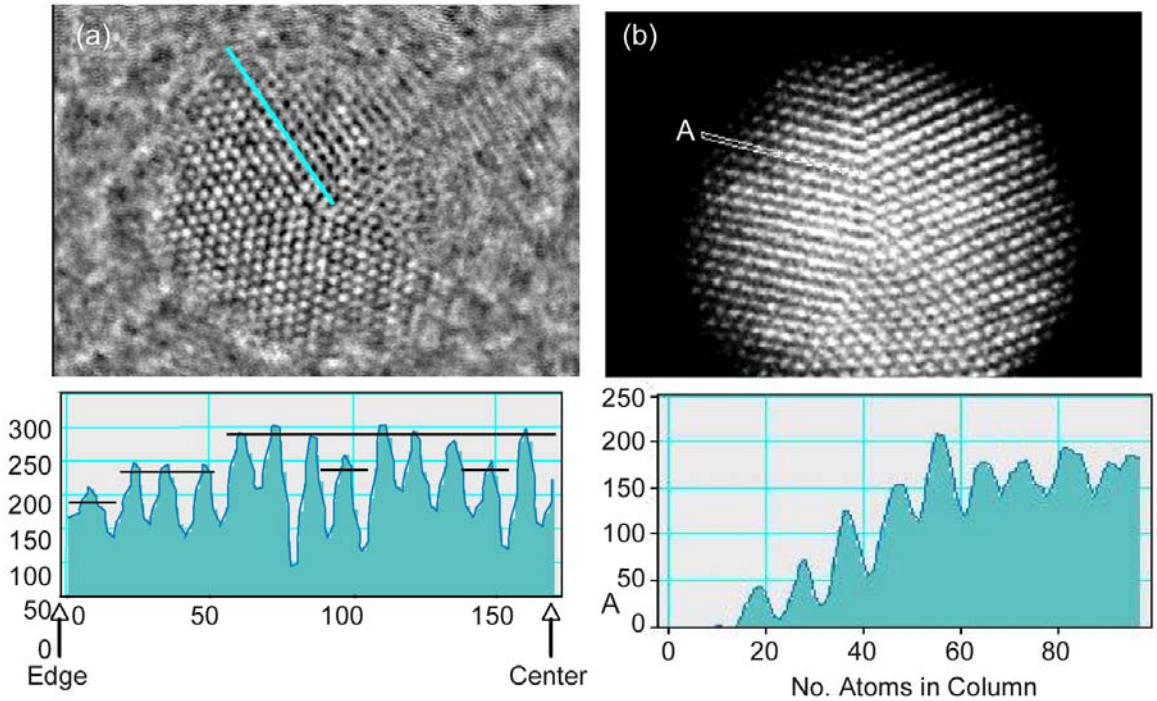

Figure 4. (a) Reconstructed BF Exit Surface Wave image of 7-nm gold particle, with intensity profile inset. The profile shows discrete steps in intensity column by column, but the carbon background makes interpretation ambiguous. (b) Direct ADF image from STEM, with intensity profile A showing number of atoms column by column.

phase contrast from the carbon film makes a significant contribution to the contrast of the atomic columns in the particle. However, in ADF images, because of its very low scattering power relative to the high atomic number of the heavy metal particle, the carbon film contributes essentially no signal to the image. Figure 4 compares the gold particle on carbon in BF [Figure 4(a)] with the gold particle on carbon [Figure 4(b)] in the ADF aberration-corrected STEM image. Because of the phase contrast due to the carbon film in the BF image, the interpretation of discrete intensity jumps column to column are ambiguous. However, a line profile along a typical row of atoms in the gold particle ADF image shows the discrete jumps from column to column. One possible interpretation of the number of atoms in the individual columns is given on the profile inset in Figure 4(b). These are the most promising results obtained to date that show the possibility for ADF imaging in the ACEM to allow full determination of the precise shape of nanometer-sized catalyst particles. Further work is needed to work out image processing methods to allow automatic analysis of particle shapes from ADF images.

Development of new reactor specimen rod: To conduct catalyst reaction experiments involving examination of catalyst powder samples in the ACEM before and after reaction in the HTML ex-situ catalyst reactor system, a new specimen rod for the ACEM had to be designed and fabricated. The new rod was built with the capability to protect the catalyst specimen from atmospheric exposure during transfer of the sample into the microscope, then back to the reactor for sequential reaction experiments. Figure 5 shows the reactor rod [Figure 5(a)] and the rod tip [Figure 5(b–d)]. The tip contains a recess to allow a small disc that would hold a specimen grid to be installed, as shown in Figure 5(c). By manipulating the control knob at the end of the rod, thin sheets of phosphor-bronze spring stock can be slid above and below the specimen grid, allowing the grid to be encapsulated in an inert gas (with a metal-to-metal seal) during the transfer. Experiments utilizing the new capability on the ACEM for reaction studies will be detailed in forthcoming quarterly reports.

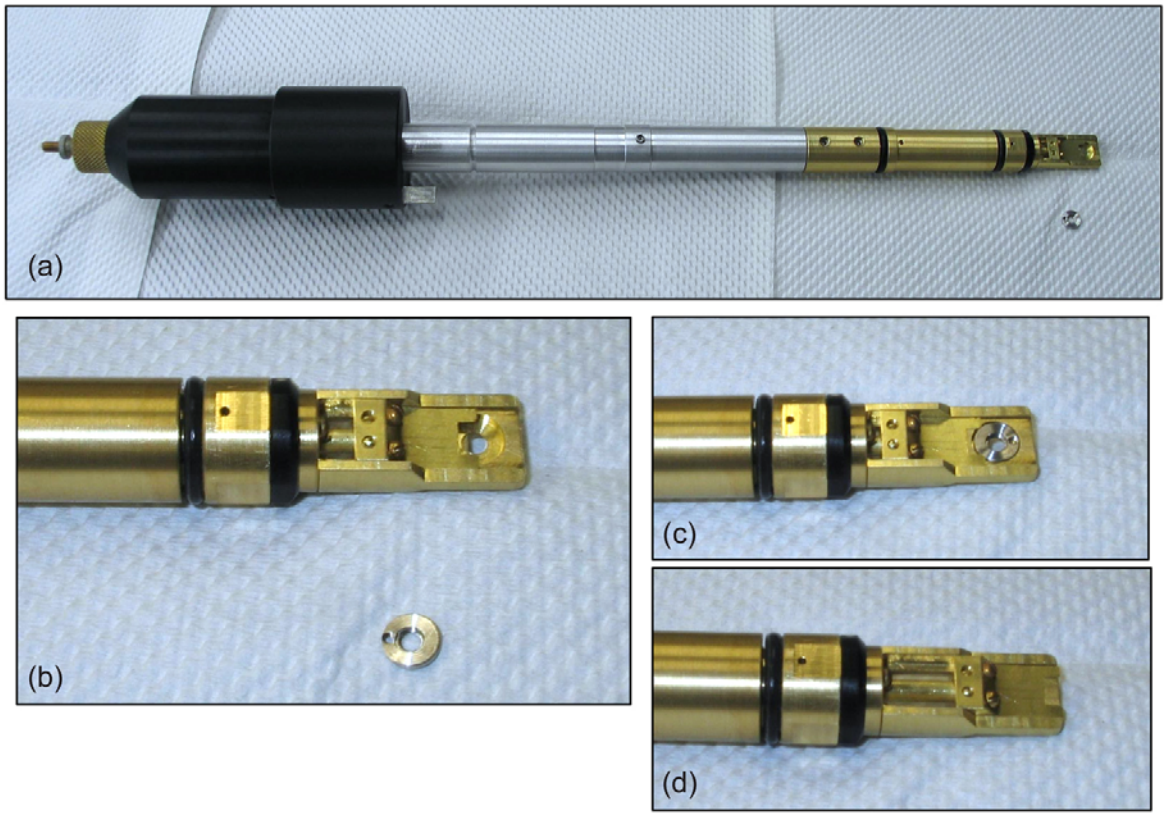

Figure 5. (a) Specimen rod designed for use with the ACEM to permit catalyst reaction studies in the HTML ex-situ reactor system. Tip details shown below. (b) Tip of specimen rod with disc to hold specimen grid adjacent. (c) Rod tip with disc in place. (d) Rod manipulated to position thin metal sheets above and below the specimen (metal-to-metal seal), allowing encapsulation of the sample in an inert gas.

Analysis of Supplier Catalysts

In partnership with colleagues at Ford Research Laboratory and the National Transportation Research Center (NTRC), catalyst materials including lean NO_x trap (LNT) and diesel particulate NO_x reduction (DPNR) materials have been characterized in a program to understand the structures and behavior of catalysts being used in vehicles overseas (Europe). The LNT materials were supplied by Umicore Co. [their GDI (gasoline direct injection) catalyst] and by Toyota (their Avensis D-CAT, or Diesel Clean Advanced Technology catalyst). Toyota also supplied DPNR material for their Avensis vehicle. These materials were characterized initially in the "fresh" or as-received condition, with general microstructure and chemistry provided by electron microprobe analysis, and further high-resolution imaging and microanalysis using the Hitachi TEM and dedicated STEM instruments in the HTML, as well as the ACEM for ultra-high resolution imaging.

A full presentation of the results of the supplier catalyst studies is beyond the scope of this report, but a few interesting observations are shown as examples. The first observation using the electron microprobe in backscattered electron imaging (BSE) mode showed the Umicore LNT catalyst bulk structure to be a standard single washcoat deposition on a porous cordierite monolith having channels with square cross section. Figure 6(a) shows a typical BSE image of a corner of washcoat, where several blocky aggregate phases are evident (in BSE mode, lighter contrast reflects higher average atomic number of the phase, so baria would be lighter in contrast than alumina, for example). The Toyota D-CAT LNT structure was similar (not shown here), except a cordierite monolith having channels with hexagonal cross section was employed.

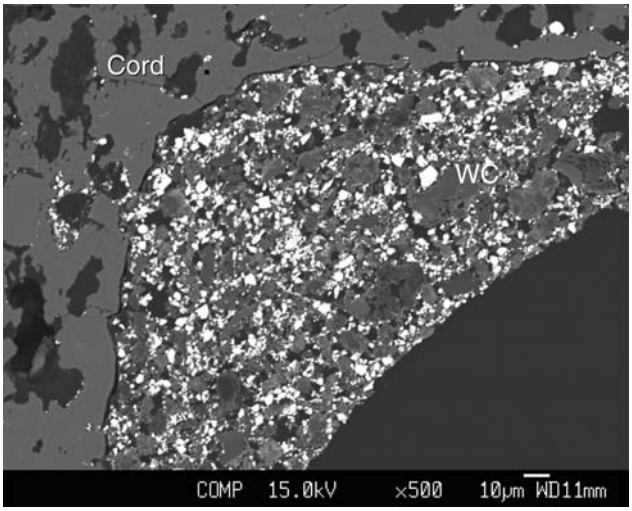

Figure 6. BSE image of corner of a channel in Umicore LNT catalyst monolith, showing single-layer washcoat composed of blocky aggregates of constituents including alumina, baria-alumina and ceria-zirconia.

In contrast to these more standard materials, the Toyota DPNR catalyst utilized a more highly porous monolith structure, and the washcoat material was much finer grained and infiltrated within the pore structure, with none remaining on the channel walls, as illustrated in Figure 6(b) and 6(c). The DPNR structure proved difficult to thin for TEM work, so results of the study of that material will be reported in a future quarterly. The LNT catalysts were prepared for TEM analysis by standard ion milling techniques, so thin sections of the washcoat were available for high-resolution imaging (see Figure 7).

The Fresh Umicore LNT structure comprised alumina, baria-alumina, and ceria-zirconia (primarily ceria) phases, with platinum as the primary heavy-metal catalytic species. Interestingly, both the alumina and baria-alumina phases contained magnesia (MgO) as a significant constituent (at the 10 wt % level), which is not typical of similar catalysts from other manufacturers. The role of MgO is not yet clear.

The Fresh Umicore material showed a dispersion of platinum clusters and ultra-fine particles that were best imaged with the ACEM, as particles ranged from the 1- to 1.5-nm size range (widely dispersed) down to uniformly dispersed clusters at the near single atom level. After a "de-greening" treatment (standard practice for LNT catalysts), the platinum dispersion was observed in the Hitachi HD-2000 STEM with ADF imaging to form discrete particles in the 2- to 10-nm size range. Images at roughly equivalent magnifications from the ACEM [Figure 8(a)] and the dedicated STEM [Figure 8(b)] illustrate this particle growth. The advantages of

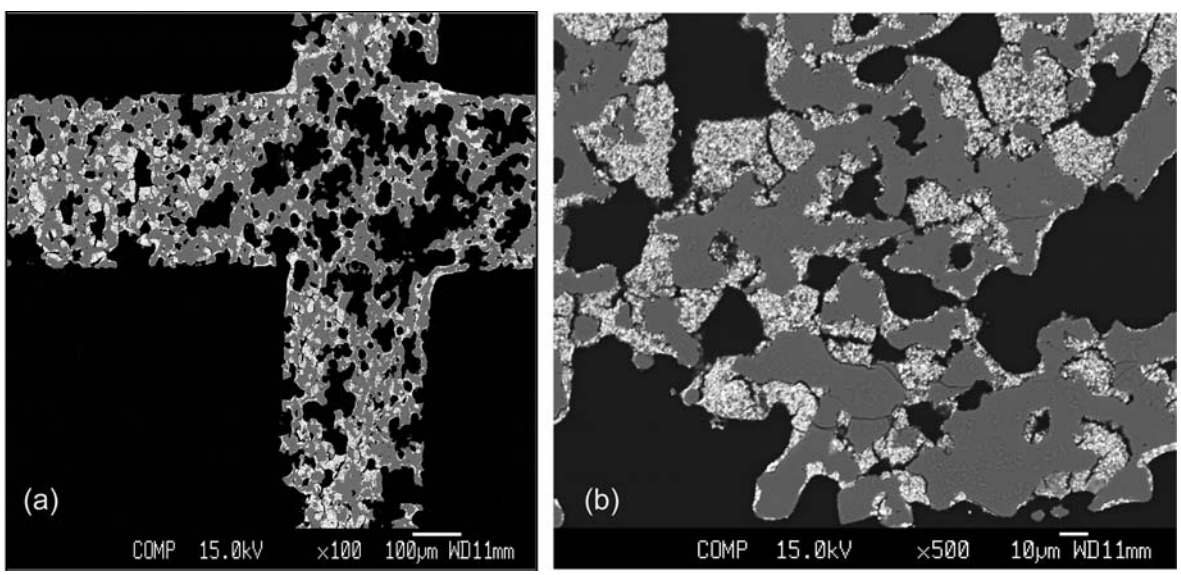

Figure 7. (a) Low-magnification image of polished cross section of Toyota DPNR catalyst structure, showing infusion of washcoat throughout pores of the cordierite monolith. (b) DPNR structure at higher magnification (compare to Figure 6). Washcoat (light contrast) is very fine grained relative to the aggregate structure of the LNT washcoat seen in Figure 6. Black areas are embedding media, and grey areas are cordierite.

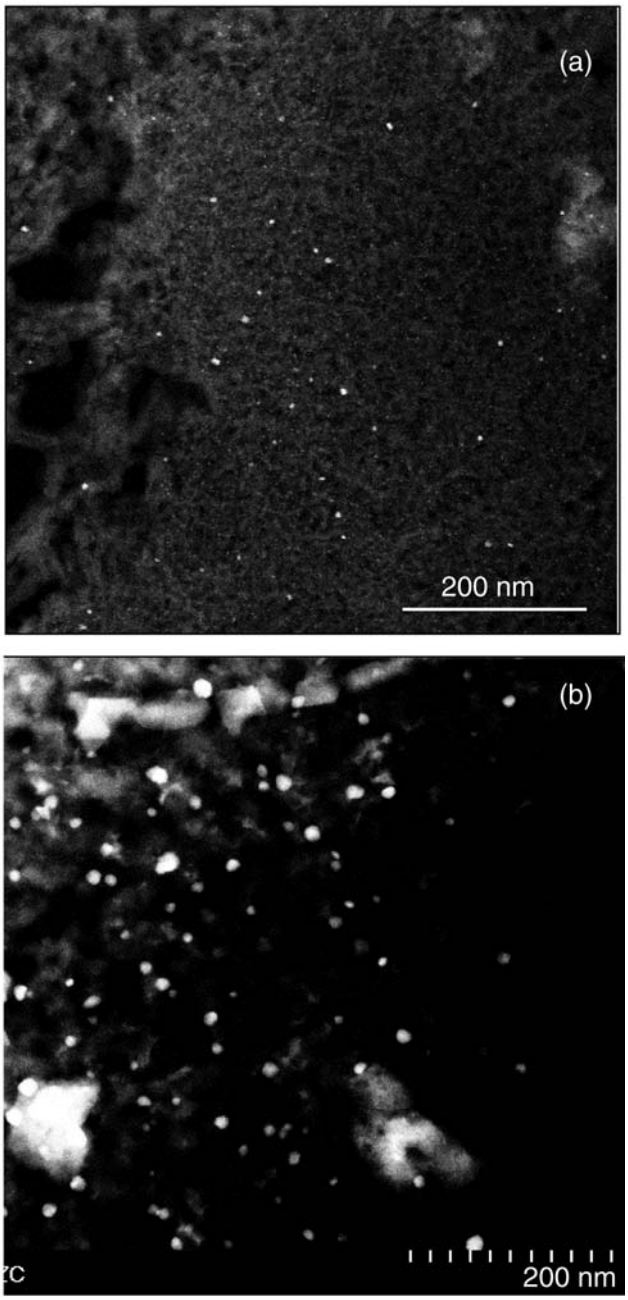

Figure 8. (a) High-resolution ACEM ADF image of ultra-fine platinum clusters level in "Fresh" Umicore LNT catalyst, in area of alumina phase. (b) ADF image from HD-2000 STEM showing particle after a "de-greening" treatment.

imaging heavy-metal particles in the dark-field mode, both with the dedicated STEM for standard resolution imaging and with the new aberration-corrected instrument are clear. The effective change in platinum particle morphologies with further treatments in a benchtop reactor should serve to permit further understanding of the degradation in performance of these LNT catalysts, and will be reported in later quarterlies.

References

1. M. A. O'Keefe, E. C. Nelson, and L. F. Allard, "Focal Series Reconstruction of Nanoparticle Exit Surface Wave," *Microscopy and Microanalysis*, 2003.

Presentations and Publications

L. F. Allard and C. K. Narula, "Electron Microscopy of LNT Materials: Microstructural Changes with Aging," Presentation at 2005 CLEERS Workshop, Dearborn, Michigan, May 2005.

V. A. Bhirud, M. J. Moses, D. A. Blom, L. F. Allard, T. Aoki, S. Mishina, C. K. Narula, and B. C. Gates, "Alumina-supported Tri-rhenium Clusters Revealed by Aberration-corrected Electron Microscopy," *Microscopy and Microanalysis* (2005) (First Place Award winner in Physical Sciences competition).

C. K. Narula. L. F. Allard, M. J. Moses, Y. Xu, W. Shelton, W. F. Schneider, G. Graham, and J. Hoard, "Lean NO_x Traps—Microstructural Studies of Real World and Model Catalysts," DEER 2005, Palmer Hilton, Chicago, August 21–25, 2005.

M. A. O'Keefe, L. F. Allard, and D. A. Blom, "HRTEM Imaging of Atoms at Sub-Ångström Resolution," *Journal of Electron Microscopy*, Special Issue in Memory of Prof. John M. Cowley, p. 1–12, August 25, 2005.

M. A. O'Keefe, L. F. Allard, and D. A. Blom, "Resolution Quality and Atom Positions in Sub-Ångström Electron Microscopy," *Microscopy and Microanalysis*, in press.

E. Microstructural Changes in NO_x Trap Materials under Lean and Rich Conditions at High Temperatures

C. K. Narula, M. J. Moses, and L. F. Allard
Oak Ridge National Laboratory
P.O. Box 2008, MS 6116
Oak Ridge, TN 37831-6116
(865)574-8445; e-mail: narulack@ornl.gov

DOE Technology Development Area Specialist: James J. Eberhardt
(202) 586-9837; fax: (202) 586-1600; e-mail: james.eberhardt@ee.doe.gov
ORNL Technical Advisor: D. Ray Johnson
(865) 576-6832; fax: (865) 574-6098; e-mail: johnsondr@ornl.gov

Contractor: Oak Ridge National Laboratory, Oak Ridge, Tennessee
Contract No.: DE-AC05-00OR22725

Objective

- Facilitate the development of nitrogen oxides (NO_x) trap catalysts for lean gasoline or diesel exhaust treatment by
  - Investigating materials issues related to deterioration of NO_x traps performance upon aging as a result of thermal and sulfation-desulfation cycles.
  - Designing new lean NO_x trap (LNT) materials that are robust under the LNT operating conditions.

Approach

- Study microstructural changes in model LNT catalyst systems under normal operating conditions and accelerated aging using simulated diesel exhaust in a reactor system to understand the causes of failure.
- Correlate microstructural changes with performance by evaluating model LNT catalyst systems on a bench-top reactor
- Design new LNT catalysts that are robust under operating and aging conditions. Rapidly screen new catalysts for microstructural changes using an ex-situ reactor system and detailed evaluation on a bench-top reactor.

Accomplishments

- Tested the updated ex-situ reactor with simulated stoichiometric, lean, rich, and lean/rich cycling exhaust capability to treat transmission electron microscopy (TEM) samples by reproducing the results of the old reactor.
- Completed a study of microstructural changes in the model LNT catalyst, 2%Pt-98%[10%CeO_2-ZrO_2-90%(2%La_2O_3-98%BaO•6Al_2O_3)], and 2%Pt/γ-Al_2O_3 using simulated diesel exhaust (without sulfur oxides) under the following conditions:
  - 60-s/5-s lean/rich cycling at 500°C/4 h for 2%Pt-98%[10%CeO_2-ZrO_2-90%(2%La_2O_3-98%BaO•6Al_2O_3)
  - 240-s/60-s lean/rich cycling at 500°C/4 h for the model catalysts and 2%Pt/γ-Al_2O_3
  - Accelerated aging at 700°C for 16 h using 60-s/5-s lean/rich cycling and 240-s/60-s lean/rich cycling for 2%Pt-98%[10%CeO_2-ZrO_2-90%(2%La_2O_3-98%BaO•6Al_2O_3)

- Carried out a preliminary study of microstructural changes under accelerated aging conditions (700°C, 16 h) using simulated exhaust (with SO_2) at 240-s/60-s lean/rich cycling for 2%Pt-98%[10%CeO_2-ZrO_2-90%(2%La_2O_3-98%BaO•6Al_2O_3).
- Neared completion of the assembly of the bench-top flow reactor and installation of software. We will initiate experiments to correlate microstructural changes in LNT materials to LNT performance.

Future Direction

- Initiate correlation of microstructural changes with LNT performance by testing model catalysts on a bench-top reactor for performance.
- Guided by the results of correlation of microstructural changes with performance, design new LNT catalyst systems and carry out systematic evaluation.

Introduction

The introduction of diesel-engine–based heavy-duty trucks and passenger vehicles depends on the successful development of a strategy to treat NO_x emissions. There presently is no catalyst or combination of catalysts that can convert NO_x into inert gases under oxidizing conditions over a complete range of exhaust temperatures. Among NO_x treatment strategies, LNTs are the most likely candidates for early deployment because they are consumer-transparent (no action is needed on the part of consumers) and they can be system-integrated into current vehicle control strategies.[1]

NO_x traps collect engine-out NO_x during lean operation and treat it during short rich operation cycles.[2]] The NO_x traps can be considered to be derived from commercial three-way catalysts (TWCs) installed to treat stoichiometric emissions from engines operating at air-fuel ratios of ~14. Therefore, the basic components of NO_x traps are identical to TWCs. The advanced version of a TWC is a two-layer system on a honeycomb substrate with the inner layer based on platinum-alumina and the outer layer on rhodium-ceria-zirconia. The NO_x traps derived from advanced TWCs are identical to these with the exception of a high baria content (the upper limit being close to 20%) in the alumina layer.

Fresh NO_x traps work very well, but they cannot sustain their high efficiency over the lifetimes of vehicles. The gradual and persistent deterioration in the performance of commercial TWCs is quite well known.[3] The performance deterioration in NO_x traps is believed to be caused by aging due to high-temperature operation and sulfation-desulfation cycles necessitated by the sulfur oxides (SO_x) in the emissions from the oxidation of sulfur in fuel. The formation of barium aluminate is also considered to be a cause of performance deterioration since barium aluminate forms on thermal aging and is an inefficient NO_x adsorber. Until last year, the aging-related microstructural changes in precious metals components were not available in open literature. In our previous reports, we summarized our studies of fresh and aged supplier samples that clearly show changes that occur on aging under various operating conditions. The prominent changes are sintering and migration of precious metals and migration of barium, leading to reduced precious metal-adsorber surface area available for NO_x adsorption in lean cycles.

In order to design a thermally durable NO_x trap, there is a need to understand the changes in the microstructures of materials that occur during various modes of operation (lean, rich, and lean/rich cycles). This information can form the basis for selection and design of new NO_x trap materials that can resist deterioration under normal operation. The first goal of the project is to determine if one or all of the microstructural changes take place during lean, rich, or lean/rich cycles.

The tasks to achieve this goal are as follows:

- Complete microstructural characterization of fresh and thermally aged NO_x trap materials to determine the species formed as a result of aging.
- Complete microstructural characterization of fresh NO_x trap materials after exposure to simulated lean, rich, and lean/rich cycling conditions with and without SO_x to determine the species formed during lean cycles.
- Complete microstructural characterization of fresh NO_x trap materials after exposure to

accelerated lean/rich aging conditions to determine the species formed as a result of elevated temperatures.

- Correlate microstructural changes with the performance of LNTs.

The second goal of the project is to investigate and design new catalyst materials that can withstand NO_x trap operating conditions without undergoing detrimental structural changes. The results from the first goal will provide insights into changes that occur in NO_x trap materials at a microstructural level upon extended exposure to NO_x trap operating conditions, enabling selection and design of materials for the second goal.

Approach

Our approach involves a detailed study of microstructural changes in model LNT catalyst systems using an updated ex-situ reactor under normal operating conditions, and accelerated aging using simulated diesel exhaust in a reactor system to understand the causes of failure and the deterioration mechanism.

The next step in this process is establishment of a correlation between microstructural changes and the performance of model LNT catalyst systems using a bench-top reactor.

Finally, we plan to design new LNT catalysts that are robust under operating and aging conditions. In this protocol, we will use microstructural changes as a rapid screening tool for new catalysts and will carry out detailed evaluation using a bench-top reactor.

Results

Our previous studies of the microstructural changes that occurred in a supplier LNT system (based on Pt/BaO–Al_2O_3 and CeO_2–ZrO_2 materials) upon aging on (1) a pulsator at Ford Motor Company (2) a dynamometer at Ford, and (3) vehicles in gasoline direct-injection spark-ignition engines in Europe show the following results.

After pulsator aging, lean and rich aged samples showed that the sintering of platinum particles occurs during aging and barium migrates into the ceria-zirconia layer. Both of these factors reduce the platinum-barium oxide surface area where NO_x adsorption and reduction takes place during lean and rich cycles, respectively. The stoichiometric aging also leads to the migration of barium into the ceria-zirocnia layer, but the sintering of platinum is less severe.

The dyno-aged samples showed extensive sintering of platinum and its migration in the ceria-zirconia layer. The sintering of rhodium was also observed. The migration of barium into the ceria-zirconia and the sintering of the precious metal component could explain the deterioration of performance.

The analysis of samples evaluated on a vehicle after 32,000 km and 80 km showed that the bulk of the sintering of precious metals occurred in the stages of on-vehicle aging.

These results primarily show precious metal sintering and barium migration to be causes of performance deterioration in NO_x trap materials in gasoline engine exhaust conditions.

While the laboratory aging protocols for diesel engines were in development, we compiled data showing early-stage changes in model NO_x trap materials under diesel conditions. We also reported the synthesis and characterization of three catalyst systems, i.e. (Pt/Al_2O_3), (2%Pt-98%[10%CeO_2-ZrO_2-90%(2%La_2O_3-98%BaO.6Al_2O_3)]), and (2%Pt, 5%MnO_2-93%[10%CeO_2-ZrO_2-90%(2%La_2O_3-98% BaO.6Al_2O_3)]). Now that the laboratory aging protocols are in public domain, we have carried out a preliminary study of microstructural changes in LNT catalyst materials under the accelerated aging conditions. The results are summarized in the following paragraphs.

Microstructural Changes in Model Catalysts

The TEM samples of a model LNT catalyst, 2%Pt-98%[10%CeO_2-ZrO_2-90%(2%La_2O_3-98%BaO•6Al_2O_3)] and a standard 2%Pt/γ-Al_2O_3 were treated under lean/rich cycling at operating (500ºC) and accelerated aging (700ºC) conditions using a simulated diesel exhaust on the updated ex-situ reactor (Figure 1). The microstructural changes in the samples were analyzed by scanning TEM (STEM). The simulated diesel exhaust contained CO, CO_2, H_2, C_3H_6, NO, H_2O, and O_2 with N_2 as a balance gas. The SO_2 was added to the simulated exhaust stream in some accelerated aging studies. All tests were run at a gas flow of 100 cc/min. A summary of the results is presented in Tables 1 and 2.

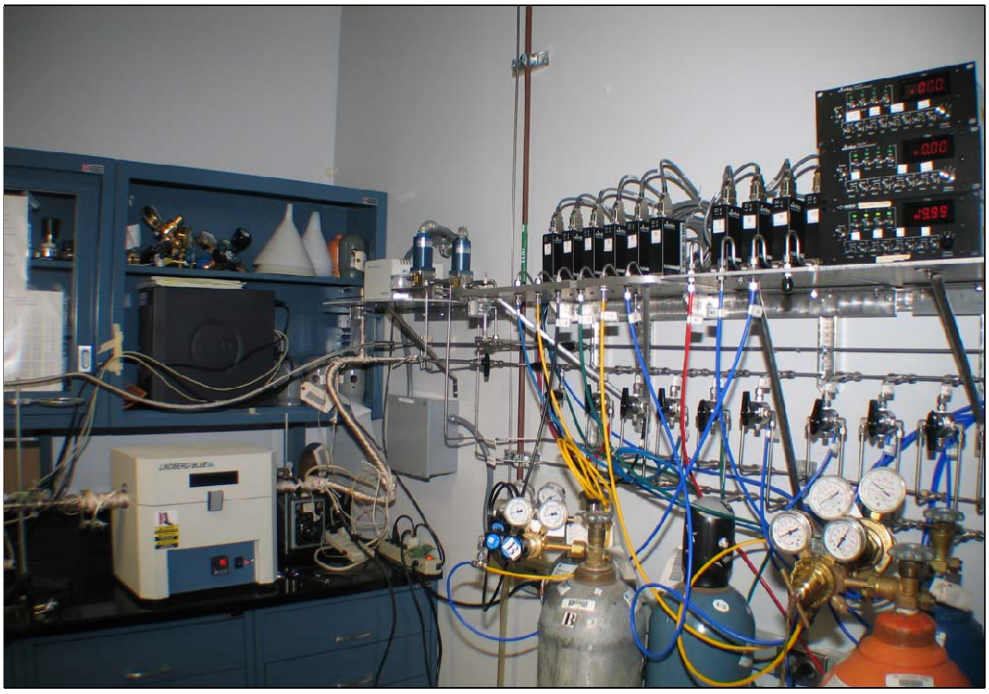

Figure 1. Ex-situ reactor set-up.

Table 1. Platinum particle size change under lean/rich cycle treatment at 500°C/4 h using simulated exhaust without SO_2

Catalyst	Fresh sample	Lean/rich diesel aging	
		60 s/5 s	240 s/60 s
2%Pt/γ-Al_2O_3	0.9–2.3 nm	—	0.7–2.7 nm
2%Pt-98%[10%CeO_2-ZrO_2-90%(2%La_2O_3-98% BaO•6Al_2O_3)]	0.7–2.2 nm	0.7–2.8 nm	0.7–2.1 nm

Table 2. Platinum particle size change under lean/rich cycle treatments at 700°C using simulated exhaust

Catalyst	Aging time	Lean/rich diesel exhaust		
		60 s/5 s	240 s/60 s	
		w/o SO_2	w/o SO_2	w/ SO_2
2%Pt-98%[10%CeO_2-ZrO_2-90%(2%La_2O_3-98% BaO•6Al_2O_3)]	Fresh	0.6–2.9 nm	0.9–2.5 nm	1.0–2.1 nm
	4h	0.5–5.0 nm	0.6–4.4 nm	1.0–3.7 nm
	8h	0.6–5.4 nm	0.8–5.3 nm	0.8–4.6 nm
	12h	0.6–5.9 nm	0.7–4.7 nm	—
	16h	—	0.7–4.7 nm	—

Operating conditions—lean/rich cycling at 500°C on ex-situ reactor: After 4 h of treatment in a simulated exhaust flow without SO_2, no platinum sintering was observed regardless of lean/rich pulse time (Figure 2).

- 60-s/5-s lean/rich cycling: 2%Pt-98% [10%CeO2-ZrO2-90%(2%La2O3-98%BaO•6Al2O3)]: STEM of the fresh sample showed platinum particles in the 0.7–2.2 nm range. The electron microscopy images show no significant growth in particle size, 0.7–2.7 nm, after aging.
- 240-s/60-s lean/rich cycling: 2%Pt-98% [10%CeO_2-ZrO_2-90%(2%La_2O_3-98%BaO•6Al_2O_3)]: STEM images of the fresh sample showed platinum particles in the 0.7–2.2 nm range. The particles showed no increase in particle size range after aging. STEM images of the fresh 2%Pt/γ-Al_2O_3 showed platinum particles in the 0.9–2.3 nm range, and no growth in particle size was seen after 4 h.

Accelerated aging—lean/rich cycling at 700°C: The accelerated aging of a model catalyst, 2%Pt-98%[10%CeO_2-ZrO_2-90%(2%La_2O_3-98%BaO•6Al_2O_3)], was carried out using simulated exhaust without SO_2 under 60-s lean/5-s rich pulses or 240-s/60-s rich pulses, and no significant difference was noted. Interestingly, platinum sintering was evident after only 4 h of sample treatment under accelerated aging conditions. A gradual growth in platinum particles in the 2.0–5.0 nm range was seen after each additional 4 h of treatment. Addition of SO_2 to the simulated exhaust did not lead to any additional noticeable platinum sintering. Figures 3 and 4 depict the results of the accelerated aging study at 240 s/60 s lean/rich cycling with and without SO_2, respectively.

60-s/5-s lean/rich accelerated aging treatment using simulated exhaust without SO_2:

- STEM images of the fresh sample showed platinum particles in the 0.6–2.9 nm range.
- After 4 h of aging, sintering of the particles could be seen in the STEM images by the appearance of particles in the 2.0–5.0 nm range.
- After each of the remaining four increments, STEM images showed further platinum sintering with a gradual increase in the number of 2.0–5.0 nm particles.

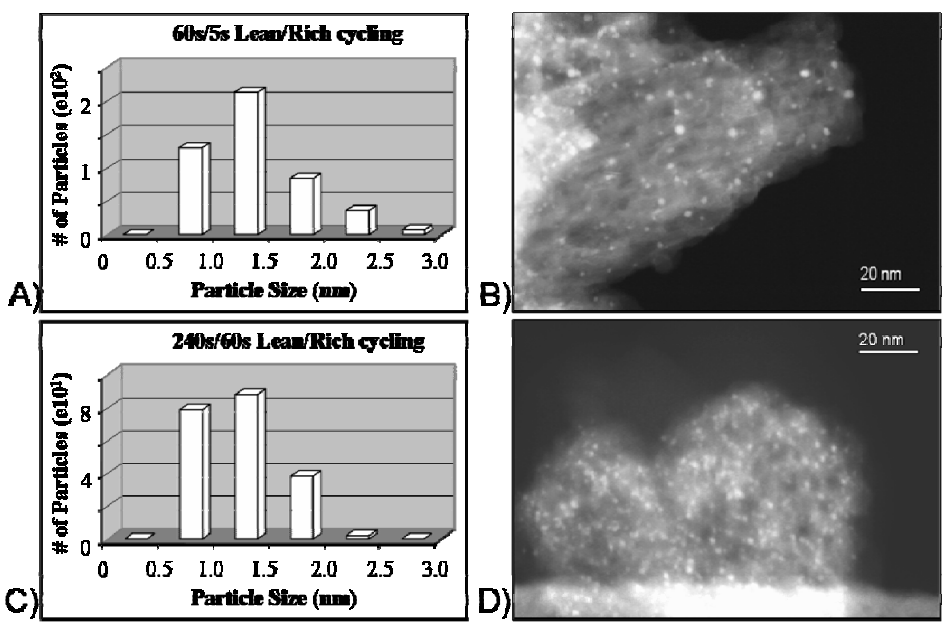

Figure 2. (a) Particle size distribution of multiple areas of a model LNT catalyst, 2%Pt-98% [10%CeO_2-ZrO_2-90%(2%La_2O_3-98%BaO•6Al_2O_3)], after lean/rich cycling and 60-s/5-s pulse using simulated exhaust without SO_2. (b) A STEM image of one area recorded in (a). (c) Particle size distribution of multiple areas of a model LNT catalyst after lean/rich aging at a cycling time of 240 s/60 s. and (d) A STEM image of one area recorded in (c).

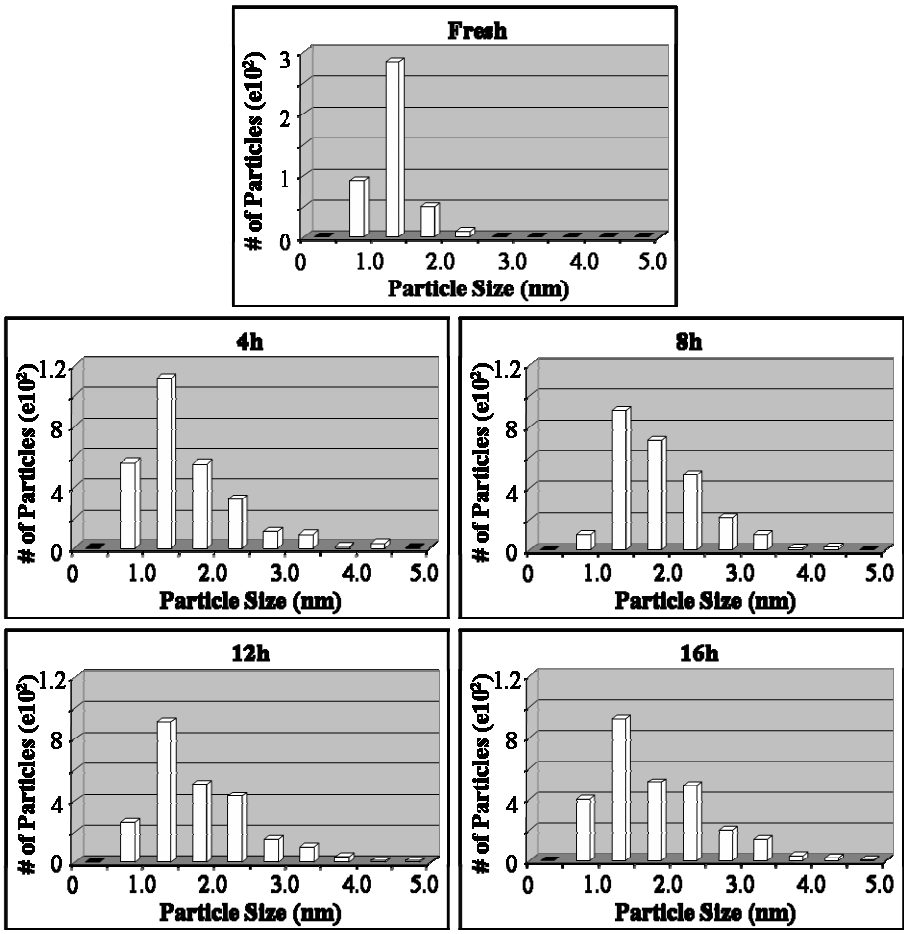

Figure 3. These graphs show platinum particle size distribution of the model LNT catalyst, 2%Pt-98%[10%CeO_2-ZrO_2-90%(2%La_2O_3-98%BaO•6Al_2O_3)], fresh and after accelerated aging at 700°C in 4-h increments for 16 h and 240-s/60-s lean/rich pulse using simulated diesel exhaust without SO_2. The same four areas of the sample were used for each distribution.

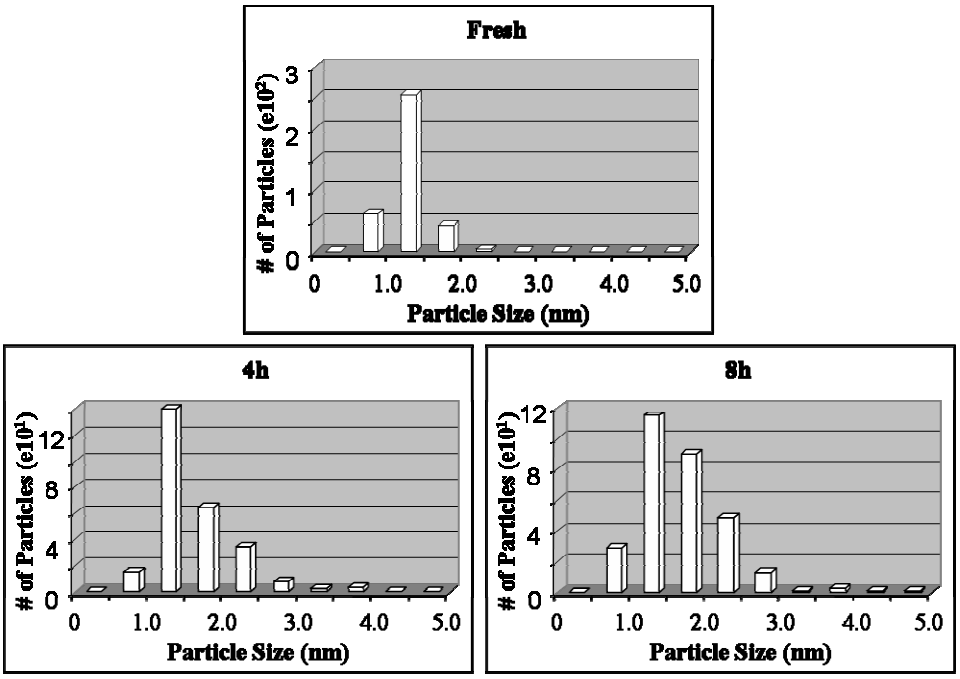

Figure 4. These graphs show platinum particle size distribution of the model LNT catalyst, 2%Pt-98%[10%CeO_2-ZrO_2-90%(2%La_2O_3-98%BaO•6Al_2O_3)], fresh and after accelerated aging at 700°C in 4-h increments for 8 h and 240-s/60-s lean/rich pulse using simulated diesel exhaust with SO_2. The same three areas of the sample were used for each distribution.

240-s/60-s lean/rich accelerated aging treatment using simulated exhaust without SO_2: STEM images of the fresh sample showed platinum particles in the 0.6–2.5 nm range.

- After 4 h of aging, sintering of the particles could be seen in the STEM images by the appearance of particles in the 2.0–5.0 nm range.
- After each of the remaining 4-h increments, STEM images showed further platinum sintering with a gradual increase in the number of 2.0–5.0 nm particles.

240-s/60-s lean/rich accelerated aging treatment using simulated exhaust with SO_2:

- STEM images of the fresh sample showed platinum particles in the 1.0–2.1 nm range.
- After 4 h of aging, sintering of the particles could be seen in the STEM images by the appearance of particles in the 2.0–4.0 nm range.
- After another 4 h of aging, STEM images showed further platinum sintering with a gradual increase in the number of 2.0–5.0 nm particles.

Modifications to Ex-situ Reactor

Final modifications to the ex-situ reactor were completed this year to include the ability to cycle through lean and rich conditions. This involved the use of a bench-top flow furnace and the installation of additional gas-flow controllers and solenoid valves that could be controlled through a computer using LabView software. A picture of the modified ex-situ reactor setup is shown in Figure 1.

Assembly of Bench-Top Flow Reactor

The assembly of the bench-top flow reactor and installation of software is nearing completion. We will initiate experiments to correlate microstructural changes in LNT materials to LNT performance.

Conclusions

Our results for microstructural changes clearly show that LNT materials are relatively stable under normal operating conditions of diesel engines. Practically no sintering of precious metals is observed that could cause performance deterioration. However, our accelerated aging studies demonstrate that

rapid sintering of precious metals can take place, leading to performance deterioration. Interestingly, SO_x appears to place an indirect role in the performance deterioration of LNTs. Since there is no significant difference in precious metal sintering during accelerated aging using simulated exhaust with or without sulfur, it would appear that SO_x plays no role in precious metal sintering, but high-temperature treatment is required only for desulfation. Thus if there were no SO_x in diesel exhaust, there would be no need for high-temperature desulfation and the LNT would be quite durable.

Our next goals are to finish accelerated aging tests in the presence of SO_2 and to start evaluating new model catalyst systems for their performance and correlate them to microstructural changes.

References

1. N. Miyoshi, S. Matsumoto, K. Katoh, T. Tanaka, J. Harada, N. Takahashi, K. Yokota, M. Sigiura, and K. Kasahra, "Development of New Concept Three-Way Catalyst for Automotive Lean-Burn Engines," paper 95-0809, Society of Automotive Engineers, Warrendale, Pennsylvania, February 11, 1995.

2. N. Takahashi, H. Shinjoh, T. Iijima, T. Suzuki, K. Yamazaki, K. Yokota, H. Suzuki, N. Miyoshi, S. Matsumoto, T. Tanizawa, S. Tateishi, and K. Kasahara, "The New Concept 3-Way Catalyst for Automotive Lean-Burn Engine: NO_x Storage and Reduction Catalyst," *Catalysis Today*, **27**, 63–69 (1996).

3. H. S. Gandhi, G. W. Graham, and R. W. McCabe, "Automotive Exhaust Catalysis," *J. Cat.,* **216**, 433–442 (2003).

Presentations and Publications

C. K. Narula, W. A. Shelton, L. F. Allard, Y. Xu, M. Moses, W. Schneider, and B. Gates, "Combining Theory and Experiments in Studies of Structural Changes in LNT Materials," presented at the Eighth DOE Crosscut Workshop on Lean Emissions Reduction Simulation, CLEERS 2005, University of Michigan–Dearborn, Dearborn, Michigan, May 17–19, 2005.

C. K. Narula, L. F. Allard, M. Moses, Y. Xu, W. Shelton, W. F. Schneider, G. Graham, and J. Hoard, "Lean NO_x Traps—Microstructural Studies of Real World and Model Catalysts," DEER 2005, Chicago, August 21–25, 2005.

C. K. Narula, C. S. Daw, J. W. Hoard, and T. Hammer, "Materials Issues Related to Catalysts for Treatment of Diesel Exhaust," *Int. J. Appl. Ceram. Tech*., **2**, 452 (2005).

C. K. Narula, M. Moses, and L. F. Allard, "Ex-situ Reactor Studies of Microstructural Changes in NO_x Traps under Operating Conditions," *J. Phys. Chem.* (in preparation).

F. Aftertreatment Catalysts Materials Research

Matthew Henrichsen and Randy Stafford
Cummins, Inc.
1900 McKinley Ave.
Columbus, IN 47203
(812) 377-3279; e-mail: randy.j.stafford@cummins.com

DOE Technology Development Area Specialist: James J. Eberhardt
(202) 586-9837; fax: (202) 586-1600; e-mail: james.eberhardt@ee.doe.gov
ORNL Technical Advisor: D. Ray Johnson
(865) 576-6832; fax: (865) 574-6098; e-mail: johnsondr@ornl.gov

Contractor: Oak Ridge National Laboratory, Oak Ridge, Tennessee
Prime Contract No: DE-AC05-00OR22725
Subcontractor: Cummins, Inc., Columbus, Indiana

Objective

- Develop knowledge and tools necessary to satisfy the U.S. Environmental Protection Agency (EPA) 2007 and 2010 diesel emissions regulations while minimizing the total cost of ownership.

Approach

- Develop reactors and test methods for understanding the fundamental behavior of catalysts.
- Evaluate novel base metal oxide catalysts for oxidation of diesel soot with conventional and microwave heating.
- Improve understanding of sulfation and desulfation of commercial NO_x reduction catalysts through reactor studies.

Accomplishment

- Completed program final report.

Future Direction

- Continue sulfation and desulfation studies with private funding.
- Continue the search for low-temperature soot oxidation catalysts.

Introduction

The 2007 and 2010 EPA regulations on particulate and NO_x emissions from diesel engines are significantly lower than the current regulatory standards. These regulations are seen as aftertreatment-forcing by the diesel industry.

NO_x traps (also referred to as NO_x storage and release catalysts) are a primary path toward compliance with the 2007 and 2010 EPA regulations. However, the poisoning effects of sulfur reduce the efficiency of NO_x traps to capture and destroy NO_x emitted from diesel engines. Even though sulfur levels will be reduced in future diesel fuels, any amount of sulfur in fuel will be detrimental because the effect of sulfur on NO_x traps is cumulative. NO_x traps can be desulfated by high-temperature reduction. Desulfation, however, can require extended time at high temperature. If the desulfation process

requires 10 min for completion for light-duty applications, then desulfation will be impractical because the average time between engine start and stop for a light-duty vehicle is less than 10 min.

Catalysts commonly used for soot oxidation in catalyzed soot filters are based on platinum group metals and cerium oxides. The use of platinum group metals significantly increases the cost of catalyst systems. Base metal oxide catalysts, while typically less active than platinum group metal catalysts, are much less expensive. There have been reports in the literature that microwave heating accelerates soot oxidation in the presence of some base metal oxide catalyst more than conventionally heating to a similar temperature accelerates oxidation. If true, this could allow very low temperature regeneration of soot filters, significantly reducing the stress on the system and the cost of regeneration.

Approach

No experimental work was conducted in FY 2005. The program final report was written and submitted to close the program.

Results

The program final report was submitted in February 2005 to close this program.

Summary and Conclusions

A test method was developed that allows a relatively inexpensive mass spectrometer to differentiate between molecules of similar mass and different chemical behavior. Reactors were developed to allow comparison of chemical kinetics with microwave and conventional heating. A reactor for artificial aging of multiple catalyst cores was designed.

Catalyzed soot oxidation with conventional and microwave heating was explored. Data from direct comparisons provided no reasonable basis to think that microwave heating significantly improves catalytic soot oxidation over conventional heating at a similar temperature. Though very low soot oxidation rates were found with some base metal oxide catalysts, these catalysts are very hygroscopic and unlikely to be successful in practical application.

One commercial NO_x adsorber catalyst was evaluated in reactor studies. While other commercial catalysts are expected to have similar qualitative behavior, temperatures required for desulfation will be higher. The temperature at which desulfation rates become reasonable is fairly sharply defined. While desulfation at 500°C removed nearly 80% of the sulfur, desulfation at 475°C failed to remove even 20%. As expected, much of the sulfur removal occurs during the early portion of a desulfation treatment, while a full performance recovery is dependent on removing most of the sulfur.

G. Catalysis by First Principles

C. K. Narula, L. F. Allard, V. Bhirud, B. Gates, M. Moses, W. Schneider, W. Shelton, Y. Xu
Oak Ridge National Laboratory
P.O. Box 2008, MS 6116
Oak Ridge, TN 37831-6116
(865) 574-8445, fax: (865) 576-6298; e-mail: narulack@ornl.govl

DOE Technology Development Area Specialist: James J. Eberhardt
(202) 586-9837; fax: (202) 586-1600; e-mail: james.eberhardt@ee.doe.gov
ORNL Technical Advisor: D. Ray Johnson
(865) 576-6832; fax: (865) 574-6098; e-mail: johnsondr@ornl.gov

---

Contractor: Oak Ridge National Laboratory, Oak Ridge, Tennessee
Prime Contract No: DE-AC05-00OR22725

Objective

Search for durable emission catalysts [lean No_x (nitrogen oxides) trap (LNT), three-way catalyst (TWC), OC] from a protocol based on

- an integrated approach between computational modeling and experimental development
- design and testing of new catalyst materials to rapidly identify the key physiochemical parameters necessary for improving the catalytic efficiency of these materials.

Approach

- Theoretical modeling
  - Density functional theory-based first-principles calculations
  - Optimization of platinum (Pt) clusters supported on alumina
  - Interaction of CO, NO_x, and hydrocarbons (HCs) with Pt clusters supported on alumina
- Experimental system
  - Synthesize Pt and rhenium (Re) nanoclusters on morphologically diverse alumina supports
  - Evaluate systems for CO, NO_x, and HC oxidation

Accomplishments

- Completed the synthesis of a series of Pt and Re clusters supported on commercial alumina.
  - The microstructural studies of freshly prepared Pt/alumina (by impregnation) show it to contain 10–20 atom clusters. Thermal treatment leads to larger particles.
  - The microstructural studies of freshly prepared Re/alumina (by impregnation) show it to contain 10–20 atom clusters. We prepared smaller clusters of 1–3 atoms from the decarbonylation of $H_3Re_3(CO)_{12}/\gamma–Al_2O_3$. Thermal treatment leads to larger particles.
- Synthesized alumina sol-gel and molecular sieve support materials and began efforts to increase the thermal stability of the molecular sieves.
- Carried out modeling of isolated Pt clusters. Theory tells us that the following are true for Pt nanoclusters:
  - Reactivity (adsorption) shows strong size dependence.

- — Smaller clusters are much more prone to oxidation.
- — Oxidized clusters adopt 1-dimensional or 2-dimensional structures.
- — In an O_2 atmosphere, higher T or lower p_{O2} leads to lower extent of oxidation and makes the reduction of oxidized Pt clusters more facile → Pt oxides becoming better oxidizing agent.
- — Lower oxide phases are more prevalent for larger clusters.

- Equipped the synthesis laboratory to enable preparation of catalyst materials under inert conditions. A benchtop catalyst testing reactor has been installed (funded by a project from DOE Office of Industrial Technologies) and is being tested before catalyst evaluation experiments start.

Future Direction

- Understand the structures of nanoclusters on support. Our results show that nano-clusters are 10–15 atoms.
  - — Develop theoretical models to understand cluster oxidation state (oxidized, reduced, in equilibrium), dependence on cluster size, and the kinetics of oxidation.
  - — Conduct experimental studies on the structures of these systems using X-ray absorption fine structure (EXAFS) and X-ray absorption near-edge structure (XANES).
- Support interaction with clusters and its impact on the structure and reactivity:
  - — cationic or zero-valent metals or both
  - — cationic metals at the metal–support interface
- Analyze the reactivity of the clusters
  - — Conduct theoretical and experimental studies on structure-reactivity correlation toward CO, NO_x, and HC oxidation studies
  - — Determine the impact of cluster size on catalytic activity
- Translate these results into the design of durable supported catalysts for LNTs (and other systems such as TWC, OC for diesel)

Introduction

This research focuses on an integrated approach between computational modeling and experimental development, design, and testing of new catalyst materials, which we believe will rapidly identify the key physiochemical parameters necessary for improving the catalytic efficiency of these materials.

The typical solid catalyst consists of nanoparticles on porous supports. The development of new catalytic materials is still dominated by trial-and-error methods, even though the experimental and theoretical bases for their characterization have improved dramatically in recent years. Although it has been successful, the empirical development of catalytic materials is time-consuming and expensive and brings no guarantee of success. Part of the difficulty is that most catalytic materials are highly non-uniform and complex, and most characterization methods provide only average structural data. Now, with improved capabilities for synthesis of nearly uniform catalysts—which offer the prospects of high selectivity as well as susceptibility to incisive characterization combined with state-of-the science characterization methods, including those that allow imaging of individual catalytic sites—we have a compelling opportunity to markedly accelerate the advancement of the science and technology of catalysis.

Computational approaches, on the other hand, have been limited to examining processes and phenomena using models that had been much simplified compared with real materials. This limitation was mainly a consequence of limitations in computer hardware and in the development of sophisticated algorithms that are computationally efficient. In particular, experimental catalysis has not benefited from the recent advances in high-performance computing that enable more realistic simulations (empirical and first-principles) of large ensemble atoms, including the local environment of a catalyst site in heterogeneous catalysis. These types of

simulations, when combined with incisive microscopic and spectroscopic characterization of catalysts, can lead to a much deeper understanding of the reaction chemistry that is difficult to decipher from experimental work alone.

Thus a protocol to systematically find the optimum catalyst can be developed that combines the power of theory and experiment for atomistic design of catalytically active sites and can translate the fundamental insights gained directly to a complete catalyst system that can be technically deployed (Figure 1).

Although it is no doubt computationally challenging, the study of surface, nanometer-sized, metal clusters may be accomplished by merging state-of-the-art, density-functional-based electronic-structure techniques and molecular-dynamic techniques. These techniques provide accurate energetics, force, and electronic information. Theoretical work must be based on electronic-structure methods, as opposed to more empirical-based techniques, so as to provide realistic energetics and direct electronic information.

A computationally complex system, in principle, will be a model of a simple catalyst that can be synthesized and evaluated in the laboratory. It is important to point out that such a system for an experimentalist will be an idealized simple model catalyst system that will probably model a "real-world" catalyst.

Thus it is conceivable that a "computationally complex but experimentally simple" system can be examined by both theoretical models and experimental work to forecast improvements to obtain optimum catalyst systems.

Approach

The theoretical modeling is based on density-functional theory (DFT) studies of Pt clusters to understand the relationship between cluster size, structure, composition, and reactivity. This, coupled with first-principles thermodynamics, provides insights into the effects of oxidizing atmosphere (O_2)—finite (T, p_{O2}), structure, composition, and redox potential on particle size. The results provide guidance for investigations of larger/supported clusters. The next steps of this work will model supported clusters, based on input from experimental results, and their interactions with CO, NO_x, and HC.

Experimentally, we have synthesized a series of Pt and Re clusters and particles supported on morphologically different γ–aluminas. The microstructural characterization reveals structural differences in 1–3 atom and 10–20 atom clusters. We will evaluate these catalysts for their CO, NO_x, and HC oxidation capability. Guided by the theoretical models and experimental results, we will synthesize a new set of catalyst materials with higher durability under operating conditions.

Results

Over the last year, theoretical studies have been carried out on the oxidation behavior of gas-phase Pt nanoparticles and metallic clusters. On the experimental side, a range of γ–Al_2O_3 supported Pt and Re clusters have been synthesized and characterized. Alumina sol-gels and molecular sieves have also been synthesized to use as supports. The results are summarized in the following subsections.

Alumina Support Materials

We synthesized sol-gel alumina by the reported procedure from the hydrolysis of $Al(sec\text{-}C_4H_9O)_3$, nitric acid peptization, and gelation. The material gives an amorphous X-ray diffraction between 5 and 70° 2θ. The alumina sol surface area calculated from a multipoint BET (Brunauer, Emmett, and Teller) measurement without degassing is 170.82 m^2/g. Scanning electron microscopy (SEM) images show some macro-pores on the surface, but no ordered structure can be seen (Figure 2).

For the synthesis of alumina molecular sieves, we employed a structure-templated method using

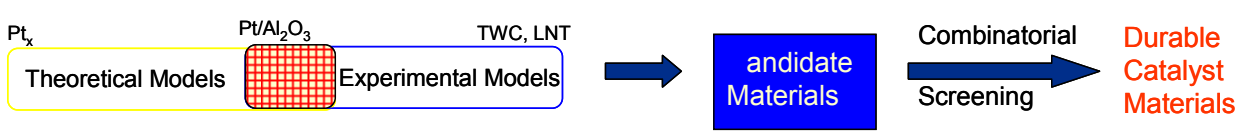

Figure 1. Theory and experiment, combined with simulation, can translate to a deployable catalyst system.

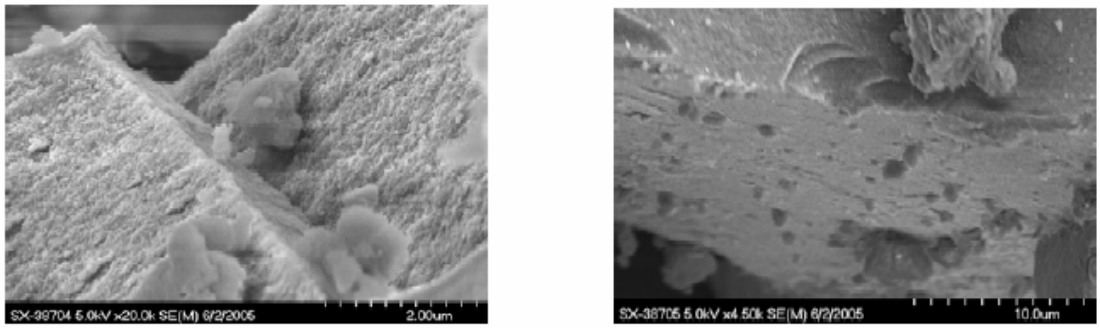

Figure 2. SEM images of sol-gel alumina.

cetyltrimethylammonium bromide, reported by Deng et al.[1] X-ray diffraction (XRD) of the alumina molecular sieves and SEM images (Figure 3) confirm the reproducibility of this synthetic route. Since the rate of stirring has a significant impact on the morphological structure of alumina molecular sieves, we carried out the synthesis using a magnetic stirrer and used stirring rates of 64 and 128 rpm. The BET surface areas of 128-rpm and 64-rpm samples were 208 m^2/g and 234 m^2/g, respectively. These values are about half of the reported BET surface areas (~470 m^2/g). Efforts are in progress to determine an accurate BET surface area before undertaking further modifications to the synthesis procedure.

Since the alumina molecular sieve structure collapses at elevated temperatures, we are exploring synthetic routes to incorporate stabilizers into the alumina molecular sieve structure. Employing the Pinnavaia method, we added lanthanum (La)

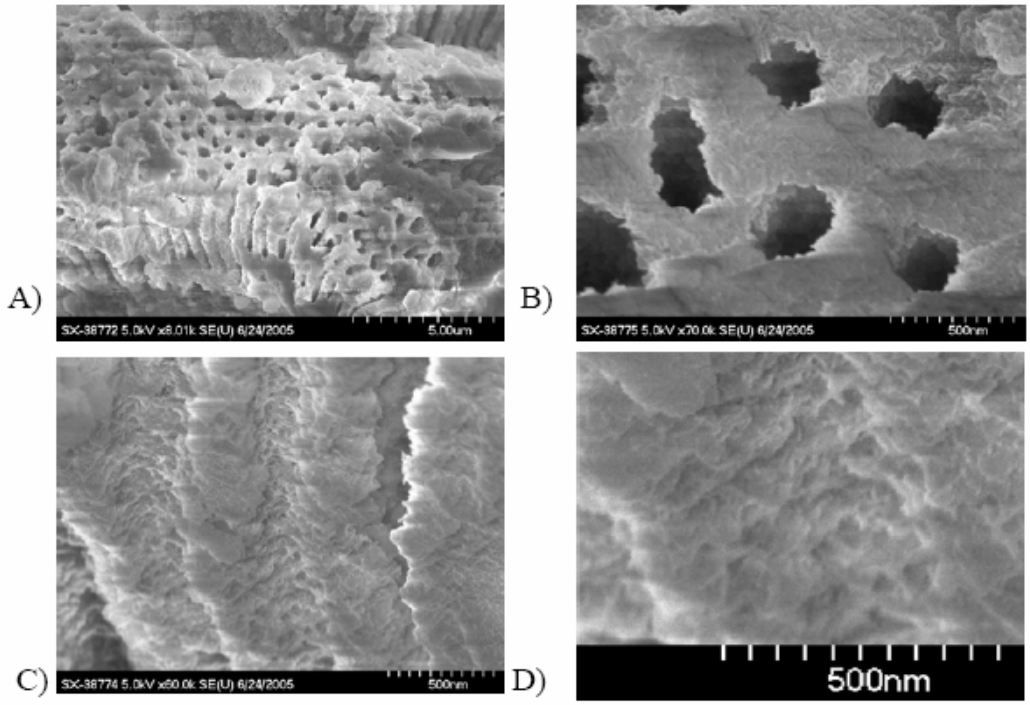

Figure 3. SEM images of the Al_2O_3 molecular sieves prepared by stirring at 64 rpm (a) shows the surface openings of the macropores (channel openings) and the channels that extend through the material. (b) is a close-up of the channel opening at an angle. (c) is close-up of macropore channels and some of the micropores within the channels can be discerned (d) shows an enlargement of the micropores within the channels from (c).

nitrate during the synthesis of alumina molecular sieves. This method did not lead to improved thermal durability of alumina molecular sieves. The powder XRD (Figure 4) of 2 wt % La-doped alumina molecular sieves, after calcining at 500°C/ 5.5 h in flowing air, exhibits no diffraction peaks, suggesting that the materials are amorphous materials. Further calcining at 700°C/5.5h and 900°C/5.5 h led to low-intensity broad peaks in powder XRD that were assigned to aluminum oxide. The SEM of La-impregnated samples resembled that of pure alumina molecular sieves after initial calcining at 500°C/5.5h (Figure 5). The impact of calcining La-impregnated alumina molecular sieves for 5.5 h at 700°C after the initial 500°C/ 5.5 h can be seen in the SEM (Figure 6). The structures

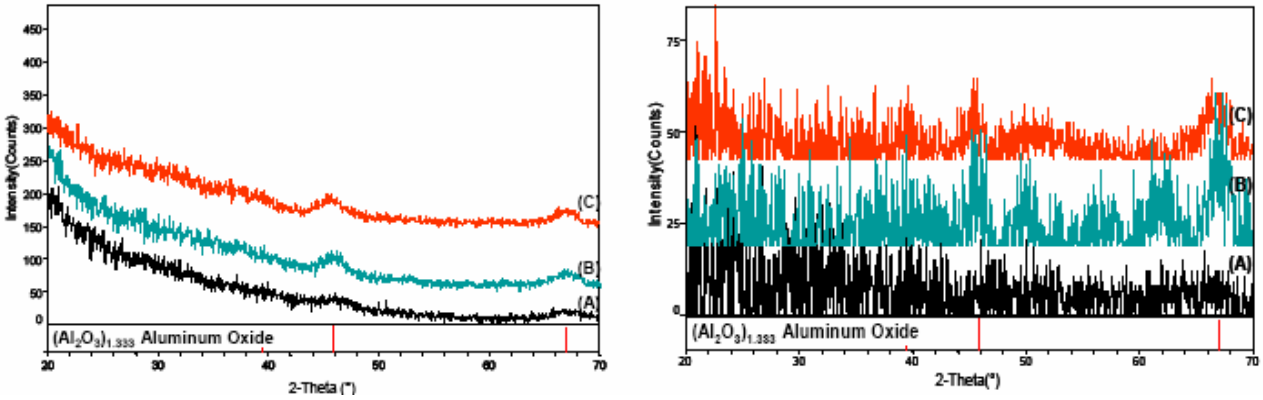

Figure 4. X-ray diffraction patterns of Al_2O_3 molecular sieves synthesized at 64 rpm, doped with 2 wt % La and calcined under flowing air at (a) 500°C/5.5 h, followed by annealing at (b) 700°C/5.5 h, and finished with a final annealing at (c) 900°C/5.5 h. The diffraction patterns on the left are without background subtraction and those on the right are with background subtraction. Diffraction lines of aluminum oxide are of JCPDF # 75-0921.

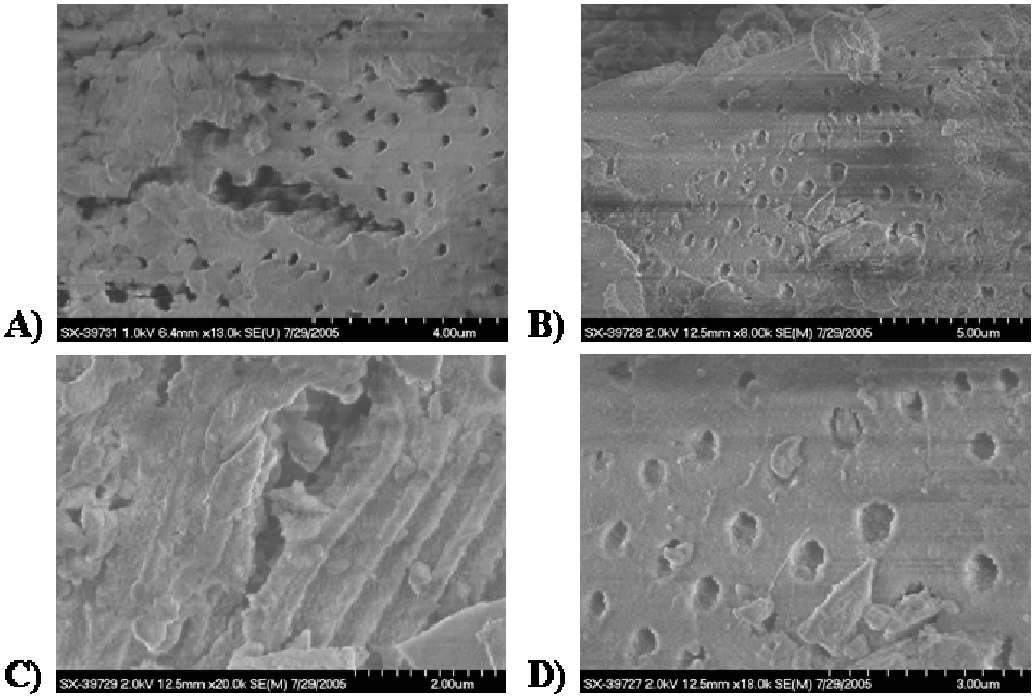

Figure 5. SEM images of the Al_2O_3 molecular sieves impregnated with 2% La and calcined at 500°C/5.5h. The images show the surface openings of the macropores (channel openings) and the channels that extend through the material.

of many porous channels were maintained; however, the coverage and uniformity of the channels have diminished. This suggests that La did not get incorporated in the molecular sieve structure. As a next step, we will explore our method of employing heterometallic alkoxides as precursors for the incorporation of La in alumina molecular sieves.

Platinum-Alumina System

While synthesis and characterization of sol-gel and molecular sieve alumina are in progress, we have synthesized and characterized Pt/Al_2O_3 materials using commercial alumina. We carried out the synthesis of nanocluster Pt/commercial γ–alumina by impregnation of γ–alumina with $H_2PtCl_6 \cdot 6H_2O$ followed by calcination in air. The scanning transmission electron microscopy (STEM) of 2% $Pt/\gamma–Al_2O_3$ (Figure 7) shows approximately 1-nm particles with a narrow distribution centered in the 1–1.5-nm range (Figure 7B). High-magnification images obtained using the aberration-corrected electron microscope (ACEM) in the HAADF-STEM mode indicate particles of 10–20 atoms and also show some smaller platinum clusters (Figure 7c and d).

Thermal treatment of this material leads to ~10-nm or larger Pt clusters supported on γ–alumina with the Pt particle size depending on the temperature and duration of thermal treatment. In order to prepare smaller clusters, a possible approach is to synthesize platinum carbonyl clusters on alumina. A variety of Pt carbonyl clusters $\{[Pt_{15}(CO)_{30}]^{2-}$, $[Pt_6(CO)_{12}]^{2-}$, $[Pt_9(CO)_{18}]^{2-}\}$ on MgO are known.[2] A synthesis of such clusters on a variety of aluminas (commercial γ–alumina, sol-gel alumina[2] and molecular sieve alumina[1] will be challenging, but a simple decarbonylation will furnish Pt clusters of fewer than 10 atoms.

The theoretical efforts, which are based on DFT, have so far been focused on the effect of cluster size and the impact of oxidation on the properties—including structure, composition, and

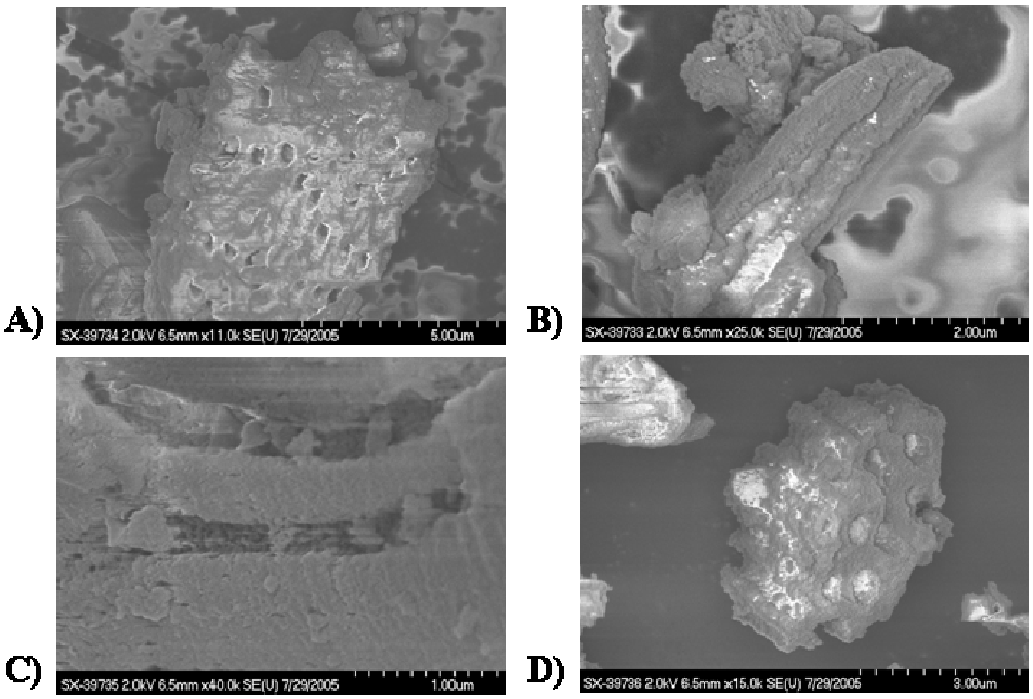

Figure 6. SEM images of the Al_2O_3 molecular sieves impregnated with 2% La and calcined first at 500°C/5.5h followed by further calcination at 700°C/5.5h (a) shows the surface openings of the macropores (channel openings) (b) shows a piece of alumina with channels that extend through the material (c) shows some channels that do not appear to extend through the entire piece of alumina (d) show a piece of alumina with a honeycomb structure.

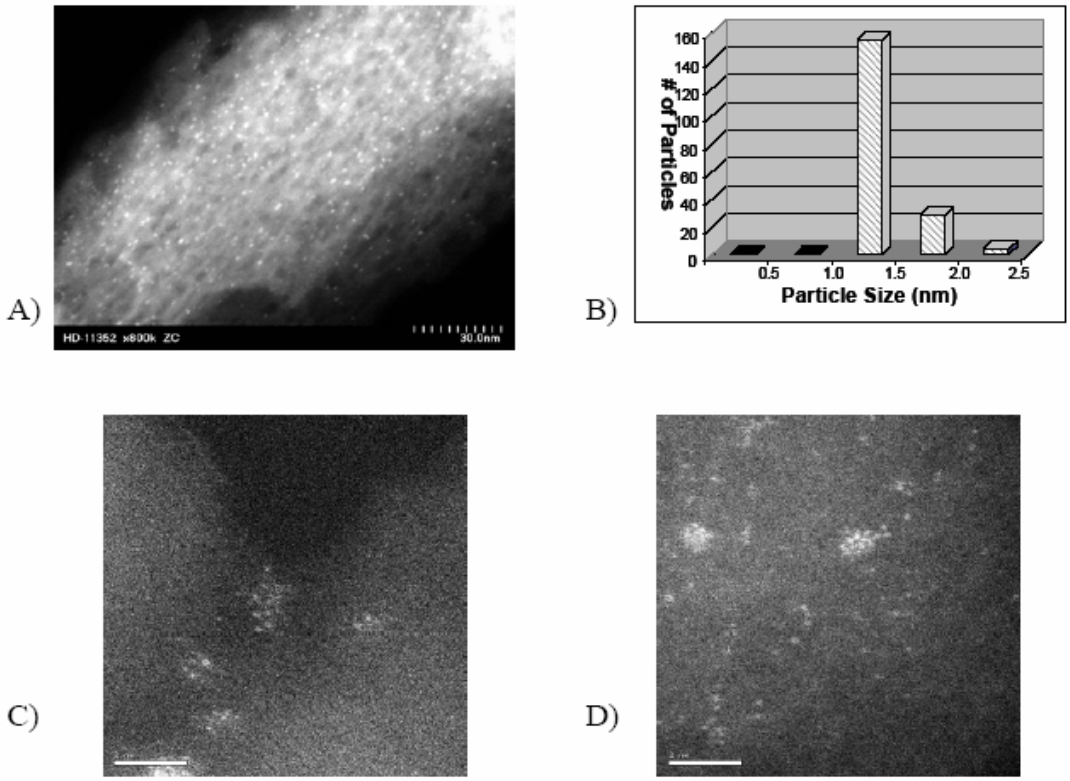

Figure 7. (a) STEM images of the 2% Pt/γ-Al_2O_3 sample and (b) the particles size distribution. (c and d) ACEM HAADF-STEM images of 2% Pt/γ-Al_2O_3.

reactivity—of isolated Pt clusters. We have concluded the investigation of Pt_x nanoclusters (x = 1, 2, 3, 4, 5, and 10) using the DFT codes VASP and Dacapo. The main results are summarized in Figure 6.

A salient feature is that the oxidation of the Pt clusters, either partial or complete, is more exothermic (more negative oxidation energy) than the oxidation of bulk Pt to the bulk oxides. The oxidation energies display strongly non-linear dependence on cluster size and generally become more exothermic as the size decreases. This means that smaller Pt clusters are much more prone to oxidation than larger Pt clusters or bulk Pt. Complete oxidation of a Pt_x cluster to Pt_xO_{2x} is favored energetically over partial oxidation to Pt_xO_x, regardless of the cluster size.

Upon oxidation, the structure of Pt clusters also changes substantially. Whereas the original Pt clusters are generally 3-dimensional, the oxidized clusters prefer flatter, 1- or 2-dimensional shapes. The Pt_xO_x clusters form closed loops, in which the Pt atoms adopt the shapes of triangles, quadrangles, pentagons, etc., with each Pt atom coordinated to two O atoms. The Pt_xO_{2x} series, on the other hand, form open, bent linear chains, in which the middle Pt atoms are each coordinated to four O atoms. The structure of the oxidized Pt clusters is also very different from the 3-dimensional matrices of the bulk oxides (Figure 8).

Bader charge analysis of the oxidized Pt nanoclusters reveals another difference between the oxidized Pt nanoclusters and the corresponding bulk oxides: the Pt-O bonds in the clusters have considerably less ionic character than those in the bulk oxides.

Both cluster size and oxidation affect the reactivity of the Pt clusters. We studied the adsorption energies of O, O_2, CO, and CO_2 on the $Pt_{1–5}$ clusters and found considerable variation with respect to cluster size. In general, adsorption on smaller clusters is more exothermic. The adsorption energies of O, O_2, and CO_2 exhibit a minimum of around x = 4 before approaching the level on an extended Pt

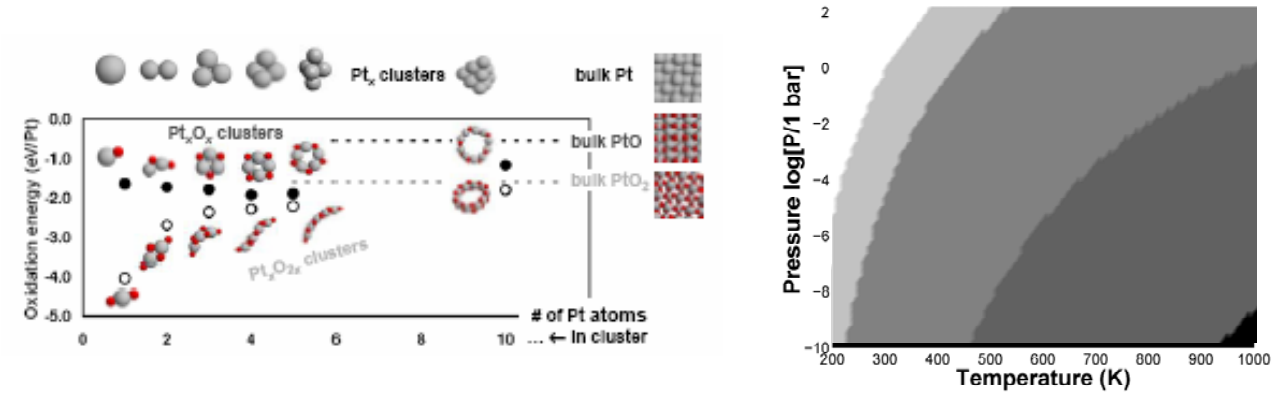

Figure 8. (Left) Oxidation energies of the Pt_xO_x (filled circles) and Pt_xO_{2x} (open circles) clusters. Black and grey dashed lines indicate bulk PtO (–0.54 eV) and β-PtO2 (–1.58 eV) formation energies, respectively. The stick-and-ball representations of the pure Pt and Pt oxide clusters are included. Red spheres represent O atoms, and grey spheres represent Pt atoms. The stoichiometries of Pt:O = 1:1 and 1:2 represent, respectively, partially and fully oxidized Pt systems. (Right) A temperature-O_2 pressure phase diagram of Pt clusters from first-principles thermodynamic model.

surface. CO adsorption grows monotonically weaker with increasing cluster size. The adsorption energies of O and CO are found to be weaker on several Pt_xO_x clusters than on the corresponding pure Pt_x clusters, suggesting that oxidation probably weakens the adsorption of atoms and molecules in general.

Since DFT results are formally obtained at 0 K and in vacuum, we developed a first-principles thermodynamic model in order to incorporate the effects of an oxygen atmosphere with finite temperature and pressure on the composition of the Pt clusters (Figure 8). A temperature–O_2 pressure phase diagram has been constructed for each of the Pt_{1-3} clusters. The results agree with the general physical insight that higher temperature or lower pressure favors lower extent of oxidation. Under conditions of interest to this project—e.g., diesel engine exhaust, which is generally found in the 400–600 K range and has an O_2 partial pressure of ~0.1 bar—the extent of oxidation is found to decrease from a dioxide to a monoxide stoichiometry with increasing cluster size. No sub-monoxides are seen in any of the three phase diagrams. Therefore, we expect larger clusters to exist primarily as monoxides under similar conditions.

In summarizing the theoretical findings, we note that both size and oxidation profoundly affect the structure, composition, and reactivity of Pt clusters, at least in the size range that we have studied so far. In the second year of this project, we will tackle the effect of another variable on the properties of Pt clusters, namely the metal oxide support that is an integral part of many heterogeneous catalysts, including automotive applications (e.g., TWC and LNT). We will study the reactivity of larger clusters, perhaps with sizes in the range of 10–20 Pt atoms, which are more accessible to current laboratory techniques. Our results so far have provided many hints that will facilitate the modeling of larger clusters and the investigation of support effects.

Theoretical study also suggests that the structure of experimentally observed 10–20 atom Pt-clusters is different from that of bulk metal and in all likelihood has some oxygen incorporated. Three-dimensional structure mapping and EXAFS studies are in progress to determine detailed cluster structure.

Rhenium-Alumina System

Since Pt-carbonyl cluster chemistry on alumina is not well developed, we chose Re-carbonyl clusters supported on alumina as surrogates for Pt-alumina clusters of fewer than 10 atoms. We initiated this work by successfully synthesizing $H_3Re_3(CO)_{12}$ by using literature methods and confirmed its formation by infrared spectroscopy.[4] In the previous report, we described the decarbonylation and characterization of decarbonylated clusters by EXAFS and XANES spectroscopy. The EXAFS parameters indicated complete decarbonylation of the Re. The data indicate the formation of tri-nuclear Re rafts, Re_3. The decarbonylated samples, modeled as tri-rhenium

rafts, are shown by the XANES data to incorporate electron-deficient (cationic) Re. On the basis of a comparison of the observed XANES signature with various XANES of various reference materials, we tentatively identify the oxidation state of Re to be +4. This statement is rough and in need of theoretical assessment.

The $H_3Re_3(CO)_{12}/\gamma–Al_2O_3$ sample was imaged on the ACEM in the HAADF-STEM mode. The intact supported tri-rhenium rafts indicated by infrared spectra, EXAFS, and XANES were confirmed by atomic-resolution STEM images (Figure 9 and inset). In addition to tri-rhenium rafts, atomic rhenium, dimers, and larger polyatomic clusters were also atomically resolved. STEM images indicate that although slightly larger clusters were present, the sample was predominately clusters comprising 1–3 Re atoms.

STEM images of $H_3Re_3(CO)_{12}/\gamma–Al_2O_3$ treated in H_2 at 400°C to decarbonylate the clusters were also obtained using the ACEM. Images at high magnification indicated uniform clusters with diameters of approximately 0.4–0.8 nm. The instability of the microscope at the time of use hindered efforts to capture images of atomic resolution. Rhenium has a radius of 1.37 Å, which suggests that the clusters are composed of 1–3 Re atoms.

Decarbonylation of $H_3Re_3(CO)_{12}/\gamma–Al_2O_3$ was also done by treatment in helium at 400°C. STEM images show metallic particles in the 1.4–3.9 nm range (Figures 10 and 11). Some small Re clusters were also present, but because of the 3-dimensional structure of the metallic nanoparticles, imaging was difficult.

Interestingly, $Re/\gamma–Al_2O_3$ synthesized by $ReCl_5$ impregnation on commercial $\gamma–Al_2O_3$ and subsequt calcining led to small (1–1.5 nm) clusters. Microstructural characterization on the ACEM shows two types of areas. In one type of area (Figure 12), 10–20-atom clusters of essentially 1 nm were observed that were reminiscent of our $Pt/\gamma–Al_2O_3$ materials (Figure 8). While these clusters are not completely random in the atomic arrangement, a 3-dimensional metallic order is not observed. The second area (Figure 13) shows smaller, less uniform clusters and single-atom structures. Neither area shows significant structure change as a result of time under the beam, suggesting a stabilizing interaction between Re and the support. The inconsistent loading may be attributed to the high Re loading.

Conclusions

We have prepared and characterized Pt and Re clusters of different sizes and properties (metallic and non-metallic) on commercial $\gamma–Al_2O_3$ ranging from single atoms to 2-nm 3-dimensional nanoparticles. Two other alumina supports with different structural properties, sol-gel and molecular sieves,

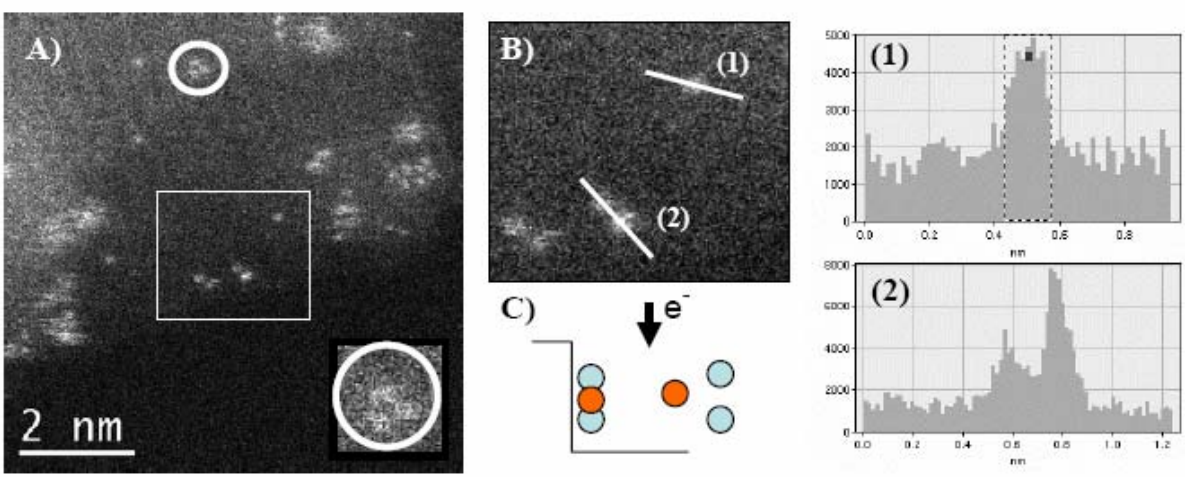

Figure 9. ACEM HAADF-STEM images of 1 wt % $Re/\gamma\text{-}Al_2O_3$. (a) Image of $H_3Re_3(CO)_{12}/\gamma\text{-}Al_2O_3$; the inset at the bottom right is an enlargement of the tri-rhenium raft located in the circle. (b) An enlargement of the boxed in area of (a). Traces 1 and 2 correspond to the particle intensity. Graphs indicate one atom in trace of particle (1) and three atoms in trace of particle (2). (c) Front and side views of Re3 cluster, tethered to a ledge parallel to the beam direction.

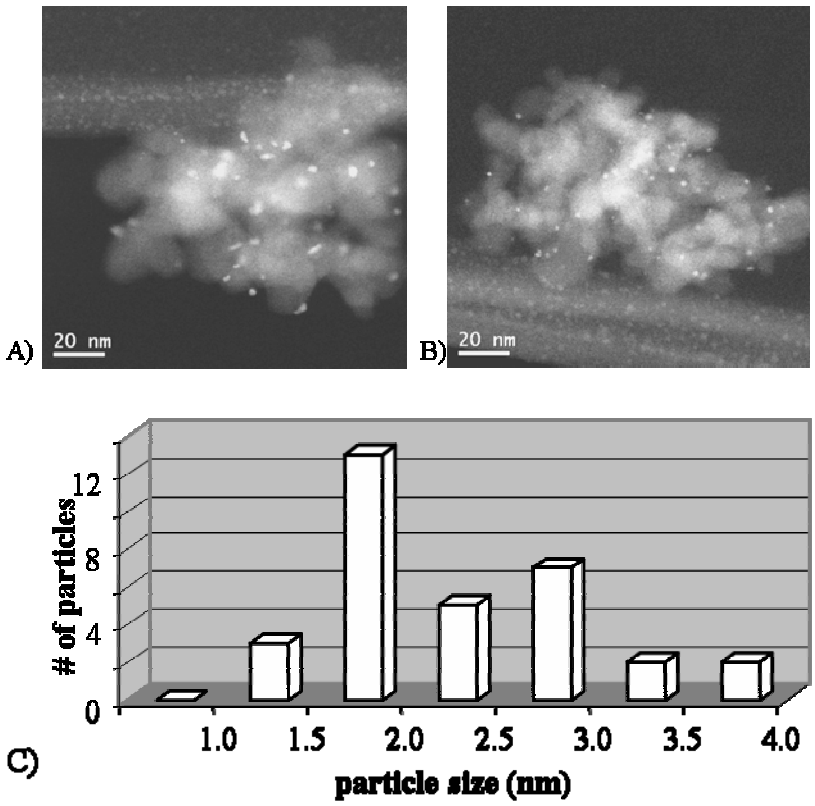

Figure 10. (a–b) show aberration corrected STEM-HAADF images of two different Re/γ-Al_2O_3 particles prepared by decarbonylating $[H_3Re_3(CO)_{12}]$/γ-Al_2O_3 in He at 400°C, and (c) shows the Re particle size distribution.

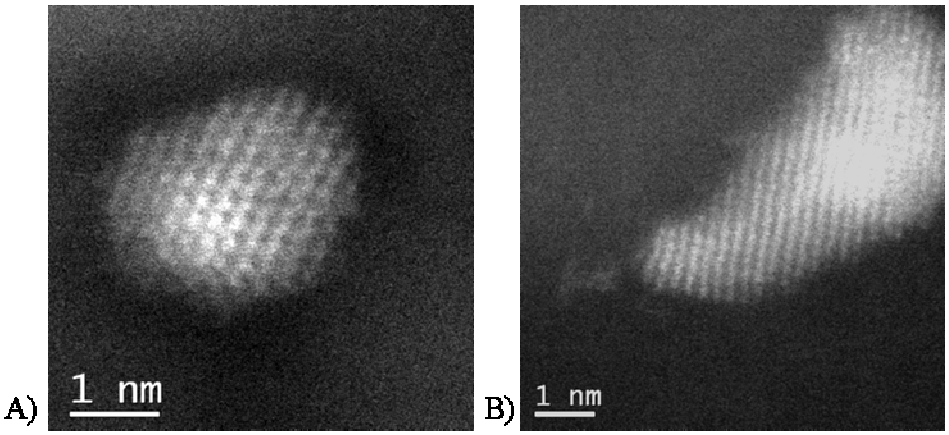

Figure 11. The high magnification ACEM images show the 3D metallic structure of the Re particles prepared by decarbonylating $[H_3Re_3(CO)_{12}]$/γ-Al_2O_3 in He at 400°C.

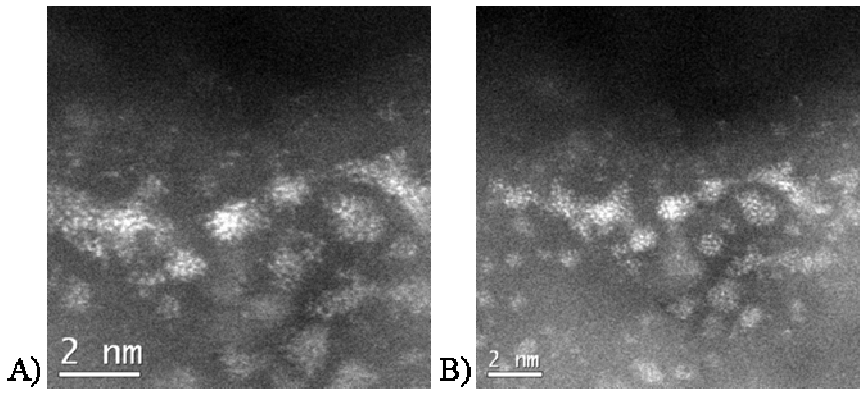

Figure 12. These ACEM images Re/γ-Al_2O_3 prepared by impregnation. The images were taken consecutively showing no movement of the clusters.

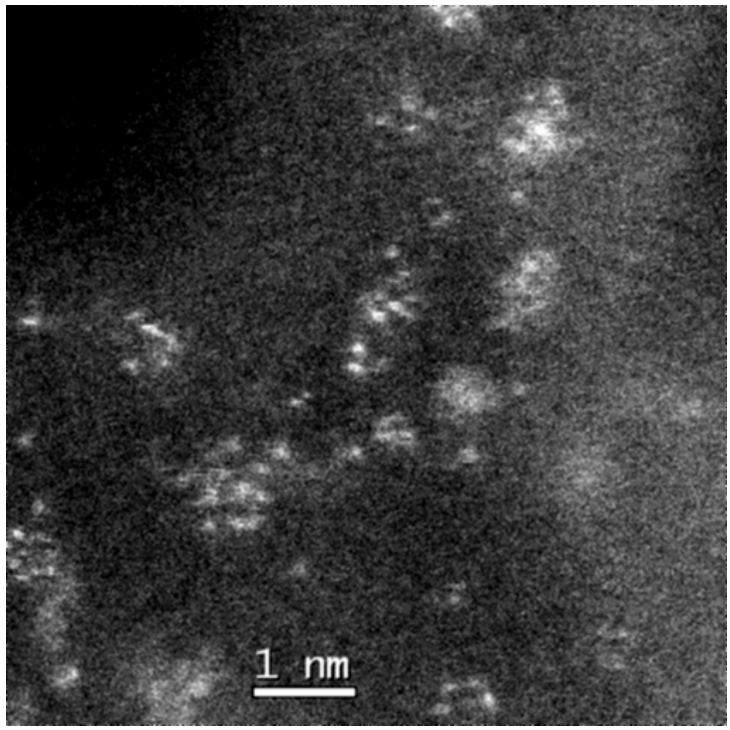

Figure 13. This high magnification ACEM image shows Re atoms and small clusters of Re/γ-Al_2O_3 prepared by impregnation method.

are being prepared and will soon be ready for Pt and Re loading. Computational calculations and simulation have shown the oxidation behavior of small Pt clusters and their energetically favored structures.

Our next goals are to finish structural characterization and preparation of the clusters supported on the three different alumina supports, obtain and compare their activity as CO oxidation catalysts, and use the experimental data as the inputs for the theoretical models.

Presentations and Publications

C. K. Narula, presentation at the Eighth DOE Crosscut Workshop on Lean Emissions Reduction Simulation, Dearborn, Michigan, May 17–19, 2005.

L. F. Allard, presentation at the annual meeting of the Microscopy Society of America.

C. K. Narula, presentation at DEER 2005, Chicago, August 21–25, 2005.

Bruce Gates and W. Schneider, presentations at the North American Catalysis Society meeting, Philadelphia, May 22–27, 2005.

V. A. Bhirud, C. Narula, and B. C. Gates, "γ-Al_2O_3 Supported Tri-rhenium Rafts: Spectroscopic and Microscopic Characterization," in *Proceedings of the 19th North American Catalysis Society Meeting*, Philadelphia, May 22–27, 2005.

Y. Xu, W. A. Shelton, and W. F. Schneider, "Effect of Particle Size on the Oxidizability of Platinum Clusters," submitted to *J. Phys. Chem. A*.

Y. Xu, W. A. Shelton, and W. F. Schneider, "Nanoscale Effects in the Reactivity of Pt Clusters towards CO oxidation," in *Proceedings of the 19th North American Catalysis Society Meeting*, Philadelphia, May 22–27, 2005.

Y. Xu, W. A. Shelton, and W. F. Schneider, "Theoretical Studies Based on Post-Hartree-Fock and DFT Methods," in *Synthesis and Applications of Oxide Nanoparticles and Nanostructures*, ed. J. A. Rodriguez, John Wiley and Sons; in preparation.

V. A. Bhirud, M. J. Moses, D. A. Blom, L. F. Allard, Jr., T. Aoki, S. Mishina, C. K. Narula, and B. C. Gates, "Alumina-supported Tri-rhenium Clusters Visible by Aberration-Corrected Dark-field STEM," *Microscopy and Microanalysis 2005*, Honolulu, July 31–August 4, 2005.

C. K. Narula, W. A. Shelton, L. F. Allard, Y. Xu, M. Moses, W. Schneider, and B. Gates, "Combining Theory and Experiments in Studies of Structural Changes in LNT Materials," Eighth DOE Crosscut Workshop on Lean Emissions Reduction Simulation, University of Michigan–Dearborn, Dearborn, Michigan, May 17–19, 2005.

References

1. W. Deng, M. W. Toepke, and B. H. Shanks, *Adv. Func. Mater.* **13**, 61 (2003).
2. B. C. Gates, *Chem. Rev.* **95**, 511 (1995).
3. C. K. Narula, S. R. Nakouzi, R. Wu, C. T. Goralski, and L. F. Allard, *AIChE Journal* **47**, 744 (2001).
4. M. A. Andrews, S. W. Kirtley, and H. D. Kaesz, *Inorg. Synth.* **17**, 16 (1977).
5. A. S. Fung, P. A. Tooley, M. J. Kelley, D. C. Koningsberger, and B. C. Gates, *J. Phys. Chem.* **95**, 225 (1991).

H. Durability of Diesel Particulate Filters (CRADA with Cummins, Inc.)

Edgar Lara-Curzio
Oak Ridge National Laboratory
P.O. Box 2008, MS-6069
Oak Ridge, TN 37831-6069
(865) 574-1749; fax: (865) 574-6098; e-mail: laracurzioe@ornl.gov

DOE Technology Development Area Specialist: James J. Eberhardt
(202) 586-9837; fax: (202) 586-1600; e-mail: james.eberhardt@ee.doe.gov
ORNL Technical Advisor: D. Ray Johnson
(865) 576-6832; fax: (865) 574-6098; e-mail: johnsondr@ornl.gov

---

Contractor: Oak Ridge National Laboratory, Oak Ridge, Tennessee
Contract No.: DE-AC05-00OR22725

Objective

- Identify and implement test techniques to characterize the physical and mechanical properties of ceramic diesel particulate filters (DPFs) and develop analysis tools for predicting their reliability and durability.

Approach

- Identify and implement test techniques to determine the physical and mechanical properties of DPF ceramic substrates.
- Investigate the applicability of probabilistic design tools to DPF ceramic substrates. In particular, the applicability of the Ceramic Analysis and Reliability Evaluation of Structures (CARES) code to predict the reliability of DPF ceramic substrates will be investigated.

Accomplishments

- Developed a procedure to prepare double-torsion test specimens of porous cordierite.
- Determined the fracture toughness and slow-crack-growth behavior of porous cordierite as a function of temperature and environment.
- Carried out a round-robin testing program to determine the precision of 4-point bending test methods to determine the flexural strength of DPF ceramic substrates.

Future Direction

- Implement probabilistic design tools to predict the reliability and durability of DPF ceramic substrates when subjected to arbitrary thermomechanical histories.

Introduction

The pollution emitted by diesel engines contributes greatly to the nation's air quality problems. Even with more stringent environmental regulations set to take effect in 2007, existing trucks and buses will continue to emit nitrogen oxides (NO_x) and particulate matter (PM), both of which contribute to serious public health problems.[1] Fortunately, there are several technologies designed to reduce pollution from existing trucks and buses, such as DPFs. A DPF is a ceramic device that collects PM in the exhaust stream. The high temperature of the exhaust heats the ceramic

structure and allows the particles inside to break down (or oxidize) into less harmful components. DPFs reduce emissions of PM, hydrocarbons, and CO by 60 to 90%.

Most DPFs consist of a ceramic honeycomb with hundreds of cell passages partitioned by walls (Figure 1). Each cell passage has a square cell opening at one end and is closed at the other end so that the cell passages are alternately closed at each end. This structure forces the exhaust gases through the porous, thin ceramic honeycomb walls. When the gases carrying the carbon particles flow through the fine pores of the walls, the carbon particles are filtered out. High porosity values, in the range of 60%, heighten filtration efficiency to more than 90% while reducing gas-flow resistance to avoid affecting the engine performance.

The process of diesel PM collection begins as soon as the engine is started and continues while the engine is operating. As the carbon particles are collected on the ceramic walls, the backpressure of the system increases. This problem is alleviated by burning the trapped PM, through a catalytic reaction using exhaust gas heat at 400°C or more, into CO_2 and water vapor that pass through the filter. This process, called regeneration, results in a cleaner filter. The regeneration process is dependent upon exhaust temperature, oxygen, NO_x content, time, and PM levels.

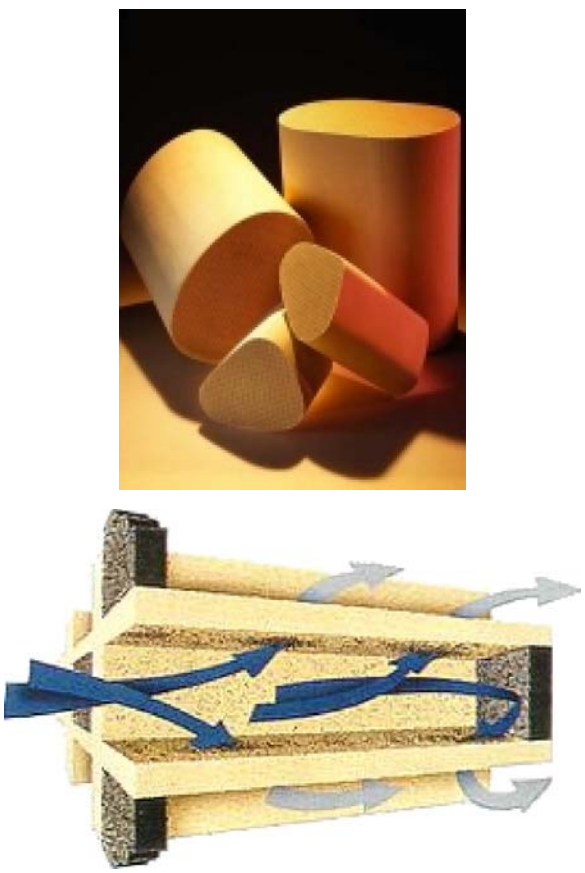

Figure 1. Corning's cordierite-based DPFs.

The key to the successful application of DPFs is to reliably regenerate the filter (e.g., to burn the PM that the filter continues to trap or collect). Traditionally, combustion of soot is done in an oxygen atmosphere (air). In air, soot will burn at about 500°C. However, this is not a typical operating temperature for diesel engine exhaust. Therefore, to burn soot in air, an active system—i.e., one that increases the temperature of the exhaust using some external heat source—is required. But if an active system is not carefully controlled, or if too much PM collects on the filter walls, the filters can experience an "uncontrolled burn" where the temperature increases to 600°C or more, resulting in damage to the filter element.

The objective of this project is to develop and implement methodologies to predict the reliability of DPFs. A useful conceptual model for this purpose is the reliability bathtub curve, which describes reliability-related phenomena of a component over its life cycle.[2] A schematic of the reliability bathtub curve is depicted in Figure 2. It consists of three stages: the infant mortality phase is characterized by premature failures due to improper manufacturing or assembly, poor workmanship, or defects introduced during processing. The second stage of the curve corresponds to the useful life of the component and

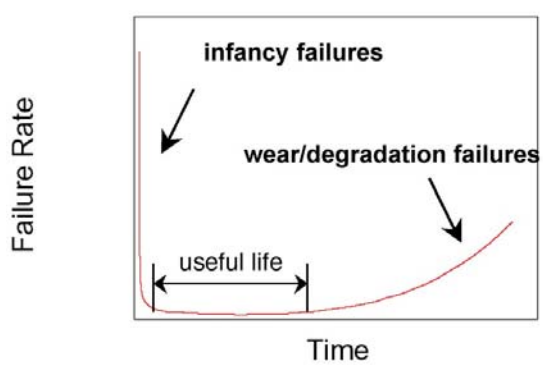

Figure 2. Reliability bathtub curves.

is characterized by a constant failure rate. In this regime, failures are typically associated with random, excessive loads. If sufficiently high safety factors are used during the design process, the magnitude of this failure rate should be negligible. The third stage of the bathtub curve is known as the wear-out phase, where the failure rate increases with time as a result of aging phenomena. Aging phenomena include thermal and mechanical fatigue, corrosion, creep deformation and environmentally assisted crack growth. The time at the onset of wear-out is often regarded as the useful life of the component.

The reliability bathtub curve can be used as a descriptor of how the failure rate of DPFs evolves over time. Infancy failures of DPFs could be related to manufacturing or process defects (large pores, inclusions, cracking) or defects introduced during assembly. Failures of DPFs during their useful life will be dictated by the intersection between the spectrum of thermomechanical loads and the distribution of DPF strengths. Such failures could result from excessive vibration, for example, or unwanted thermal excursions during transients associated with regeneration. Wear-out and degradation failures of DPFs could be associated with the growth of microcracks assisted by thermal fatigue, and/or by the chemistry of the environment, and/or by chemical and microstructural changes in the material due to long-term exposure to elevated temperatures in the exhaust environment.

The objective of this project is to develop life prediction methods for DPFs and, by using those methods, to design durable, reliable DPFs.

Approach

Designing DPFs that are durable and reliable poses significant challenges. For example, the porosity of DPFs, which allows them to remove PM from the exhaust gas stream, has a deleterious effect on their mechanical strength. This is important because DPFs will experience demanding thermomechanical conditions during service. These include, for example, thermal shock resulting from rapid heating/cooling and stresses that arise from temperature gradients. The approach that will be followed in this project includes identifying and implementing test techniques for the nondestructive evaluation of ceramic substrates to assess their integrity. Their physical and mechanical properties and the mechanisms responsible for their degradation in the various stages of the bathtub curve also will be determined and identified. These properties include thermal expansion, thermal conductivity, heat capacity, density, porosity, elastic properties, strength, fracture toughness, and resistance to crack growth at ambient and elevated temperatures, in air and in relevant environments.

The information generated will be used in turn to implement probabilistic design tools. In particular, the applicability of the CARES code[3] to predict the reliability of DPF ceramic substrates will be investigated. Such probabilistic design methodologies are based on a combination of experimentally determined strength data, stress analyses of the component using a finite-element analysis, and selection of appropriate failure criteria. The durability (service life) of the component can also be predicted using this framework by considering the mechanisms that are responsible for the degradation of material strength, such as slow crack growth or creep. While these methodologies have been successfully applied to design structural components using dense ceramics, their applicability to the analysis and design of porous ceramic components has not been validated.

Results

During FY 2005, a procedure was developed to prepare double-torsion test specimens to determine the fracture toughness and slow-crack-growth behavior of porous cordierite. The double-torsion test configuration (Figure 3) consists of symmetric four-point loading around a crack or a notch on one end of a rectangular plate. One feature of this loading configuration is that the stress intensity factor is, at a first approximation, independent of crack length for a range of crack lengths. This feature makes double-torsion testing ideally suited for the evaluation of opaque and non-reflective plate-like test specimens where direct crack length measurements could be difficult to make. The double-torsion test method is also attractive for slow-crack-growth studies because of the relative stability of crack extension, in contrast to other testing configurations (e.g., SENB, CT).

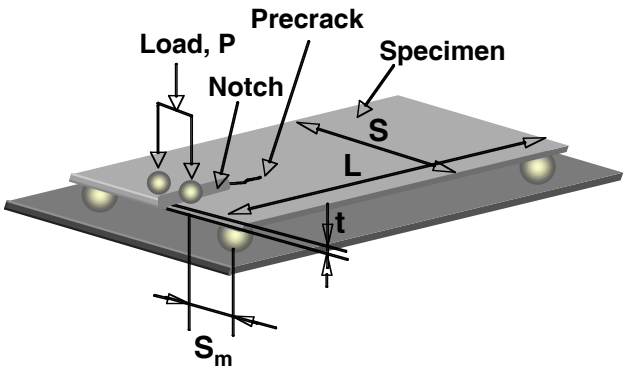

Figure 3. Schematic of the double-torsion test configuration.

The preparation of double-torsion test specimens of porous cordierite, which poses challenges because the thickness of the DPF cell walls is of the order of 300 µm, was accomplished following dry cutting/grinding operations. Sections from a DPF with a cell size of 2.25 × 2.25 mm and approximately 50% porosity were sliced using a diamond cut-off blade. Then subsequent material removal was accomplished using a diamond grinding wheel (150 grit, 4000 rpm, 25 µm down feed). To ensure parallelism and flatness of the surfaces of the test specimen, a special fixture was fabricated using a precision vice and gage blocks. Test specimens were prepared with the notch aligned either parallel or perpendicular to the orientation of the walls, and the final thickness of the test specimens was 280 µm. Figure 4 illustrates the sample preparation process.

The fracture toughness of porous cordierite test specimens was determined by loading pre-cracked test specimens to failure at a constant crosshead displacement rate of 0.01 mm/s. The fracture toughness was calculated from the peak load using Equation 1:

$$K_{IC} = PS_m \left[\frac{3(1+\nu)}{St^4 \xi} \right]^{1/2} , \qquad (1)$$

where P is the peak load, S is the width of the test specimens, S_m is the moment arm, t is the specimen thickness, ν is Poisson's ratio, and ξ is a finite beam thickness correction factor given by

$$\xi = 1 - 1.26\left(\frac{t}{S}\right) + 2.4\left(\frac{t}{S}\right)e^{\left(-\frac{\pi S}{2t}\right)} . \qquad (2)$$

Figure 5 shows a cordierite test specimen after a fracture toughness test, illustrating the trajectory of

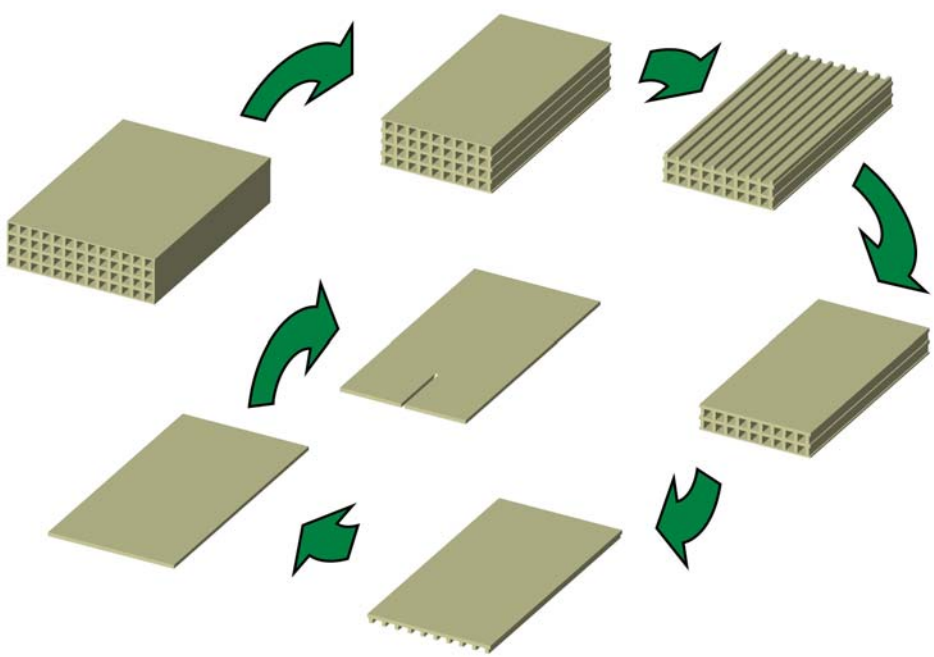

Figure 4. Schematic of procedure followed for the preparation of double-torsion test specimens.

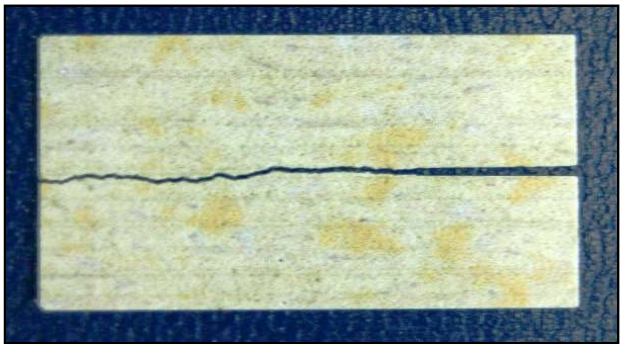

Figure 5. Photograph of double-torsion test specimen after fracture toughness testing.

the crack, which propagated along the major axis of the test specimen. In Figure 5, the notch is located on the right of the test specimen. It was found that the propagation of the crack was significantly influenced by the microstructure of the material, as illustrated by the scanning electron micrograph in Figure 6. To better characterize the interaction between the microstructure and crack propagation, exploratory work was carried out to determine the feasibility of imaging the propagation of the crack through a double-torsion test specimen using X-ray computerized tomography (CT) scans. In addition to providing information on the role of the microstructure in the resistance of the material to crack propagation, this work could lead to the implementation of nondestructive evaluation techniques. Figure 7 shows a reconstructed image of a porous cordierite test specimen. Additional work will be pursued in this area in FY 2006. The fracture toughness of porous cordierite was found to decrease with temperature from a value of 0.45 ± 0.02 MPa$\sqrt{m}$ at 20°C to 0.36 ± 0.07 MPa$\sqrt{m}$ at 800°C. The plot in Figure 8 summarizes those results.

During FY 2005, work was initiated to investigate the slow-crack-growth behavior of porous cordierite using the load relaxation version of the double-torsion test specimen. According to this test procedure, a pre-cracked test specimen is loaded at a constant crosshead displacement rate that is lower than the load associated with fracture toughness. Then the crosshead is arrested and the load is monitored as a function of time. From the rate of load relaxation, which results from the increase in

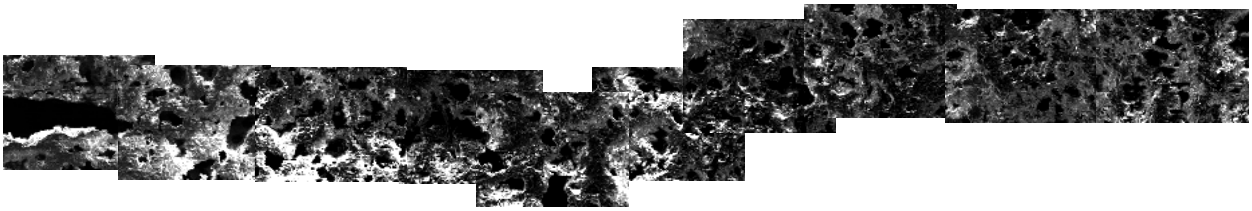

(a)

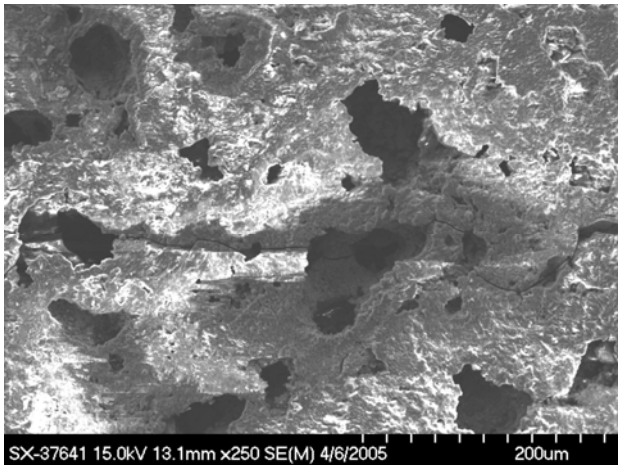

(b)

Figure 6. Scanning electron micrograph illustrating the influence of microstructure on crack propagation: (a) low magnification and (b) high magnification.

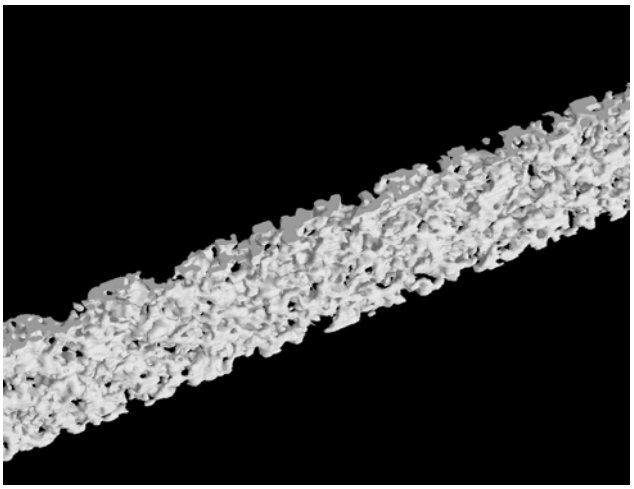

Figure 7. Reconstructed image of porous cordierite test specimen from X-ray CT scan.

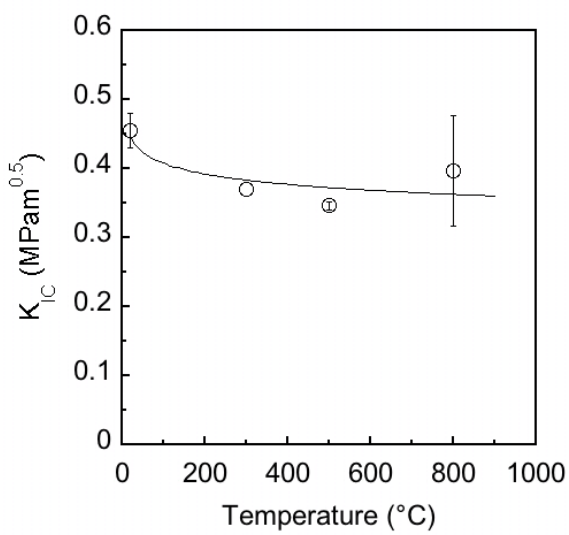

Figure 8. Fracture toughness of porous cordierite as a function of temperature.

compliance of the test specimen, it is possible to determine the rate of crack growth using Equation 3:

$$\frac{da}{dt} = -\frac{P_i}{P^2}\left[a_i + \frac{D}{B}\right]\left(\frac{dP}{dt}\right) \quad , \qquad (3)$$

where P_i is the initial load, a_i is the initial crack length, and D and B are experimental constants associated with the load train compliance.

In parallel with these efforts, a series of dynamic fatigue tests were also initiated in FY 2005 to determine the slow-crack-growth behavior of porous cordierite according to ASTM C1465-00, "Standard Test Method for Determination of Slow Crack Growth Parameters of Advanced Ceramics by Constant Stress-Rate Flexural Testing at Elevated Temperatures." According to this test method, the flexural strength of honeycomb test specimens is determined as a function of applied stress rate. The strength degradation exhibited with decreasing applied stress rate is the basis of this test method, which enables the evaluation of slow-crack-growth parameters of a material.

This dual approach to the characterization of the slow-crack-growth behavior of porous cordierite is necessary to distinguish between material behavior, which will be obtained through the double torsion testing of test specimens obtained from the walls of cellular structures, and structural behavior, which will be obtained through dynamic fatigue flexural testing of beam test specimens with cellular structure. The results from these two sets of tests will provide the kinetics for crack growth to enable the prediction of the service life of porous cordierite DPFs using CARES. The slow-crack-growth behavior of porous cordierite and porous cordierite DPFs with cellular structure will be determined in air, water-vapor, a reducing environment, and simulated diesel exhaust environments.

In FY 2005, a round-robin testing program was organized between Oak Ridge National Laboratory (ORNL) and Cummins to determine the precision in the determination of the 4-point flexural strength of cordierite DPFs. Each laboratory was responsible for testing 40 test specimens with nominal dimensions of 100 × 26 × 13.5 mm. Tests were carried out at ambient conditions under a constant crosshead displacement of 0.35 mm/min, using inner and outer spans of 19 and 89 mm. The test results, which were analyzed using Weibull statistics, are presented in Figure 9. It was found that the average and standard deviations of all tests were 6.73 and 0.83 MPa, respectively, and that the repeatability and reproducibility standard deviations were 0.35 and 0.9 MPa, respectively. The Weibull modulus, which was determined according to the maximum likelihood method, was found to be 24.1. The discrepancies in the characteristic strength values were associated with procedures used to determine the dimensions of the test specimens.

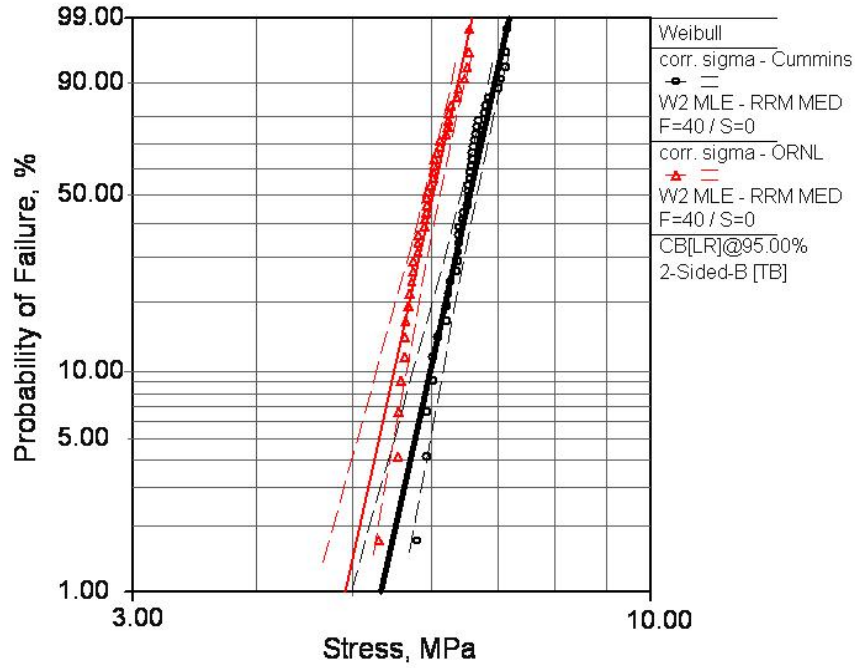

Figure 9. Weibull plot summarizing flexural strength results from round-robin testing program. (△: ORNL data; ○: Cummins data).

Summary

A procedure was developed to prepare test specimens from cellular DPFs to determine the fracture toughness of porous cordierite by the double-torsion test method. Using this test method, the fracture toughness of porous cordierite was found to decrease with increasing temperature from 0.45 ± 0.02 MPa$\sqrt{m}$ at 20°C to 0.36 ± 0.07 MPa$\sqrt{m}$ at 800°C. Work was initiated to determine the slow-crack-growth behavior of porous cordierite and cellular structures of porous cordierite, using the load relaxation variation of the double-torsion test method and the constant stress-rate flexural test method according to ASTM C1465, respectively. The results from these tests will enable prediction of the service life of porous cordierite DPFs. A round-robin testing program was completed to assess precision in the determination of the 4-point flexural strength of cordierite DPFs. It was found that the average and standard deviations of all tests were 6.73 and 0.83 MPa, respectively and that the repeatability and reproducibility standard deviations were 0.35 and 0.9 MPa, respectively. The Weibull modulus was found to be 24.1

References

1. United States Environmental Protection Agency, Office of Transportation and Air Quality EPA420-F-03-017, June 2003. "Questions and Answers on Using a Diesel Particulate Matter Filter in Heavy-Duty Trucks and Buses."

2. G. S. Wasserman, *Reliability Verification, Testing and Analysis in Engineering Design*, Marcel Dekker, New York, 2003.

3. N. N. Nemeth, L. P. Powers, L. A. Janosik, and J. P. Gyekenyesi, "Ceramics Analysis and Reliability Evaluation of Structures Life Prediction Program: Users and Programmers Manual," NASA-GRC, Life Prediction Branch (1993).

Collaborators

Amit Shyam, H-T. Lin, Randy Parten, and Claire Luttrell.

Presentations and Publications

A. Shyam and E. Lara-Curzio, "The Double-torsion Testing Technique for the Determination of Fracture Toughness and Slow-Crack Growth Behavior of Materials: A Review," accepted for

publication in the *Journal of Materials Science* (2005).

T. Yonushonis and E. Lara-Curzio, "Durability of Particulate Filters—PM 10461," presented at the FY 2005 Heavy Vehicle Materials Program Review, Oak Ridge National Laboratory, Oak Ridge, Tennessee, September 14, 2005.

4. MATERIALS FOR AIR HANDLING, HOT SECTION, AND STRUCTURAL COMPONENTS

A. High-Temperature Advanced Materials for Lightweight Valve Train Components

Jeremy S. Trethewey, Principal Investigator
John Grassi, David Longanbach, and Chad Logan
Caterpillar, Inc.
Tech Center 854-80 TC-E
14009 Old Galena Rd.
Mossville, IL 61552
(309) 578-0056; fax: (309) 578-2953; e-mail: Trethewey_Jeremy_S@cat.com

DOE Technology Development Area Specialist: James J. Eberhardt
(202) 586-9837; fax: (202) 586-1600; e-mail: james.eberhardt@ee.doe.gov
ORNL Technical Advisor: D. Ray Johnson
(865) 576-6832; fax: (865) 574-6098; e-mail: johnsondr@ornl.gov

---

Contractor: Oak Ridge National Laboratory, Oak Ridge, Tennessee
Contract Number: DE-AC05-00OR22725
Subcontractor: Caterpillar, Inc., Peoria, Illinois

Objective

- Evaluate prospective lightweight valve materials and determine feasibility of implementation in heavy-duty diesel and natural gas applications.

Approach

- Design, procure, and evaluate γ-phase titanium aluminide (TiAl) and silicon nitride (Si_3N_4) heavy-duty engine valves.
- Demonstrate performance and durability advantages by performing 1000-h durability test on valves in a Caterpillar G3406 natural gas engine.
- Develop finite-element analysis (FEA)-based life prediction model (NASA CARES/Life) that will generate life prediction curves for advanced valve materials.
- Evaluate the thermal, chemical and mechanical properties of TiAl and Si_3N_4 that are critical to on-engine valve performance and durability.
- Investigate manufacturing considerations (i.e., machinability and quality inspection technique) of these novel materials.

Accomplishments

- Procured 12 TiAl and 45 Si_3N_4 heavy-duty engine valves.
- Performed pretest characterization on all valves [laser-scatter nondestructive evaluation (NDE), dimensional check with coordinate measuring machine, surface roughness].
- Completed preliminary life prediction model for Si_3N_4.

- Kicked-off studies to examine friction, wear, corrosion, and machinability characteristics of TiAl.
- Donated a Caterpillar C15 ACERT™ engine to the National Transportation Research Center (NTRC) for future component testing.

Future Direction

- Complete current G3406 engine test on TiAl and Si_3N_4 valves;
  - — perform laser scatter NDE scans to track crack/defect propagation;
  - — perform fast fracture on specimens extracted from the valves to determine retained strength;
  - — correlate results with life prediction model.
- Procure additional TiAl valve blanks for second round of engine tests; will use life prediction model as a design tool to optimize valve geometry.
- Refine NASA/CARES Life prediction model to include non-axisymmetric deformation modes, enable TiAl modeling, and evaluate Probabilistic Design System (PDS) methodology.
- Extend friction, wear, corrosion, and machinability studies of TiAl.

Introduction

Valve train components in heavy-duty engines operate under high stresses, at elevated temperatures, and in severely corrosive environments. Structural ceramics and emerging intermetallic materials are highly corrosion and oxidation resistant and possess high strength and hardness at elevated temperatures. These properties are expected to allow higher engine operating temperatures, lower wear, and enhanced reliability. In addition, the lighter weight of these materials (~50% of production alloys) will lead to lower reciprocating valve train mass that could improve fuel efficiency.

Over the past decade, the automotive engine industry has demonstrated moderate success with TiAl as a valve material. Eylon et al.[1] demonstrated a 2% fuel savings on a Chevrolet Corvette that ran for 25,000 km with TiAl valves. This fuel efficiency increase is attributed to the decrease in valve train parasitic frictional losses. In another study with TiAl valves, Maki et al.[2] demonstrated a 1000-rpm increase in over-speed performance on a Nissan VRT35 engine. This capability would allow more efficient engines to operate in more demanding regimes. The current research and development program at Caterpillar, Inc., extends this body of knowledge from the automotive community and examines TiAl and Si_3N_4 in the context of heavy-duty diesel and natural gas engine environments.

The valve train material development effort will provide the materials, design, manufacturing, and economic information necessary to bring these new materials and technologies to commercial realization. With this information, component designs will be optimized using probabilistic lifetime prediction models, and validated in rig bench tests and short- and long-term engine tests. After establishing proof-of-concept with valves, this design approach will be applied to other components made from high-temperature materials.

Approach

Because the broad goal of this project is to evaluate TiAl and Si_3N_4 materials for use in valve applications, many perspectives must be considered. As such, there are several facets to this project. The primary thrust toward component validation is achieved by fabricating TiAl and Si_3N_4 valves and testing them on a Caterpillar G3406 (in-line 6 cylinder) natural gas engine. Previous annual reports documented the design process used to modify the current baseline metallic valve to accommodate the limited ductility of ceramic and intermetallic materials.[3] For example, the head dimensions were changed to reduce the stress concentration experienced in the fillet radius. Silicon nitride and TiAl valve blanks were formed, rough machined, friction welded to a Ti-6Al-4V shaft (TiAl only), and finish machined.

A parallel effort to develop a design tool for high-strength, brittle materials is also being pursued. A FEA-based life prediction code (NASA CARES/Life) is used to evaluate component design and generate life prediction curves. This approach

uses material properties and thermo-mechanical boundary conditions as the primary inputs. A probability-based code then calculates the accumulated damage through the life of the valve and creates a life prediction curve.

A variety of other studies contribute to the understanding of the behavior of TiAl and Si_3N_4 and how they may perform in an engine environment. Several studies examine the fundamental properties of the materials: tensile strength, creep strength, thermo-physical properties, friction coefficient, wear resistance, oxidation resistance, and corrosion resistance. Two other studies examine the manufacturability of the materials: the effect of machining damage on fatigue resistance and a NDE technique to evaluate surface quality.[4]

Results

Valve fabrication

Twelve TiAl and forty-five Si3N4 valves were fabricated and are under final preparations before engine testing. Figure 1 shows the steps of the fabrication process for a TiAl valve. Once the design was finalized, the geometry was sent to the suppliers for blank fabrication. The valve is then rough machined and friction welded to a Ti-6Al-4V valve. This friction weld procedure is performed for three reasons: (1) cost effectiveness, (2) difficulty in maintaining the straightness specification on castings with high aspect ratio and (3) high-temperature strength is not required in stem. The final procedure, finish machining, is required to minimize the probability of a brittle failure caused by surface defects.

As was noted in this program's previous annual report[5] a supplier oversight resulted in incorrect surface finish that resulted in an early life failure on an impact rig. Subsequently, the valves were returned to the supplier for corrective finish machining. It is clear from the laser scatter NDE scans (Figure 2) that the majority of the machining damage was removed after the second finish machining procedure.

Additional preengine test characterization was performed on all valves. A coordinate measuring machine (CMM) was used to ensure that the valves met the dimensional specifications. Also, a profilometry scan was performed on several critical sections of the valves to verify that finish machining achieved the necessary surface roughness. It was confirmed that the surface roughness specification was met for nearly all of the measured regions on all of the valves.

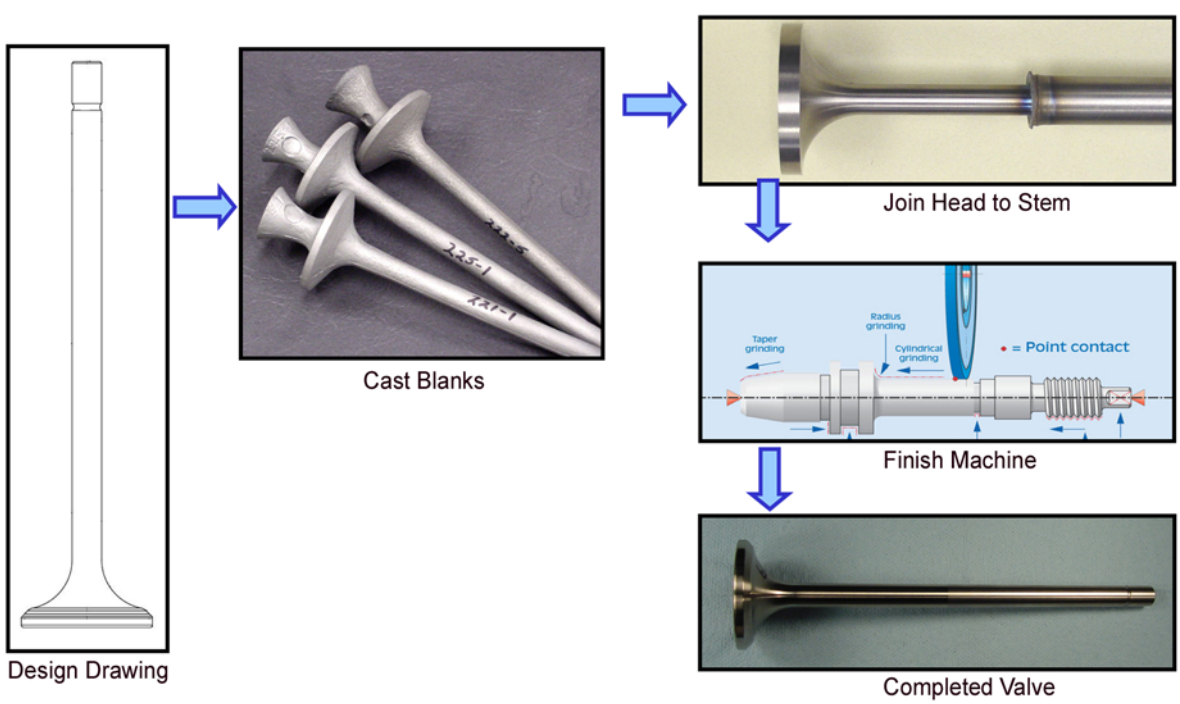

Figure 1. Critical steps of the fabrication process for a TiAl valve. Si_3N_4 valves are subject to every step except the joining of the head to stem because they are formed as a single piece.

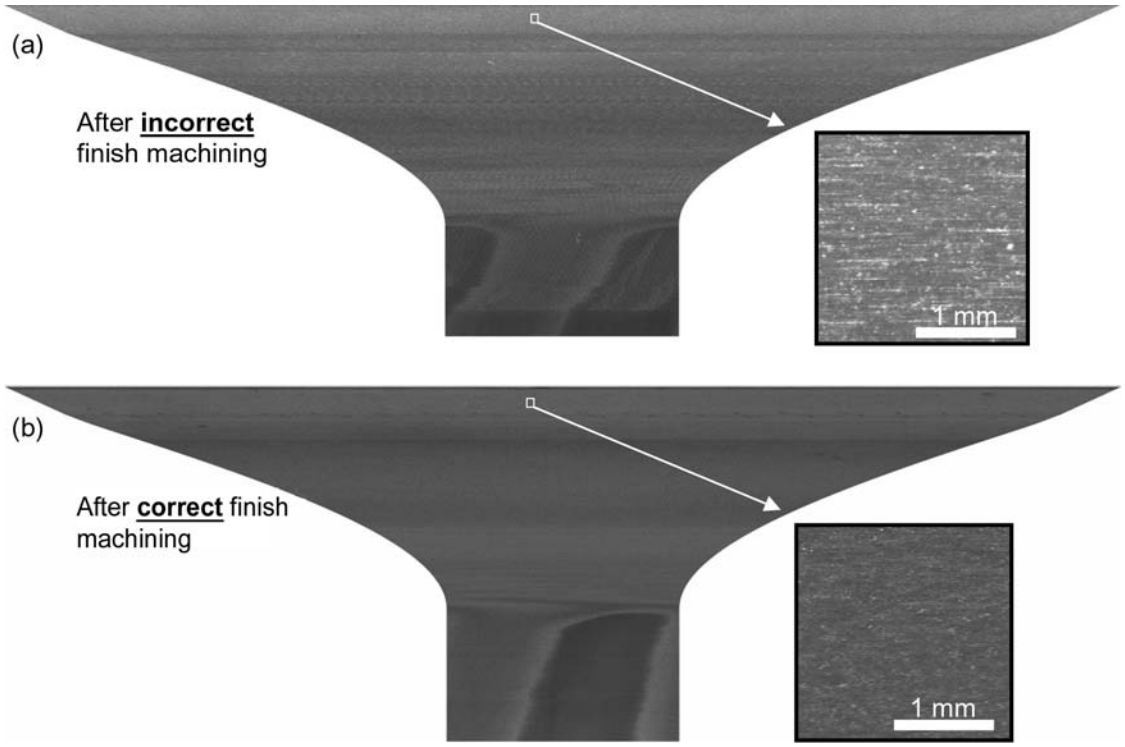

Figure 2. Laser scatter NDE scans of the same Si_3N_4 valve after poor finish machining (a) and after correct finish machining (b). Note that the machining defects (white streaks) are minimized after the valve is finish machined properly.

Valve engine testing

Arrangements have been made to perform engine tests at the National Transportation Research Center (NTRC) located in Oak Ridge, Tennessee. These tests will be executed with the intention to compare valve performance and reliability of advanced materials to current production materials. The valves will be tested on a Caterpillar G3406 natural gas genset platform. A G3406 cylinder head was outfitted with 32 thermocouples embedded in 4 intake and 4 exhaust valve seat inserts. Pressure transducers were installed in each of the six cylinders, the intake manifold and exhaust manifold. In addition, several custom valve train components have been designed to accommodate the modified valve design (i.e. thicker head, change in keeper geometry). Custom seat inserts, valve guides, keeper locks and bridges have been procured and are ready for installation in the G3406 engine.

A test plan has been generated to evaluate TiAl, Si_3N_4, and production valves performance in parallel. The material responses that will be studied are as follows: wear rates will be evaluated via profilometry and micrographic analysis; crack initiation and propagation will be evaluated using laser scatter and ultrasonic NDE; deposition formation will be evaluated via chemical analysis. The valves will be evaluated at various time intervals while accumulating 1000 h of engine test exposure.

As previously mentioned, the valves have been finish machined and are ready for on-engine evaluation (Figure 3). However, there must be an acceptable familiarity with the performance of these novel valve materials prior to evaluation on engine tests. Thus, a set of two Si_3N_4 intake valves and two TiAl exhaust valves is currently accumulating time on an impact test rig (20 h to date) to assess early life wear and crack propagation.

Valve modeling

To rigorously evaluate the performance of a component made from a brittle material, it is insightful to consider the component's lifetime as a function of thermal stresses, mechanical stresses, and the cyclic nature of these loads. With Caterpillar's input, Jadaan Engineering & Consulting has been developing a lifetime prediction model, using NASA

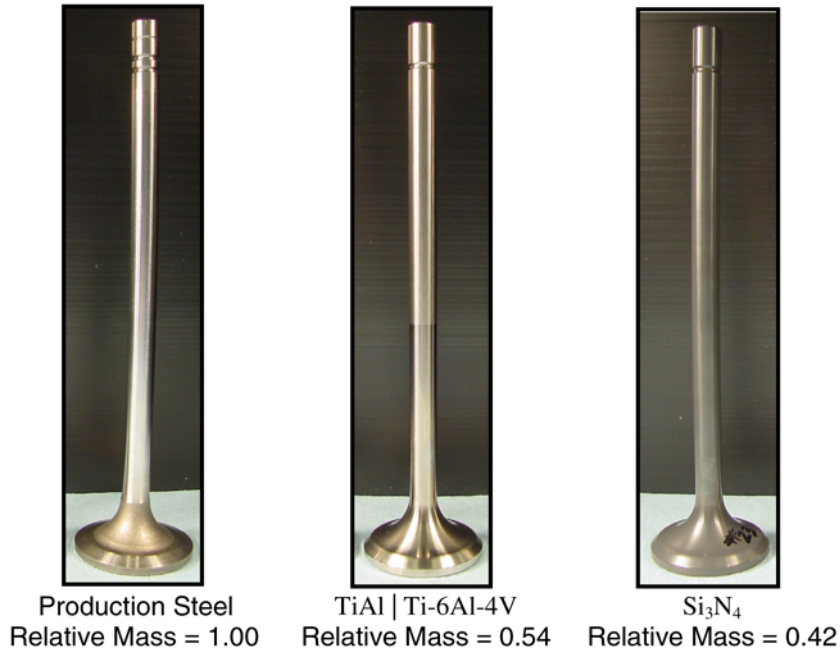

Figure 3. Finish valves ready for engine testing.

CARES/Life code, for a Si_3N_4 exhaust valve subjected to the typical stresses seen in a G3406 engine environment. The inputs to this code follow:

- FEA model to establish the valve geometry [Figure 4(a)]
- Mechanical boundary conditions as a function of crank angle [Figure 4(b)]
- Thermal boundary conditions
- Mechanical properties of the valve material

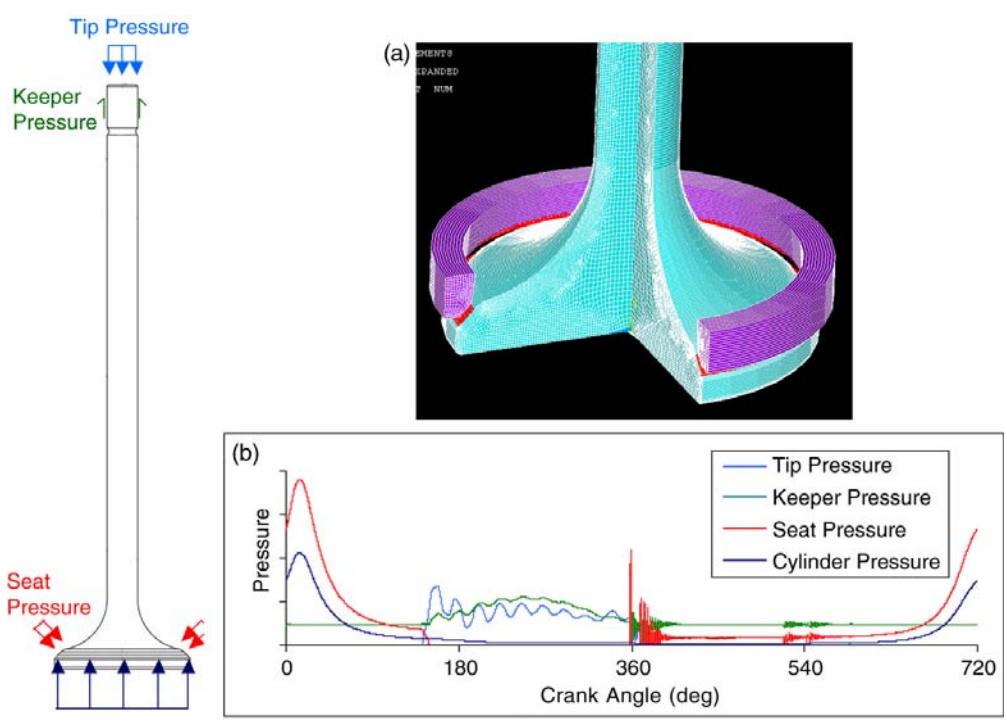

Figure 4. Inputs for the probabilistic life prediction model. (a) FEA valve model. (b) Mechanical boundary conditions as a function of crank angle.

These inputs were supplied to Jadaan Engineering & Consulting for a G3406 valve experiencing representative operating conditions. A FEA model was then generated, and a transient reliability analysis was performed. Subsequent to applying the mechanical and thermal boundary conditions onto the valve geometry, Si_3N_4 material properties are assigned to the elements. The mechanical load spectrum [Figure 4(b)] was discretized into a finite number of steps, and the stress state was calculated for each set of loads. Using the calculated stress fields, a computational transient reliability analysis is performed. In this approach, the material is susceptible to slow crack growth (fatigue) and the probability of failure depends on both the number of cycles and load history sequence. The probability of failure during a given time step is directly impacted by those in the previous time steps. Hence, because of fatigue damage the probability of failure will increase with time as damage accumulates with additional load cycles. The generated life prediction curve is shown in Figure 5. According to this curve, at a safety factor of three, there is <0.0001% probability of failure after 10 years of continuous operation! Although these results may seem to be extraordinarily promising, they must be interpreted with caution. Note that four loads that have been modeled are not the only loads present; they have only served to explore the model's capability. Further refinement of the valve's loading conditions must be made to model the valve's true operating conditions (i.e., non-axisymmetric bending loads). It is expected that when more rigorous boundary conditions are applied that the probability of failure will increase compared to this preliminary model.

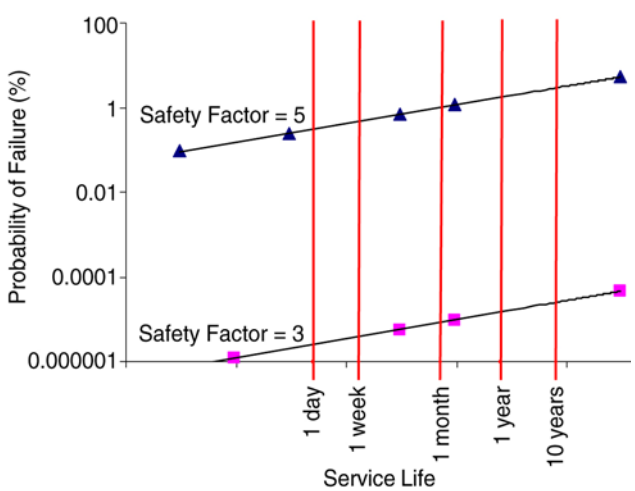

Figure 5. Life prediction curve generated from the preliminary probabilistic model. Safety factor represents the multiplication factor between the defined mechanical boundary conditions and the value used to calculate the probability of failure (i.e., if tip pressure was defined as 10 MPa; the set of data with safety factor = 5 used a tip pressure of 50 MPa).

In addition to refining the model's boundary conditions (i.e., implementing a 3-D model in place of the current axisymmetric model), several new capabilities will be added to the model. The model will be extended to enable the modeling of TiAl. Titanium aluminide will be modeled as a material with a 3-parameter Weibull distribution.[6] Also, the ANSYS/PDS (Probabilistic Design System) will be employed to evaluate the effect that model parameter variation (of e.g., dimensional tolerance, external loading, characteristic strength) has on the life prediction result.

Material characterization

Investigation of basic material properties and manufacturing considerations supplement the engine test and modeling effort. For instance, fundamental thermo-physical and mechanical data were collected on two varieties of TiAl and several varieties of Si_3N_4. The machinability of TiAl and Si_3N_4 and the friction coefficients of these materials are two subjects of particular interest.

Machining processes account for a significant portion of the cost of valve components. This is especially true for high-temperature materials such as intermetallics and ceramics because these materials show a greater sensitivity to surface features than metallic alloys. Thus, it is necessary to identify the most economical method of machining that achieves the required specifications (i.e., geometric tolerances, surface roughness). A series of experiments are planned that will investigate the capability of three machining techniques (turning, grinding, laser-assisted machining) on TiAl test specimens. The surface finish achieved by each technique will be quantified based on microscopy and profilometry measurements. These test specimens will then be subjected to axial stepped fatigue tests at room temperature and engine operating temperatures to evaluate the effect of machining damage and temperature on the fatigue performance of TiAl. These fatigue tests are to be performed at Oak Ridge National Laboratory.

Friction is a fundamental phenomenon in the valve train system. It behaves in both a detrimental manner (e.g., wear of valve seat contact) and beneficial manner (e.g., traction that allows retention of the rotocoil). There is currently no comprehensive database that captures the friction behavior of valve materials and their peripheral components. To address this, a matrix of experiments has been developed that will explore the interaction of various valve materials (TiAl, Si_3N_4 and austenitic steel) with the materials that they contact (seat insert, valve guide, keeper and bridge). These tests will be performed on an in-house Cameron-Plint test apparatus in an environment that matches the engine operating conditions as closely as possible. Results from these tests will aid modeling efforts and highlight the consequences of changing valve materials from the well-known production steel to an advanced material.

Conclusions

Lightweight, high-strength, high-temperature materials are enablers for advanced combustion concepts and fuel-efficient engine designs. This effort aims to examine two prospective materials, TiAl and Si_3N_4, in the context of heavy-duty diesel and natural gas engine environments. In this year progress has been made on several fronts: (1) toward conducting engine tests on these valve materials, (2) development of a probabilistic life prediction model, and (3) compilation of material properties of TiAl and Si_3N_4 that are critical to implementation of these materials in the extreme environment of a heavy-duty engine.

Twelve TiAl and forty-five Si_3N_4 valves have completed the fabrication process. Their incorrect surface finish provided by the machining supplier was rectified. The valves have been subjected to several preengine test characterization assessments: CMM, profilometry and laser-scatter NDE. The first set of valves has accumulated 20 h on an impact rig and has demonstrated acceptable performance. Upon successful completion of the impact rig test, the valves will be tested on a Caterpillar G3406 engine at the NTRC. In addition to fabricating custom components that will enable this engine to accept the new modified valve design, the engine has been instrumented to capture the performance of each cylinder.

Significant progress has been made toward developing a NASA CARES/Life prediction model. A preliminary model has been developed, and a life prediction curve has been generated. It was speculated that this preliminary curve significantly underpredicts the probability of failure due to incomplete representation of the boundary conditions. Model enhancements are currently underway and updated results will be correlated to the engine performance of the valve hardware.

Thermo-physical properties (e.g., coefficient of thermal expansion, thermal conductivity, density) and mechanical properties (e.g., ultimate tensile strength, Young's modulus, ductility) of TiAl and Si_3N_4 have been collected. Properties specific to implementation of these advanced materials in a valve environment are also under investigation (e.g., machinability, frictional coefficients, corrosion resistance).

This diverse effort will help to equip design engineers with the information required to implement advanced lightweight materials in a valve train application. This program has made significant progress toward this goal in FY 2005 and is poised to significantly advance the case for TiAl and/or Si_3N_4 as a future valvetrain material in FY 2006.

References

1. D. Eylon et al., "Development of permanent-mold cast TiAl automotive valves," *Intermetallics*, **6**, 1998.

2. K. Maki et al., "Development of a high-performance TiAl exhaust valve," SAE Paper 960303, Warrendale, Pennsylvania, 1996.

3. M. J. Andrews and J. Chapa-Cabrera, "High-temperature advanced materials for lightweight valve train components," *Heavy Vehicle Propulsion Materials 2003 Annual Progress Report*, Energy Efficiency and Renewable Energy Office of FreedomCAR and Vehicle Technologies, March 2004.

4. J. G. Sun, "NDE development for ceramic valves for diesel engines," *Heavy Vehicle Propulsion Materials 2004 Annual Progress Report*, Energy Efficiency and Renewable Energy Office of FreedomCAR and Vehicle Technologies, May 2005.

5. J. S. Trethewey et al., "High-temperature advanced materials for lightweight valve train components," *Heavy Vehicle Propulsion Materials 2004 Annual Progress Report*, Energy Efficiency

and Renewable Energy Office of FreedomCAR and Vehicle Technologies, May 2005.

6. Biery et al., "Use of Weibull statistics to quantify property variability in TiAl alloys," *Metallurgical and Materials Transactions A*, **33A**, 3127–3136 (October 2002).

Presentations and Publications

J. M. Zhang, J. G. Sun, M. J. Andrews, A. Ramesh, J. S. Trethewey, and D. M. Longanbach, "Characterization of subsurface defects in ceramic rods by laser scattering and fractography," presented at the 32nd Annual Review of Progress in Quantitative Nondestructive Evaluation, Bowdoin College, Brunswick, Maine, July 31–August 5, 2005, and paper to be published in conference proceedings.

J. G. Sun, J. M. Zhang, J. S. Trethewey, J. A. Grassi, M. P. Fletcher, and M. J. Andrews, "Nondestructive evaluation of machining and bench-test damage in silicon nitride ceramic valves," paper presented at the American Ceramic Society's 29th Ann. Intl. Cocoa Beach Conf. & Exposition on Advanced Ceramics & Composites, Cocoa Beach, Florida, January 23–28, 2005, and to be published in conference proceedings.

J. S. Trethewey, H.-T. Lin, and J. G. Sun, "Lightweight valve train materials," presented at Department of Energy Merit Review, Oak Ridge National Laboratory, September 15, 2005.

B. Engineered Surfaces for Diesel Engine Components

M. Brad Beardsley
Caterpillar, Inc.
Technical Center Bldg. E/854
P.O. Box 1875
Peoria, IL 61656-1875
(309) 578-8514; fax: (309) 578-2953; e-mail:Beardsley_M_Brad@cat.com

DOE Technology Development Area Specialist: James J. Eberhardt
(202) 586-9837; fax: (202) 586-1600; e-mail: james.eberhardt@ee.doe.gov
ORNL Technical Advisor: D. Ray Johnson
(865) 576-6832; fax: (865) 574-6098; e-mail: johnsondr@ornl.gov

Contractor: Oak Ridge National Laboratory, Oak Ridge, Tennessee
Contract No.: DE-AC05-00OR22725
Subcontractor: Caterpillar, Inc., Peoria, Illinois

Objectives

- Develop coating processes to apply amorphous steels and quasicrystal materials to engine pistons and cylinder heads for use as thermal barrier coatings in homogenous charged combustion ignition (HCCI) engine designs.
- Quantify the diffusion stability of new quasicrystalline material at engine operating temperatures.

Approach

- Use high-velocity oxygen fueled (HVOF) processes to apply amorphous and quasicrystalline materials to engine piston and cylinder head.
- Use microprobe analysis of diffusion couples to determine the stability of quasicrystalline and bond coating couples at engine operation temperatures.

Accomplishments

- Coated HCCI pistons with amorphous steel for single cylinder engine testing.
- Measured diffusion profiles for the quasicrystalline material and three different bond coating materials.

Future Direction

- Modify the thickness and uniformity of the amorphous steel coating if needed after initial engine testing.
- Develop graded coating structures for the quasicrystalline material based upon the diffusion profiles developed.

Introduction

Two new materials, amorphous steels and quasi-crystalline materials, are investigated as thermal barrier coatings. Both materials are capable of being sprayed using high-velocity oxygen fuel (HVOF) processes that produce denser coatings with higher strengths than plasma spraying. The denser coating structure of HVOF coatings eliminates the need for sealing of the coating porosity and the higher strength enhances the coating durability. Amorphous steel coatings are reported to have low thermal conductivity as well as high hardness and toughness, making them attractive as thermal barrier coatings.[1,2]

The quasicrystal being studied, $Al_{71}Co_{13}Cr_8Fe_8$, has been shown to be capable of 1100°C operation in a turbine engine.[3] Application of thermal barrier coatings (TBCs) to new homogeneous charged combustion ignition (HCCI) engine components can result in lower fuel consumption and lower engine component temperatures similar to that shown in standard diesel engine configurations (Figure 1).

Approach

Amorphous Steel Coatings

The SHS717 amorphous steel produced by The NanoSteel Company, Maitland, Florida, was selected for use as a TBC. Thermal diffusivity of HVOF sprayed SHS717 shows that the amorphous structure is retained up to approximately 700ºC (Figure 2). New HCCI engine designs have surface temperatures below this range allowing the use of the amorphous coatings. New piston designs were procured, and coating processes were developed to apply up to 3.5-mm coating to the piston bowl.

The piston components were coated using a kerosene-fueled HVOF torch manufactured by Praxair TAFA. The geometry of the part is shown in Figure 3. Because the geometry of the pistons consists of surfaces that are up to 60° from normal, they represent a challenge to coat uniformly. It is also necessary to maintain the torch orientation as close to 90° to the surface to obtain the highest coating density.

		Water-Cooled Baseline	Unsealed TTBC	Sealed TTBC
Recip. BMEP	KPa	1427	1411	1406
Air Flow	kg/h	274	288	249
Vol. Efficiency	%	85.5	81.3	80.3
Air/Fuel Ratio		30.4	30.3	29.5
Peak Cyl. Pressure	MPa	16.0	16.0	16.0
Recip. SFC	G/kW·h	217.1	231.7 (+6.7%)	206.5 (-4.9%)
Recip. SHR	kW/kW	0.479	0.499	0.399

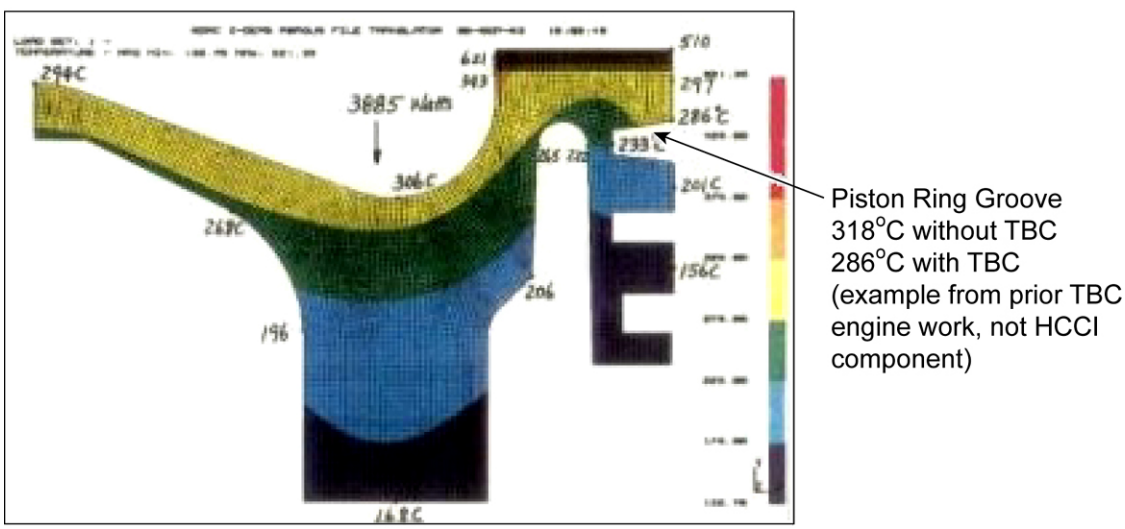

Figure 1. High-density (sealed) TBCs can reduce fuel consumption and provide temperature reduction needed for HCCI engine components.

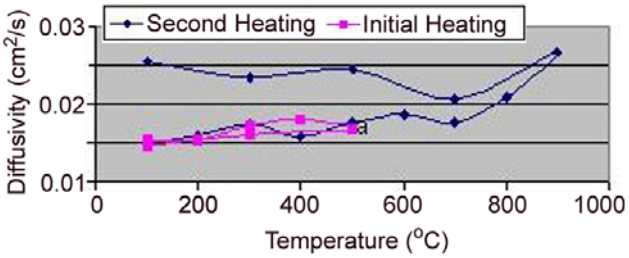

Figure 2. Exposure to temperatures above glass transition temperature (700°C) causes an increase in thermal diffusivity of amorphous steel.

Figure 3. Coated piston geometry.

Two types of robotic motion were investigated for coating deposition: (1) single radial [Figure 4(a)], and (2) raster combined with a short radial motion to cover the 60° angled part [Figure 4(b)]. The raster type motion is the easiest to program to achieve a uniform coating thickness but results in a high wastage of coating material due to the torch traversing off the part for much of the cycle. The radial motion is more efficient in material usage (lower cost) but difficult to program as the speed control of the robot is uncertain due to the high acceleration/deceleration rates required. As the circumference of the spray footprint depends on the position with respect to the center, the robot speed was adjusted accordingly to achieve a uniform deposition rate. Initially, practice piston geometries were used to develop the coating. The pistons were rotated in a lathe for either robotic motion with the rotation speed at 1700 rpm.

The raster type motion provides an easier method to control the deposition rate because each pass over the part is done at a constant speed. However, the raster type motion results in a part of the surface being sprayed under 30° angle rather than 90°. Also, the stand-off distance is not held constant and varies by half of the bowl depth. In total, 20 practice pistons were coated using the radial type motion and 2 using the raster type motion. Final two pistons coated for engine testing used the raster type motion as this provides the most uniform coating. Further work to achieve coating uniformity with the radial motion is required and will be pursued if the initial engine testing is successful.

Quasicrystalline Materials

Microprobe analysis of diffusion couples is being used to assess the thermal stability of the quasicrystalline coatings for use as thermal barrier coatings. HVOF coatings of the $Al_{71}Co_{13}Cr_8Fe_8$ material were previously produced for diffusion couple testing: (1) the quasicrystal and steel substrate, (2) the quasicrystal, a Ni-17Cr-6Al-0.5Y bond coat, and steel substrate, (3) the quasicrystal, a Ni-31Cr-11Al-0.6Y bond coat, and steel substrate, and (4) the quasicrystal, a Fe-26Cr-8Al-0.4Y bond coat, and steel substrate. The diffusion couples were produced by spraying a steel sample, 12.5 mm diameter by 19 mm, with 0.5-mm-thick layers of the bond coatings and quasicrystal. These samples were then sealed in evacuated quartz tubes and held at temperatures of 500, 700, and 900°C for 25, 100, and 500 h. The samples were water quenched after annealing, and samples were prepared for examination by optical microscopy, scanning electron microscopy (SEM), and microprobe analysis.

Results

Amorphous Steel Coatings

The microstructure of the coatings was evaluated using optical microscopy. The microstructure of the sample deposited using the raster motion

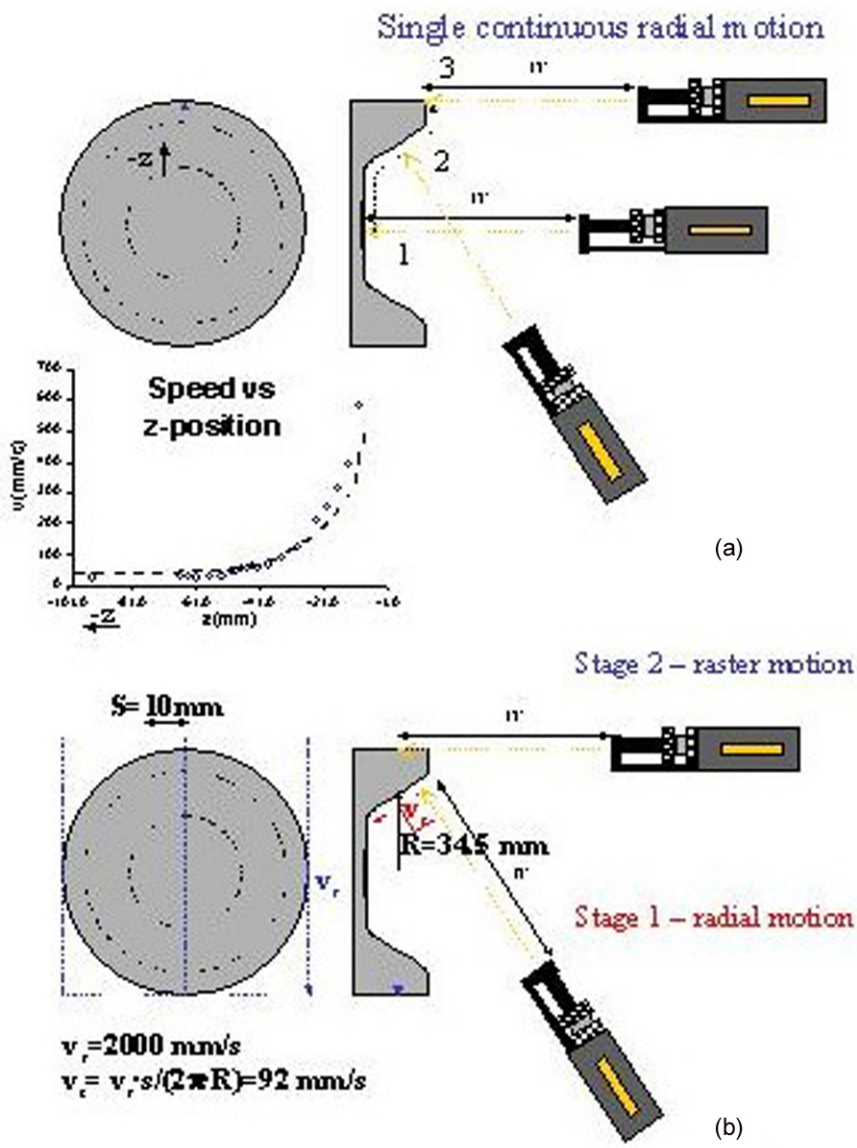

Figure 4. Coating motions used (a) continuous radial motion (top) and (b) two-stage raster motion (bottom).

(Figure 5) was compared to the microstructure produced using the radial motion (Figure 6). The coating deposited using the raster motion exhibits higher porosity in the radius area at the bottom of the bowl. This is caused by the turbulence created by the bowl geometry. The coating deposited using the radial motion exhibits higher density that is more uniform along the radius of the piston. However, thickness uniformity in coatings formed using a radial motion remains a challenge. Pistons coated using the raster motion were supplied for engine testing but have not yet been tested.

Quasicrystalline Materials

Microprobe analysis of the diffusion couple samples shows high mobility of aluminum into both the nickel- and iron-based bond coatings in only 25 h at 700ºC (Figures 7 and 8). Cobalt shows higher mobility into the iron based bond coating than the nickel. Further analysis of the diffusion zones at various temperatures and times is under way to provide a better understanding of the diffusion behavior of various species.

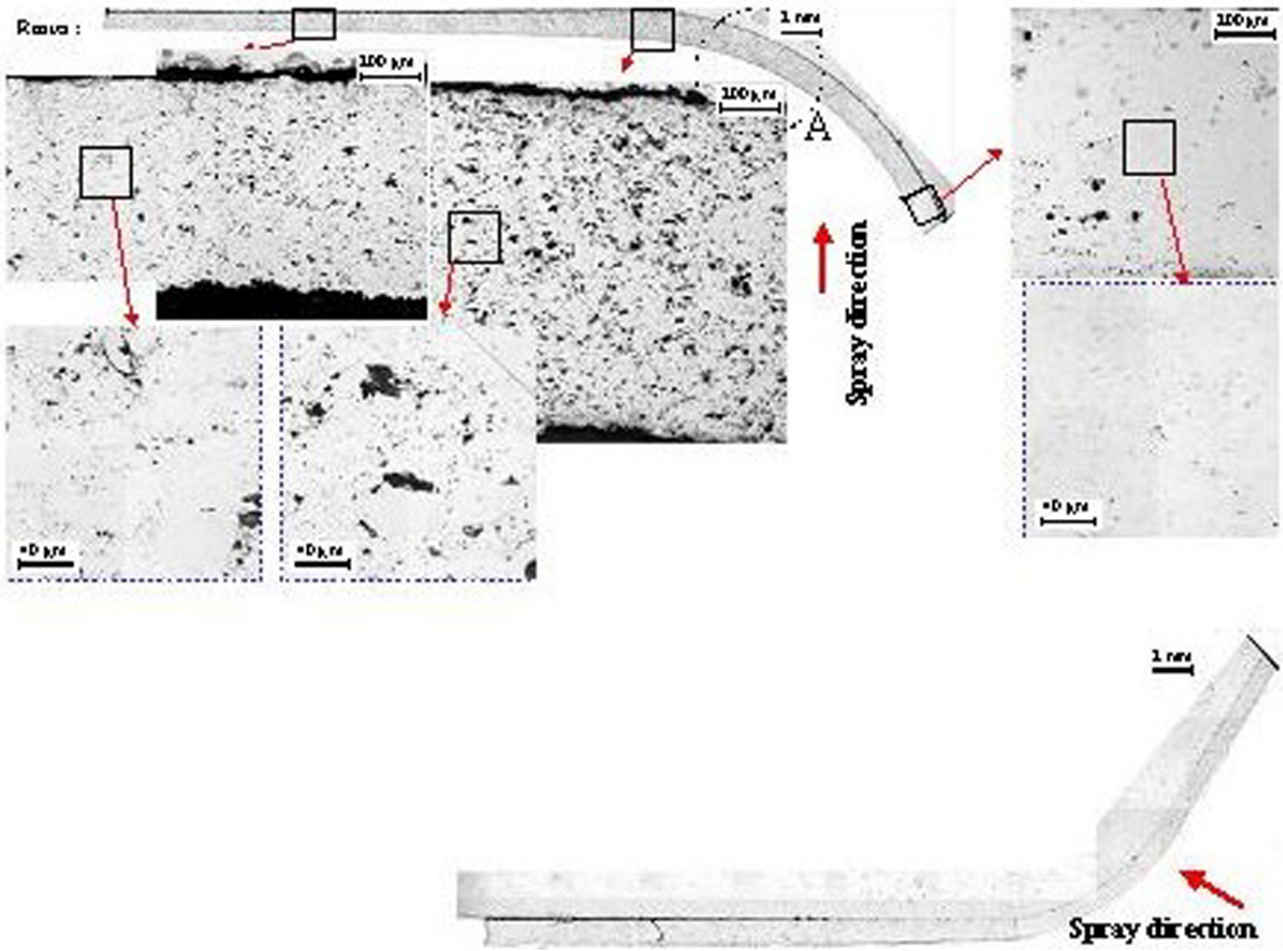

Figure 5. Microstructure of the practice piston 9 sprayed using a raster type motion showing higher porosity in the radius area of the bowl.

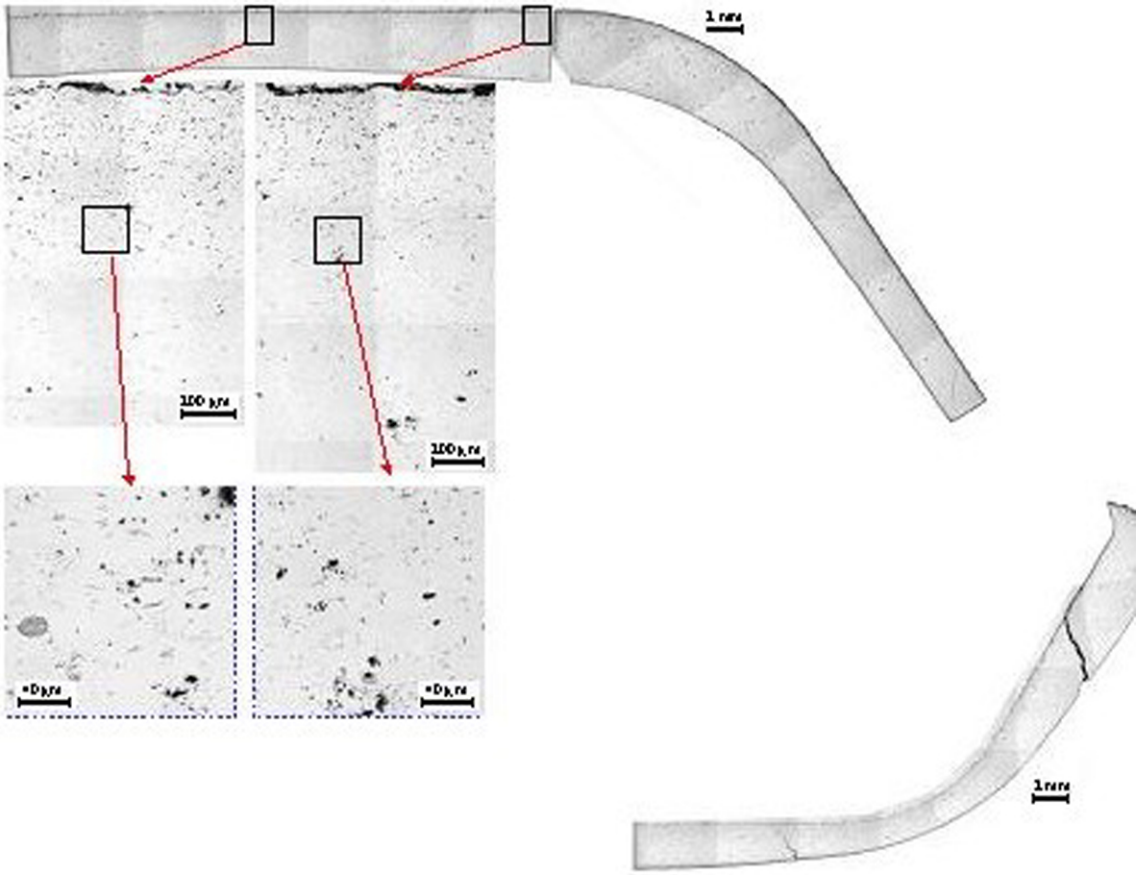

Figure 6. Microstructure of the practice piston 20 sprayed using a radial type motion showing lower porosity in the radius area of the bowl.

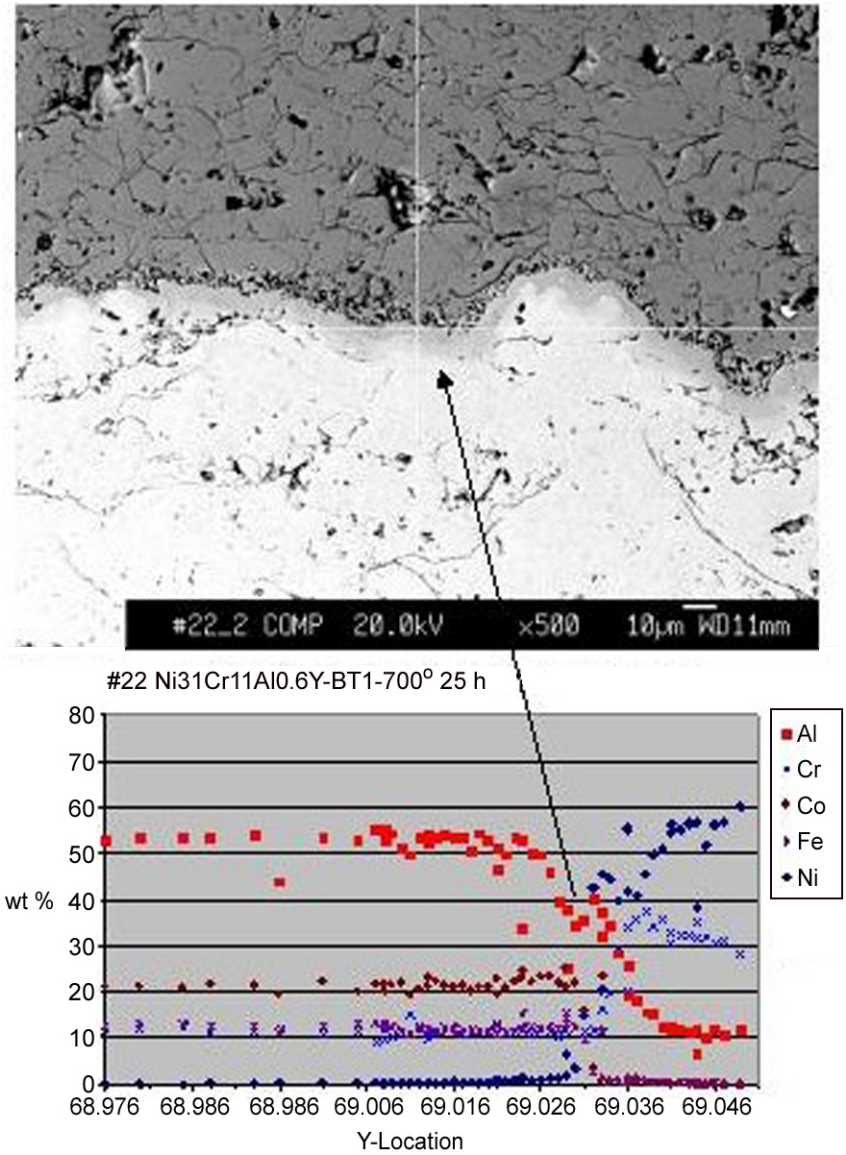

Figure 7. Microprobe results for the quasicrystal and nickel-based bond coating showing high mobility of the aluminum into the bond coating.

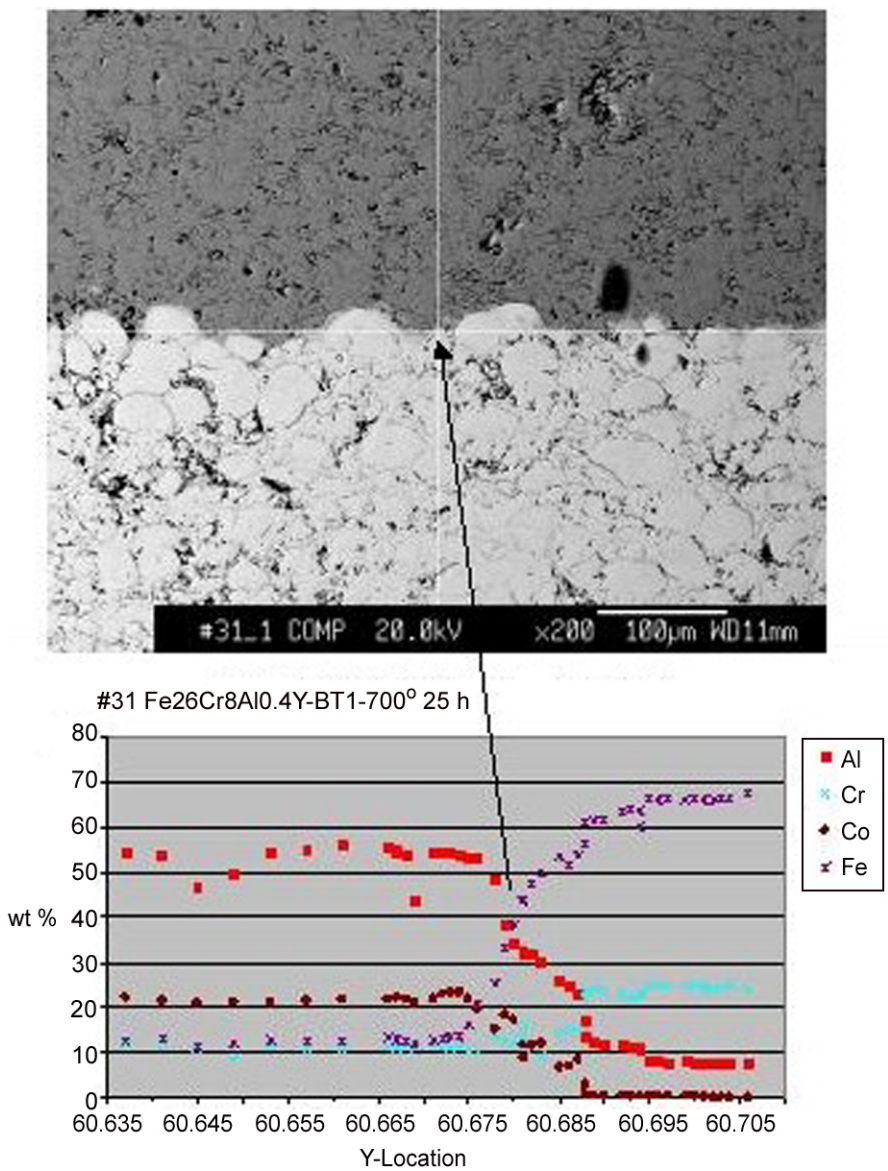

Figure 8. Microprobe results for the quasicrystal and iron-based bond coating showing mobility of the cobalt in the bond coating.

Conclusions

Amorphous Steel Coatings

The microstructures of the coatings applied to engine test pistons can be improved using the radial motion, but the coating thickness uniformity will need to be improved. Successful engine testing of the initial coated pistons will provide the emphasis to further develop these coatings.

Quasicrystalline Materials

The reaction zone between the quasicrystalline and bond coatings of iron and nickel show high mobility of the aluminum at 700ºC. Because the interface of the bond coating and quasicrystalline material will be below 500°C, this should not preclude their use as a thermal barrier coating system. Graded designs may be limited by this reactivity, and further analysis of the diffusion kinetics will be done to verify the temperatures of use for the quasicrystal and bond coatings combinations.

References

1. D. J. Branagan, W. D. Swank, D. C. Haggard, and J. R. Fincke, "Wear Resistant Amorphous and Nanocomposite Steel Coatings," *Met. & Mat. Transactions A*, **32A**, 2615–2621 (2001).

2. D. Shin, F. Gitzhofer, and C. Moreau, "Development of Metal Based Thermal Barrier Coatings (MBTBCs) for Low Heat Rejection Diesel Engines," Proceedings of the 2005 International Thermal Spray Conference, 915–919 (2005).

3. A. Sanchez, F. J. Garcia, J. M. Algaba, J. Alvarez, P. Valles, M. C. Garcia-Poggio, and A. Aguero, "Application of Quasicrystalline Materials as Thermal Barriers in Aeronautics and Future Perspectives of Use for These Materials," *Mat. Res. Soc. Symp. Proc*., **553**, 447–458 (1999).

C. Cermet Composites for Wear Applications

M. Anderson, T .M. Yonushonis, R. J. Stafford, M. Henrichsen, D .J. Gust, B. Seegmiller, and J. Stephan**
Cummins, Inc.
Columbus, IN 47202-3005
(812) 377-3279; fax: (812) 377-7226; e-mail: randy.j.stafford@cummins.com

**CoorsTek, Golden, Colorada*

DOE Technology Development Area Specialist: James J. Eberhardt
(202) 586-9837; fax: (202) 586-1600; e-mail: james.eberhardt@ee.doe.gov
ORNL Technical Advisor: D. Ray Johnson
(865) 576-6832; fax: (865) 574-6098; e-mail: johnsondr@ornl.gov

Contractor: Oak Ridge National Laboratory, Oak Ridge, Tennessee
Prime Contract No.: DE-AC05-00OR22725
Subcontractor: Cummins, Inc., Columbus, Indiana

Objectives

- Optimize injection molding binder composition and sintering cycles to achieve 99+% density. This will include the determination of the shrink rate during sintering for prototype tool construction and demonstration.
- Test prototype components in intended application on Cummins' fuel system test rigs to show viability of material in an application.

Approach

- Verify properties, microstructure, and shrinkage in test bars manufactured from new source of NiAl powder in injection molded powder composition. Ensure that the properties are the same as for the previous NiAl powder.
- Test prototypes of powder injection molded near net shape components of TiC/Ni_3Al cermet on abuse tests at Cummins Fuel Systems.

Accomplishments

- Found that new source of powder has not compared favorably with the previous source. More work is in progress to define the powder and what steps are needed to improve the strength.
- Did not stabilize prototype component designs during the year, so little progress was made in defining a molding tool for the prototype components.

Future Direction

- Finalize process development for powder using the new source of NiAl powder.
- Evaluate powder injection mold prototype components on abuse test rigs at Cummins.

Introduction

Increasingly stricter diesel engine combustion emission standards and the customer's desire for maintained or improved fuel economy requires fuel injection systems to become more advanced. Injection pressures need to increase (helps with emissions), and more precise control of when and how much fuel is injected (helping both emissions and

fuel economy) is required. New materials that exhibit excellent wear properties against steel components are needed for application where components are sliding and impacting against each other. One material that Cummins is interested in was developed under a DOE Cooperative Agreement DE-FC05-97OR22538: TiC/Ni_3Al.

TiC/Ni_3Al is a composite of TiC powder in a Ni_3Al matrix that was developed in collaboration with Oak Ridge National Laboratory (ORNL) and CoorsTek. Its composition was established to match the unique properties required for Cummins Fuel Systems applications. CoorsTek and ORNL have developed the processing methods to make the material, while Cummins has been responsible to finding an application for it and testing the material as fuel system components and evaluating their performance vs other materials.

Approach

The established composition of TiC/Ni_3Al cermet will be processed using the new source powder and ten powder injection molded components for evaluation of properties. The microstructure, density, and shrinkage rate will be evaluated to determine the suitability of the new powder. Coinciding with this work, fuel systems will refine and finalize the design of some prototype components to be near net shape molded. Following confirmation of the properties and final design, prototype components will be manufactured for rig testing to evaluate the performance and wear resistance of the cermet material in a potential application in the next-generation fuel system at Cummins.

Results

The benchmark strength for the TiC/Ni_3Al powder from pressed and sintered bars is shown below. The initial powder injection molding with the same formulation powder showed a loss of ~10% strength (see below). This was not considered as significant because the debinding process was not optimized for the powder. The powder injection molding with the new NiAl powder showed an additional loss of 15%. This loss was confirmed with tests of the powder pressing and sintering (see below). Evaluation of the test bars showed the presence of NiAl. This may account for the lower strength.

The prototype component design was stabilized, and a final drawing was created for a mold tool to create the powder injection molded components.

Material	Mean strength (ksi)	Standard deviation (ksi)	Coefficient of variation (%)
Baseline (pressed)	152	20.4	13
Injection molded (old)	137	21.5	16
Injection molded (new)	114	5.6	5
Pressed (new)	108	7.0	6

Conclusions

Powder processing is critical to the properties of the material. Additional work is needed to bring the powder properties to the same level as the material using the old source of NiAl powder.

Stabilized design of the prototype is necessary to manufacture the prototype pieces for testing.

D. Processing and Characterization of Structural and Functional Materials for Heavy-Vehicle Applications

J. Sankar, Z. Xu, and S. Yarmolenko
North Carolina A &T State University
1601 East Market Street
Greensboro, NC 27411
(336) 256-1151, extension 2282; fax: (336) 256-1153; e-mail: sankar@ncat.edu

DOE Technology Development Area Specialist: James J. Eberhardt
(202) 586-9837; fax: (202) 586-1600; e-mail: james.eberhardt@ee.doe.gov
ORNL Technical Advisor: D. Ray Johnson
(865) 576-6832; fax: (865) 574-6098; e-mail: johnsondr@ornl.gov

---

Contractor: Oak Ridge National Laboratory, Oak Ridge, Tennessee
Contract No.: DE-AC05-00OR22725
Subcontractor: North Carolina A&T State University, Greensboro, North Carolina

---

Objectives

- Produce yttria-stabilized zirconia (YSZ) thin coatings using electrophoretic deposition (EPD) technique for solid oxide fuel cells (SOFCs).
- Study the effect of the processing parameters on the porosity of the NiO/YSZ anode substrates.
- Study liquid-phase sintering technique of YSZ.

Approach

- Study the experimental parameters for the EPD process and deposit YSZ thin film coatings using this technique.
- Characterize the coatings using scanning electron microscopy (SEM) and X-ray diffraction (XRD).
- Study the batch preparation, pressing, and sintering parameters for the anode substrate fabrication.
- Examine the anode microstructure by SEM.
- Study the liquid-phase sintering of YSZ dense electrolyte and porous substrate using a sintering aid.

Accomplishments

- Obtained dense and thin YSZ electrolyte coatings on porous cathode substrates.
- Identified the effects of the processing parameters of the die-pressing and sintering technique on the porosity of the anode substrates.
- Acquired dense and porous YSZ according to the requirements using liquid-phase sintering at lower temperatures.

Future Direction

- Optimize the processes to prepare electrodes and electrolyte layers.
- Fabricate single SOFCs and conduct performance tests.
- Develop materials for electrolyte with higher conductivities than YSZ.

Introduction

Low-cost production of the high-quality components for SOFCs by various techniques is of great importance and is the focus of this research project. Techniques that could help to reduce the overall cost of the fuel cell are identifying cost-effective, relatively low-purity raw materials; mass production of cell components; use of inexpensive and simplified fabrication processes; and enhanced cell life.[1–5] The future of SOFCs greatly depends on the outcome of these techniques. Currently, the cost of the fuel cell is mainly influenced by the number of processing steps during the fabrication process, apart from the direct cost of raw materials. Generally, the SOFC is fabricated in either one of the two most common designs, tubular or planar cell. Electrode-supported planar cells are the most popular and commercially efficient cell design, due to their high power densities.[6] There are various steps at each stage of the fuel cell fabrication: developing the anode, depositing electrolyte layer, sintering the cell, etc. Each step consumes enormous time and cost. This presents a major hindrance in the commercialization of the fuel cell. The cost and time involved in the fabrication can be reduced a lot by careful selection of process techniques and parameters. In this project, three different cost-effective techniques were used for producing SOFC components. The results of the experimental studies of each technique will be reported.

Electrophoretic deposition (EPD) technique is especially attractive for SOFC application owing to simplicity, low-cost equipment, and ease of deposition of films of controlled thickness on substrates with even complex shape. EPD is a process in which the charged particles in an appropriate solvent move under the influence of the direct electric field toward an oppositely charged electrode and coagulate thereon to form a stable deposit. In the past research and applications, it was used to prepare ceramic laminates[7,8] and components in electrochemical cells,[9] etc. It was recently introduced to the area of the manufacturing SOFCs, since thin film electrolytes are highly desired for the fuel cells to work at reduced temperatures and higher efficiencies.

Optimization of the processing parameters by having an experimental design called a factorial design for obtaining data with a minimum expenditure of time and resources and by meticulous analysis of the data, called analysis of variance (ANOVA) is the key to the low-cost production of the SOFC components. The analysis provides detailed insight into the direct effect of process variables on part's porosity as well as into the intensity of the numerous interactions between variables. This kind of response surface methodology (RSM) helps to determine, on the basis of one experiment, where to move in the next experiment toward the optimal point on the underlying response surface[10]. The optimized results will help to reduce cost and time involved in the fabrication process. In this research, the factorial design was used for the production of anode substrates with optimized porosities.

High energy expense in the sintering of the fuel cell components, especially the YSZ electrolyte, is one of the major causes for the cost. Usually the sintering of the YSZ powders needs a temperature higher than 1500°C for many hours to obtain a fully densified electrolyte. Reduction of the sintering temperature will save the energy for sintering and also save the investment on expensive high-temperature furnaces. Previous research has already shown that YSZ can be sintered at a substantially lower temperature by adding a small fraction of low melting-point oxides, for example, bismuth oxide. Bismuth oxide itself is a good oxygen ion conductor. However, the purpose of the research at this time is to achieve desired microstructures with this technique for fuel cell components. The effect of the sintering aid addition on the conductivity of the electrolyte materials will be addressed in the ongoing research.

Approach

For the EPD technique, the electrolyte coatings were produced by depositing the charged YSZ particles in a powder suspension under a direct current (dc) electric field. The suspensions were prepared by dispersing the powders in the mixture of two organic solvents, that is, acetylacetone (acac) and ethanol at different ratios ranging from pure acac to pure ethanol. The powder concentrations used were 5, 10, 25, and 40g/L. All the suspensions were subjected to ball milling for 48 h and ultrasonic agitation for 0.5 h before use. Stainless steel with the size of 15 × 15 × 0.3-mm substrates was used for all the depositions for parametric studies. The coatings were also applied on porous cathode substrates

which were made of strontium-doped lanthanum manganite (LSM) produced in our laboratory by slurry casting. The coated specimens were dried at room temperature for more than 20 h and then sintered to obtain a dense electrolyte layer.

In this study, NiO and YSZ, the most preferred anode material for SOFCs, were used as the raw materials along with the pore former graphite. A full 2^4 factorial design was used. The four variables that were considered for the experimental design are graphite (vol %), ratio of NiO to YSZ, compaction pressure, and sintering temperature. The two levels for each variable are listed in Table 1. A total of 16 sets of experiments with two replicates for each set (32 total experiments) were conducted. Powders are weighed according to the design. They were mixed by ball milling along with ethanol for 48 h and then dried. The powder mixture was uniaxially pressed. The green samples were sintered in air for 1 h. The dimensions and weight of the sintered samples were measured using the laboratory calipers and digital balance, respectively. The measured dimensions were used for the porosity calculations.

For the liquid-phase sintering study, 4.5 wt % bismuth oxide powders were added into YSZ powder. The green form of the YSZ laminates was prepared by slurry casting. The slurry was prepared by mixing the powders with polymeric binder, dispersant, plasticizer, and ethanol. To investigate the effect of the liquid-phase sintering on the densification of the YSZ particles with different sizes, the green forms with –325 mesh YSZ power were cast and dried firstly. A thin layer comprising the suspension of the mixed YSZ powders of 66.7 wt % of –325 mesh, 23.1 wt % of 56 nm and 13.2 wt % of 20 nm in ethanol solution stabilized with poly(dimethyldiallylammonium chloride) (PDDA) was sprayed onto the dried green form YSZ substrate. The coated specimens were sintered at the maximum temperature of 1000°C in air. Figure 1 shows the programmed sintering cycle for the liquid-phase sintering. The microstructure of the sintered specimens was examined with scanning electron microscopy (SEM).

Table 1. Level design for the experimental parameters

Independent variable	Treatment level	
	Level 0	Level 1
Graphite (vol %)	40	30
YSZ/NiO weight ratio	50:50	42.5:57.5
Compaction pressure (MPa)	150	125
Sintering temperature (°C)	1350	1200

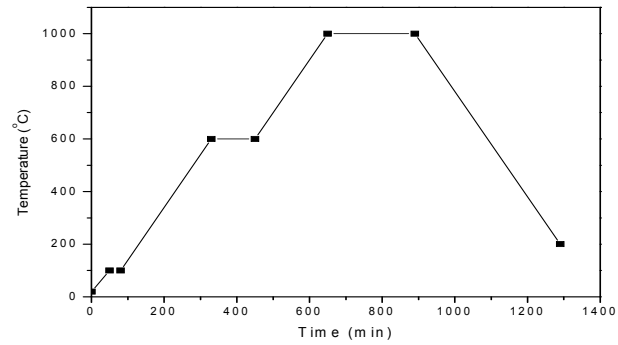

Figure 1. Sintering cycle for liquid-phase sintering of YSZ specimens.

Results

Effect of the Solvent on the Preparation of YSZ Coatings by EPD

To produce dense, homogeneous green forms of the coatings with EPD, a dilute, well-dispersed, and stable colloidal suspension is of great importance. In this case the stable suspension was obtained by absorbing free protons on the surface of the particles, while the free protons were produced by the reaction between acac and ethanol. Figure 2 shows the weight gains as a function of the fraction of ethanol in its mixture with acac. It can be noticed that deposits were obtained in all the different mixtures. The weight gain in pure acac is obviously much higher than in any other mixtures in constant current deposition mode (curve a). However, this advantage is much less in constant voltage mode (curve b). If we examine the voltage required for pure acac in Figure 3, it is ten times more than the lowest one. We can suggest that the amount of the free proton is much less in pure acac than in any other mixtures and even in pure ethanol. High electrical energy input led to the high yield. At the constant voltage mode, even though the input power in pure acac is the lowest, the deposition yield was still the highest one. In constant voltage mode, the power inputs in all the mixtures are higher than either in pure acac and ethanol. Nevertheless, the deposition yields were gradually decreased with the

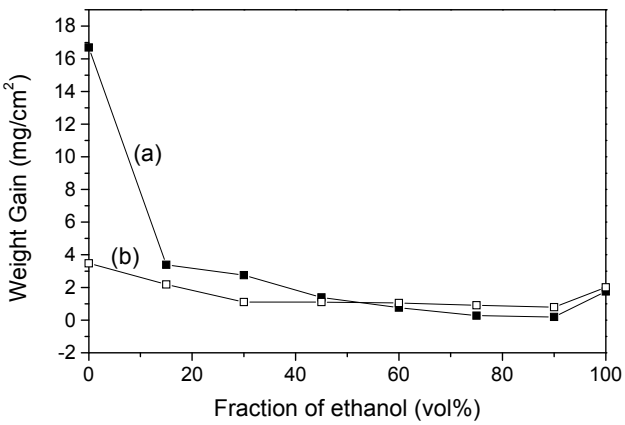

Figure 2. Weight gains as functions of the volume fraction of ethanol in its mixture with acac. Depositions were carried out at (a) a constant current density of 0.20 mA/cm^2 and (b) a constant voltage of 50 V. Deposition time was 120 s with a powder concentration of 5 g/L.

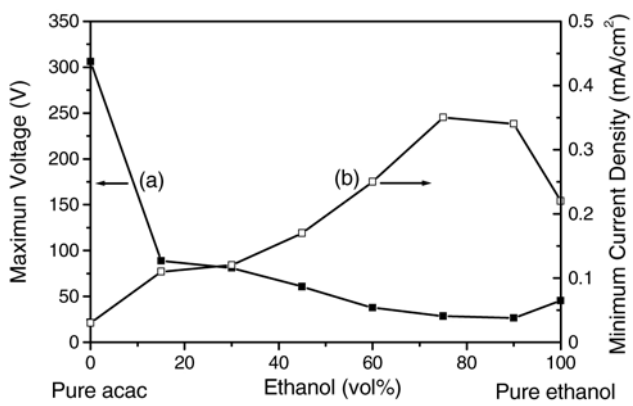

Figure 3. Current and voltage as functions of the mixing ratios of ethanol and acac during the 120-s depositions. (a) Maximum voltage required to maintain a constant current density of 0.20 mA/cm^2, and (b) minimum current density when a constant voltage of 50 V was applied.

increase of the fraction of ethanol in the mixture. It is recommended that in these mixtures, there are free protons in addition to those absorbed by the YSZ particles. The moving of these free protons partially contribute to the total electric current; the deposition rates were hence lower than the expectations.

The microstructures were examined with SEM. Figure 4 shows the micrographs taken from the surfaces of the deposited green forms at the constant voltage of 50 V. Figure 4(a) and (c) show poorly packed green forms from the suspensions with pure acac and pure ethanol. The poor packing resulted from the large agglomerates in the suspensions. This means that in the solvents of either pure acac or pure ethanol, the YSZ particles were not well dispersed because of the low free proton levels. Figure 4(b) shows a homogeneous packed deposit in the suspension with 45 vol % ethanol/55 vol % acac as the solvent. The particle sizes are much smaller than in the other samples. Therefore, the deposition behavior was further studied for suspension in the solvent with the mixing ratio of ethanol and acac 1:1.

Effect of the Parameters in the Factorial Experiments

The obtained porosity values after sintering are shown in Table 2, which will be used as the inputs for the ANOVA subsequently.

The effects of the processing parameter on the porosity of the sintered anode pellets were analyzed by the ANOVA method. It was understood that the porosity of the anode increased slightly with the increasing of the NiO component in the mixture, and the increasing rates were in accordance with the level of the pressure used to make the pellets. The sintering temperature was found to be one of the very significant factors in the porosity control. The

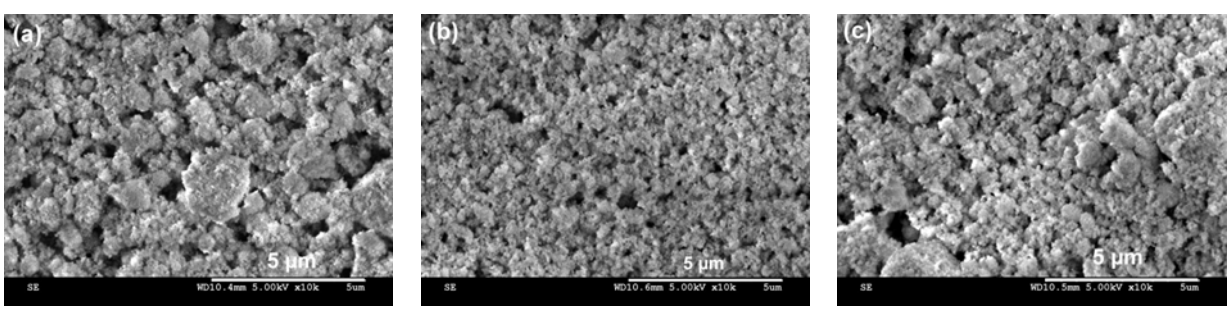

Figure 4. Micrographs of the dried green forms deposited on stainless steel substrates at a constant voltage of 50 V for 120 s. The depositions were conducted in the suspensions of 5 g/L YSZ in solvents of (a) pure acac, (b) 45 vol % ethanol/55 vol % acac, and (c) pure ethanol for 120 s.

Table 2. Porosity values of sintered NiO/YSZ samples

Design No.		1	2	3	4	5	6	7	8
Porosity (%)	**Set 1**	6.85	40.62	8.00	41.41	10.85	42.94	10.68	40.38
	Set 2	7.09	41.80	8.39	41.41	10.47	42.57	10.03	40.92
Design No.		9	10	11	12	13	14	15	16
Porosity (%)	**Set 1**	9.58	34.38	9.38	33.80	11.16	35.15	9.31	33.83
	Set 2	9.75	33.68	10.23	34.13	9.68	35.08	9.69	35.77

porosity of the anode sintered at 1200°C was four times more than that sintered at 1350°C. The effect of the amount of graphite used as the pore former was shown to be significant, too. The porosity of the anode increased as the graphite amount increased within the experimental range.

Effect of the Sintering Temperature in Liquid-Phase Sintering

A comparison of the effect of the sintering temperatures on the densification of YSZ was made. Figure 5 shows the micrographs of the specimens sintering at 1000°C and 1100°C, respectively. From images in Figure 5(a) and (b) that were magnified to 20,000 times, it seems that both specimens that sintered at 1000 and 1100°C are fully sintered. From the images in Figure 2(c) and (d), which were taken at a lower magnification from the same specimens mentioned above, it is shown that there are still many pores over the samples. This set of images demonstrates that the densification at 1000°C and 1100°C did not make significant difference.

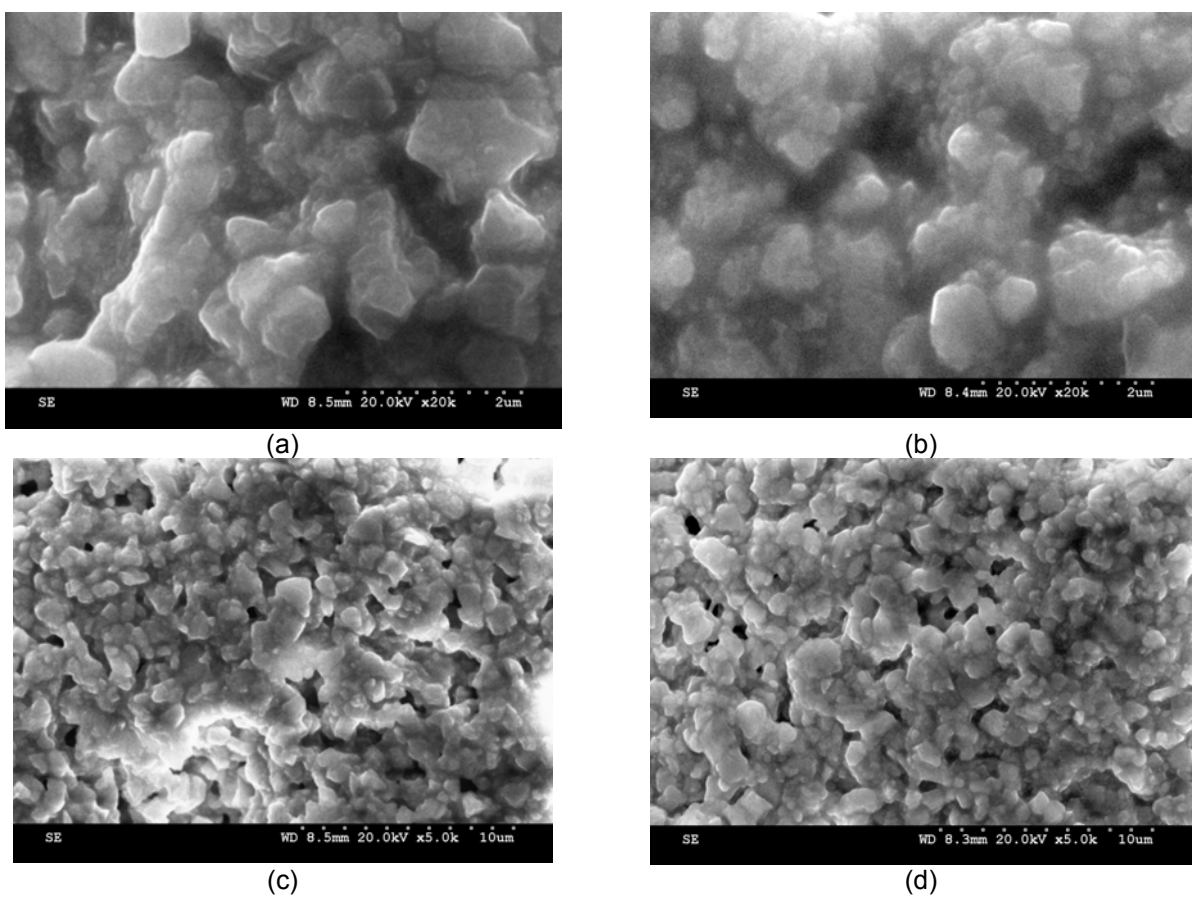

Figure 5. Micrographs of liquid-phase sintered YSZ with addition of 4.5 wt % of bismuth oxide sintered at different temperatures, (a) and (c) 1000°C; (b) and (d) 1100°C for 4 h.

Therefore, a temperature of 1000°C was chosen for all the sintering thereafter. On the other hand, this experiment revealed a potential to produce porous YSZ frame structure at lowered temperatures using liquid-phase sintering.

Effect of the YSZ Particle Size in Liquid-Phase Sintering

As is stated above, sintering experiments were conducted for the samples with substrate and coating layered structure. The substrate comprises YSZ particles of a larger size (–325 mash), while the coating consists of YSZ particles of mixed sizes. The purpose of doing it this way is to explore the possibility of producing a dense YSZ layer on a porous YSZ substrate using one liquid-phase sintering process. The knowledge of solid-state sintering advises that small particles have higher densification rates than the large particles during sintering because of two main reasons. First, large particles have lower packing density than the small particles. The material comprised with large particles needs more diffusion energy and time to reach densification than one with small particles. Secondly, small particles, especially nano particles, have higher chemical potentials than large particles. As a result, the material with small particles possesses higher diffusion rates than one with large particles. This will further enlarge the difference of the densification during sintering between materials with different particles sizes. These factors will also take effect in liquid-phase sintering.

Figure 6 shows the SEM images taken from the top and bottom surfaces of a coated specimen after liquid-phase sintering at 1000°C for 4 h. This observation proved that it is effective to produce dense coating on porous substrate by using different particle sizes in the two different parts of the structure during liquid-phase sintering. This method can be employed in production of SOFC sandwich structures, which will reduce the manufacturing cost substantially by simplifying the fabrication process and saving sintering energy.

Conclusions

Three cost-effective techniques used to produce SOFC components were investigated. In the EPD for preparation of YSZ electrolyte coatings, microstructure suggested that deposits obtained in the suspensions with ratio of ethanol to acac at about 1:1 outcome homogeneously packed green form that forms dense coatings after sintering even through depositions can be achieved in any of the mixing compositions. For the anode factorial experiments, the effects of these parameters were examined against the porosities of the sintered anode samples. The sintering temperature and graphite usage were found to have very significant effects, while the ratio of NiO/YSZ and the pressing pressure were found to have less significant effects on the porosity of the anodes. The effects are planned to be further analyzed by ANOVA. Experiments demonstrated that liquid-phase sintering is an energy-efficient process, and Bi_2O_3 is an effective low melting point material to perform liquid-phase sintering of YSZ.

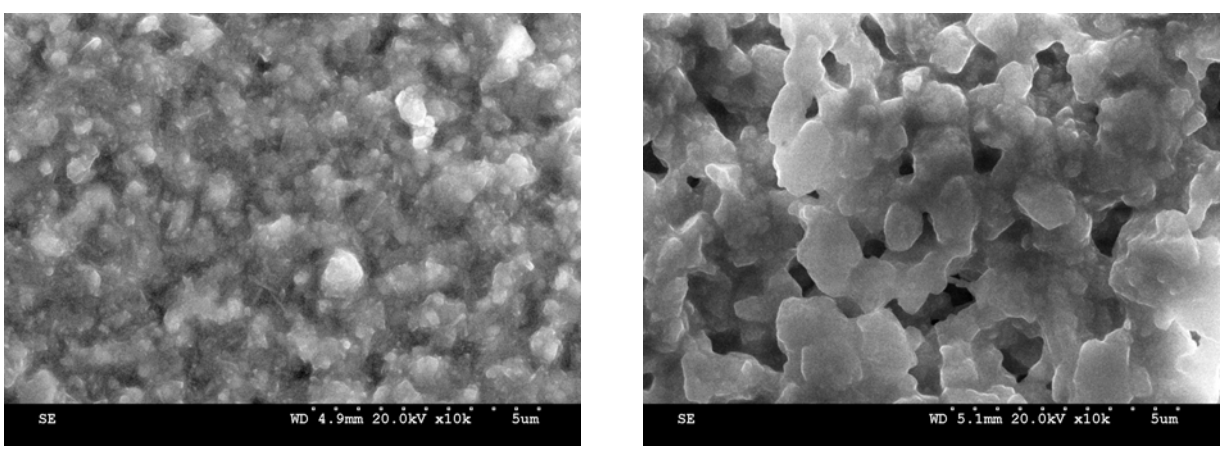

(a) (b)

Figure 6. Micrographs of the (a) coating and (b) substrate sintered at 1000°C for 4 h in liquid phase in one process.

References

1. S. C. Singhal, "Status of solid oxide fuel cell technology," In *Proceedings of the 17th Risø International Symposium on Materials Science: High Temperature Electrochemistry: Ceramics and Metals*," eds. F. W. Poulsen, N. Bonanos, S. Linderoth, M. Mogensen, and B. Zachau-Christiansen. Risø National Laboratory, Denmark, 123–138 (1996).

2. F. Tietz, F. J. Dias, D. Simwonis, and D. Stöver, "Evaluation of commercial nickel oxide powders for components in solid oxide fuel cells," *Journal of the European Ceramic Society,* **20**(8), 1023–1034 (2000).

3. G. Rietveld, P. Nammensma, and J. P. Ouweltjes, "Status of SOFC component development at ECN," In *Proceedings of the Seventh International Symposium on Solid Oxide Cells* (*SOFC-VII*), eds. H. Yokokawa and S. C. Singhal. *The Electrochemical Society Proceedings Series* (PV 2001-16), Pennington, New Jersey, 125–130 (2001).

4. R. N. Basu, C. A. Randall, and M. J. Mayo, "Fabrication of dense zirconia electrolyte films for tubular solid oxide fuel cells by electrophoretic deposition," *Journal of the American Ceramic Society,* **84**, 33–40 (2001).

5. T. Ishihara, T. Shibayama, H. Nishiguchi, and Y. Takita, "Nickel–Gd-doped CeO_2 cermet anode for intermediate temperature operating solid oxide fuel cells using $LaGaO_3$-based perovskite electrolyte," *Solid State Ionics,* **132**, 209–216 (2000).

6. J. W. Kim, A. V. Virkar, K. Z. Fung, K. Mehta, and S. C. Singhal, "Polarization effects in intermediate temperature, anode supported solid oxide fuel cells," *Journal of the Electrochemical Society*, **146**, 69–78 (1999).

7. P. Sarkar, X. Huang, and P. Nicholson, *J. Am. Ceram. Soc.*, **76**, 1055 (1993).

8. P. S. Nicholson, P. Sarkar, and X. Haung, *J. Mater. Sci.*, **28**, 6274 (1993).

9. C. E. Baumgartner, V. J. Decarlo, P. G. Glugla, and J. Grimaldi, *J. Electrochem. Soc*., **132**, 57 (1985).

10. C. R. Hicks and K. V. Turner, Jr., "Fundamental concepts in the design of experiments," *Oxford University Press*, 5th edition (1999).

Publications and Presentations

"Property Control of Cathodes and Anodes Produced by Slip Casting for Planar Solid Oxide Fuel Cells," *Ceramic Engineering and Science Proceedings*, **26**(4), 185–90 (2005).

"Influence of Processing Parameters on Porosity of NiO-YSZ Solid Oxide Fuel Cell Anode Material," *Ceramic Engineering and Science Proceedings*, **26**(4), 177–83 (2005).

"Exploration of Combustion CVD Method for YSZ Thin Film Electrolyte of Solid Oxide Fuel Cells," accepted for publication in *Mixed Ionic Electronic Conducting Perovskites for Advanced Energy Systems*, eds. N. Orlovskaya and N. Browning, Kluwer Academic Publication, 2005.

"Exploration of Electrophoretic Deposition of YSZ Electrolyte for Solid Oxide Fuel Cells," K8.2, *MRS Proceedings*, Volume **835**, eds. P. Knauth, C. Masquelier, E. Traversa, and E. D. Wachsman, December 2004.

E. NDE Development for Valve-Train Components for Diesel Engines

Jiangang Sun
Argonne National Laboratory
9700 South Cass Avenue
Argonne, IL 60439
630-252-5169; fax: 630-252-4798; e-mail: sun@anl.gov

DOE Technology Development Area Specialist: James J. Eberhardt
(202) 586-9837; fax: (202) 586-1600; e-mail: james.eberhardt@ee.doe.gov
ORNL Technical Advisor: D. Ray Johnson
(865) 576-6832; fax: (865) 574-6098; e-mail: johnsondr@ornl.gov

---

Contractor: Oak Ridge National Laboratory, Oak Ridge, Tennessee
Contract No.: DE-AC05-00OR22725
Subcontractor: Argonne National Laboratory, Argonne, Illinois

---

Objectives

- Develop laser-scattering and other nondestructive evaluation (NDE) methods for detection and characterization of surface and subsurface defect/damage in diesel-engine valve-train components made from advanced materials such as ceramics and intermetallics.
- Develop quantitative NDE analysis tools to identify strength-limiting flaws and failure mechanisms, evaluate damage evolution and growth, and predict mechanical properties for advanced materials.

Approach

- Develop fast and reliable automated laser-scattering NDE systems for surface/subsurface inspection of ceramic and intermetallic valves.
- Inspect valve surfaces to determine the level of machining damage and accumulated damages from bench or engine tests.
- Correlate NDE data with microstructure and strength of silicon-nitride specimens for prediction of fracture initiation defects and mechanical properties.

Accomplishments

- Successfully implemented a photomultiply tube (PMT) detector coupled with an optical fiber in a NDE valve-scan system. The PMT detector is more sensitive and more than six times faster in scan speed so it allows for fast NDE inspection of a large number of valves to meet the engine test schedule.
- Evaluated 25 finish-machined SN235P silicon nitride valves. Verified significant improvement in machined valve surfaces especially at keeper groove where a severe machining damage had caused a premature valve failure in a rig test.
- Inspected machined surfaces of 11 as-processed TiAl valves.
- Completed analysis and correlation of NDE data with microstructure and strength for cylindrical SN235P specimens machined at various conditions.

Future Direction

- Establish laser-scatter NDE detection sensitivity and characterization capability for surface damage in TiAl intermetallic specimens.
- Complete NDE evaluation for damage accumulation in prototype SN235P and TiAl valves by periodic inspections of these valves during planned engine duration tests.
- Develop quantitative image-processing methods for prediction of strength-limiting subsurface defects/damage in silicon nitride ceramics.

Introduction

Advanced ceramics and intermetallics are leading candidates for high-temperature engine applications that offer improved fuel efficiency and engine performance. Among them, silicon nitrides (Si_3N_4) and titanium aluminide (TiAl) are being evaluated as valve-train materials for diesel and natural gas engines because of their lighter weight and high strength and corrosion resistance at elevated temperatures. However, these materials are brittle so microscopic defect/damage near the surface may significantly degrade their mechanical properties. Material damage in the subsurface may be induced by machining or from service due to impact, wear, and corrosion. For silicon nitrides, material strength may also be limited by inherent defects such as voids and porosities within subsurface. To detect and characterize these defects, Argonne National Laboratory (ANL) developed a laser scattering NDE method to measure detailed surface/subsurface microstructure for these materials. The objective of this research is to demonstrate that this method can be used to assess/evaluate the cost-effectiveness and reliability of valve-train components manufactured from advanced ceramic and intermetallic materials for diesel engines. The primary effort in FY 2005 was to develop a fast NDE valve-scan system and to inspect finish-machined SN235P silicon nitride valves to determine the improvement in machined surface quality from their initial rough machining conducted in FY 2004. Another effort was directed on analysis and correlation of NDE data with microstructure and strength for cylindrical SN235P specimens machined at various conditions. This research is collaborated with Caterpillar, Inc.

Approach

The critical region for brittle ceramic and intermetallic components in structural applications is near surface. The common types of defects in this region are mechanical, such as cracks, spalls, inclusions, and voids. The size of the defects that limits the component strength is generally small, say ~100 μm. To detect these defects, a laser-scattering method based on cross-polarization detection of optical scattering originated from surface and subsurface microstructure can be used for noncontact, NDE of these materials. Because ceramics are partially translucent to light, optical penetration can reach the subsurface to directly interact with the subsurface defects. For metallic or intermetallic materials, optical penetration is not possible. However, using the cross-polarization detection approach, optical scattering from rough surface or open cracks can be significantly enhanced against the smoother background. By scanning the entire surface (flat or curved) of a component and constructing a two-dimensional (2-D) scatter image, surface/subsurface defects can be readily identified as they exhibit excessive scattering over the background, and their type and severity may be analyzed. To apply this technology for NDE of Si_3N_4 and TiAl valves, an automated laser-scatter system was developed by ANL for scanning the entire valve surface at high spatial resolutions. This system utilizes two-rotation and two-translation stages to align and focus the laser beam on the valve surface during the scan, and the resulting 2-D scattering image data are used to identify the location, size, and relative severity of subsurface defects/damage. Analysis of the NDE data can determine the statistical properties of the component surface, which can be correlated with machining or service conditions. Development of quantitative image-processing methods may lead to automated identification of strength-limiting defect/damage for prediction of mechanical properties.

Results

Development of a Fast Valve-Scan NDE System

Prototype silicon nitride and titanium aluminide valves have been planned for engine duration tests in FY 2006. Because of a large number (24) of valves to be used and a tight schedule for intermittent valve evaluation, the NDE system must be able to scan each valve at a fast speed to meet the engine test schedule. The previous valve-scan system was limited by the speed of a silicon detector; a photomultiplier tube (PMT) was therefore selected to replace the silicon detector for detection of back-scattered signal. The PMT detector has a data acquisition speed up to 20 kHz with 16-bit dynamic range, which is more than six times faster and more than five times higher in detection sensitivity than the silicon detector.

Figure 1 is a photograph of the new automated laser-scatter system. The system utilizes a multimode optical fiber to collect and deliver the back-scattered light to the PMT detector. A long translation stage was used to allow for scanning of entire valve surface (head and stem) within one pass. In addition, data acquisition software was modified to improve synchronization between data acquisition and stage motion along the valve profile. The improved system can scan the complex valve-head surface in an hour.

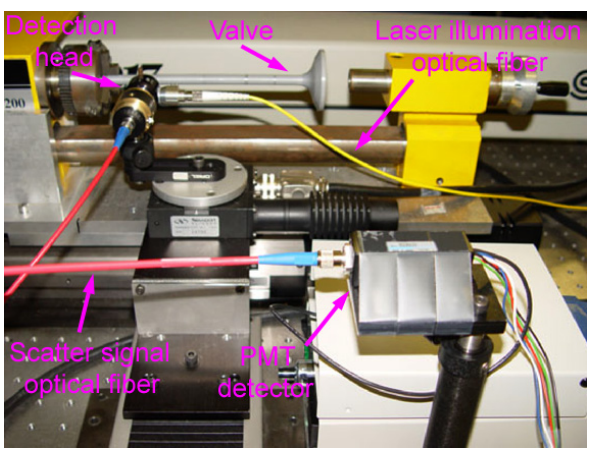

Figure 1. Photograph of automated laser-scattering NDE system.

Evaluation of Finish-Machined SN235P Valves

Twenty-five finish-machined SN235P silicon nitride valves were evaluated by the automated laser-scatter system. They are natural-gas intake and exhaust valves to be used by Caterpillar Inc. in an engine duration test. These valves were initially machined in FY 2004. Because of a process error, most of the valve head and keeper-groove surfaces were rough machined, resulting in significant machining damage on these surfaces.[1] NDE data of the finish-machined valves were compared with those of initial machined to verify improvement in machined surfaces.

Figures 2 and 3 show, respectively, laser-scatter images of SN235P natural-gas intake valve No. 8 at before and after the finish machining. Spatial resolution in both scan directions was ~10 µm. In Figure 2, significant machining damage can be found on the entire valve head surface except the stem surface near the bottom of the image. These damages are seen as bright lines (of higher scattering intensities) along the machining direction, as shown in the detailed image in Figure 4(a). The lengths of the machining damage are typically near 1 mm. In

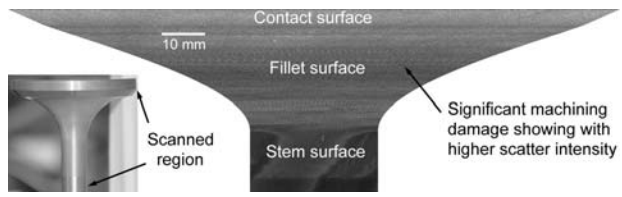

Figure 2. Laser-scatter scan image of SN235P valve 8 after initial rough machining.

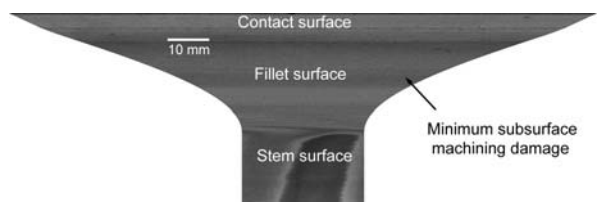

Figure 3. Laser-scatter scan image of SN235P valve 8 after finish machining.

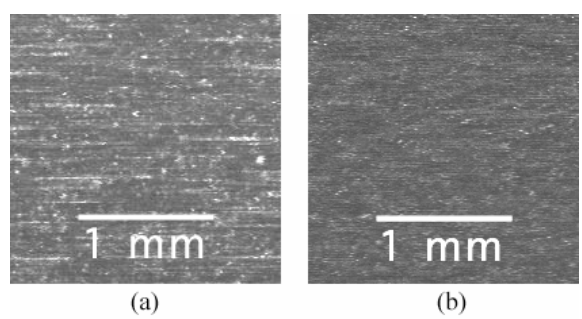

Figure 4. Detailed laser-scatter images in contact surface of SN235P valve 8 after (a) initial rough machining and (b) finish machining.

addition, the overall optical scatter intensity of the valve-head surface is high, indicating a higher level of overall damage. In comparison, the finish-machined surface shows minimum machining-damage indications as seen in Figure 3 and the detailed image in Figure 4(b). The higher scatter-intensity spots in Figures 4(a–b) come from material inherent defects such as porosities with sizes typically smaller than 50 μm. Therefore, it is apparent that the finish machining essentially removed all machining damages induced in the initial rough machining of these SN235P valves.

Laser scattering scan was also conducted in the keeper groove region of the SN235P valves. Before the finish machining, a severe machining damage was found around the entire circumference of the keeper-groove edge, which caused premature failure of a SN235P valve in a rig test.[2] In the finish-machined valves, this damage was also removed. However, because the edges are still sharp, some chip damage can be detected along the keeper-groove edges. Figure 5 shows detected edge chips in a laser-scatter image and photomicrographs.

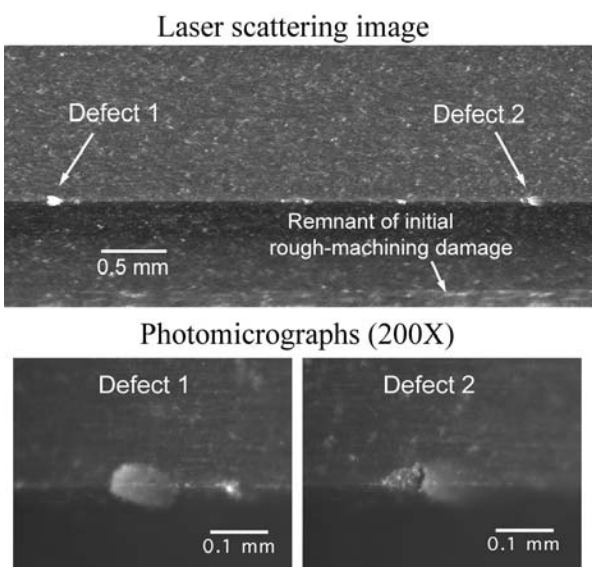

Figure 5. Detailed laser-scatter image and photomicrographs of chip flaws at keeper groove edge of a SN235P valve.

Inspection of As-Processed TiAl Valves

Eleven as-processed TiAl intermetallic valves were inspected by the valve-scan NDE system. Figure 6 shows a laser-scatter image of a typical TiAl valve-head surface. Spatial resolution in both

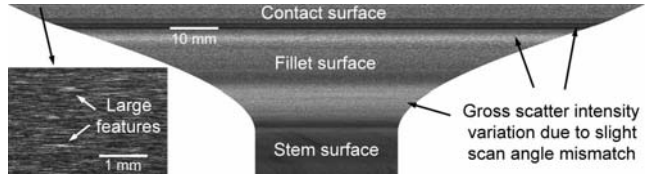

Figure 6. Laser-scatter scan image of an as-processed TiAl valve.

scan directions was ~10 μm. Because intermetallic surface is highly reflective to light and the surface mismatch during the scan can cause gross change in measured scatter intensity, especially at regions with sharp curvatures as seen in Figure 6. The enlarged image in Figure 6 shows machining marks; the nature of these marks will be further investigated.

Laser scatter scans were also performed for the joint region between the TiAl stem and the titanium alloy (Ti-6V-4Al) stem. Figure 7 presents a typical scan image of the joint surface, which shows clearly the joint line and no apparent defect. The image also shows axial stripes along the machining direction in this region; the nature of these stripes will be further studied.

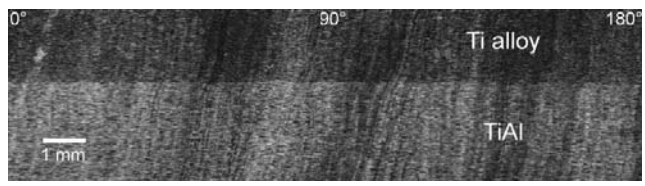

Figure 7. Laser-scatter scan image of joint surface of a TiAl valve.

Correlation of NDE Data with Microstructure and Strength

Three sets of 32 cylindrical SN235P silicon nitride specimens machined by two vendors at various conditions were initially examined by laser scatter in FY 2004. After fracture test, eight specimens were further studied for correlation of the NDE data with material microstructure and strength. In the microstructure study, fractographic examinations were performed to identify the fracture sites on the fracture surfaces. These fracture sites were then mapped into the tensile (or cylinder) surface to locate the fracture initiation positions. As expected, each fracture initiation position corresponds to a defect detected in the laser scatter NDE data. The results for all eight SN235P specimens are summarized in Figure 8, which shows the fracture strength of each specimen and its corresponding fracture

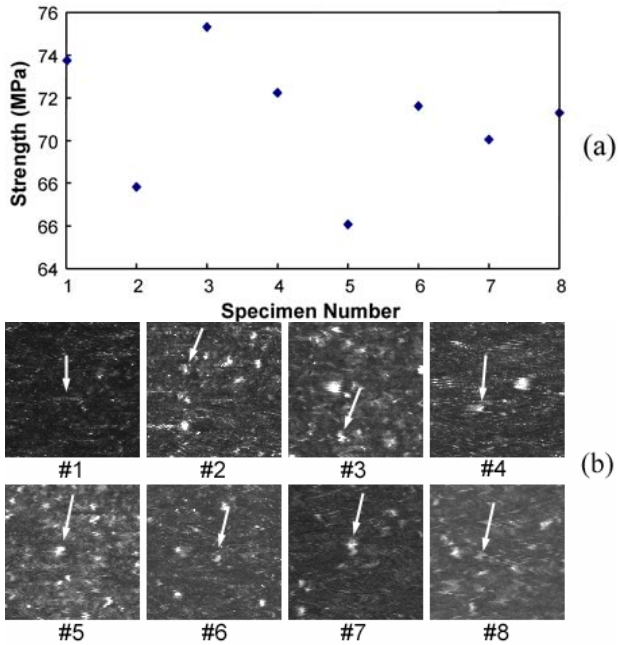

Figure 8. (a) Fracture strength and (b) corresponding fracture origins in scattering images (image size is 0.5 mm × 0.5 mm) of eight ground rods.

origin in the scanning image. It is clear that all specimens fractured from inherent material flaws (high-porosity defects), except specimen 1, which fractured from a machining damage (likely a lateral machining crack). The lowest fracture strength occurred in specimens 2 and 5. For specimen 2, there are a group of material flaws along the fracture line, which may explain its low fracture strength. As for specimen 5, its fracture origin is more intensive (likely deeper flaw) and slightly bigger (~35 μm) than those of the other specimens (~25 μm); therefore, its strength is lower.

Statistical parameters of laser scatter data were correlated with fracture strength. These statistical parameters include standard deviation, skewness, skewness/standard deviation, and coefficient of variance Cv (standard deviation/mean). Figure 9 shows fracture strength as functions of statistical parameters for the eight specimens. The standard deviation and skewness in Figures 9(a–b) generally correlate well with the fracture strength. Both show a similar trend, that is, strength decreases with the increase of standard deviation or skewness. These results are physically reasonable. Because standard deviation represents the second-order and skewness the third-order difference of local scatter intensity from the

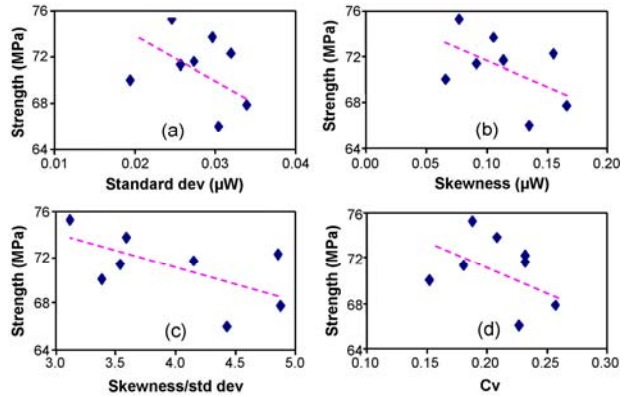

Figure 9. Correlation of fracture strength with statistical parameters processed from laser-scatter data around fracture regions.

background, a higher standard deviation or skewness indicates the presence of severe subsurface damages/defects that generate higher scattered light intensity above the background. Note that the nondimensional parameters skewness/standard-deviation and Cv in Figures 9(c–d) also show the same trend. These nondimensional parameters can be good candidates for predicting the fracture strength.

Conclusions

A high-speed automated laser-scatter system was developed. It utilizes a PMT detector coupled with an optical fiber for collecting and delivering scatter signal. The PMT detector is more sensitive and more than six times faster in data acquisition than a silicon detector. With this new system, scanning of a complex valve-head surface will be reduced to about an hour, which allows for fast NDE inspection of large number of valves to be evaluated in engine duration tests scheduled for FY 2006.

Twenty-five finish-machined SN235P silicon nitride valves and eleven as-processed TiAl valves were inspected by the valve-scan system. The SN235P valves had been rough-machined in FY 2004, which induced significant machining damage on the valve surface. In particular, a severe damage at keeper groove caused premature failure of a valve in a rig test. Laser-scatter examination verified that there is a significant improvement in the surface quality of these finish-machined valves, that is, most rough-machining damages were removed although minor chip damages were detected on the edges of keeper grooves. For the as-processed TiAl valves, because intermetallic surface is highly

reflective to light and the surface scatter is weak, it was challenging to align the laser-scatter system with the valve profile during the entire scan. Nevertheless, laser scatter images were obtained for the valve-head and stem-joint surfaces for these valves, and machining marks and material variation can be readily observed. However, correlation of NDE data with surface microstructure for TiAl materials need to be further investigated.

Laser scatter measurements were conducted for three sets of 32 cylindrical SN235P silicon nitride specimens that were machined at different conditions. After fracture test, eight of these specimens were delivered to ANL for correlation of NDE data with microstructure and strength. In microstructure study, fractographic examinations were performed to identify the fracture sites that were then correlated with NDE data to locate fracture initiation defects on tensile surfaces of the specimens. The correlation allowed for direct determination of the size, severity, and type of defect/damage that caused the fracture. The fracture strength was also correlated with statistical parameters of laser scatter NDE data. These statistical parameters included standard deviation, skewness, skewness/standard deviation, and coefficient of variance (standard deviation/mean). It was found that strength decreases as these parameters increase; which is physically meaningful because these parameters become larger when the number or severity of defects increases.

References

1. J. G. Sun, "NDE Development for Ceramic Valves for Diesel Engines," *Annual Report for FY 2004, Heavy Vehicle Propulsion Materials Program*.

2. J. S. Trethewey, "High-Temperature Advanced Materials for Lightweight Valve Train Components," *Annual Report for FY 2004, Heavy Vehicle Propulsion Materials Program*.

Presentations and Publications

J. G. Sun, J. M. Zhang, J. S. Trethewey, J. A. Grassi, M. P. Fletcher, and M. J. Andrews, "Nondestructive Evaluation of Machining and Bench-Test Damage in Silicon-Nitride Ceramic Valves," in *Ceramic Eng. Sci. Proc*., eds. D. Zhu and W. M. Kriven, **26**(2), 127–132 (2005), and presented at the 29th International Cocoa Beach Conference and Exposition on Advanced Ceramics & Composites, Cocoa Beach, Florida, January 23–28, 2005.

J. M. Zhang, J. G. Sun, M. J. Andrews, A. Ramesh, J. S. Trethewey, and D. M. Longanbach, "Characterization of Subsurface Defects in Ceramic Rods by Laser Scattering and Fractography," paper accepted for publication in the *Proceeding of the 32nd Annual Review of Progress in Quantitative Nondestructive Evaluation, Bowdoin College, Brunswick, Maine, July 31–August 5, 2005*.

F. Durability of Diesel Engine Component Materials

*Peter J. Blau, Jun Qu, and John J. Truhan, Jr.**
Oak Ridge National Laboratory
P.O. Box 2008, Mail Stop 6063
Oak Ridge, TN 37831-6063
(865) 574-537; fax: (865) 574-6918; e-mail: blaupj@ornl.gov

**University of Tennessee, Knoxville*

DOE Technology Development Area Specialist: James J. Eberhardt
(202) 586-9837; fax: (202) 586-1600; e-mail: james.eberhardt@ee.doe.gov
ORNL Technical Advisor: D. Ray Johnson
(865) 576-6832; fax: (865) 574-6098; e-mail: johnsondr@ornl.gov

Contractor: Oak Ridge National Laboratory, Oak Ridge, Tennessee
Contract No.: DE-AC05-00OR22725
Subcontractor: University of Tennessee, Knoxville, TN

Objectives

- Provide test data, analyses, and models that enable the use of durable, lower-friction moving parts in diesel engines in heavy-vehicle propulsion systems.
- Develop test methods that simulate the environment of scuffing-prone engine parts.
- Conduct structural and tribological characterizations of promising new materials, surface treatments, composites, and coatings.

Approach

- Identify and focus on diesel engine components that require durability and low-friction behavior and might benefit from advanced materials. These include (a) wastegate bushings for exhaust gas recirculation (EGR) components and (b) fuel injector components.
- Identify materials, coatings, and/or surface treatments that have the potential to increase the durability of the selected engine components.
- Develop test methods to evaluate and quantify the performance of candidate materials under simulated use conditions.
- Develop graphical methods and models to portray the effects of operating parameters, like speed, load, and surface finish, on the scuffing response of the materials.

Accomplishments

- Designed, built, and used a high-temperature oscillatory scuffing test system that operates at wastegate bushing temperatures (~600–700°C).
- Published results of tests on a range of metallic alloys, ceramics, and coatings to determine which of these had the best durability under high-temperature conditions.
- Developed a novel, ‘pin-on-twin’ scuffing test to evaluate fuel injector materials in diesel fuel and low-sulfur fuel environments.

- Developed criteria for the onset of scuffing damage and evaluated traditional steel fuel injector materials as well as ceramics, advanced cermets, and hard coatings in diesel fuel and low-sulfur fuel. Represented results in terms of 'scuffing maps' and transition diagrams.
- Developed a model for scuffing tendency that considers lubricant characteristics and solid material characteristics. Prepared a final report that explains the model and its rationale.

Future Direction

- The focus on fuel systems and exhaust gas recirculation (EGR) components ended in FY 2005. It will be succeeded by a new effort that focuses on valve train durability issues.

Introduction

The diesel engine industry continues to face the important challenge of improving fuel efficiency while meeting increasingly strict emissions regulations. These challenges are being addressed by modifying engine designs and control systems and by developing exhaust gas after-treatments. Such modifications affect the mechanical, thermal, and chemical environments in which the engine materials must operate, and currently used materials may fall short of meeting these needs. New materials are needed to enable new technological goals.

The objective of this effort is to enable the selection and use of durable, lower-friction moving parts in diesel engines for heavy-vehicle propulsion systems through the systematic evaluation of promising new materials, surface treatments, composites, and coating technologies. The current approach involves developing test methods, analyzing microstructures of candidate materials, developing design maps with variables like surface finish and frictional behavior, and modeling the damage process itself. The focus on exhaust gas recirculation (EGR) components and fuel injector plungers was based on discussions with diesel engine manufacturers. Before developing tests to evaluate materials for improved durability, it was necessary to conduct a tribosystem analysis to understand the conditions under which the surfaces of these components operate in a diesel engine. The nature of contact damage on engine components was reviewed to ensure that laboratory test methods would adequately reproduce that kind of damage. Then suitable tests were developed, surface damage and friction data were analyzed, and modeling tasks were undertaken.

Approach

In FY 2001, and based on the definition of several key durability problems, a test method and apparatus were developed to study the high-temperature friction and wear characteristics of candidate EGR system materials. That methodology has seen continued use for evaluating metal alloys, ceramics, coatings and other experimental materials for moving parts in waste gate bushings. In FY 2002, the effort was extended to include an investigation of the scuffing of fuel injector component materials. Laboratory tests were developed and refined to produce and measure the type of fine-scale surface damage that is observed in fuel system parts. In FY 2003, research continued in two areas: (1) evaluating the effects of diesel fuel sulfur reductions on scuffing and (2) identifying materials and coatings for high-temperature scuffing resistance in EGR components. During FY 2004, a three-dimensional 'scuffing map' was developed to depict conditions for scuffing initiation and propagation in time and space domains. By the end of FY 2004 a new scuffing model, one that integrates boundary film characteristics with material properties, had been proposed. The model recognizes the complexities of reciprocating sliding in which velocity is continually changing and the direction of motion reverses periodically. In FY 2005 the model was refined and improved to consider optimization of surface finish and the role of abrasion in reducing the tendency for materials to adhere to one another.

Results

The results presented here are an abbreviated version of a more detailed final report. A milestone

report, dated March 2004, described the reciprocating sliding experiments in which results led to the conceptual framework for the three-regime model for scuffing. That model considers the failure of a lubricating film and the increased deformation of the contact surfaces to produce progressively severe surface damage. It represents an interdisciplinary approach and integrates concepts from both lubrication theory and materials science. The model, schematically shown in Figure 1, uses three submodels whose applicability depends on whether the contact is effectively lubricated (solid surfaces that are not touching), boundary-lubricated, or subjected to significant solid contact and plastic deformation. The higher the contact pressure, the less likely the lubricant will effectively separate the moving surfaces and the other regimes will come into play.

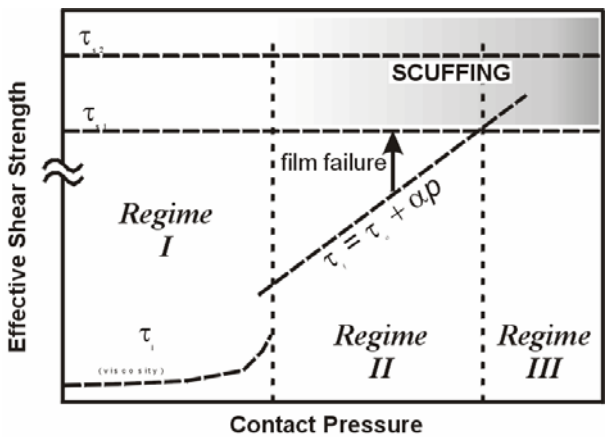

Figure 1. The scuffing model can be represented in three distinct regimes depending on the relative roles played by the liquid lubricant (I), thin boundary films (II), and the contacting solids (III).

Conceptually, the horizontal axis, labeled 'Contact Pressure' in Figure 1, can also be used to represent time. First, there is a period of effective operation whose duration depends on the nature of the materials, mechanical design and operating parameters, surface finish, and the regime of lubrication. Parts can perform very effectively in Regime I for millions of cycles if all goes well. However, the system can also operate in a boundary lubrication regime (II) in which some contact occurs.

As components and lubricants age, or if the contact pressure is too large to sustain a full film condition, then Regime I may either be finite in length or not observed at all, and the system may find itself in Regime II, which is governed by the thin boundary films that form from species initially present in the lubricant (or fuel). One can indirectly monitor the stability of the shear strength of interfacial films by observing the time-dependence of the friction coefficient. If the duration of contact is expressed in terms of numbers of oscillating cycles, as in a fuel injector plunger, then the transition from Regime I to Regime II can be expressed as follows:

$$\mu_x = \mu_{ff} + \Delta\mu\left(\frac{x}{L}\right)^n \quad , \qquad (1)$$

where μ_x = friction coefficient at x cycles, μ_{ff} = friction coefficient for full-film lubrication, $\Delta\mu$ = the change in friction during the transition from full-film to boundary lubrication, x = current number of oscillating cycles, L = number of cycles to reach Regime II, and n = a constant that reflects the rate of change during the transition period. In Eq. (1), the change in friction during the transition is simply

$$\Delta\mu = \mu_{bl} - \mu_{ff} \quad , \qquad (2)$$

where μ_{bl} = the friction coefficient for boundary lubrication at the start of Regime II. Assigning typical values of $\mu_{ff} = 0.01$, $\mu_{bl} = 0.12$, and letting L = 1,000,000 cycles, we can plot Eq. (1) for a finite life in Regime I for several values of n (see Figure 2). The greater the magnitude of the rate constant (n), the longer is the incubation period, but the more rapid the transition.

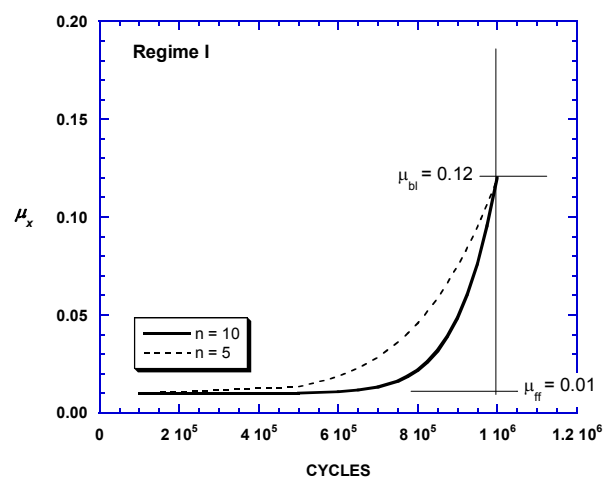

Figure 2. Portrayal of a finite-length Regime I with various transition rates.

Physically, the exponent n in Eq. (1) reflects such processes as a loss in lubricant load carrying capacity from oxidation or degradation of the additive package (in closed systems), a change in the contamination level in the system due to debris buildup or contaminant entrainment, or even phase-transformation-induced swelling of the plunger material to reduce bore clearance and increase surface contact. The referenced final report describes a second submodel for the localized changes in the composite surface roughness of the contact as scuffing initiates and propagates from the ends of the reciprocating stroke to its midpoint.

A smooth, hard material may work very well sliding against a soft counterface as long as the adhesion of the latter can be mitigated by a lubricating boundary film. That can only happen if there is sufficient clearance in the plunger bore to enable the formation of such a film.

Light abrasion can prevent the buildup of adhesive patches (transfer layers). In the absence of significant adhesion (reduced by lubrication), a factor that indicates the tendency for abrasion (AT) can be defined as

$$\mathrm{AT} = S\frac{H_h}{1.2H_s} \quad , \qquad (3)$$

where H_h = the scratch hardness of the harder side, H_S, = the scratch hardness of the softer side, and S = the deviation from the optimal roughness. The factor 1.2 enters because of classic work by David Tabor (ca. 1951) on hardness that suggests for many materials, there must be about 20% difference in hardness in order for abrasion to occur. The deviation from the optimum surface roughness can be defined as

$$S = \left|R_h - R_{opt}\right|^m \quad , \qquad (4)$$

where R_h = the roughness of the harder surface, R_{opt} = the optimal roughness (determined by experiments), and m = a weighting factor for the importance of this function Reciprocating scuffing test data for a series of materials were used to evaluate scuffing based on the foregoing relationships. This work showed an optimal roughness of about 0.07 μm for the given tribosystem and indicated values for the time to initiate scuffing.

The AT parameter is plotted vs the initiation period for various materials against 52100 steel (including zirconia, TiN hard coatings, Ni_3Al bonded cermets, and 52100 steel itself) in low-sulfur fuel in Figure 3. A linear fit to the data, excluding the self-mated steel, was quite good (R = 0.931). The implications of the relationship may initially seem counterintuitive because the more abrasive (i.e., the higher the AT parameter), the longer the period for the onset of scuffing. Closer consideration of the physical situation, however, suggests that scuffing is controlled by adhesive processes, and if abrasion of the surface prevents the formation of adhesive bonds, then a small amount of abrasion can in effect retard the onset of scuffing. Adhesion is promoted by self-mated materials, like the case for 52100 steel, and therefore, the circled data in Figure 3 show a markedly reduced resistance to the onset of scuffing. Adhesion also promotes the transfer of soft material than can fill up valleys in the surface that might otherwise serve as lubricant reservoirs. While a modicum of abrasion may be good for scuffing reduction, too much abrasion could result in an unacceptably high degree of abrasive wear damage and an unacceptable loss of clearance between mating parts. Therefore, there must be a balance between effective boundary lubrication and the light abrasiveness of optimally rough surfaces to avoid adhesive contact.

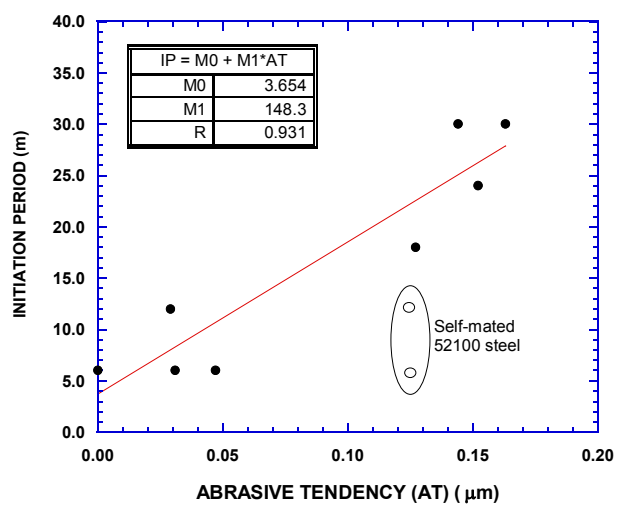

Figure 3. Relationship between the AT parameter and the initiation period for scuffing in reciprocating sliding in Jet A, low-sulfur fuel.

Summary and Conclusions

- The 3-D friction-scuffing maps can be developed to depict scuffing initiation in both time and space domains. These maps can be used to construct scuffing transition diagrams that correlate scuffing resistance to surface finish and sliding velocity.
- Current and candidate fuel injector material combinations seem to exhibit an optimum surface finish (neither too smooth nor too rough), which can extend the times to initiate and propagate scuffing damage. The optimum surface finish is a function of the geometric conditions, the normal load, the characteristics of the fluid film that is trapped in the valleys of the surface roughness, and the adhesion characteristics of the mating surfaces.
- Abrasion can play a subtle role in avoiding adhesive junction formation. Therefore, harder/softer material combinations (like zirconia on steel) can be successful in scuffing-sensitive applications. That works if the surface finish is optimized and abrasion is kept to a minimum.
- A new scuffing model was developed and reported.

Presentations and Publications

P. J. Blau, "Challenges for the application of engineered surfaces to tribosystems with multiple contact modes," invited presentation at the symposium on Integrated Surface Engineering, ASME/STLE Tribology Conference, Ponte Vedra, Florida, October 28, 2003.

P. J. Blau, J. J. Truhan, and J. Qu, "*Scuffing Transition Diagrams for Fuel Injection System Materials*, Project Milestone Report, Oak Ridge National Laboratory, Oak Ridge, Tennessee, March 2004.

P. J. Blau, J. Qu, and J. J. Truhan, *On the Definition and Mechanisms of Scuffing in Fuel System Components—An Integrated Process Model*, Project Milestone Report, Oak Ridge National Laboratory, Oak Ridge, Tennessee, September 2004.

J. Qu, J. J. Truhan, and P. J. Blau, "Detecting the Onset of Localized Scuffing with the Pin-on-Twin Fuel-Lubricated Test for Heavy Duty Diesel Fuel Injectors," *SAE International Journal of Engine Research*, **6**(1), 1–9 (2005).

J. Qu, J. J. Truhan, and P. J. Blau, "Evaluating Candidate Materials for Heavy Duty Diesel Fuel Injectors Using a 'Pin-On-Twin' Scuffing Test," *Tribology International*, **38**(4), 381–390 (2005).

P. J. Blau, J. Qu, and J. J. Truhan, "A Multi-Stage Model for Scuffing of Reciprocating Components with Special Consideration of Fuel Injector Plungers," Oak Ridge National Laboratory, Oak Ridge, Tennessee, September 30, 2005 (in press).

G. Life Prediction of Diesel Engine Components

H. T. Lin, T. P. Kirkland, and A. A. Wereszczak
Oak Ridge National Laboratory
P.O. Box 2008, MS-6068
Oak Ridge, TN 37831-6068
(865) 576-8857; fax: (865) 475-6098; e-mail: linh@ornl.gov

Jeremy Trethewey and Craig Habeger
Caterpillar, Inc.
Peoria, IL 61656-1875
(309) 578-0056; fax: (309) 578-2953; e-mail: trethewey_jeremy@cat.com

DOE Technology Development Area Specialist: James J. Eberhardt
(202) 586-9837; fax: (202) 586-1600; e-mail: james.eberhardt@ee.doe.gov
ORNL Technical Advisor: D. Ray Johnson
(865) 576-6832; fax: (865) 574-6098; e-mail: johnsondr@ornl.gov

---

Contractor: Oak Ridge National Laboratory, Oak Ridge, Tennessee
Contract No.: DE-AC05-00OR22725
Subcontractor: Caterpillar, Inc., Peoria, Illinois

Objective

- Generate a database and characterize damage mechanisms of candidate advanced ceramics and intermetallic alloys.
- Apply and verify probabilistic life prediction and component design and verification methods for advanced diesel engine components.

Approach

- Evaluate the dynamic fatigue, rotary bending fatigue, and high-temperature fatigue and creep performance of candidate silicon nitride ceramics and TiAl alloys at elevated temperatures in air before and after long-term exposure to simulated engine environments, as well as engine field tests.
- Characterize the evolution and role of damage mechanisms, and changes in microstructure and chemistry, linked to the long-term mechanical performance and reliability of ceramics and intermetallic alloys.
- Predict the failure probability and reliability of complex-shaped diesel engine components subjected to application conditions via the use of life prediction codes.

Accomplishments

- Completed development of a dynamic fatigue database at elevated temperatures up to 1000°C in air for a commercial-grade silicon nitride, SN147-31E, acquired from Ceradyne, Inc.
- Completed characterization of the mechanical strength and microstructure for 16 prototype NT551 silicon nitride exhaust valves, as well as half-cylindrical valve stems, after a 500-h bench rig test at Caterpillar.
- Completed dynamic fatigue studies for diesel particulate filter (DPF) material at elevated temperatures in air.

Future Direction

- Characterize the retained mechanical properties and microstructure of Kyocera SN235P silicon nitride and TiAl exhaust valves designed for a Caterpillar natural gas engine after a field test, and verify the probabilistic component design and life prediction.
- Develop a static fatigue performance database at elevated temperature for specimens extracted from DPF substrates for long-term mechanical reliability and life prediction.
- Develop a high-temperature tensile creep and step-stress rupture database of TiAl alloys for probabilistic component design and life prediction for diesel exhaust valve and turbine wheel component application.
- Develop a mechanical database for biaxial discs extracted from TiAl turbine wheel airfoils to verify probabilistic component design and life prediction.

Introduction

There has been considerable interest in the potential for extensive use of advanced ceramics and intermetallic alloys in advanced diesel engine systems because of their superior thermomechanical properties at elevated temperatures. The implementation of components fabricated from these advanced materials would lead to significant improvement in engine efficiency and long-term durability and reduced nitrogen oxides (NO_x) and CO exhaust emissions as required in the 21st Century Truck Program. Interest has focused primarily on research into characterization and design methodology development (life prediction) for advanced silicon nitride ceramics and TiAl alloys to enable the manufacture of consistent, reliable complex-shaped components for diesel engine. The valid prediction of mechanical reliability and service life is a prerequisite for successful use of these materials in internal combustion engine components.

This research project has three primary goals: the generation of a mechanical engineering database, from ambient to high temperatures, of candidate advanced materials before and after exposure to simulated engine environments; the microstructural characterization of failure phenomena in these advanced materials and in components fabricated from them; and the application and verification of probabilistic life prediction methods using diesel engine components as test cases. For all three stages, results will be provided to both material suppliers and component end-users for use in refining and optimizing processing parameters to achieve consistent mechanical reliability, and in validating the probabilistic design and life prediction of engine components made from these advanced materials.

Approach

All flexural test specimens were longitudinally or transversely machined according to ASTM standard C1161 from production billets purchased from material suppliers and diesel engine components acquired from end-users.[1] Flexure testing was conducted in ambient air in a 4-point-bending apparatus using 20/40-mm, α-SiC, semi-articulating fixtures at temperatures ranging from 20 to 1000°C and at stressing rates of 30 MPa/s and 0.003 MPa/s. The 30-MPa/s test condition was chosen to evaluate the inert characteristic strength as a function of temperature, while the 0.003-MPa/s test condition was chosen to measure the change in slow crack growth (SCG) susceptibility at elevated temperatures. The dynamic fatigue tests were carried out per ASTM C1465 (Ref. 2). Pneumatic actuators were programmed with a PC to produce the desired loading rate (and corresponding stressing rate). Load was continuously measured as a function of time, and flexure strength was calculated using ASTM C1161. The accumulated strength data were then further analyzed. The strengths for each test set were fit to a two-parameter Weibull distribution using the program CERAMIC,[3] which uses maximum likelihood estimation as advocated in ASTM C1239 (Ref. 4). Reported results are uncensored because fractography analysis was not conducted in detail to identify strength-limiting flaws for all of the bend bars tested. Following the dynamic fatigue test, both optical and scanning electron microscope analysis were carried out on fracture surfaces and polished cross-sections of selected bend bars to characterize the fracture and degradation mechanisms. X-ray analysis was also carried out to evaluate the possible phase changes resulting from oxidation during dynamic fatigue tests or after long-term exposure to

simulated engine environments, which could possibly cause degradation in mechanical performance and reliability.

Results

Dynamic Fatigue Response of Ceradyne SN147-E Silicon Nitride

Studies were completed of the dynamic fatigue behavior of a commercial-grade silicon nitride—SN147-31E, manufactured by Ceradyne Advanced Ceramic, Inc., CA—at temperatures of up to 1000°C in air. The SN147-31E has been processed with oxide sintering additives (i.e., Al_2O_3 and Y_2O_3) and contains a crystalline secondary phase achieved by proprietary post–heat treatment. The SN147-31E silicon nitride test specimens were longitudinally and transversely machined per the revised ASTM C1161 standard with a 600-grit surface finish.[1] The dynamic fatigue tests were carried out at 20 and 850°C and at stressing rates of 30 and 0.003 MPa/s in air per ASTM C1465 (Ref. 2). The 30 MPa/s rate is used to evaluate the inert characteristic strength as a function of temperature, and 0.003 MPa/s is applied to measure the slow crack growth (SCG) susceptibility at temperatures. Limited samples were also tested at 1000°C and at 30 MPa/s to evaluate high-temperature application limits and changes in life-limiting processes. The upper temperature limit in a diesel engine environment is about 850°C.

Dynamic fatigue results at 30 MPa/s showed that the transversely machined SN147-31E silicon nitride exhibited little or no decrease in characteristic strength at temperatures up to 1000°C compared with those obtained at 20°C (as shown in Table 1).

Also, the SN147-31E samples exhibited higher Weibull moduli at elevated temperatures than at 20°C, indicative of a change in strength-limiting flaws as a function of test temperature. On the other hand, mechanical results at 850°C indicated that there is an apparent decrease in characteristic strengths (about 19%) when tested at 0.003 MPa/s. In addition, the fatigue exponent of transversely machined SN147-31E decreased from 338 at 20°C to 39 at 850°C, indicative of an increased susceptibility to SCG processes at high temperature (Figure 1). The decrease in dynamic fatigue exponent value at elevated temperatures could be attributed to the change in material state (e.g., softening of secondary phase), as seen in the case for the GS44 silicon nitride.[5] The low fatigue exponent obtained for SN147-31E at elevated temperatures suggests that the secondary phase was not

Table 1. Summary of uncensored Weibull and strength distributions for Ceradyne SN147-31E silicon nitride specimens longitudinally and transversely machined per ASTM C1161. Data for SN147-31N machined longitudinally as well as transversely are used for reference

Material	Number of specimens tested	Stressing rate (MPa/s)	Temperature (°C)	Uncens. Weibull modulus	± 95% uncens. Weibull modulus	Uncens. char. strength (MPa)	± 95% uncens. char. strength (MPa)
SN147-31N-Long	15	30	20	21.73	14.07. 31.09	836	814, 858
SN147-31N-Long	15	30	850	20.35	13.58, 28.20	777	755, 799
SN147-31N-Long	15	0.003	850	16.19	10.57, 23.02	732	706, 757
SN147-31N-Trans	15	30	20	13.76	8.96, 19.59	677	649, 705
SN147-31N-Trans	15	30	850	18.26	11.67, 26.47	639	619, 659
SN147-31N-Trans	15	0.003	850	19.95	12.83, 28.63	620	602, 638
SN147-31E-Long	15	30	20	17.30	10.86, 25.58	668	645, 690
SN147-31E-Long	15	0.003	20	16.19	10.60, 22.98	620	598, 642
SN147-31E-Long	15	30	850	9.36	6.01, 13.62	604	567, 641
SN147-31E-Long	15	0.003	850	12.06	7.70, 17.52	509	485, 533
SN147-31E-Long	15	30	1000	16.49	10.61, 23.66	585	564, 605
SN147-31E-Trans	15	30	20	7.44	4.89, 10.58	623	575, 671
SN147-31E-Trans	15	0.003	20	8.99	5.61, 13.45	607	568, 646
SN147-31E-Trans	15	30	850	43.94	28.37, 62.78	642	634, 651
SN147-31E-Trans	15	0.003	850	18.02	11.93, 25.18	521	505, 538
SN147-31E-Trans	15	30	1000	34.66	21.97, 50.70	602	591, 611

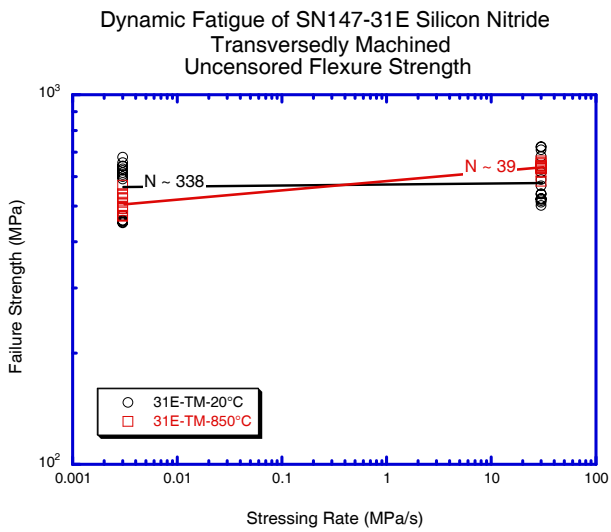

Figure 1. Failure strength versus stressing rate curve of SN147-31E transversely machined and tested at 20 and 850°C in air.

completely crystallized, and thus the post–heat treatment procedure needs to be refined to ensure high-temperature mechanical performance and reliability.

Mechanical Characterization of NT551 Silicon Nitride Exhaust Valves

Mechanical strength testing was conducted on 16 NT551 silicon nitride valves (14 with 30° and 4 with 45° valve seat angles) after testing on a 500-h bending rig at Caterpillar. In general, optical microscopy examinations showed that no surface damage or flaws were apparent after the bench rig test. However, there were distinct valve seat markings at the valve and stainless steel valve seat contact point. Strength testing was carried out at room temperature, with a compression text figure specially designed in-house, to evaluate the effects of a 500-h bench rig test on mechanical performance (Figure 2). The test results of as-received NT551 valves obtained using a hydraulic chamber facility were used as a baseline for comparison (Figure 3). Mechanical results for the valves tested at 500 h show that the characteristic strength and the Weibull strength distribution were similar to those obtained for the as-machined valves, suggesting no surface/subsurface damage was introduced during the bench rig test (Figure 4). Note that nondestructive evaluation carried out at Argonne National Laboratory on the valves tested at 500 h also indicated no apparent damage/flaws, consistent with the present mechanical testing results.

Studies were also conducted of the mechanical properties of NT551 silicon nitride valve stems after a 500-h bench rig test. The objective was to see whether the 500-h bench rig test would introduce any surface damage to the valve stem surfaces and thus degrade the mechanical strength. The half-cylindrical valve stems were machined and then

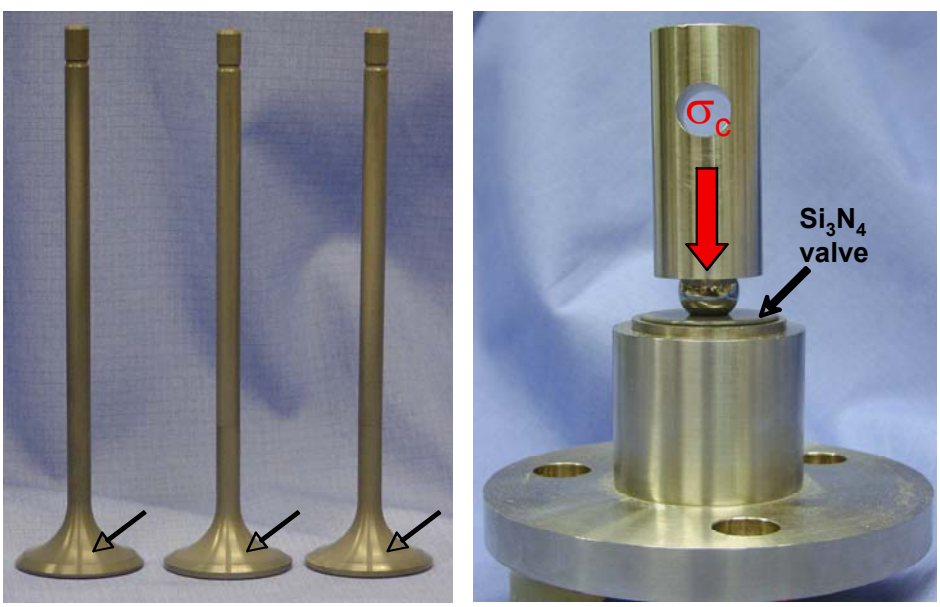

Figure 2. Photos of silicon nitride exhaust valves after testing on a 500-h bend rig at Caterpillar and on a mechanical testing fixture. The valve strength test was on a Universal Instron machine.

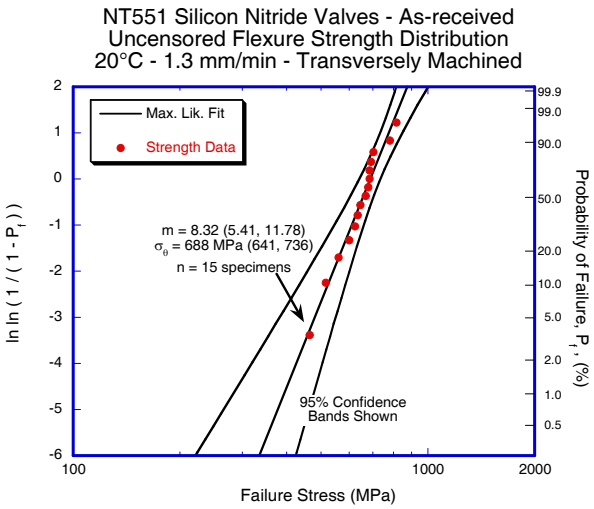

Figure 3. Strength distribution of as-received Norton NT551 silicon nitride valve transversely machined and tested at 20°C.

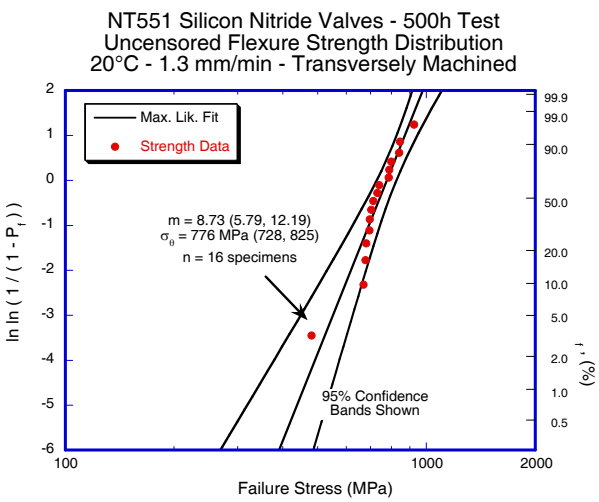

Figure 4. Strength distribution of Norton NT551 silicon nitride valve transversely machined and tested for 500 h at 20°C.

tested using a fixture with 30/60-mm spans with a 2-mm/min crosshead speed at room temperature. Figure 5 shows the uncensored Weibull strength distribution of these half-cylindrical valve stem specimens. The mechanical results show a characteristic strength of 1135 MPa and Weibull modulus of 12.7, comparable to and/or better than the as-machined cylindrical samples. The results indicate excellent wear resistance. The slight increase in characteristic strength might be due to

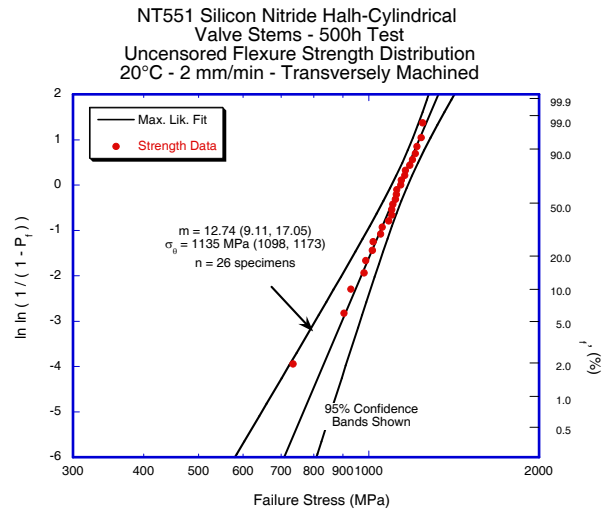

Figure 5. Strength distribution of Norton NT551 silicon nitride half-cylindrical valve stems transversely machined and tested for 500 h at 20°C.

the surface smoothing effect resulting from the contact between the silicon nitride valve stem and the valve guide.

Dynamic Fatigue Performance of Diesel Particulate Filters

Studies of the mechanical properties of a DPF substrate, especially dynamic fatigue behavior at elevated temperatures, were initiated and carried out during this fiscal year. The objective is to develop a mechanical database for predicting long-term reliability and durability. Two different types of samples, with 3×4 cells and 4×6 cells, were employed to evaluate how size influences the mechanical response and fracture process. Tests were carried out at temperatures of 600, 800, and 900°C at stressing rates of 5, 0.005, and 0.00005 MPa/s in air. The dynamic fatigue procedures carried out for DPF materials are similar to those employed for monolithic ceramic specimens (ASTM C1465). Figure 6 shows the preliminary dynamic fatigue results for DPF samples with 4 × 6 cells. The results showed that the DPF material exhibited similar low dynamic fatigue exponents (N ~ 40–44) in the temperature range employed. The low fatigue exponents obtained suggest that the DPF material might exhibit susceptibility to SCG processes at temperatures. More test specimens and a lower stressing rate need to be

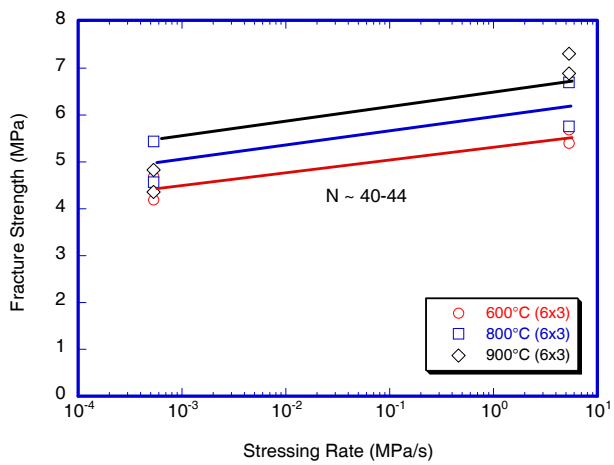

Figure 6. Fracture strength versus stressing rate of DPF material as a function of test temperature.

studied to provide a better understanding of long-term reliability and life-limiting processes.

References

1. "Standard Test Method for Flexural Strength of Advanced Ceramics at Ambient Temperatures," ASTM C1161, *Annual Book of ASTM Standards*, Vol. 15.01, American Society for Testing and Materials, West Conshohocken, Pennsylvania, 1999.

2. "Standard Test Method for Determination of Slow Crack Growth Parameters of Advanced Ceramics by Constant Stress-Rate Flexural Testing at Elevated Temperatures," ASTM C1465, *Annual Book of ASTM Standards*, Vol. 15.01, American Society for Testing and Materials, West Conshohocken, Pennsylvania, 1999.

3. *Life Prediction Methodology for Ceramic Components of Advanced Heat Engines, Phase 1*, ORNL/Sub/89-SC674/1-2, prepared by AlliedSignal Engines, DOE Office of Transportation Technologies, 1995.

4. "Practice for Reporting Uniaxial Strength Data and Estimating Weibull Distribution Parameters for Advanced Ceramics," ASTM C1239, *Annual Book of ASTM Standards*, Vol. 15.01, American Society for Testing and Materials, West Conshohocken, Pennsylvania, 1999.

5. A. A. Wereszczak, H. -T. Lin, T. P. Kirkland, M. J. Andrews, and S. K. Lee "Strength and Dynamic Fatigue of Silicon Nitride at Intermediate Temperatures," *J. Mater. Sci.*, **37**, 2669–2684 (2002).

Presentations and Publications

H. T. Lin, T. P. Kirkland, A. A. Wereszczak, and M. J. Andrews, "Strength Retention of Silicon Nitride After Long-term Oil Immersion Exposure," *J. Mater. Sci.* (in press).

H. Low-Cost Manufacturing of Precision Diesel Engine Components

P. J. Blau and J. Qu
Oak Ridge National Laboratory
P.O. Box 2008, MS-6063
Oak Ridge, TN 37831-6063
(865) 574-5377; fax: (865) 574-6918; e-mail: blaupj@ornl.gov

DOE Technology Development Area Specialist: James J. Eberhardt
(202) 586-9837; fax: (202) 586-1600; e-mail: james.eberhardt@ee.doe.gov
ORNL Technical Advisor: D. Ray Johnson
(865) 576-6832; fax: (865) 574-6098; e-mail: johnsondr@ornl.gov

---

Contractor: Oak Ridge National Laboratory, Oak Ridge, Tennessee
Contract No.: DE-AC05-00OR22725

Objectives

- Enable the use of advanced materials such as ceramic composites, cermets, and titanium alloys in diesel engines by understanding their machining characteristics on a basic and applied level.
- Develop new, ceramic-based cutting tool materials for high-speed titanium machining.
- Work with a small business (Third Wave Systems, Inc.) in the development of software packages for manufacturers to optimize high-speed machining processes.

Approach

- Quantify the grinding characteristics of TiC/Ni_3Al matrix cermets that are promising candidates for diesel engine fuel injector plungers and wear parts.
- Investigate the possibility of using cermets as cutting tool materials for high-speed titanium machining.
- Participate with a consortium of manufacturers led by Third Wave Systems, Inc., to develop finite-element analysis (FEA)-based machining modeling software and to acquire new machining process modeling capabilities.

Accomplishments

- Worked with a visiting faculty member from Louisiana State University to study the effect of wheel condition and grinding parameters on the machinability of Ni_3Al-bonded advanced composites with varying amounts of titanium carbide particles.
- Worked with the University of Michigan and the ceramic processing staff at Oak Ridge National Laboratory (ORNL), to prepare, characterize, and test experimental cermet composites as possible tooling inserts for the high-speed machining of titanium alloys.
- Tested and helped to evaluate a new software package designed to optimize high-speed drilling of titanium alloys.

Future Direction

- The current project ended in FY 2005. A new effort on synergistic process-enhanced grinding of advanced materials is planned to begin in FY 2006.

Introduction

Manufacturing broadly comprises the conversion of raw materials into useful products. It encompasses a broad range of engineering disciplines and unit processes, including machining and finishing. Since the industrial revolution of the late 1800s, U.S. industry has invested hundreds of billions of dollars in the development of manufacturing technology to promote economic health and security. However, with the continuing egress of manufacturing facilities to foreign soil, needed improvements in domestic manufacturing facilities and the knowledge base to develop new machining technology has been eroding. The machine tool industry in the United States has largely closed up shop, and most new machine tools are made by foreign sources. It is vital therefore, to avoid full dependence on foreign sources, to promote applied machining science within the United States.

Driven by the high price of fuel and increasingly stringent emissions regulations, the diesel industry is revising its engine designs. Some of these designs could benefit from the use of high-performance materials, but the ability to machine these hard, durable materials cost-effectively becomes a key enabler. Therefore, the current project is intended to enable the introduction and use of advanced materials for diesel engine components by better understanding and optimizing their machining characteristics.

Approach

Three tasks addressed new machining technology for diesel engine components. The first two are experimental studies and the latter an effort in modeling with experimental verification.

- Characterizing the machining characteristics of advanced composite materials containing an intermetallic-alloy binder with hard carbides.
- Developing and testing new cutting tool materials for machining lightweight alloys for fuel-efficient heavy vehicles.
- Working with software developers to test new process-specific computer modeling packages for machining of advanced materials.

Results

Grindability of TiC-Ni_3Al cermets

TiC-Ni_3Al metal matrix composites containing 40–60 vol % Ni_3Al were developed as candidate materials for diesel fuel injector plungers. They possess good mechanical properties and have thermal expansion coefficients similar to those of the steel typically used for injector bores. Previous studies have confirmed their high scuffing resistance in fuel-lubricated environments. However, cost-effective machining of these composites requires the achievement of a high material removal rate (MRR). That is difficult due to their relatively high toughness and the distribution of hard phases in the microstructure.

Working in collaboration with Prof. W. Liao, Louisiana State University, creep feed and conventional surface grinding characteristics of a TiC-Ni_3Al (50 vol %) composite were studied and compared with two baseline ceramic materials, alumina and silicon nitride. The investigation was conducted using an instrumented grinder with a 220-grit resin-bonded diamond wheels using the grinding conditions in Table 1. Selected properties of the workpiece materials and the measured maximum MRRs are shown in Table 2. The composite is tougher but lower in hardness than the two ceramics, but it had a much lower maximum MRR than alumina.

Table 1. Grinding conditions

Wheel diameter (mm)	228.6
Grinding width (mm)	11.43
Wheel speed (rpm)	4500, 2500
Depth of cut (mm)	0.051, 0.254, 1.016, 1.27
DOC[a] × work speed (mm^2/min)	164, 254, 328, 645

[a]DOC = depth of cut

Table 2. Hardness, toughness, and maximum MRRs

Material	Vickers microindentation hardness (GPa)	Fracture toughness (MPa-m$^{1/2}$)	Maximum MRR (mm^3/s)
TiC-Ni_3Al (50 vol %)	9.5	12	62.5 for conventional[a] 48.4 for creep feed[b]
Si_3N_4	19.4	5	(Not measured)
Al_2O_3	24.8	3–4	>125

[a]Reciprocating surface grinding with relatively shallow DOCs.
[b]Deeper DOCs but with a slower feed rate.

Grinding forces, spindle power, vibration, and acoustic emission signals were monitored and analyzed. In general, the cermet required higher grinding forces and spindle power than the two ceramics for a given MRR (see Figure 1), but it also exhibited the best surface finish (see Figure 2). Higher fracture toughness is likely to be responsible for both results because it requires more power to overcome the higher toughness, but it also leads to less microfracturing of surface.

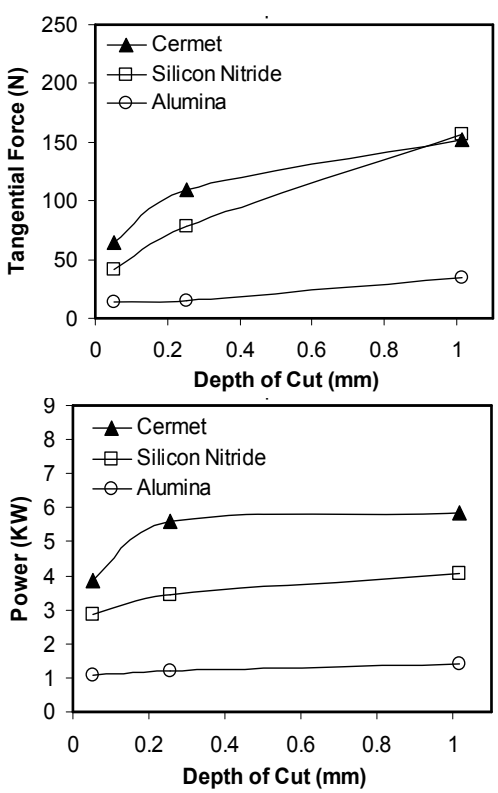

Figure 1. Grinding forces and power of grinding different work materials in steady-state wheel condition (MRR = 48.4 mm^3/s).

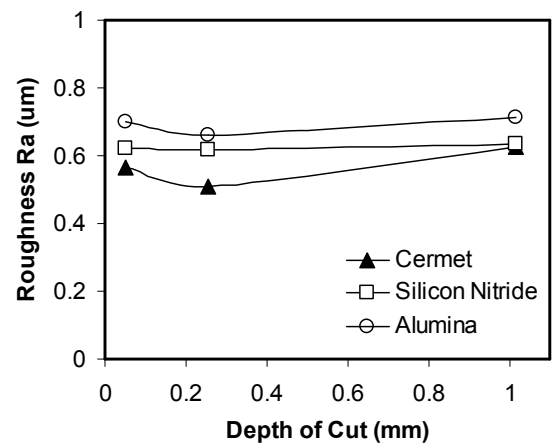

Figure 2. Arithmetic average surface roughness of different workpiece material surfaces ground under steady-state wheel conditions at a MRR of 48.4 mm^3/s.

Scanning electron microscopy (SEM) revealed the response of the cermet surfaces to differing degrees of grinding severity. More surface and subsurface damage occurred for creep feed grinding than for conventional grinding. However, no excessive cracking or pull-out of TiC particles was observed (see Figure 3). This indicates good bonding between the Ni_3Al matrix and the hard TiC particles that appear darker gray in the image.

New Cutting Tools and Process Modeling for High-Speed Titanium Machining

Experimental Cutting Tool Materials: Two TiC-Ni_3Al cermets with 5 vol % and 9 vol % matrix material, respectively, were prepared with the cooperation of T. Tiegs at Oak Ridge National Laboratory. Their microindentation hardness is compared to that for a commercial WC-Co (6 vol %) tool

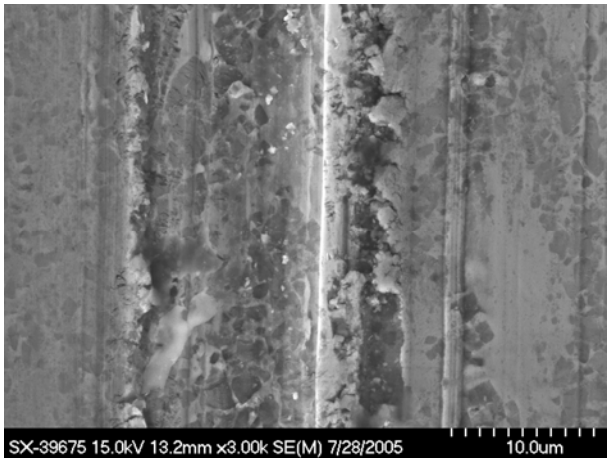

Figure 3. SEM image of a ground cermet surface showing one of the deeper cutting grooves. Ductile tearing is evident on the ridges of the groove, but there is little evidence for TiC particle pull-out.

insert in Table 3. Figure 4 shows a more uniform and less porous microstructure for the TiC-Ni_3Al (9 vol %) composition than for the TiC-Ni_3Al (5 vol %).

Tool inserts for turning were prepared in the triangular shape shown in Figure 5. The material was cut by four-axis wire electro-discharge tapered sides and corners were manually polished by 600 grit SiC abrasive paper to remove the EDM recast layer.

These TiC-Ni_3Al tool inserts were used to turn Grade 2 (commercially pure) titanium at University of Michigan (UM) using 80-, 160-, and 640-ft/min cutting speeds, 0.01-in./rev feed rate, and 0.04 in. DOC. Compared with commercial WC-Co tools, the TiC-Ni_3Al tools showed moderately higher cutting forces. This could partially be due to the imperfect tool geometry and low sharpness of the manually polished cutting edges. The tool wear and tool life issues were also briefly studied at UM. Table 4 summarizes these results. Unlike the progressive wear on the WC-Co tool, chipping was the dominant failure mode of the TiC-Ni_3Al tools, especially at

Table 3. Microindentation hardness comparison

Material	HV (GPa, 200 g)
TiC-Ni_3Al(5%)	20.6
TiC-Ni_3Al(9%)	17.3
WC-Co(6%)	18.5

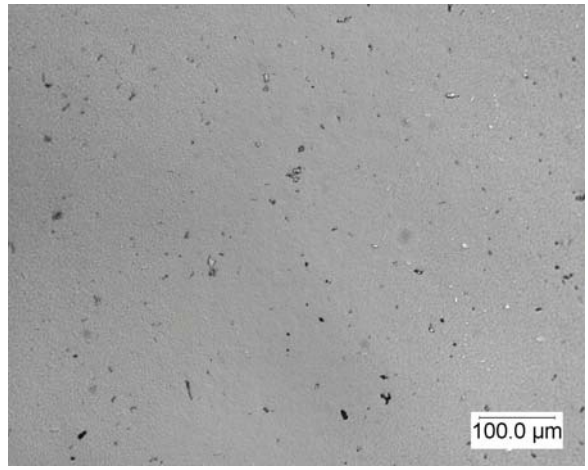

(a) TiC-Ni_3Al (5 vol %)

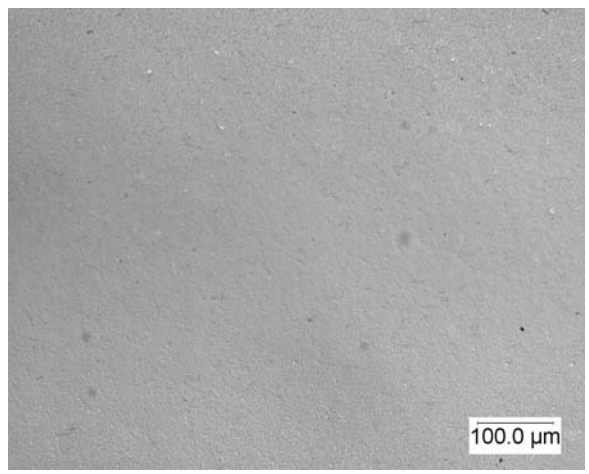

(b) TiC-Ni_3Al (9 vol %)

Figure 4. Microstructures of TiC-Ni_3Al cermets.

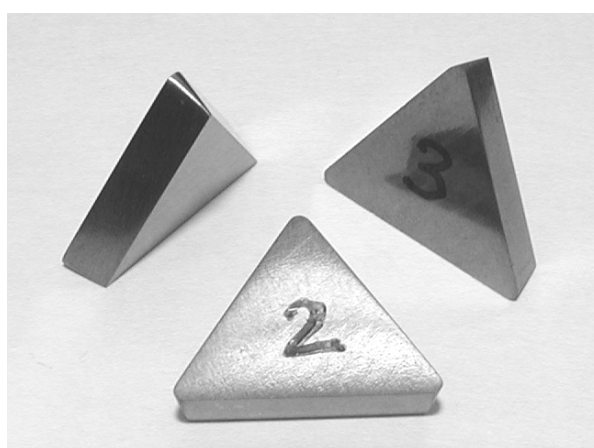

Figure 5. Tool inserts made of TiC-Ni_3Al cermets.

Table 4. Tool life in machining of titanium

Tool life (s)	Cutting speed (ft/min)		
	80	160	640
TiC-Ni_3Al (5%)	245.3	18.4	15.3
TiC-Ni_3Al (9%)	*Not tested*	>294.4	9.2 (tip 1) 33.7 (tip 2)
WC-Co	*Not tested*	*Not tested*	69

machining (EDM), the top and bottom surfaces were ground by a diamond grinding wheel, and the high cutting speeds. Due to the high porosity as shown in Figure 4(a), TiC-Ni_3Al (5 vol %) tools broke at all cutting speeds. The TiC-Ni_3Al (9 vol %) tools survived at 160 ft/min with progressive wear after 294.4 s, but broke fairly quickly at 640 ft/min. The wide variability in tool life (9.2 and 33.7 s at high cutting speed) for TiC-Ni_3Al (9 vol %) tools suggests either nonuniformity of the microstructure or inconsistent cutting edge sharpness, or both. The performance of the TiC-Ni_3Al (9 vol %) tools might be improved by automated production grinding, but in light of the current results and the fact that the current project is ending, no further studies of this material are planned.

Machining model testing and verification: Work continued on the testing and validation of software for high-speed machining. Good correlations have been obtained between computer modeling using Thermal Wave Systems (TWS) *AdvantEdge*™ software and lathe turning experiments.

For example, in titanium machining, cutting chips are known to catch fire when their temperature rises above about 1200°C. The TWS *AdvantEdge*™ was used to simulate chip ignition in titanium turning. Machining simulations and verification experiments were conducted on a Ti-6Al-4V workpiece using a Micrograin AR6 (WC-Co) tool. The feed rate was 0.1 mm/rev, and DOC ranged from 30 and 75 µm. Table 5 data show very good agreement between the simulation and the experiments. The simulated temperature profiles of the titanium chips at different DOCs are illustrated in Figure 6.

Characterization of tool coatings: The physical, mechanical, and thermal properties of the tool coatings significantly affect the cutting performance and tool life. Selected production tool coatings have been characterized to provide input for machining models. The data are given in Table 6. The coating thickness and microstructure were examined by SEM as shown in Figure 7. There was a relatively large range of coating thickness (2.5–6.0 µm), despite the manufacturers' claims that they were all supposed to be 3 µm. Nanoindentation showed similar hardness and lower modulus of elasticity of these coatings compared to that of the WC substrate. The thermal conductivities of these thin coatings were measured using a new photoacoustic technique at the Microscale Thermophysical Properties Laboratory at Purdue University. All coatings exhibited

Table 5. Simulation and experimental results for titanium chip ignition

DOC (µm)	30	75
Simulation	No ignition (Chip T_{max} < 1000°C)	Ignition (Chip T_{max} > 1400°C)
Experiment	No ignition	Ignition

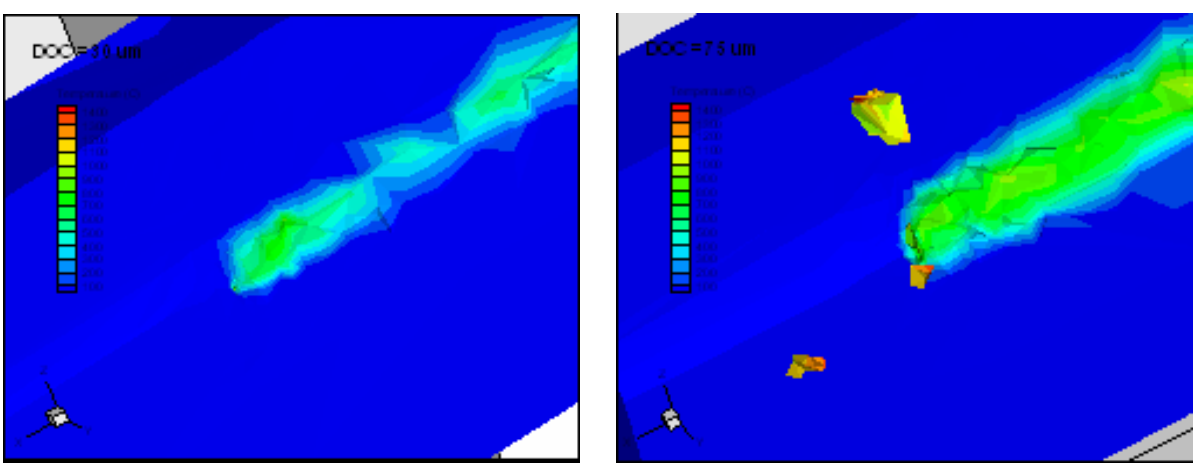

Figure 6. Simulation of titanium chip ignition (left: no ignition left, right: ignition).

Table 6. Physical, mechanical, and thermal properties of tool coatings

Grade (kennametal)	Tool insert material	Coating characteristics			
		Thickness (μm)	Nanoindentation		Thermal conductivity (W/m-K)
			H[a] (GPa)	E[b] (GPa)	
K313	WC-Co (6% Co)	—	23.2	545.2	80.99
KC730	K313+PVD **TiN**	2.5	23.1	408.5	18.69
SP39AH	K313+PVD **TiCN**	6.0	25.5	448.7	17.53
KC5010	K313+PVD **TiAlN**	3.0	25.0	355.3	1.86

[a]H = nanoindentation hardness number.
[b]E = elastic modulus obtained from nanoindentation.

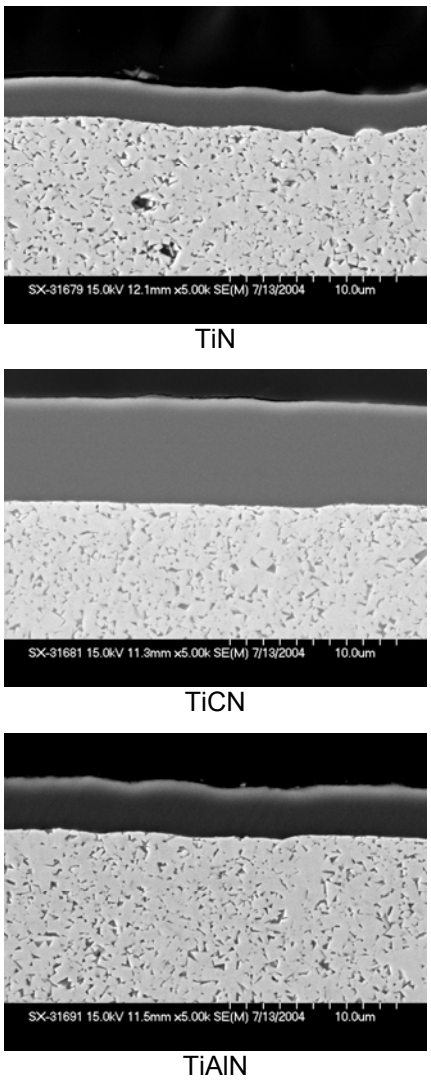

Figure 7. Cross sections of tool coatings clearly indicated a variation in thickness.

much lower thermal conductivity than the WC substrate. Results imply that the longer tool lives obtained from the coated tools were not due to better thermo-physical properties (they were actually worse than the substrate), but from improved tribological characteristics, such as less adhesion to reduce edge buildup. The latter is described in the next section on tool wear characterization.

Tool wear characterization: In titanium machining, the high tool wear, particularly "diffusion wear," significantly limits the cutting speed and tool life. The wear of four turning WC-Co based tools with different coatings and/or corner radii was measured and characterized. The four tool inserts were collected at the point of tool failure (dramatic increase in the cutting force) in titanium machining, as shown in Table 7.

The wear patterns on tool tips were mapped by laser profilometry (Rodenstock RM600). Results are shown in Figure 8. Different "tool failure" mechanisms were observed: the tools with 0.8-mm corner radius showed high crater wear [Figures 8(a) and 8(b)], while the 0.1-mm corner radius tools failed because the work material transferred and built up on the cutting edge. Energy dispersive X-ray analysis confirmed a high titanium concentration on the builtup material. The volumes of the crater wear and edge buildup were then quantified using the True Map™ 3D image analysis package, and summarized in Table 7. The TiB_2 coated tool (0.8 mm r_c) had slightly higher wear rate compared to the noncoated tool, but last much longer. That is possibly due to its slower rate of edge buildup, which dramatically reduces the edge sharpness and causes high adhesion to the work material. For a corner radius of 0.1 mm, the TiB_2 coated tool significantly outperformed the TiAlN coated tool due to the much lower edge buildup rate, as shown in Table 7.

Table 7. Tool wear results

Tool coating	Corner radius r_c (mm)	Tool life (s)	Crater wear rate (mm^3/s)	Edge buildup rate (mm^3/s)
N/A	0.8	69	1.0×10^{-4}	0.4×10^{-4}
TiB_2	0.8	199	1.3×10^{-4}	0.1×10^{-4}
TiAlN	0.1	38	—	11×10^{-4}
TiB_2	0.1	115	—	0.9×10^{-4}

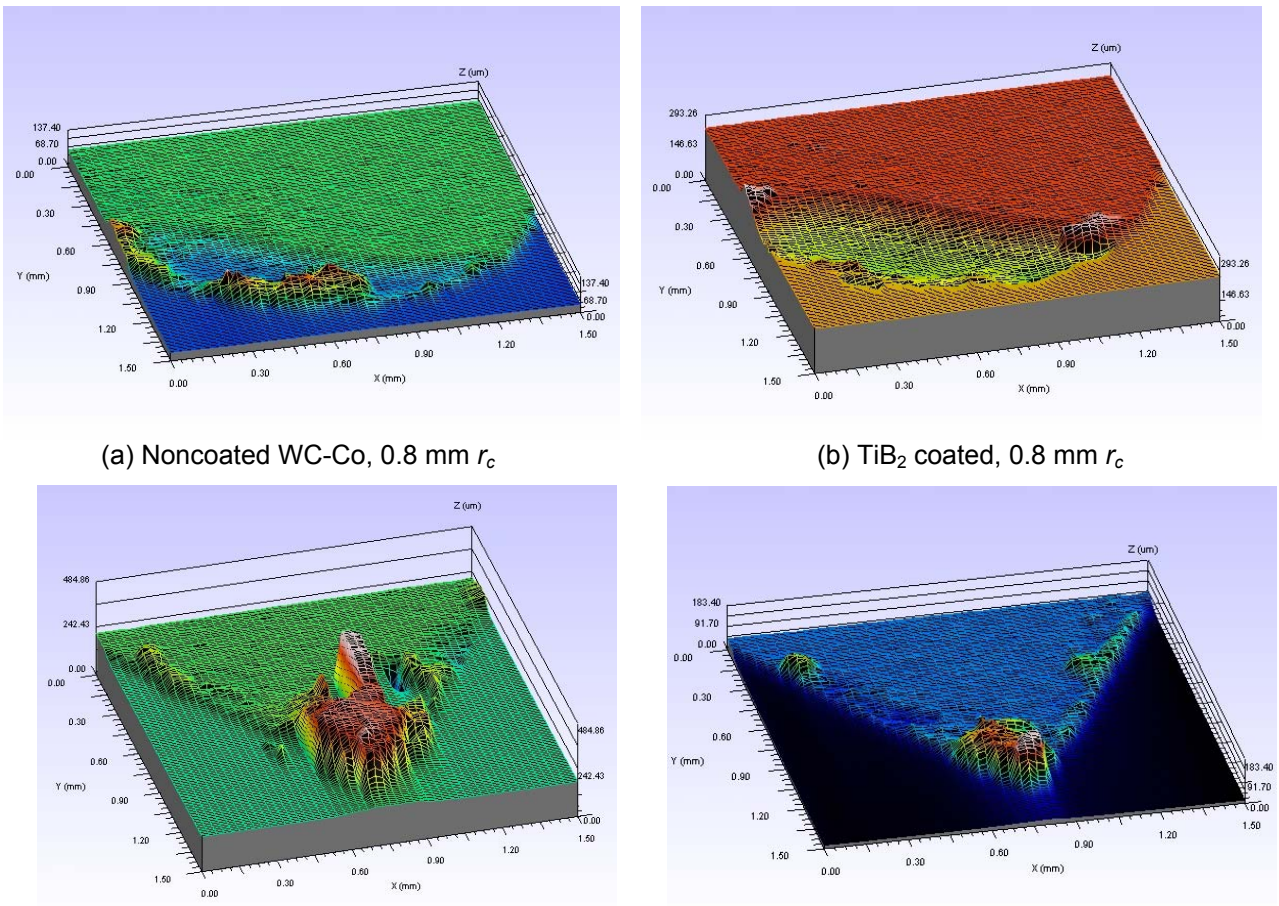

(a) Noncoated WC-Co, 0.8 mm r_c

(b) TiB_2 coated, 0.8 mm r_c

(c) TiAlN coated, 0.1 mm r_c

(d) TiB_2 coated, 0.1 mm r_c

Figure 8. 3-D profiles of the worn tool tips.

Presentations and Publications

R. Li, A.J. Shih, and J. Qu, "High Speed Machining of Titanium at ORNL/UM," 2005 Third Wave AdvantEdgeTM International Users' Conference, Dearborn, Michigan, May 4, 2005.

J. Qu, T. W. Liao, P. J. Blau, J. E. Shelton, and T. N. Tiegs, "Grindability of TiC-Ni_3Al Metal Matrix Composites," to be presented at The 30th International Conference & Exposition on Advanced Ceramics & Composites, Cocoa Beach, Florida, January 22–27, 2006.

I. Cost-Effective Machining of Titanium Materials

Albert J. Shih
Mechanical Engineering
University of Michigan
Ann Arbor, Michigan 48109-9739
(734) 647-176; fax: (734) 936-0363; e-mail: shiha@umich.edu

DOE Technology Development Area Specialist: James J. Eberhardt
(202) 586-9837; fax: (202) 586-1600; e-mail: james.eberhardt@ee.doe.gov
ORNL Technical Advisor: D. Ray Johnson
(865) 576-6832; fax: (865) 574-6098; e-mail: johnsondr@ornl.gov

---

Contractor: Oak Ridge National Laboratory, Oak Ridge, Tennessee
Contract No.: DE-AC05-00OR22725
Subcontractor: University of Michigan, Ann Arbor, Michigan

Objective

- Investigate new technologies for cost-effective machining of titanium alloys.
- Develop the cost-effective, high-speed machining processes.
- Investigate new tool material, geometry, coating, and process parameters to enhance process capability and product quality.
- Provide accurate prediction of temperature and stress for tool selection and design.

Approach

- Conduct turning test using new tool material.
- Develop high-speed titanium drilling technology.
- Carry out the finite-element modeling and inverse heat transfer analysis to study titanium turning and drilling processes.
- Validate the modeling with experimental results.

Accomplishments

- Compared the performance of new TiC-based tool material with WC-Co for turning titanium.
- Demonstrated the feasibility of high-speed drilling process over 180-m/min cutting speed for titanium.
- Achieved accurate predictions of the temperature distribution of the tool in titanium drilling.

Future Direction

- Continue the exploration of high-speed, cost-effective machining of titanium alloys.
- Advance the thermal analysis and management of the cutting tool.
- Conduct the 3-D finite-element-based thermal-mechanical coupled drilling modeling to advance the knowledge in mechanics of material deformation during the titanium chip formation process.

Introduction

Titanium and its alloys are lightweight, corrosion-resistant, biocompatible, and high-temperature materials. The poor machinability of titanium alloys has been summarized in several review articles.[1–4] Due to the inherent properties of titanium, particularly the low thermal conductivity, the tool temperature in machining of titanium is high and concentrated at the tool tip.[1] High temperature softens the tool material and promotes rapid diffusion wear and severe tool edge chipping.[5,6]

A new tool material, the TiC-Ni_3Al cermet, was developed at Oak Ridge National Laboratory with the goal to increase high-temperature stability and reduce the diffusion wear in titanium machining. Titanium turning tests are performed, and results are compared with that of a conventional WC-Co tool.

Among various machining processes, drilling has a major economical importance because it is typically utilized in final steps in production. Technical difficulties of cost-effective drilling of titanium include (1) high drill temperature, (2) severe drill wear, even at moderate feed rate and spindle speed, (3) limited cutting speed and productivity, (4) difficulty to eject long ribbon titanium chip, and (5) exit burr formation. The main objective of this year is to investigate the drilling mechanism and develop the new technologies to overcome the technical difficulties mentioned above.

Approach

Tool Wear Test of TiC-Ni_3Al Material

The TiC-Ni_3Al materials were made at ORNL. The tool blank face was machined by wire electro-discharge machining (EDM) and polished to the same geometry as the Kennametal TPG160308 tool. A set of turning tests was conducted using this new tool material at the University of Michigan to evaluate the wear of TiC-Ni_3Al tool.

Figure 1 shows the optical microscopic image of the polished TiC-Ni_3Al. The TiC with 5% Ni_3Al shows relatively high porosity, compared to commercial tool material. The high porosity results in the brittleness of tool under high stress. Increasing the content of Ni_3Al to 9% reduces the material porosity, but sacrifices the hardness of TiC-Ni_3Al, as shown in the hardness indention results in Table 1.

The tool wear tests were conducted at 24.4-, 48.8-, and 195-m/min cutting speeds in lathe turning with 0.25-mm/rev feed and 1-mm depth of cut. Both TiC-Ni_3Al and WC-Co tool were evaluated, and the cutting forces and tool life were compared.

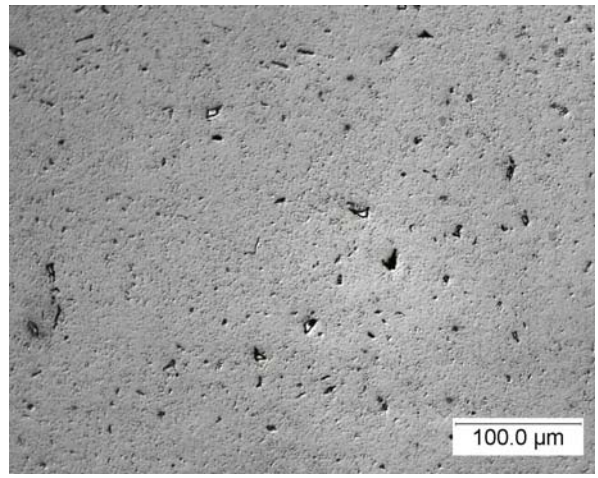

(a) TiC-Ni_3Al (5%)

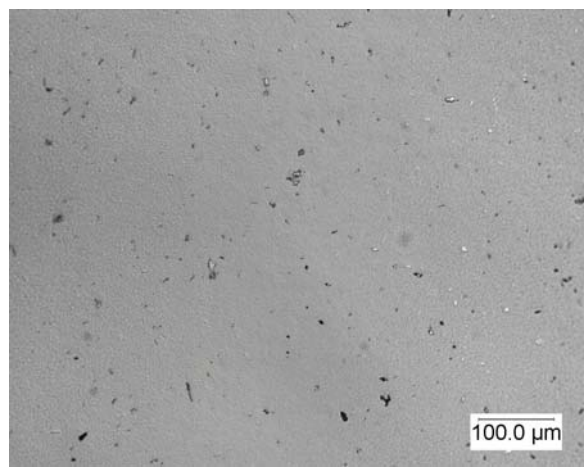

(b) TiC-Ni_3Al (9%)

Figure 1. Microstructures of TiC-Ni_3Al cermets.

Table 1. Micro-indentation hardness

Material	HV (GPa, 200 g)
TiC-Ni_3Al (5%)	20.6
TiC-Ni_3Al (9%)	17.3
WC-Co (6%)	18.5

High-Speed Drilling of Ti-6Al-4V

High cutting speed is essential to reduce the machining cost and increase the productivity. It is particularly important, but difficult to achieve, in the machining of titanium and titanium alloys. As shown in Table 2, the drilling speed for titanium alloys is very low in industrial applications. This has

Table 2. Comparison of drilling speed

Drill material	Al alloys	Cast iron	Ti-6Al-4V
HSS[7]	105	49	11
WC-Co[7]	245	90	46
Other[8]	533	235	—

hindered the productivity and increased the cost of machining titanium. The goal of this research is to enable the high-speed drilling of titanium.

Three types of drills, (1) M2 HSS twist drill (Greenfield Industries 44210), denoted as HSS Twist, (2) WC-Co web thinned point twist drill (Kennametal KWCD00344), denoted as WC-Co Twist, and (3) WC-Co spiral point drill (Kennametal K285A01563), denoted as WC-Co Spiral, are evaluated. All drills are double-flute with 4 mm in diameter. The workpiece material is 6.35-mm thick Ti-6Al-4V plate.

The titanium drilling tests were conducted at a constant feed of 0.051 mm per revolution or 0.025-mm feed per tooth. By changing the spindle speed, various drill feed rates and peripheral cutting speeds could be achieved. Cutting fluid plays an important role to reduce the tool and workpiece temperatures and enhance the tool life.[6] Two ways to supply the cutting fluid, internally from two through-the-drill cutting fluid holes and externally from outside the drill, were studied. The cutting fluid was 5% CIMTECH 500, a synthetic metal-working fluid. The thrust force and torque during drilling were measured.

Four sets of experiments, denoted as Exps. I, II, III, and IV, were conducted. Exp. I was conducted using the HSS Twist drill at three peripheral cutting speeds, 9.1, 13.7, and 18.3 m/min, without cutting fluid. This is the baseline test. To study the effect of cutting fluid, Exp. II was conducted with external cutting fluid supply using HSS Twist drill at higher peripheral cutting speeds at 13.7, 18.3, and 27.4 m/min. Exp. III was conducted to compare the thrust force, torque, energy consumption, and burr formation of three types of drill (HSS Twist, WC-Co Twist, and WC-Co Spiral) at 18.3-m/min peripheral cutting speed without cutting fluid. Exp. IV was high-speed drilling of titanium using the WC-Co Spiral drill at 183-m/min peripheral cutting speed. Drilling under dry as well as with internal and external cutting fluid supply conditions was evaluated.

Figure 2 illustrates three stages, marked as A, B, and C, in drilling. Stage A occurs when the drill has

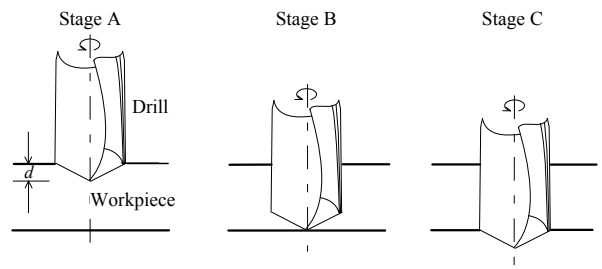

Figure 2. Illustration of three stages A, B, and C in drilling.

traveled by a distance *d*, which is called the drill point length, from the initial contact. For the HSS Twist, WC-Co Twist, and WC-Co Spiral drills used in this study, *d* is 1.24, 1.19, and 0.74 mm, respectively. Neglecting the deformation of the workpiece, the drill cutting edge becomes fully engaged with the workpiece at this stage. When the drill tip reaches the back surface of the plate, as shown in Figure 2, it is marked as Stage B. Stage C is defined when the drill cutting edge is disengaged with the workpiece without considering the deformation of the workpiece and burr formation.

The torque and force changed throughout the drilling process. The value of thrust force and torque at Stage A, denoted as F_A and T_A, and maximum thrust force and torque during drilling, denoted as F_m and T_m, respectively, were compared to distinguish different drilling conditions.

Besides thrust force and torque, another parameter to compare drilling setup is the energy *E* required to drill a hole.

$$E = \int_l F dl + \int_l \frac{2\pi T}{f} dl \quad ,$$

where *l* is the depth of drilling, *F* is the thrust force, *T* is the torque, and *f* is the feed per revolution. In titanium drilling, the *E* is dominated by the torque term, which typically accounts for more than 95% of the *E*.

Inverse Heat Transfer Solution of Tool Temperature in Drilling of CP Titanium

Understanding the heat generation rate and tool temperature distribution is important in titanium drilling. The inverse heat transfer method, which utilizes the temperature measured by thermocouples embedded on the drill flank surface as the input, is applied to predict the heat flux on the drill chisel and cutting edges. Thermocouples are routed from the

frank surface, via through-the-drill cutting fluid holes, to outside the tool.[9] During drilling, these thermocouples do not contact nor interfere with the chip. A validation process can be performed by comparing the drill temperature distributions to thermocouple measurements.

The drilling experiment was conducted in a Mori-Seiki TV-30 vertical machining center. Figure 3 shows the experimental setup with the stationary 9.92-mm-diameter spiral point drill and the 38-mm-diameter CP titanium bar rotated by spindle. The drill was stationary because four thermocouples embedded on the flank face could be routed through cutting fluid holes in the drill body to a data acquisition system during drilling.[9] The drill and machine spindle axes were aligned by a test indicator to less than 10-µm eccentricity. Under the drill holder was a Kistler 9272 dynamometer to measure the thrust force and torque. Figure 4 shows the locations of four thermocouples, denoted as TC1, TC2, TC3, and TC4, on the drill frank surface.

Three drilling experiments were conducted at three spindle speeds, 780, 1570, and 2350 rpm, which corresponded to 24.4-, 48.8-, and 73.2-m/min drill peripheral cutting speed, respectively. The feed remained fixed at 0.051 mm/rev. All the experiments were conducted dry without cutting fluid.

Figure 5 shows the finite-element mesh of the drill, which is modeled by 68,757 four-node tetrahedral elements. As shown in Figure 5(b), 13 nodes are located on the chisel edge, and 11 nodes are placed on each cutting edge to achieve good resolution in the analysis of drill temperature distribution in titanium drilling.

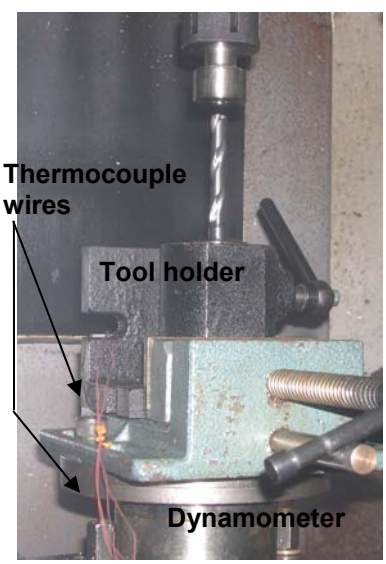

Figure 3. Experimental setup with workpiece in the holder of spindle and drill in a vertical tool holder.

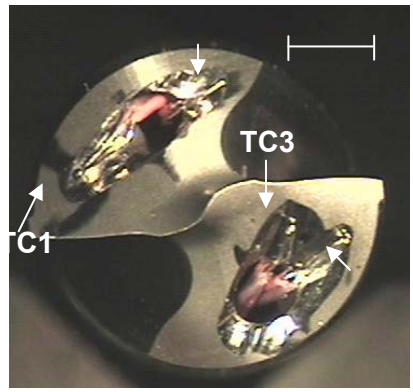

Figure 4. Thermocouple locations in the drill flank face.

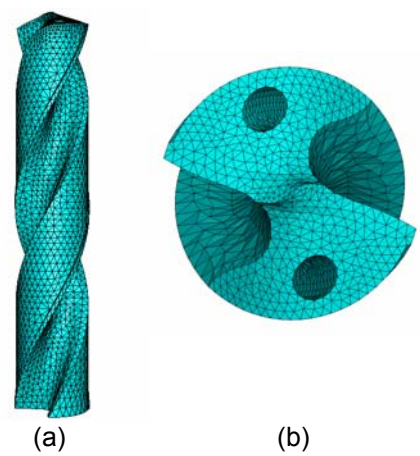

Figure 5. Mesh for the 3-D finite-element thermal model: (a) side view and (b) top view.

Results

Tool Wear Test of TiC-Ni_3Al Material

Cutting forces are summarized and compared with a WC-Co tool in Figure 6. Consistently, the TiC-Ni_3Al tools showed higher cutting forces than that of the WC-Co tool. This was likely due to the imperfect tool geometry with less sharp cutting edges of the TiC-Ni_3Al tools.

The tool life was also evaluated. The major failure mode of TiC-Ni_3Al tools is the catastrophic tool breakage. Table 3 summarizes the tool life of the TiC-Ni_3Al tools compared to the WC-Co tool. Due to the high porosity, TiC-Ni_3Al (5%) tools broke at all cutting speeds. The TiC-Ni_3Al (9%) tools

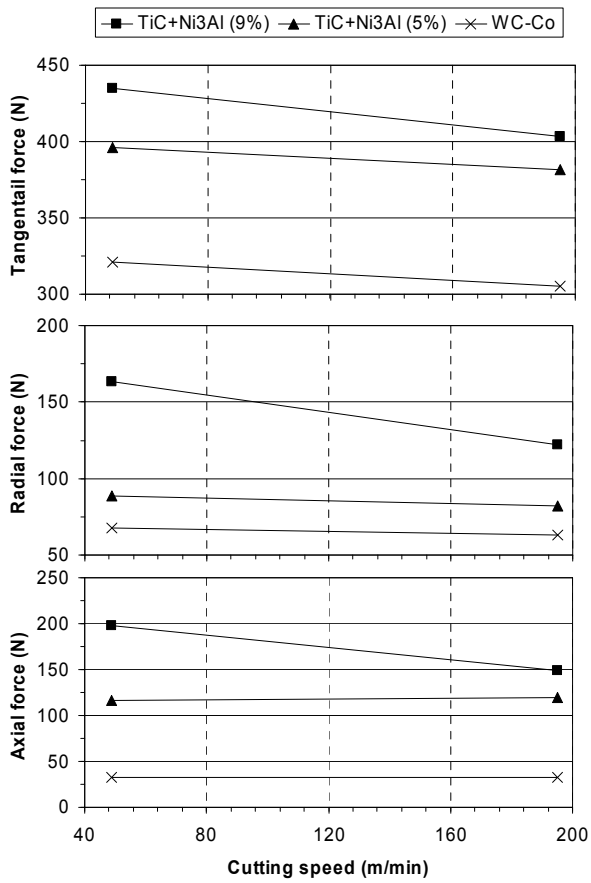

Figure 6. Cutting forces of TiC-Ni_3Al and WC-Co tools in lathe turning of titanium.

Table 3. Tool lives in machining titanium

	Cutting speed (m/min)		
	24.4	48.8	195
TiC-Ni_3Al (5%)	245.3	18.4	15.3
TiC-Ni_3Al (9%)	*Not tested*	>294.4	9.2/33.7
WC-Co	*Not tested*	*Not tested*	69

survived at 48.8 m/min with progressive wear after 294 s, but broke early at 195 m/min. Significantly different tool lives, 9.2 and 33.7 s, at high cutting speed (195 m/min) were obtained on two tips of a TiC-Ni_3Al (9%) tool insert, indicating the non-uniformity of the microstructure or the non-consistent condition of the cutting edges. The higher Ni_3Al content improves the performance of TiC-Ni_3Al tool material, but some efforts like better preparation of tool edge and surfaces are still needed to achieve or exceed the performance of WC-Co. We are working with Kennametal to grind the TiC-Ni_3Al tool to the right geometry.

High-Speed Drilling of Ti-6Al-4V

Table 4 summarizes the Stage A and peak thrust force and torque, and energy consumption in Exps. I–IV. Performance of each type of drill is discussed as follows.

The HSS Twist drill has limited cutting speed and material removal rate in drilling titanium. The drill tip melted in the second hole due to high temperature at 18.3- and 27.4-m/min peripheral cutting speeds under dry and external cutting fluid supply conditions, respectively.

The WC-Co Spiral drill has the lowest thrust force and torque among all three drills. This drill is selected for high-speed titanium drilling. The drill can perform at 183-m/min peripheral cutting speed (14700 rpm) under the dry as well as with external and internal cutting fluid supply conditions. As listed in Table 5, the tool life is short without the supply of cutting fluid. Using flood external cutting fluid supply just slightly increased the tool life because the high spindle speed generates high centrifugal force, which prevents the cutting fluid from reaching the cutting region. The internal cutting fluid supplied through machine spindle and drill makes significant improvement of the tool life because the cutting fluid can reach the tool-chip interface and also assist the chip ejection.

Figure 7 shows the thrust force and torque in drilling at 183 m/min with internal cutting fluid supply before the drill breakage. Gradual increase of the thrust force and torque can be observed.

Inverse Heat Transfer Solution of Tool Temperature in Drilling of CP Titanium

Temperatures at four thermocouples are shown in Figure 8. Good matches between experimental and modeling temperature can be recognized at three drilling speeds.

The temperature distribution near the tip of the spiral point drill after 12.7-mm depth of drilling the

Table 4. Experiment design, summary of the Stage A and peak thrust force and torque, and energy consumption in Exps. I–IV

Exp.	Drill type	Cutting fluid	Peripheral cutting speed (m/min)	F_A (N)	T_A (N – m)	F_m (N)	T_m (N – m)	E (J)
I	HSS twist	No	9.1	401–413	0.40–0.44	401–413	0.56–0.58	391–400
			13.7	464–486	0.39–0.40	464–486	0.72–0.79	426–455
			18.3	390	0.36	390	0.80	453
II	HSS twist	External	13.7	417–420	0.40–0.44	417–420	0.5–0.54	367–390
			18.3	430–446	0.39–0.41	430–446	0.70–0.76	387–427
			27.4	400	0.3	410	0.75	412
III	HSS twist	No	18.3	390	0.36	390	0.80	453
	WC-Co twist			233–235	0.28–0.32	235–257	0.71–0.82	603–628
	WC-Co spiral			166–169	0.38–0.42	177–178	0.46–0.48	351–375
IV	WC-Co spiral	No	183	178–185	0.24–0.27	178–185	0.82–1.47	497–596
		External		175–178	0.28–0.31	175–190	0.53–1.45	504–574
		Internal		162–210	0.25–0.55	182–230	1.07–1.17	586–783

Table 5. WC-Co tool life (number of holes) at high drilling speed (183 m/min)

Dry	External cutting fluid	Internal cutting fluid
10	14	101

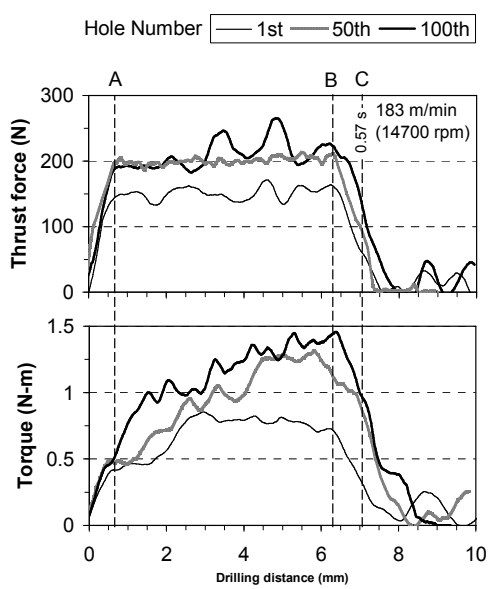

Figure 7. Thrust force and torque of high-speed drilling of Ti-6Al-4V at 183-m/min peripheral cutting speed with internal cutting fluid supply.

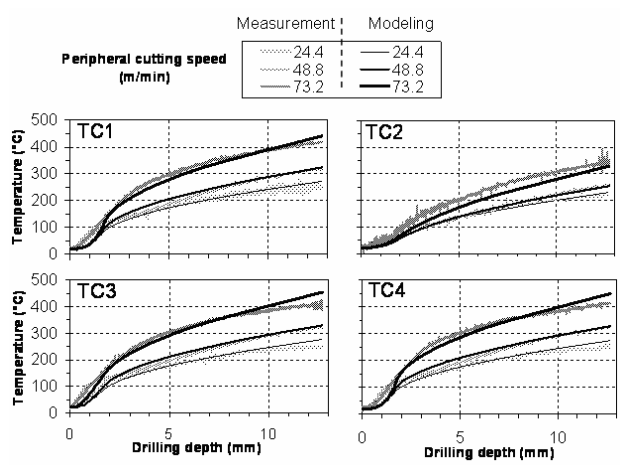

Figure 8. Comparison of the measured and calculated temperature at four thermocouple locations in titanium drilling.

titanium is shown in Figure 9. High temperature is concentrated along the cutting edge at the drill tip.

High cutting speed generates high temperature in the drill. The peak temperature increases from 445 to 893°C when the drill peripheral cutting speed is increased from 24.4 to 73.2 m/min. The peak temperature is located on the cutting edge near the drill margin for all three cutting speeds.

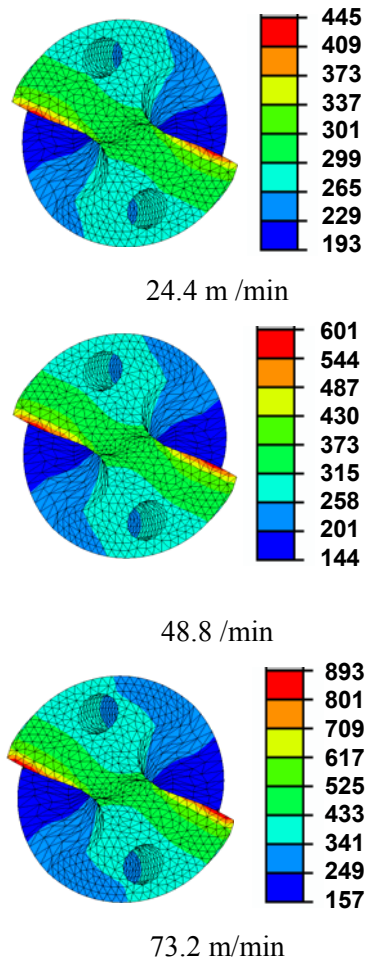

Figure 9. Temperature distributions at the drill tip.

Conclusions

This study demonstrated that high-speed, cost-effective machining of titanium and titanium alloys was possible. Exploratory evaluation of TiC-Ni_3Al cermet for machining of titanium had been conducted. Cutting forces were measured and compared with the results when using WC-Co tool at different cutting speeds and feeds. The porosity of the material was improved with higher Ni_3Al content, but the manufacturing technique and surface and cutting edge preparation of the tool inserts had been identified for further improvement.

This study demonstrated the feasibility of cost-effective drilling of Ti-6Al-4V with peripheral cutting speed over 180 m/min (600 sfpm) using commercially available advanced drill geometry and tool material. The limitation of HSS drill on cutting speed and material removal rate was apparent. The test of three drills at the same process conditions demonstrated benefits of the spiral point drill design. The WC-Co Spiral drill outperformed the HSS Twist and WC-Co Twist drills in terms of thrust force, torque, energy consumption, and burr size. The importance of cutting fluid supply on drill life was identified. The improvement of drill life from dry to external cutting fluid supply was limited at high-speed drilling. Internal cutting fluid supply was proven to be critical on the drill life.

The inverse heat transfer method was developed to analyze the tool temperature in titanium drilling. High drill temperature was observed in drilling titanium, particularly at high cutting speed. Temperature measured at various thermocouples provided not only the input for inverse heat transfer solution but also the validation of the finite-element drill temperature model. The proposed method has been validated by reasonably good agreement with experimental measurements. Detailed finite-element analysis of the drill temperature distribution was performed to gain insight in titanium drilling.

References

1. A. R. Machado and J. Wallbank, "Machining of Titanium and Its Alloys—A Review," *Proceedings of Institution of Mechanical Engineers*, *Part B: Management and Engineering Manufacture*, **204**(1), 53–60 (1990).

2. E. O. Ezugwu and Z. M. Wang, "Titanium alloys and their machinability—a review," *Journal of Materials Processing Technology*, **68**(3), 262–274 (1997).

3. X. Yang and C. R. Liu, "Machining Titanium and Its Alloys," *Machining Science and Technology*, **3**(1), 107–139 (1999).

4. M. Rahman, Y. S. Wong, and A. R. Zareena, "Machininability of Titanium Alloys," *JSME International Journal, Series C: Mechanical Systems, Machine Elements and Manufacturing*, **46**(1), 107–115 (2003).

5. M. C. Shaw, *Metal Cutting Principles*, Oxford University Press, New York, 1984.

6. E. M. Trent and P. K. Wright, *Metal Cutting*, Butterworth-Heinemann, Boston, 2000.

7. *Machining Data Handbook*, Metcut Research Associates, Inc., 1980

8. X. Lin and J. Ni, "Drill Design For High Throughput Hole Making," *International Conference on Advanced Manufacturing Technology, June 16–18, 1999, Xi'an, China*, 162–166 (1999).

9. J. S. Agapiou and D. A. Stephenson, "Analytical and Experimental Studies of Drill Temperatures," *Journal of Engineering for Industry*, **116**(1), 54–60 (1994).

Presentations and Publications

R. Li and A. J. Shih, "Finite Element Modeling of 3D Turning of Titanium**,**" presented at the 2004 ASME IMECE Anaheim, California, November 2004.

R. Li and A. J. Shih, "Finite Element Modeling of 3D Turning of Titanium," *International Journal of Advanced Manufacturing Technology* (in print).

R. Li and A. J. Shih, "Inverse Heat Transfer Solution of Tool Temperature in Titanium Drilling," *Journal of Manufacturing Science and Engineering* (submitted).

J. Advanced Cast Austenitic Stainless Steels for High-Temperature Components

P. J. Maziasz, J. P. Shingledecker, and N. D. Evans
Metals and Ceramics Division
Oak Ridge National Laboratory
P.O. Box 2008, MS-6115
Oak Ridge, TN 37831-6115
(865) 574-5082; fax: (865) 754-7659; e-mail: maziaszpj@ornl.gov

M. J. Pollard
Advanced Materials Technology
Caterpillar Technical Center
14009 Old Galena Rd.
Mossville, IL 61552
(309) 578-6133; fax: (309) 578-2953; e-mail: pollard_michael_j@cat.com

DOE Technology Development Area Specialist: James J. Eberhardt
(202) 586-9837; fax: (202) 586-1600; e-mail: james.eberhardt@ee.doe.gov
ORNL Technical Advisor: D. Ray Johnson
(865) 576-6832; fax: (865) 574-6098; e-mail: johnsondr@ornl.gov

---

Contractor: Oak Ridge National Laboratory, Oak Ridge, Tennessee
Contract No.: DE-AC05-00OR22725

Objectives

- Commercialize new CF8C-Plus cast austenitic stainless steel.
- Complete a high-temperature properties database for test specimens from commercial heats and determine the properties of prototype components.

Approach

- Support Caterpillar (CAT) evaluation efforts to upgrade turbochargers from cast iron to cast austenitic stainless steel.
- Perform and evaluate direct comparisons between commercial CF8C-Plus steel and cast stainless steels used by component suppliers to establish performance benefits at 700–850°C.

Accomplishments

- Demonstrated that CF8C-Plus cast stainless steel is far superior to SiMo cast iron at 600°C and above. CF8C-Plus also shows strength, creep resistance and aging resistance benefits compared with other commercial cast stainless steels being considered for heavy-duty diesel turbocharger housings at 750°C.
- Successfully cast a good-quality 6700-lb gas-turbine end-cover from CF8C-Plus at MetalTek and cast >30,000 lb cast for various applications.

Future Direction

- Characterize the microstructure and properties of several different prototype CF8C-Plus steel components to facilitate various commercial applications.

- Evaluate the properties of commercial heats of new CF8C-Plus Cu/W steel, which boosts tensile and creep strength at 750°C and above.

Introduction

Advanced heavy truck diesel engines are increasingly required to have higher fuel efficiency and reduced exhaust emissions without sacrificing durability and reliability. The most demanding normal duty cycles require exhaust manifolds and turbocharger housing materials to withstand temperatures ranging from 70 to nearly 800°C. Such materials must withstand prolonged, steady high-temperature exposure (which requires tensile strength and creep and oxidation resistance) as well as more rapid and severe thermal cycling (which requires resistance to aging and thermal fatigue). New emissions reduction technology and transient power excursions can push temperatures in these critical components even higher.

Higher diesel engine exhaust temperatures push components made from SiMo ductile cast iron well beyond their current strength and corrosion limits. The first Oak Ridge National Laboratory (ORNL)/CAT cooperative research and development agreement (CRADA) (3y) developed a new, modified CF8C cast austenitic stainless steel (CF8C-Plus) as an upgrade alternative to SiMo cast iron and performed the initial mechanical properties testing on a lab-scale heat. The CF8C-Plus steel was found to have outstanding creep resistance at 850°C. The second ORNL/CAT CRADA project (3y) capitalized on the initial success and began commercial scale-up of the new CF8C-Plus. The new material was found to have good castability, as well as much better mechanical properties at 600–850°C than standard CF8C steel, including resistance to aging, creep, and fatigue/thermal fatigue. The new CF8C-Plus cast steel won a 2003 R&D 100 Award, and in 2004 testing continued of different commercial casting process effects (static, centrifugal, and larger heats). This year, efforts to commercialize CF8C-Plus expanded dramatically, and this CRADA project was extended for 2 more years. In 2004–2005, successful casting trials of CF8C-Plus were carried out for components ranging from exhaust manifolds to industrial turbine casing. In addition, the first commercial heats of CF8C-Plus Cu/W were made in 2004–2005 to boost strength and creep resistance at 750–850°C. Three companies have taken trial licenses and, to date, over 30,000 lb of the new steel has been produced commercially.

Approach

In 2005, three U.S. foundries obtained trial licenses for CF8C-Plus steel: MetalTek International, Wollaston, and Stainless Foundry and Engineering. CAT and ORNL both ordered additional heats of CF8C-Plus and cast pieces in various sizes, using both static casting in sand molds and centrifugal casting of rings of varying thickness, to enable more comprehensive mechanical properties testing. In addition, a large industrial gas turbine end-cover component cast for Solar Turbines (a CAT company) by MetalTek in FY 2004 was evaluated at the CAT Technical Center for quality and defects and then cut up for mechanical testing. ORNL also had MetalTek make a 500-lb commercial heat of the new CF8C-Plus Cu/W, selected for testing from screening of lab-scale heats, to evaluate further improvements in strength and creep-resistance above 750°C. Finally, CAT began exploring CF8C-Plus steel and other commercial cast stainless steels to replace SiMo cast iron for turbocharger casing applications, which should enable increased durability at the increased engine temperatures needed to allow a 3% decrease in fuel consumption for on-highway trucks. Both CAT and ORNL do specific mechanical properties testing and microcharacterization in support of these various applications or efforts.

Technical Progress

Caterpillar

The large industrial turbine end-cover cast of CF8C-Plus steel (8000-lb heat to yield 6700-lb finished component) by MetalTek for Solar Turbines was shipped to the CAT Technical Center, as shown in Figure 1. Visual and other inspection techniques showed no defects. Then sectioning was completed, and those initial observations also found no obvious cases of hot tearing at the side flange. This is significant because fully austenitic alloys such as CF8C-Plus are usually more susceptible to hot tearing than similar steel with a much higher δ-ferrite content (standard CF8C steel has 15–25% such

Figure 1. A-6700-lb gas turbine combustor housing centrifugally cast from CF8C-Plus stainless steel by MetalTek. No indications of hot tearing have been observed (M. J. Pollard is pictured with the casting).

content). Further nondestructive analysis will be performed to ensure a complete absence of internal hot tears. Fatigue and mechanical properties test samples of the bulk material from this housing have been produced, and mechanical testing began at the end of FY 2005. It is hoped it will show that the properties do not change significantly in thick-section components (slow cooling rates) compared with smaller test castings (faster cooling rates).

The 21st Century Truck Partnership technical goal of developing emission-compliant engine systems for Class 7–8 highway trucks is an improvement in engine efficiency from 42 to 50% by 2010. CAT has determined that replacing SiMo cast iron exhaust components with CF8C-Plus cast stainless steels allows a 90°C increase in exhaust gas temperatures, which translates directly into a 3% increase in fuel economy while also significantly improving performance and durability. Efforts to produce prototype cast stainless exhaust manifolds and turbocharger housings began this year. New stainless steel diesel-engine turbocharger housings have been ordered for a small quantity off-road diesel engine application. Because of current supplier agreements, these first trial turbo-housings are being cast from a standard commercial stainless alloy, KN2, produced by Diado in Japan. However, another part of this effort is side-by-side testing of KN2 and CF8C-Plus cast steels at ORNL to directly compare properties. This prototyping effort will give the designers at CAT confidence with cast stainless steel as well as experience with the necessary design changes for cast stainless.

ORNL

In 2004, ORNL began the creep testing that showed an overwhelming advantage of CF8C-Plus steel over SiMo cast iron in terms of tensile and creep-rupture strength and thermal fatigue resistance above 550–600°C. That creep-rupture testing was expanded and completed and includes comparison of CF8C-Plus with standard CF8C steel and Ni-resist austenitic cast-iron (an upgrade for some applications relative to SiMo cast-iron). The results of various creep rupture tests at different temperature and stress levels are plotted as a function of the Larson-Miller parameter (LMP) in Figure 2. CF8C-Plus cast steel is much stronger than either SiMo or Ni-resist cast-irons, and it is almost twice as strong as standard CF8C steel. The latter comparison is important to the potential gas- and steam-turbine applications, as well as many other chemical/petrochemical, energy, or metals processing applications.

Creep-rupture ductility is shown in Figure 3. Clearly, CF8C-Plus has much more creep ductility than standard CF8C steel, despite also being stronger. This is due to the lack of δ-ferrite in the as-cast structure of CF8C-Plus, which makes it resistant to the formation of embrittling σ-phase during aging.

Finally, comparison of CF8C-Plus cast stainless with the best commercially available creep-resistant austenitic stainless steels and alloys on an LMP plot (Figure 4) shows that CF8C-Plus is as strong as or stronger than NF709 austenitic stainless alloy, and comes close to the creep-strength of alloy 617, a Ni-Cr-Co superalloy, particularly at the highest temperatures.

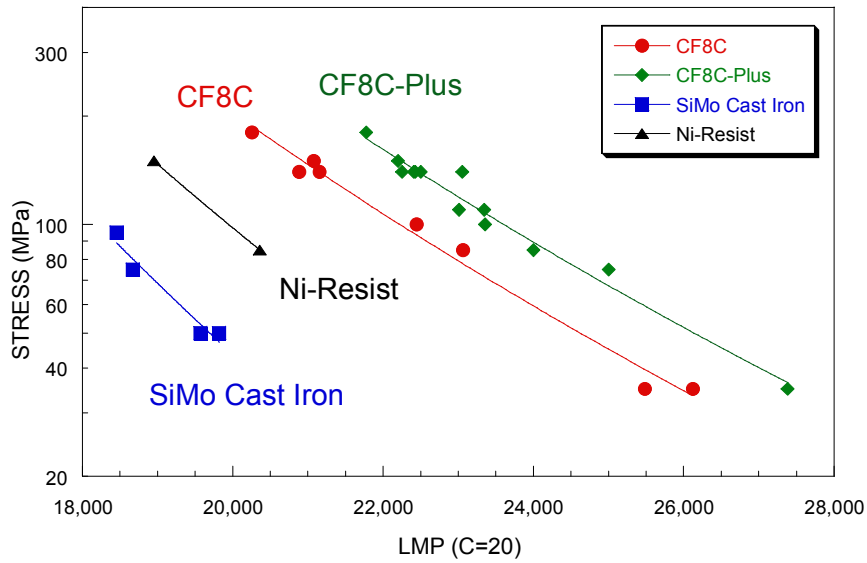

Figure 2. Creep-rupture stress plotted vs LMP for various ORNL creep-rupture tests at 500–850°C in air of various commercial heats of SiMo ductile and Ni-resist austenitic cast irons and standard CF8C and CF8C-Plus. CF8C-Plus shows significant creep-strength advantage over the standard steel or the cast irons.

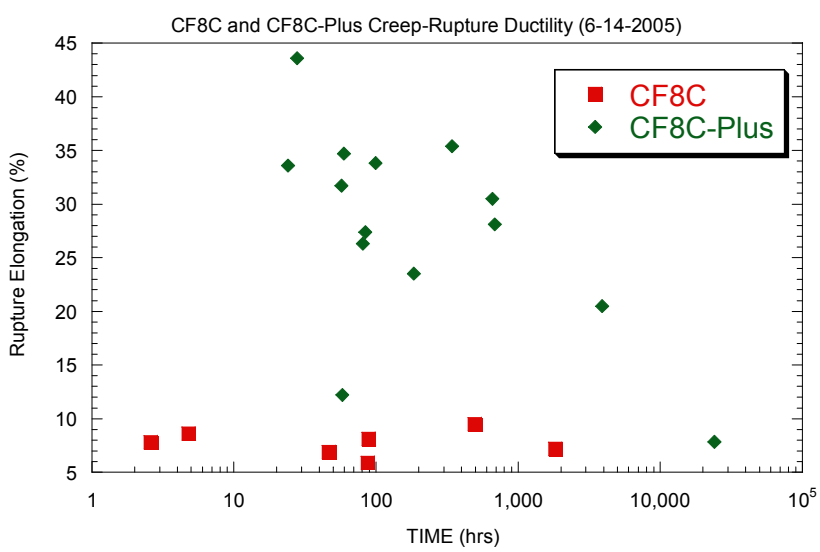

Figure 3. Comparison of creep rupture ductility data vs rupture time for cast CF8C-Plus and standard CF8C (same data as in Figure 2) for creep-rupture testing in air at 650–850°C and 35–200 MPa.

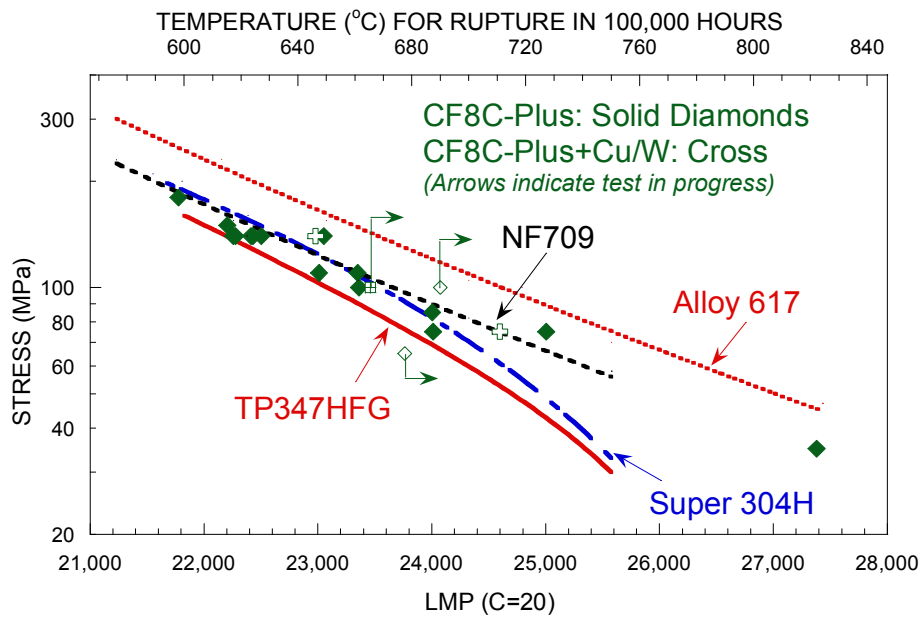

Figure 4. Creep-rupture stress plotted vs LMP for various ORNL creep-rupture tests at 700–850°C in air of CF8C-Plus and CF8C-Plus Cu/W. CF8C-Plus has better creep-strength than most wrought heat-resistant austenitic stainless steels and alloys and compares well with alloy 617, a Ni-Cr-Co superalloy.

In FY 2005, ORNL began testing new commercial scale-up heats of CF8C-Plus Cu/W produced by MetalTek. A 500-lb heat of the new CF8C-Plus Cu/W was cast as centrifugal rings and as kiel blocks in sand, together with similar castings of CF8C-Plus and standard CF8C steels for comparison. The CF8C-Plus Cu/W has higher yield-strength than CF8C-Plus at 600–900°C, and the few creep-tests conducted indicate better creep strength as well (Figure 4). Comparison of creep-strain versus time plots for tests at 750°C (Figure 5) clearly shows that the new CF8C-Plus Cu/W has a

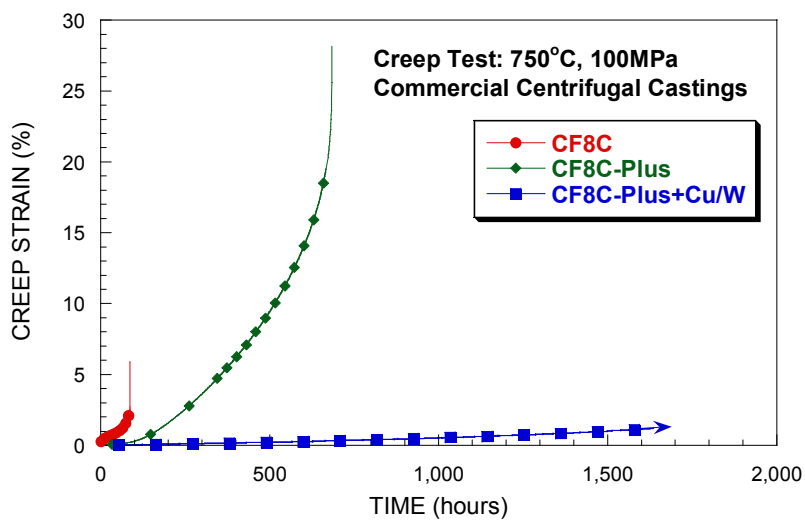

Figure 5. Plots of creep-strain vs time for heats of standard CF8C, CF8C-Plus and the new CF8C-Plus Cu/W, all tested in air at 750°C. Clearly the CF8C-Plus Cu/W has much more creep-resistance, with an extended secondary creep-regime and a very low steady-state creep rate.

prolonged period of creep at a very low creep rate (secondary creep regime) relative to standard CF8C or CF8C-Plus steels.

In 2006, ORNL will continue testing and aging studies on the new CF8C-Plus Cu/W steel. ORNL will also finish and analyze the side-by-side comparison of CF8C-Plus and the Diado KN2 cast stainless steels to support and enable CAT's development of cast stainless steel turbocharger housings.

Conclusions

ORNL and CAT have finished the initial commercialization phase for CF8C-Plus cast stainless steel, and have begun the second stage of producing more and larger heats of steel. They will expand the preliminary testing and include long-term aging, creep-rupture and more complex mechanical testing (fatigue, thermal-fatigue and creep-fatigue) and begin commercial component casting trials. To date, more than 30,000 lb of commercial CF8C-Plus stainless steel has been cast for various applications, and all prototype component castings have been successful on the first trial as a result of good castability. Efforts to expand commercial applications and facilitate licensing continue.

For advanced diesel-engine exhaust manifold and turbocharger applications, CF8C-Plus steel has an overwhelming high-temperature strength and creep-resistance advantage over conventional exhaust component materials, such as SiMo or Ni-resist cast irons. CF8C-Plus also has enough of a creep-rupture strength advantage over standard CF8C steel and other heat-resistant stainless steels and alloys that it is being considered and tested for gas turbines, advanced steam turbines, and various other applications.

Based on ORNL lab-scale trial heats, a new heat of CF8C-Plus Cu/W has been melted commercially by MetalTek. Testing began this year and will continue next year. The CF8C-Plus Cu/W has better yield strength than CF8C-Plus at 600°C and above, and preliminary creep testing at 750°C shows improved creep resistance as well.

Publications/Presentations

P. J. Maziasz, I. G. Wright, J. P. Shingledecker, T. B. Gibbons, and R. R. Romanosky, "Defining the Materials Issues and Research Needs for Ultra-Supercritical Steam Turbines," pp. 602–622 in *Proc. 4th Internat. Conf. on Advances in Materials Technology for Fossil Power Plants*, ASM-International, Materials Park, Ohio, 2005.

J. P. Shingledecker, P. J. Maziasz, N. D. Evans, and M. J. Pollard, "Creep Behavior of a New Cast Austenitic Alloy," to be published in *Proc. ECCC Conference on Creep and Fracture in High Temperature Components—Design and Life Assessment Issues,* London, UK, September 12–14, 2005.

J. P. Shingledecker, P. J. Maziasz, N. D. Evans, and M. J. Pollard, "Alloy Additions for Improved Creep-Rupture Properties of a Cast Austenitic Alloy," pp. 129–138 in *Proc. Conf. Creep Deformation and Fracture, Design, and Life Extension*, The Materials Society, Warrendale, PA, 2005.

P. J. Maziasz, J. P. Shingledecker, N. D. Evans, and M. J. Pollard, "Update on ORNL/CAT CRADA on CF8C-Plus Cast Stainless Steel: Progress on Commercial Scale-Up in 2004/2005," presented at DOE FreedomCAR and Vehicle Technologies Review at Oak Ridge National Laboratory, March 2, 2005.

M. J. Pollard, P. J. Maziasz, and J. P. Shingledecker, "Development of Low-Cost Cast Austenitic Stainless Steel for Diesel Engine and Gas Turbine Applications," presented at DOE Project Review at Caterpillar, Peoria, Illinois, April 27, 2005.

P. J. Maziasz, J. P. Shingledecker, N. D. Evans, and M. J. Pollard, "Development, Properties, and Applications of CF8C-Plus," presented during a visit to Stainless Foundry and Engineering, Inc., Milwaukee, Wisconsin, June 16, 2005.

P. J. Maziasz, J. P. Shingledecker, N. D. Evans, and M. J. Pollard, "Development, Properties, and Applications of CF8C-Plus," presented during a visit to MetalTek International, Waukesha, Wisconsin, June 27, 2005.

J. P. Shingledecker, P. J. Maziasz, N. D. Evans, and M. J. Pollard, "Creep Behavior of a New Cast Austenitic Alloy," plenary session talk at the European Creep Collaborative Committee (ECCC) Conference on Creep and Fracture in High-Temperature Components—Design and Life Assessment Issues, London, UK, September 12–14, 2005.

Special Recognitions and Awards/Patents Issued

The review panel for the FY 2005 DOE Heavy Vehicles Materials Program Merit Review and Peer Evaluation Meeting awarded this project the highest

overall score in the Heavy Vehicles Propulsion Materials sub-program. The project also received the highest individual evaluation category grades for relevance, technical accomplishments, and technology transfer.

The original patent application for both CF8C-Plus and CN-12-Plus filed in 2000 by Caterpillar was split and continued as two patents: "Heat and Corrosion Resistant Cast CN-12 Type Stainless Steels With Improved High Temperature Strength and Ductility" (US 2003/0084967) and "Heat and Corrosion Resistant Cast CF8C Stainless Steels With Improved High Temperature Strength and Ductility" (US 2003/0056860), both by P. J. Maziasz and R. W. Swindeman (ORNL), T. McGreevy (University of Bradley/CAT), M. J. Pollard, and C. W. Siebenaler (CAT). Actions to obtain final patent approval continued in FY 2005.

K. Viscoplastic Twinning in an Ultrafine TiAl/Ti_3Al Laminate Composite

Luke Hsiung
Chemistry and Materials Science Directorate
Lawrence Livermore National Laboratory
L-352, P.O. Box 808
Livermore, CA 9455-9900
(925)-424-3125; fax: (925) 424-3815; email: hsiung1@llnl.gov

DOE Technology Development Area Specialist: James J. Eberhardt
(202) 586-9837; fax: (202) 586-1600; e-mail: james.eberhardt@ee.doe.gov
ORNL Technical Advisor: D. Ray Johnson
(865) 576-6832; fax: (865) 574-6098; e-mail: johnsondr@ornl.gov

Contractor: Oak Ridge National Laboratory, Oak Ridge, Tennessee
Contract No.: DE-AC05-00OR22725
Subcontractor: Lawrence Livermore National Laboratory

Objectives

- Exploit thermomechanical-processing techniques to fabricate TiAl/Ti_3Al nanolaminate composites with lamella widths down to nanometer length scales.
- Characterize microstructure and elevated-temperature creep resistance of the nanolaminate composites.
- Investigate the fundamental interrelationships among microstructures, alloying additions, and mechanical properties of the nanolaminate composites to achieve the desired properties of the composites for high-temperature structural applications.

Approach

- Employ in-situ laminate composites with nominal compositions of Ti-47Al-2Cr-2Nb, Ti-46Al-3Nb-1W-0.1B, and Ti-46Al-3Nb-2W-0.1B (at. %). The in-situ laminate composites were fabricated at Oak Ridge National Laboratory (ORNL) by hot extrusion of cast alloys at 1350°C.
- Conduct creep tests in a dead-load creep machine with a lever arm ratio of 16:1. Tests were performed in air in a split furnace with three zones at 760 and 815°C.
- Examine the microstructures of creep-deformed samples using a JEOL-200CX transmission electron microscope (TEM).

Introduction

Two-phase [TiAl (γ-L10) and Ti_3Al (α2-DO19)] fully lamellar TiAl alloys have recently attracted much attention because of their low density (ρ = 3.9 g/cc), high specific strength, adequate oxidation resistance, and good combination of ambient-temperature and elevated-temperature mechanical properties, which are of interest for aerospace and transportation applications such as high-temperature components in turbine and combustion engines. Through alloy design and microstructural refinement, significant progress has been made recently to improve both room-temperature ductility/toughness and high-temperature creep resistance of the material.[1–5] One of the interesting deformation substructures of the laminate material with an ultrafine microstructure is the formation of

high-density twin lamellae with the widths in the sub-micrometer or nanometer length scale.[5] The most unique characteristic of the twinning phenomenon observed from the TiAl/Ti_3Al laminate material is that it can even take place at elevated temperatures under loading conditions such that the steady creep rate is as low as 10^{-7} s^{-1} and with a stress level much lower than its yield strength. This viscoplastic twinning phenomenon is different from the twinning phenomenon that commonly occurs in conventional metals and alloys deformed under low-temperature and/or high strain-rate conditions. It has been reported previously that the occurrence of {111}<112>-type twinning in the TiAl/Ti_3Al laminate material is intimately related to the dissociation of dislocations in laminate interfaces and the homogeneous glide of $1/6 < 11\bar{2} >$ twinning dislocations in the {111} planes of γ lamellae.[6] Results obtained from more rigorous TEM analyses are reported here in order to further elucidate the underlying mechanisms for the occurrence of viscoplastic twinning in the TiAl/Ti_3Al laminate material.

Approach

The ultrafine two-phase [TiAl-(γ)/Ti_3Al-(α_2)] lamellar alloy was fabricated by a powder metallurgy process, which involves hot extrusion of gas-atomized titanium aluminide powder with a nominal composition of Ti-47Al-2Cr-2Nb (at. %) at 1400°C. After extrusion, the material was stress relieved at 900°C in a vacuum (~10^{-4} Pa) for 2 h. Creep tests were conducted at 760°C in a dead-load creep machine with a lever arm ratio of 16:1. Detailed information regarding the creep experiment and experimental data were reported elsewhere.[5] For the current study, the deformation substructure of a specimen tested at 138 MPa with a steady creep-rate of 2.0×10^{-9} s^{-1}, and that of a specimen tested at 518 MPa with a steady creep-rate of 2.5×10^{-7} s^{-1} were examined. TEM foils were prepared by twin-jet electropolishing in a solution of 60 vol % methanol, 35 vol % butyl alcohol and 5 vol % perchloric acid at ~15 V and –30°C. The microstructures of both as-fabricated material and tested samples were examined using a JEOL-200CX TEM equipped with a double-tilt goniometer stage. Images of microstructures were recorded using high-resolution lattice imaging techniques and weak-beam dark field (WBDF) imaging techniques under *g (3g)* two-beam diffraction conditions with the deviation factor ω (= $\xi_g s$) > ~1, where ξ_g is the extinction distance and *s* is the deviation distance from the exact Bragg position. The $g \cdot b$ invisibility criteria used for determining the Burgers vector of Shockley partials are described as follows:[7]
(a) invisible if $g \cdot b = 0$ or ±1/3; (b) invisible if $g \cdot b = -2/3$ but visible if $g \cdot b = +2/3$ provided the deviation factor ω > ~1; (c) invisible if $g \cdot b = +4/3$ but visible if $g \cdot b = -4/3$, provided the deviation factor ω > ~1.

Results

Movement and Pileup of Interfacial Dislocations

The results of an in-situ TEM experiment that directly observed cooperative movement of interfacial dislocations in a TiAl/Ti_3Al laminate sample under room-temperature straining conditions have been reported previously.[8] Figure 1 is a typical example showing that the interfacial dislocations can be blocked by impinged lattice dislocations during their movement along a laminate interface. Here, a dislocation network formed by the reaction between impinged lattice dislocations and interfacial dislocations can be readily seen in a γ/α_2 interface. Figure 2 shows the results of an in-situ TEM experiment, which evidence the motion and pile-up

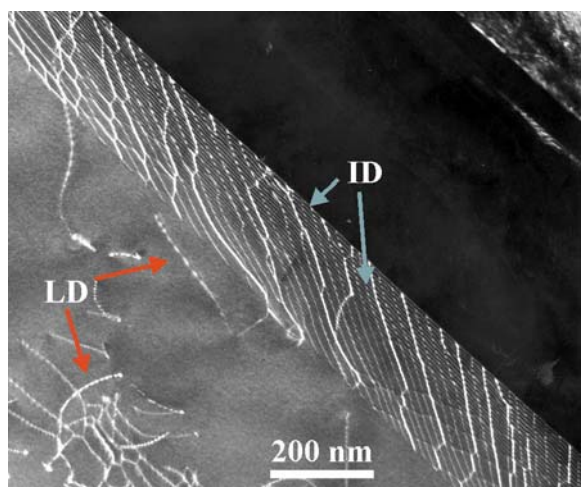

Figure 1. A WBDF TEM image shows that the movement of interfacial dislocations is hampered because of the formation of dislocation networks as a result of the reaction between impinged lattice dislocations (LD) and interfacial dislocations (ID).

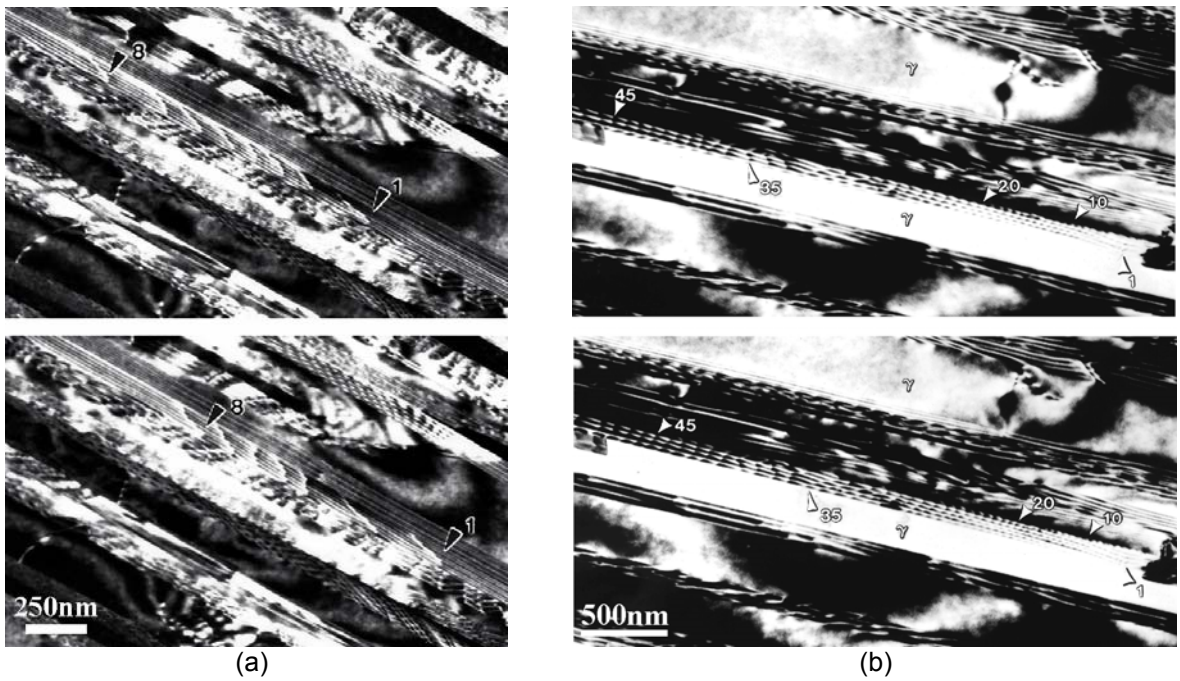

Figure 2. Consecutive in-situ TEM images show (a) the movement of an interfacial dislocation array in a laminate interface (time span: 30 s), and (b) the movement and pile-up of interfacial dislocations in a laminate interface adjacent to the tip of an α_2 fragment (time span: 30 s).

of interfacial dislocations during electron-beam heating of a thin foil (prepared from a sample pre-crept at 760°C and 138 MPa) that contains residual stress. The original idea of this experiment assumes that the relaxation of residual stress can result in the motion of interfacial dislocations. Since the purpose of the study is only to demonstrate the interfacial dislocation motion, the amount of temperature increase by beam heating is not a major concern. It is also noted that local heating can be achieved when an electron beam is focused on a small spot the size of several micron meters. Figure 2(a) shows the cooperative motion of a dislocation array of eight interfacial dislocations on a laminate interface. It is interesting to note that the motion of each dislocation was in a viscous drifting or pinning/unpinning fashion, and each of them has a different drifting velocity. Here, after beam focusing (heating) for 30 s, the No. 1 leading dislocation of the array moved about 375 nm, and the No. 8 trailing dislocation moved about 425 nm. This suggests that each dislocation has different mobility as a result of the solute-dragging effect. Figure 2(b) shows the motion of interfacial dislocations within a dislocation pileup on a laminate interface. Here, the head of the dislocation pileup is at the tip of a faulted α_2-lamella adjacent to the No. 1 dislocation. Notice that the dislocation spacing increases with increasing distance from the head of the pile-up, and those dislocations close to the head of the pile-up moved slower than those distant from the head. For instance, the No. 10 and No. 20 dislocations moved about 170 nm, and the No. 35 and No. 45 dislocations moved about 250 nm after beam focusing (heating) for 30 s. That is, during beam heating, dislocations in the pile-up start to squeeze, which causes the increase of dislocation density within the pile-up.

These in-situ observations of interfacial dislocation motion and pile-up are rationalized below. Since the thin foil contains residual stress, each dislocation starts to move under a heating condition with a velocity $v = MF$, where v is the (drift) velocity of dislocation, M is the mobility of dislocation, and F is the effective force acting on the dislocation. An explicit expression for the dislocation mobility M limited by solute drag can be found in Ref. 9:

$$M = \frac{D_s \Omega}{\beta b^2 C_o k T} \quad ,$$

where β is a constant, b is the length of Burgers vector, Co is the solute concentration, Ds is the solute diffusion coefficient, and Ω is the atomic volume of the solute. The effective force (F) acting on the i-th dislocation in a dislocation array or pile-up can be expressed as

$$F = \tau b - \frac{\mu b^2}{2\pi(1-\nu)} \sum_{\substack{j=0 \\ j\neq i}}^{n} \frac{1}{x_i - x_j} \quad ,$$ [10]

where the term

$$\frac{\mu b^2}{2\pi(1-\nu)} \sum_{\substack{j=0 \\ j\neq i}}^{n} \frac{1}{x_i - x_j}$$

represents the sum of internal forces acting on the i-th dislocation by the other dislocations of the pile-up; $x_i - x_j$ represents the distance between the i-th and j-th dislocations. Accordingly, v increases as a result of the increase of dislocation mobility as temperature (T) increases during beam heating, and v diminishes as temperature decreases to an ambient temperature. The velocity of dislocations close to the head of the pile-up becomes slower, indicating that the internal stress acting on the dislocations increases as the dislocations move closer to the head, and therefore reducing the effective force (F) acting on the dislocations.

Viscoplastic Deformation Twinning

When an alloy sample was creep-deformed at 760°C with a constant applied stress of 518 MPa under a strain rate of 3×10^{-7} s^{-1}, a deformation substructure associated with deformation twins was developed within γ lamellae. Typical $(\bar{1}11)$ [211]-type twin lamellae formed within γ lamellae are shown in Figure 3. Notice that one of the twin lamellae in Figure 3(a) (labeled by an arrow) was still growing toward another interface. Similar features were also observed elsewhere in the same sample. This suggests that the laminate interface is the major source for the occurrence of viscoplastic deformation twinning. The viscoplastic twinning phenomenon can be viewed as a relaxation process to relieve the local stress concentration caused by the pile-up of interfacial dislocations. The effective stress (τe) at the head of the pile-up of n dislocations can be evaluated by $\tau e = n\tau I$ (Ref. 11), where τi is the resolved shear stress acting on the interface. To relieve the stress concentration, deformation twinning in γ layers is therefore taking place by a dislocation reaction based upon a stair-rod cross-slip mechanism, as schematically illustrated in Figure 3(b). For the formation of a $(\bar{1}11)$-type twin lamella, the corresponding dislocation reaction is $1/6[\bar{1}2\bar{1}]$ (111) [$\mathbf{b_1}$] → $1/6$[011] (100) [$\mathbf{b_2}$] + $1/6[\bar{1}1\bar{2}]$ $(\bar{1}11)$ [$\mathbf{b_3}$]. The $(\bar{1}11)$-type twin is accordingly formed within γ lamella by successively dissociating the [$\mathbf{b_1}$] interfacial dislocations in the pile-up and emitting the [$\mathbf{b_3}$] twinning dislocations into the $(\bar{1}11)$ γ plane and leaving the [$\mathbf{b_2}$] stair-rod dislocations in the (100)γ plane. Figures 3(c) and 3(d) show the edge-on views of the $(\bar{1}11)$-type twin lamellae, in which their widths were measured as varying between 3 and 20 nm.

The formation of [$\mathbf{b_2}$] stair-rod dislocations at the intersections between twin and α_2 lamellae is evidenced in Figures 4(a) and 4(b), in which the array of $1/6$[011] stair-rod dislocations becomes invisible [Figure 4(a)] or visible [Figure 4(b)] when a reflection vector (g) 200 or 021 is used for imaging. It is noted that the individual stair-rod dislocation is not resolvable because of a narrow distance (0.25 nm) between two stair-rod dislocations. The formation of [$\mathbf{b_3}$] twinning dislocations for the $(\bar{1}11)$-type twin lamella is evidenced in Figures 4(c) and 4(d), in which the array of $1/6$[112] twinning dislocations becomes visible [Figure 4(c)] or invisible [Figure 4(d)] when a reflection vector of 111 or $\bar{2}02$ is used for imaging. The significance of the proposed mechanism is to reveal that there are several barriers to be overcome in order to activate the twinning reaction. These barriers include (1) the repulsive force between the interfacial (Shockley) and stair-rod dislocations, (2) the increase of line energy due to the dislocation dissociation, and (3) the increase of interfacial energy due to the formation of twin faults. Among which the repulsive force (F) between the interfacial (Shockley) and stair-rod dislocations is considered to be the rate-limiting process. That is, a critical stress (τ_c) is required to activate for the twinning reaction, i.e., to activate the dissociation reaction for twinning. Assuming an isotropic elasticity, the critical stress (τ_c) can be approximately evaluated as

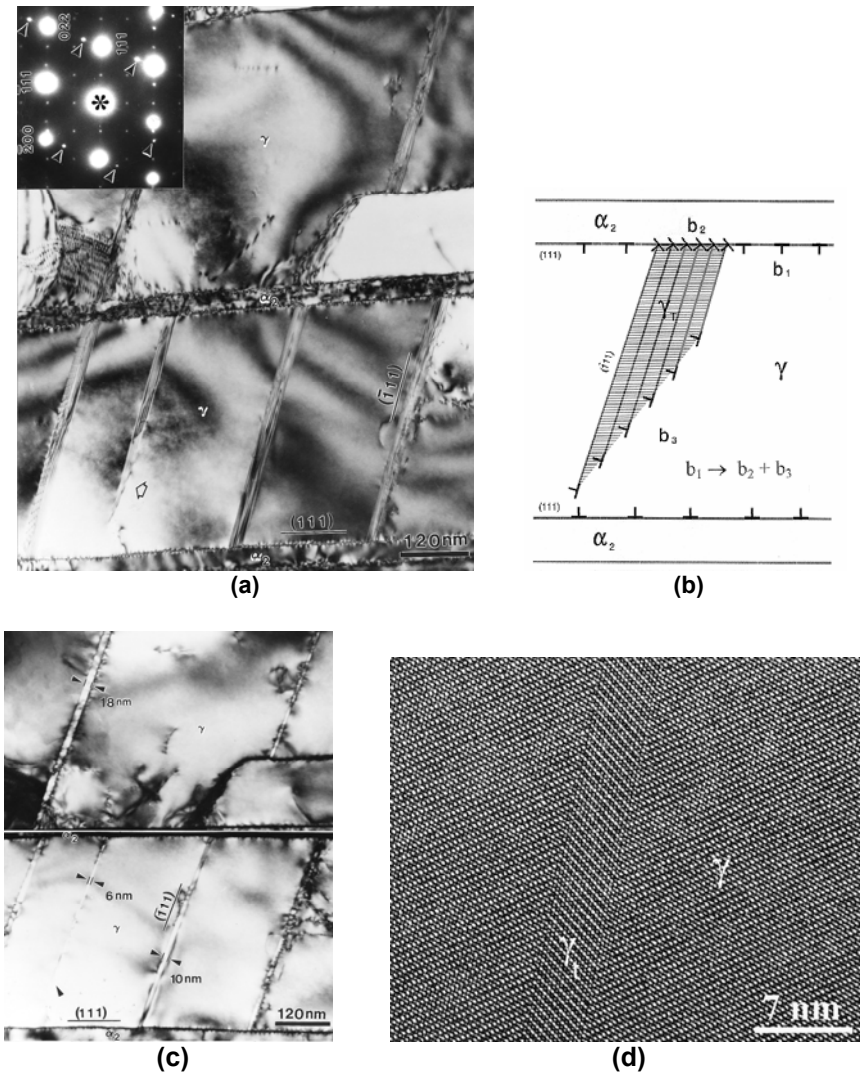

Figure 3. A dark-field TEM image shows several ($\bar{1}11$) type twin lamellae formed within a γ lamella (a); a schematic illustration of the nucleation of a ($\bar{1}11$) type twin lamella (γ_t) from a γ/α_2 interface (b), where b_1, b_2, and b_3 denote the interfacial, stair-rod, and twinning dislocations, respectively; and edge-on views of twin lamellae show the widths of the ($\bar{1}11$)-type twin lamellae (c) and (d).

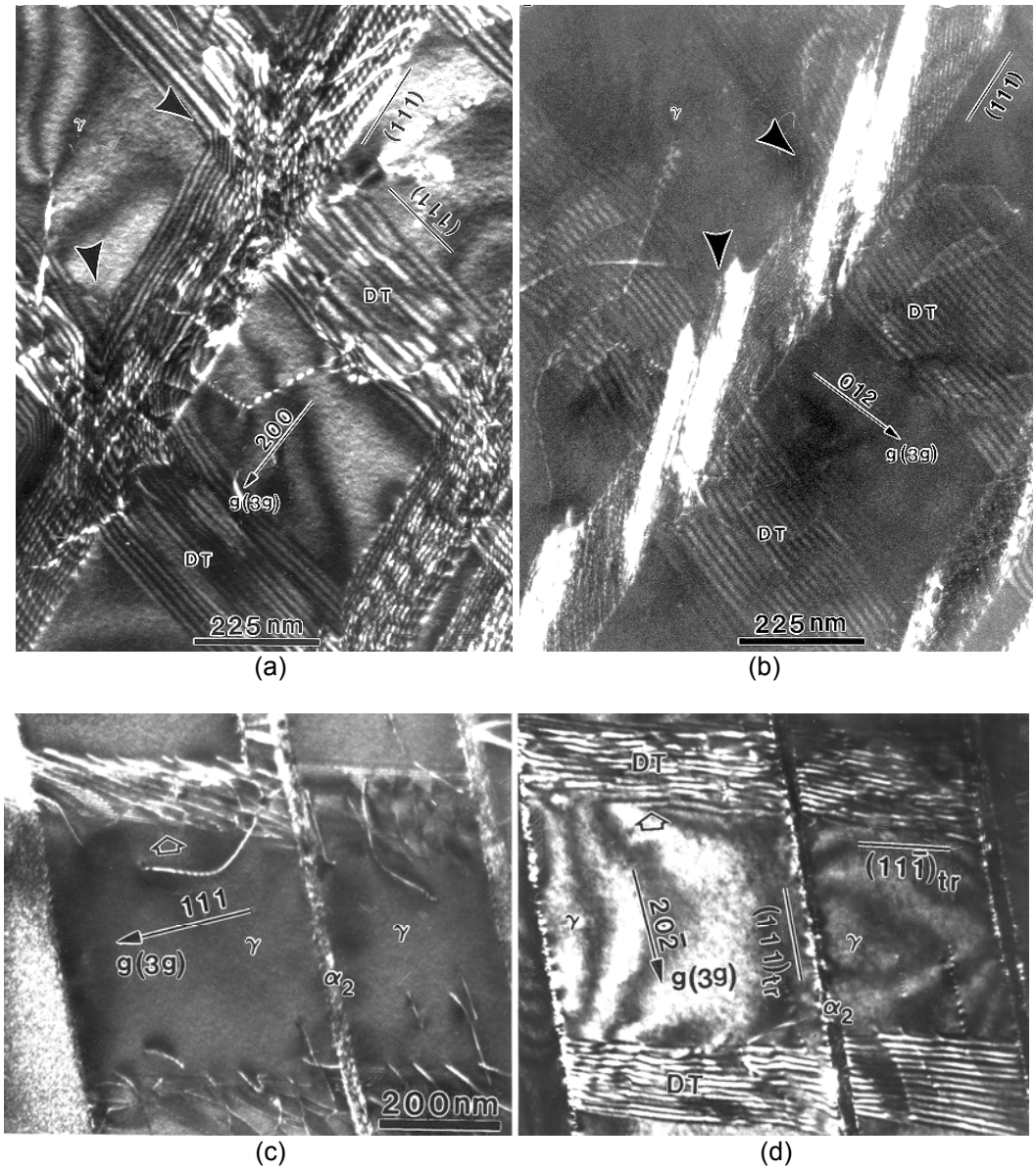

Figure 4. WBDF TEM images show the g·b contrast visibility analyses 7 for the arrays of [b_2] 1/6[011] stair-rod dislocations formed at the intersections (indicated by arrows) between the ($\bar{1}$11)-type deformation twins (DT) and α_2 lamellae: (a) Z (zone axis) ≈ [0$\bar{1}$2], g = 200, g·b = 0 (invisible), (b) Z ≈ [0$\bar{1}$2], g = 021, g·b =1/2 (visible); and the analyses for the arrays of [b_3] 1/6[112] twinning dislocations of the (11$\bar{1}$)-type deformation twins: (c) Z ≈ [$\bar{1}$2$\bar{1}$], g = 111, g·b = 2/3, (visible), and (d) Z ≈ [$\bar{1}$2$\bar{1}$], g = 20$\bar{2}$, g·b = 1/3 (invisible).

$\tau_c b_1 = F \approx \eta\mu b_1 b_2 \cos\theta/2\pi r$, where $\eta = 1$ for screw dislocations and $\eta = 1/(1 - \upsilon)$ for edge dislocations; υ is Poisson's ratio (~0.3); μ is shear modulus (~56 GPa at 760°C) (Ref. 12); b_1 = 0.163 nm; and b_2 = 0.094 nm for Shockley and stair-rod dislocations, respectively; θ (= 54.4°) is the angle between ($\bar{1}$11) and (100) planes; and r (0.25 nm) is the distance between the two dislocations. The critical stress (τ_c) required for twinning is thus approximately 1.95 GPa for screw dislocations and 2.79 GPa for edge dislocations.

In the case of a low applied stress (138 MPa), the resolved shear stress (τi) acting on the interface plane is about 69 MPa (assuming Schmid factor = 0.5), and the number of pile-up dislocations required to create a sufficient stress concentration (i.e., $\tau e = n\tau i \geq \tau c$) for twinning to occur is $n \geq 29$. In the case of a high applied stress (518 MPa), the resolved shear stress acting on the same interface plane is about 259 MPa, and the number of pile-up dislocations required for twinning to occur is $n \geq 8$. Thus the accumulation creep strain required to bring on the viscoplastic twinning is smaller and therefore easier to reach. Besides, the average velocity of dislocations is relatively faster when tested under a high applied stress, since the strain rate is higher, which gives a shorter time to develop a pile-up configuration when tested under high applied stresses. That is, it is more feasible that the viscoplastic twinning will take place when the laminate is creep-deformed under high applied stresses. A recent report on deformation twinning of the same material creep-deformed under different loading conditions has evidenced that the twinning occurred shortly after the creep strain reached 0.67% under a high applied stress (518 MPa), whereas the twinning took place when the creep strain reached ~1.5% under a low applied stress (138 MPa).[13]

Conclusion

The viscoplastic twinning phenomenon, which takes place within an ultrafine $TiAl/Ti_3Al$ laminate composite subjected to an elevated-temperature creep deformation, has been studied. The viscoplastic twinning phenomenon is found to be intimately related to the movement, pile-up, and dissociation of the pre-existing dislocation arrays in laminate interfaces. When the arrays of interfacial dislocation (e.g., *1/6*<112> Shockley partials) move along the interfaces, obstacles such as impinged lattice dislocations, and interfacial ledges can impede their movement. The dislocation arrays start piling up behind an obstacle because an individual Shockley partial is energetically unfavorable to undergo cross-slip or climb that otherwise will generate stacking fault on its wake if it moves away from the interface. Thus the arrays of interfacial dislocations can easily be piling up even at elevated temperatures. The viscoplastic twinning within the creep-deformed laminate can accordingly be rationalized as a relaxation process to dissipate the internal stress resulting from dislocation pile-up. The twinning process involves the dissociation of interfacial dislocation into stair-rod (or residual) and twinning dislocations, i.e., $1/6[\bar{1}2\bar{1}]\,(111) \rightarrow 1/6[011]\,(100) + 1/6[\bar{1}1\bar{2}]\,(\bar{1}11)$ for $(\bar{1}11)\,[\bar{1}1\bar{2}]$–type twinning. It is concluded that the dislocation pile-up configuration is a prerequisite to begin the process of deformation twinning, which is more likely to occur under low-temperature and high strain-rate deformation conditions for conventional metals and alloys. The occurrence of time-dependent viscoplastic twinning in the $TiAl/Ti_3Al$ laminate reveals that the dislocation pile-up configuration can be readily formed along laminate interfaces even at elevated temperatures.

References

1. Y-W. Kim and D.M. Dimiduk, *JOM*, **43**(8), 40 (1991).
2. Y–W. Kim, *Acta Metall. Mater.*, **40**, 1121 (1992).
3. C. T. Liu, J. H. Schneibel, P. J. Maziasz, J. L. Wright, and D. S. Easton, *Intermetallics*, **4**, 429 (1996).
4. C. T. Liu, P. J. Maziasz, and J. L. Wright, *Mat. Res. Soc. Symp. Proc.*, **460,** 83 (1997).
5. L. M. Hsiung and T. G. Nieh, *Matls. Sci. & Engrg.*, **A364**, 1 (2004).
6. L. M. Hsiung and T.G. Nieh, *Matls. Sci. & Engrg.*, **A239-240**, 438 (1997).
7. J. W. Edington, *Practical Electron Microscopy in Materials Science*, Van Nostrand Reinhold, New York, 1976.
8. L. M. Hsiung, A. J. Schwartz, and T. G. Nieh, *Intermetallics*, **12**, 727 (2004).
9. E. Arzt, M. F. Ashby, and R. A. Verrall, *Acta Metall*,. **31**, 1977 (1983).
10. J. Weertman, *J. Appl. Phys.*, **28**, 1185 (1957).
11. J. D. Eshelby, F. C. Frank, and F. R. N. Nabarro, *Phil. Mag.*, **42**, 351 (1951).
12. S. C. Huang and J. C. Chesnutt, *Intermetallic Compounds: Principles and Practice 2*, eds. J. H. Westbrook and R. L. Fleischer, John Wiley & Sons, p. 73, 1995.
13. J. G. Wang, L. M. Hsiung, and T. G. Nieh, *Scripta Mater.*, **39**, 957 (1998).

Presentations and Publications

L. M. Hsiung and T. G. Nieh, "In-Situ TEM Study of Interface Sliding and Migration in an

Ultrafine Lamellar Structure," presented at the 2005 MRS spring meeting.

L. M. Hsiung, "TEM Study of Microstructures in a Creep-Deformed TiAl/Ti_3Al Nanocomposite," *Heavy Propulsion Materials Program Quarterly Progress Report for October through December 2004*, U.S. Department of Energy, Washington, D.C., 2004.

L. G. Zhou, L. M. Hsiung, and Hanchen Huang, "Nucleation and Propagation of Deformation Twin in Polysynthetically Twinned TiAl," *Computer Modeling in Engineering and Sciences*, **6**(3) (2004) 245–252.

L. Ti-6Al-4V Billet Feedstock Manufacture and Evaluation

S. M. Abkowitz, S. Abkowitz, and H. Fisher
Dynamet Technology, Inc.
Eight A Street
Burlington, MA 01803
(781) 272-5967; fax: (781) 229-4879; e-mail: sabkowitz@dynamettechnology.com

DOE Technology Development Area Specialist: James J. Eberhardt
(202) 586-9837; fax: (202) 586-1600; e-mail: james.eberhardt@ee.doe.gov
ORNL Technical Advisor: D. Ray Johnson
(865) 576-6832; fax: (865) 574-6098; e-mail: johnsondr@ornl.gov

---

Contractor: Oak Ridge National Laboratory, Oak Ridge, Tennessee
Contract No.: DE-AC05-00OR22725
Subcontractor: Dynamet Technology, Inc., Burlington, Massachusetts

---

Objectives

- Develop low-cost Ti-6Al-4V billet feedstock using a blend of titanium (Ti) and alloy powders and inexpensive Ti-6Al-4V machine turnings, or using 100% turnings.
- Evaluate this low-cost Ti alloy feedstock as a starting billet material for casting, forging, and extrusion operations.

Approach

- Develop a procedure for producing low-cost Ti billet using a combination of inexpensive Ti alloy machine turnings and Ti and alloy powders, or 100% machine turnings. Evaluate the billet for density and microstructure.
- Subject the feedstock billets to casting, forging, and extrusion operations. The three operations will yield Ti-6Al-4V test bars.
- Evaluate the quality of the test bars produced through chemistry and mechanical testing.

Accomplishments

- Produced a high-density billet containing 60% turnings/40% Ti alloy powder that was produced using a core of 100% turnings, surrounded by a "can" made from Ti alloy powder.
- Produced a billet using 100% turnings, achieving full density, using cold+hot isostatic pressing (CHIP) technology with conventional canning in mild steel for the HIP operation.
- Extruded a billet, composed of 100% turnings surrounded by a "can" made from Ti alloy powder, to high density barstock.
- Cast plates from a billet of 100% Ti-6Al-4V machine turnings. The tensile strength and ductility of the resultant cast plate exceeded the specified properties for Ti-6Al-4V castings.
- Determined that contaminants in the turnings caused low ductility in the extruded barstock and characterized these contaminants by metallographic analysis and analysis of tensile fracture surfaces using SEM/EDS.
- Demonstrated that the contaminants can be eliminated by melting the low cost feed stock.

- Preformed economic analyses that showed that extruded bar can be produced from billet cast from low cost feedstock at a savings of 48 to 58% over conventional extrusions.

Future Direction

- Demonstrate that bar meeting the typical mechanical properties of conventional Ti-6Al-4V can be extruded from cast extrusion billet produced by the low cost feedstock process in order to realize the commercial potential of this technology.

Summary

Dynamet Technology has developed a novel method of producing low-cost Ti alloy billet from Ti scrap turnings by powder metallurgical processing. Dynamet's process consists of consolidating the turnings using a combination of cold isostatic pressing and vacuum sintering, followed by HIP, if necessary (Figure 1).

The result is feedstock that can be used to produce cast extrusion billet that can then be used to produce extrusions. This process promises to produce extrusions that are a low-cost alternative to extrusions produced from conventional ingot. Dynamet's economic analysis estimates the cost savings in producing extrusions at 48 to 58%. The use of low-cost billet made by Dynamet's process in manufacturing Ti alloy parts for heavy duty vehicles will save energy, increase payloads, and reduce emissions. Indeed, the availability of low-cost Ti would make Ti attractive to any industry that can

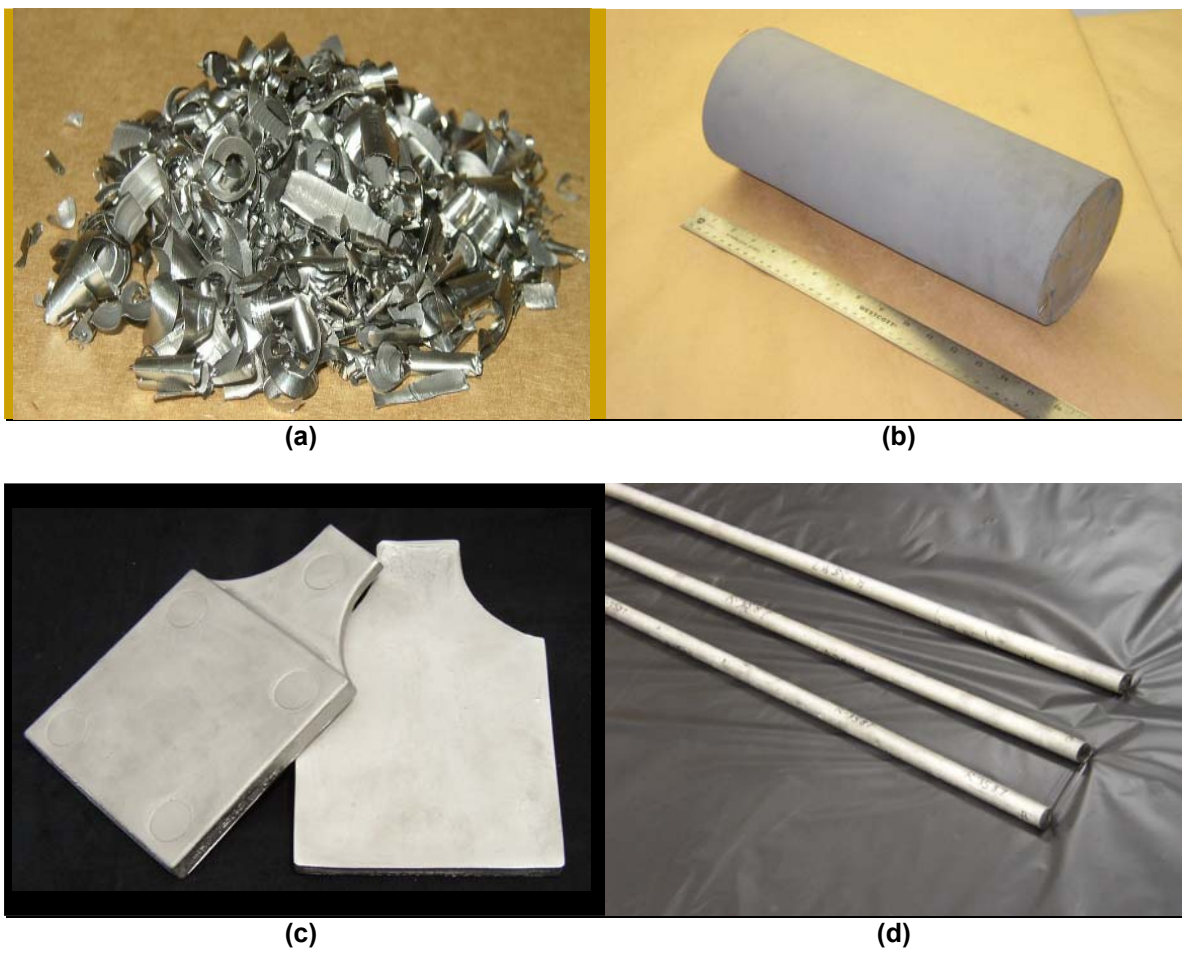

Figure 1. The dynamet powder metallurgical process (a) Ti-6Al-4V turnings, (b) LCFP billet, (c) cast test plates, and (d) extrusion produced from LCFP billet.

benefit from the metal's advantages as a structural material. Dynamet's process would also result in significant energy reduction by recycling Ti turnings and thus reducing the industry's dependence on energy-intensive Kroll process sponge and the subsequent more extensive metalworking.

The next step is to demonstrate that bar meeting the typical mechanical properties of conventional Ti-6Al-4V can be extruded from cast extrusion billet produced by the low cost feedstock process in order to realize the commercial potential of this technology (Figure 2).

Presentations and Publications

Dynamet Technology, Inc., *Ti-6Al-4V Billet Feedstock Manufacture and Evaluation—Final Report*, Burlington, Massachusetts.

Figure 2. Bar with the properties of Ti-6 Al-4V can be developed from cast extrusion billets produced by the low-cost feedstock process.

M. High-Density Infrared Surface Treatment of Materials for Heavy-Duty Vehicles

T. N. Tiegs, F. C. Montgomery, D. C. Harper, J. O. Kiggans, and C. A. Blue
Oak Ridge National Laboratory
P.O. Box 2008, MS-6087
Oak Ridge, TN 37831-6087
(865) 574-5173; fax: (865) 574-4357; e-mail: tiegstn@ornl.gov

DOE Technology Development Area Specialist: James J. Eberhardt
(202) 586-9837; fax: (202) 586-1600; e-mail: james.eberhardt@ee.doe.gov
ORNL Technical Advisor: D. Ray Johnson
(865) 576-6832; fax: (865) 574-6098; e-mail: johnsondr@ornl.gov

Contractor: Oak Ridge National Laboratory, Oak Ridge, Tennessee
Prime Contract No: DE-AC05-00OR22725

Objectives

- Use high-density infrared (HDI) technology to produce corrosion and/or wear resistance coatings on metal substrates.
- Use lighter or more cost-effective bulk materials with coatings applied to surfaces where improved properties required.

Approach

- Examine a couple of approaches on surface modification that would be of interest to materials for heavy-duty vehicles.
- Examine the application and formation of adherent, wear/corrosion-resistant coatings.
- Base the initial tests on hard metal compositions applied onto iron-based parts that are currently used in diesel engines.

Accomplishments

- Determined that plain hard metal coatings without binder additions have a very narrow window of HDI process conditions and are not practical on a large scale.
- Correlated coating process parameters (compositions, HDI parameters) with coating microstructural development.

Future Direction

- Investigate the coating of complex shaped parts by HDI technology.
- Determine potential for producing wear-resistance diffusion coatings for heavy-duty vehicle applications.

Introduction

High-density infrared (HDI) technology is relatively new to the materials processing area and is gradually being exploited in materials processing. The HDI processing facility at Oak Ridge National Laboratory utilizes a unique technology to produce extremely high-power densities of up to 3.5 kW/cm^2 with a single lamp. Instead of using an electrically

heated resistive element to produce radiant energy, a controlled and contained plasma is utilized.

Because the technology is relatively new, its utility to the surface treatment of materials for applications in heavy-duty vehicles is being explored. In most cases, the need for wear resistance, or corrosion resistance, or high strength is only necessary in selected areas of the part that is exposed to the working environment or under high stress. Therefore, it would be desirable to use materials that are lighter or less expensive for the bulk of the part and only have the appropriate surface properties where required. In addition, the HDI approach would be more cost-effective than other competitive processes such as physical vapor deposition.

Non-line-of-sight coatings are of interest for application on heavy-duty vehicle parts, such as gears. Pack cementation is an industrial process currently used to apply diffusion coatings onto metal parts. Other research has shown that microwave heating can be used to produce superior diffusion coatings with alloying additives such as aluminum, silicon, and boron. The project will examine the potential to produce wear-resistance diffusion coatings by both HDI technology and microwave pack cementation.

Results

Earlier work had shown that adherent coatings of hard metal compositions could be applied to a variety of metal substrates (D2 tool steel, 4140 alloy steel, and cast iron). However, a problem with the earlier coatings was that a preheat step was required to minimize sintering of the slurry coating prior to bonding with the substrate. When the slurry coating was heated too fast, it tended to peel off from the substrate and crack. The preheating step allowed the substrate to get hot enough so bonding occurred.

Samples were fabricated that used either WC or TiC particles only for the coating. The sintering temperature for these plain carbides is significantly higher than the melting point of the substrates. Consequently, because no binder additions (i.e., Ni or Ni_3Al) will be present, sintering and cracking will be inhibited. This will allow the coating to heat up to a sufficiently high temperature so that the underlying substrate will melt and be wicked into the coating by capillary action. Previous work has shown that WC-cast iron composites have excellent wear behavior, so these will be the initial compositions.

Samples were fabricated with varying coating thickness (50 and 100 μm) and particle type (WC, TiC, W, or WC/W). The samples were infrared (IR) treated at numerous exposure conditions. Cracking of the coatings was observed in a similar behavior to previous tests where the binder was included. A preheat step helped to minimize the cracking. However, getting the coatings hot enough to melt the underlying substrate was extremely sensitive. The conditions to go from little bonding to where extensive melting of the entire sample occurred were very narrow. Control of the coating process without the incorporation of binder particles in the coating is very difficult.

Additional examinations of coatings with binders was done to correlate coating process parameters with coating microstructural development. Some of the parameters included substrate composition, binder chemistry, ceramic particle type, and HDI heating cycles. Previous results had shown excellent wear resistance for coatings having Ni_3Al as the binder in the hard metal coating. Consequently, most of the correlations were done with these coating types.

Examples of WC-Ni_3Al coatings on substrates of D2 tool steel, 4140 alloy steel, and cast iron are shown in Figures 1–3, respectively. The coatings are much thicker than the intended ~100 μm, indicating significant mixing with the underlying substrate. A penetration zone of Ni_3Al into the D2 tool steel was significant (≤100 μm), whereas only a minor reaction layer (~10 μm) was observed at the interface on the 4140 alloy steel. No reaction layer was evident with the cast iron substrate; however, there appeared to be a diffuse mixing zone within the coating. In addition, the cast iron had graphite precipitates throughout the coating which were more pronounced adjacent to the interface. Some grain growth of the WC was observed at the interface between the coating and the D2 tool steel. Conversely, more uniform grain sizes were observed across the coatings on the 4140 alloy steel and the cast iron. Note that, in general, the grain sizes were on the order of the initial starting particle sizes, indicating little to no grain growth during the HDI thermal treatments.

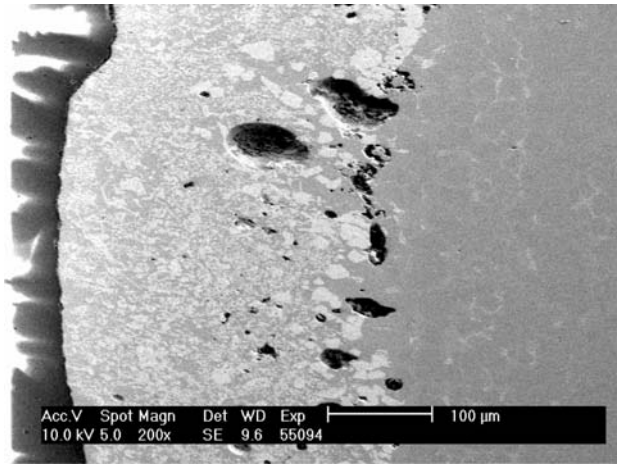

Figure 1. Cross-section of WC-Ni_3Al coating on D2 tool steel. The coating was initially intended to be 100 µm thick. Coating bonded by HDI thermal treatment using a 4-cm defocus setting and lamp parameters of 0 to 300 amps in 5 min (preheat), followed by 900 amps for 3.5 s for bonding.

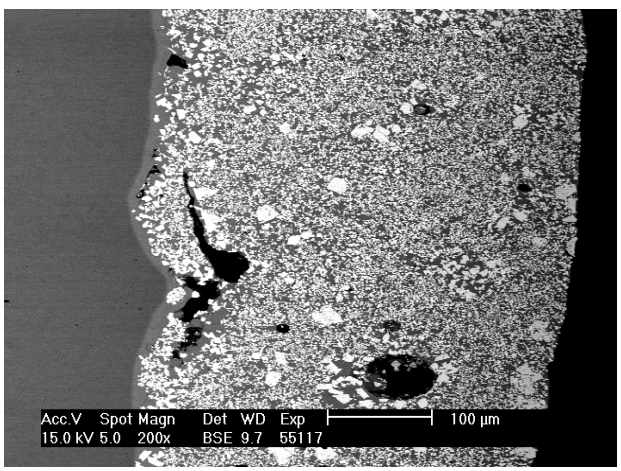

Figure 2. Cross-section of WC-Ni_3Al coating on 4140 alloy steel. The coating was initially intended to be 100 µm thick. Coating bonded by HDI thermal treatment using a 4-cm defocus setting and lamp parameters of 0 to 300 amps in 5 min (preheat), followed by 900 amps for 3.5 s for bonding.

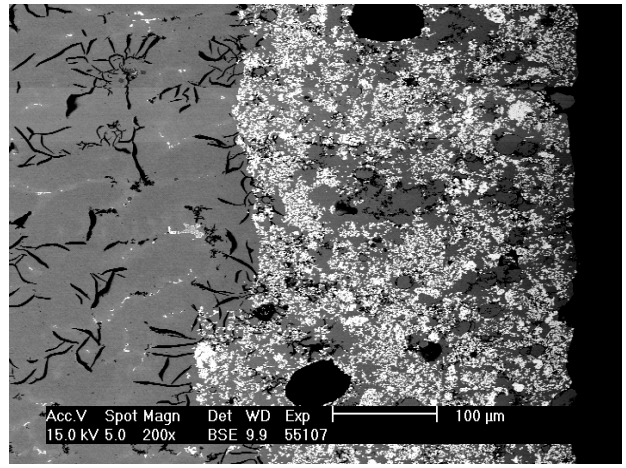

Figure 3. Cross-section of WC-Ni_3Al coating on cast iron. The coating was initially intended to be 100 µm thick. Coating bonded by HDI thermal treatment using a 4-cm defocus setting and lamp parameters of 0 to 300 amps in 5 min (preheat), followed by 900 amps for 3.5 s for bonding.

A cross-section of a WC-Co coating on D2 tool steel is shown in Figure 4. Less penetration of the Co into the D2 tool steel (~25 µm) compared to the Ni_3Al was evident. Less mixing between the coating and the substrate resulted in a uniform grain size across the coating.

When TiC (with Ni_3Al) was used for the coating there appeared to be less penetration of the Ni_3Al into the D2 tool steel substrate (Figure 5). This needs to be confirmed with additional characterization. Normally, TiC grains are quite faceted; however, the TiC grains in the coating were rounded, indicating alloying of the Ni_3Al binder with iron from the substrate. In addition, no core-rim structures, which are typically observed with TiC grains in Ni_3Al, were evident. This indicates only minimal dissolution and reprecipitation of the TiC during melting of the coating. Like the WC-based materials, the final grain size was similar to the starting TiC particle size.

The effect of the use of multiple HDI treatments on the microstructure of a WC-Ni_3Al coating on D2 tool steel is shown in Figure 6. The major effect of the double treatment was to minimize bubbles in the

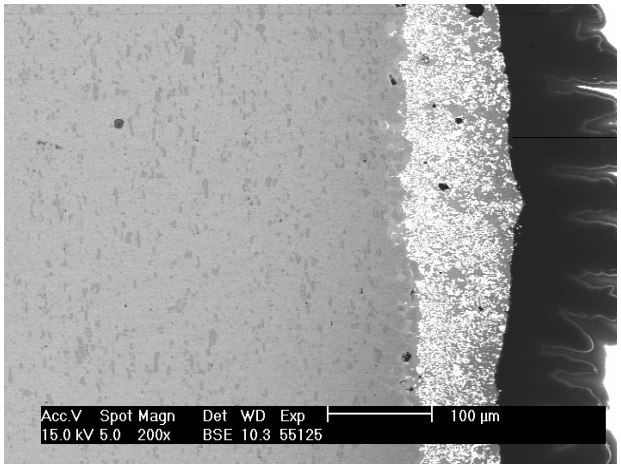

Figure 4. Cross-section of WC-Co coating on D2 tool steel. The coating was initially intended to be 100 µm thick. Coating bonded by HDI thermal treatment using a 4-cm defocus setting and lamp parameters of 0 to 300 amps in 5 min (preheat), followed by 1000 amps for 3.5 s for bonding.

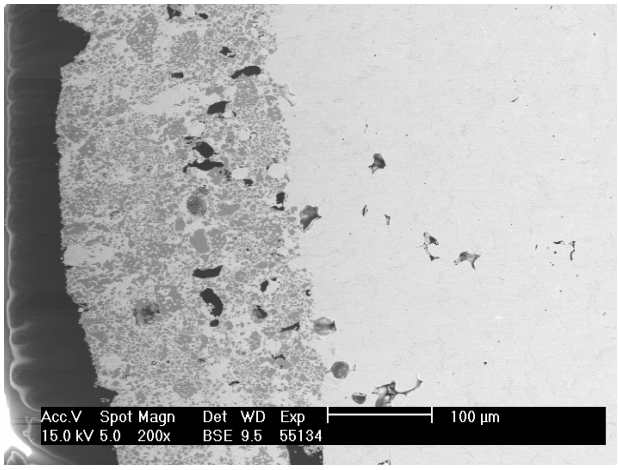

Figure 5. Cross-section of TiC-Ni_3Al coating on D2 tool steel. The coating was initially intended to be 100 µm thick. Coating bonded by HDI thermal treatment using a 4-cm defocus setting and lamp parameters of 0 to 400 amps in 5 min (preheat), followed by 900 amps for 2 s and 900 amps for 1 s for bonding. There was approximately 15 s between high-energy exposures.

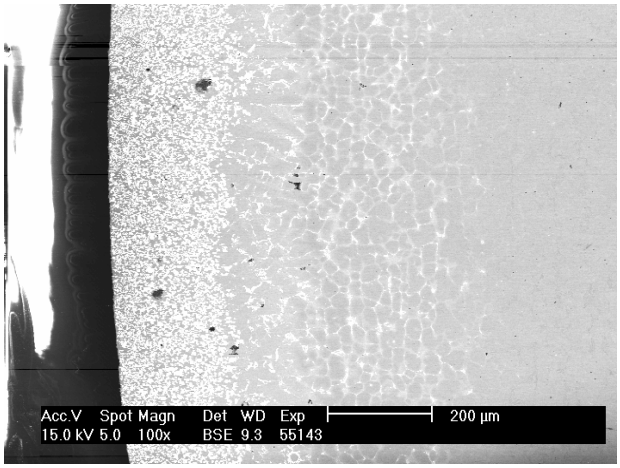

Figure 6. Cross-section of WC-Ni_3Al coating on D2 tool steel. The coating was initially intended to be 100 µm thick. Coating bonded by HDI thermal treatment using a 4-cm defocus setting and lamp parameters of 0 to 400 amps in 5 min (preheat), followed by 900 amps for 2 s and 900 amps for 1 s for bonding. There was approximately 15 s between high-energy exposures.

coating. It is hypothesized that during the second HDI exposure, the coating is remelted and any trapped bubbles can be released. However, the double treatment increases penetration of the Ni_3Al into the D2 tool steel from ~100 µm for a single exposure to ~300 µm for the multiple heating. The WC grain size was also increased by the second HDI heat treatment.

Conclusions

It was determined that plain hard metal coatings without binder additions have a very narrow window of HDI process conditions and are not practical on a large scale. Significant interactions and mixing occur between the coatings and the underlying substrates. In most cases, little to no grain growth by WC or TiC was observed during HDI heat treatments.

Presentations and Publications

T. N. Tiegs, "High Density Infrared Surface Treatment," at the Heavy Vehicles Materials Peer Review, Oak Ridge, Tennessee, September 13–15, 2005.

N. High-Temperature Aluminum Alloys

Yong-Ching Chen
Materials Engineering
Cummins, Inc.
1900 McKinley Ave.
Columbus, IN 47201-3005
(812) 377-8349; fax: (812) 377-7226; e-mail: yong-ching.c.chen@cummins.com

DOE Technology Development Area Specialist: James J. Eberhardt
(202) 586-9837; fax: (202) 586-1600; e-mail: james.eberhardt@ee.doe.gov
ORNL Technical Advisor: D. Ray Johnson
(865) 576-6832; fax: (865) 574-6098; e-mail: johnsondr@ornl.gov

---

Contractor: Oak Ridge National Laboratory, Oak Ridge, Tennessee
Contract No.: DE-AC05-00OR22725
Subcontractor: Cummins, Inc., Columbus, Indiana

Objectives

- Develop high-temperature aluminum alloys with adequate properties and shape capability for turbocharger compressor wheel and housing application.

Approach

- Develop ternary-phase compositions by means of modeling of the equilibrium-phase diagram, castings, and evaluating the properties of alloys identified.
- Perform physical and mechanical property measurements on specimens provided by the National Aeronautics and Space Administration (NASA) and by Eck Industries to characterize the material and determine the optimal properties possible by this method.
- Evaluate a nanophase particulate-reinforced aluminum alloy patented by Chesapeake Composites, Inc.

Accomplishments

- Predicted the binary phase diagrams of Al-Y and Al-Yb accurately and verified them using ThermoCalc.
- Found that the improvement in high-temperature strength of the NASA 388 alloy was not significant enough for further pursuing.
- Observed that the dispersion-strengthened composite (DSC) material exhibited significantly lower thermal conductivity and lower coefficient of thermal expansion than those of current production aluminum alloys.
- Found that the tensile strength of the DSC sample produced in 2005 was much lower than that of the billets tested in 2002. The inferior strength of the current DSC billets was most likely due to the presence of aluminum veins and defects inside the aluminum matrix. Improvement in quality is needed.
- Completed machinability studies of DSC material. Optimal operation parameters for cutting, turning, and milling were determined. The tool wear was minimal, similar to the machining of 6061-T6 aluminum.

Future Direction

- Use ThermoCalc to generate the Al-Y-Yb ternary system and identify optimal compositions for casting trial and material property characterization.

- Improve billet quality, and complete notch sensitivity and creep tests of DSC material.
- Use DSC material for rig testing machine turbocharger compressor wheel.

Introduction

The new emission requirement in internal combustion of diesel engines mandates that the turbocharger compressor be operated at significantly higher temperature and pressure. This condition makes standard castable aluminum alloys unusable as new-generation turbocharger material, because their strength deteriorates at elevated temperatures. Therefore, there is a need to develop high-strength, high-temperature aluminum alloys, which will replace these standard alloys. Work at Cummins has identified three potential paths to improve the high-temperature strength and fatigue resistance of aluminum casting alloys. These paths have been partially investigated under cooperative agreement DE-FC05-97OR22582. Each path showed some promise, and further work is needed to determine the useful applications.

Approach

The scope of work in the program covers investigation of three different paths of providing strength retention in aluminum alloys at high temperatures. Path 1 uses a ternary-phase aluminum alloy utilizing rare earth metals to provide precipitate size control and stability. Limited information on these alloys indicates high-temperature strength and stability; however, the predicted cost of the alloy is high. Additional work is performed to determine if additional rare earth (or other metal) elements produce beneficial properties at a reasonable cost. The main goal of this path is to generate the phase diagram of Al-Y-Yb, using ThermoCalc software. Because there are few published data and assessments on these rare-earth elements, a prudent approach demands that a systematic investigation be carried out. Path 2 uses a conventional aluminum alloy, which has been chemically modified by a process developed at NASA-Huntsville. The elevated temperature properties reported by NASA are attractive, but it is preferred for Cummins to use alloy with lower silicon content. Eck Industries purchased the license for the NASA-developed technology on high-silicon casting alloy and has expanded the range to include conventional low-silicon casting alloys. Limited testing of these modified conventional low-silicon alloys at Cummins has not shown the property improvement anticipated. Currently NASA 388-T5 alloy is being evaluated to characterize the material and to determine possible process improvement. Path 3 uses a particulate-loaded aluminum alloy patented by Chesapeake Composites Inc. The nanophase particulates at 50 vol % provide adequate high-temperature strength in early experiments; however, the particulate-loaded alloy could only be forged or squeeze cast so complex shape capability is limited. The mechanical behavior of this DSC material is being fully characterized. Casting modifications will be investigated to determine shape capability for the alloy.

Results

Path 1: Ternary-Phase Aluminum Alloy Development

In a previous report, the ternary-phase diagram of the Al-Fe-Mn was developed by using ThermoCalc software. The versatility of the ThermoCalc had been demonstrated. A binary Al-Y phase diagram was then generated by using the ThermoCalc, and it was validated against literature data. The work on thermodynamic assessment of Al-Yb binary by using ThermoCalc was also carried out. In general, it is in good agreement with the standard phase diagram published in the literature.

However, it is important to note that unlike most elements, the rare-earth elements yttrium and ytterbium are not widely used. For the ternary Al-Y-Yb system to be predicted, the minimum information needed is the assessment of Y-Yb system. Without any experimental data, it is not possible to know if such ternary predictions are accurate or not. So the minimum step we need is to get Y-Yb system; otherwise, one axis of our ternary diagram may not be correct. We need data in terms of the actual thermodynamics of the system, for example, heat of mixing and activity data. We have to estimate the actual Gibbs energy for the compounds and then make the fit to the polynomial terms. Much effort was focused on experimentally

generating the Y-Yb binary phase diagram. This will allow us to predict the Al-Y-Yb ternary system.

Path 2: NASA 388-T5 Aluminum Alloy

Extensive mechanical tests were conducted on the NASA 388-T5 and T6 alloys. Tests included elevated-temperature tensile tests and rotating-beam fatigue tests of samples with or without long-term thermal soaking. Test results were compared to those of the current production materials. Slight improvement in the tensile strength was only realized at test temperatures above 300ºC for the NASA 388-T5 alloy as compared to the current materials. The degree of improvement was deemed to be insignificant as compared to the further development needed for the new casting process and prototype trials. The decision was made to discontinue the evaluation work for the NASA 388-T5 alloy for intended application.

The NASA 388-T5 alloy was originally developed for automotive engine components such as pistons to utilize less material, which can lead to reducing part weights, material cost, as well as improving gas mileage and engine durability. The potential application of the NASA 388-T5 alloy in diesel engine pistons was communicated to the piston suppliers. One of the piston suppliers conducted fatigue tests of the NASA 388-T5 alloy and their production aluminum alloy at 350ºC. The NASA 388-T5 alloy exhibited slightly better fatigue strength at 350ºC than the production aluminum alloy. However, the NASA 388-T5 alloy was found to be difficult to cast in diesel piston size without defects. The piston supplier also decided not to pursue the development of NASA 388-T5 alloy in the piston application.

Path 3: Particulate-Reinforced Alloy

This task involves a nanophase particulate-loaded aluminum alloy patented by Chesapeake Composites Inc. A patented, low-cost, liquid-metal infiltration process is utilized to produce a billet form ready for secondary operations. This composite material combines the enhanced elevated-temperature strength, toughness, and ductility of dispersion-strengthened alloys with the stiffness and low coefficient of thermal expansion (CTE) of metal matrix composites (MMCs). It was claimed that this composite can be readily turned using tungsten carbide (WC) tooling and drilled and tapped using high-speed steel tools. Potential applications include pistons, compressor wheel, and engine components.

Initial tensile and fatigue tests of 1090 Al and 2024 Al alloy reinforced with nano-scale Al_2O_3 particles at elevated temperatures showed impressive results. Almost 100% improvement in tensile strength and yield strength was obtained on the DSC material as compared to those of the current production materials. No degradation in the tensile strength and fatigue strength was observed in the DSC material after 500 h of thermal soaking at 400ºC.

1. Microstructural Characterization

Extensive microstructural characterization of 2024Al-DSC material has been carried out. Particular attention was focused on developing an understanding of microstructural development in a 2024Al-Al_2O_3 composite during heat treatment. Figure 1 shows the variation of microhardness as a function of aging time for 2024Al-Al_2O_3 composite aged at 130°C and 190°C. Generally speaking, the aging time at peak hardness for the unreinforced all 2024 alloys is about 10 h (Ref. 1). However, the composite material reaches peak hardness after only 1 h of aging, which confirms the accelerated aging phenomenon we have discussed previously. Over-aging and drop in hardness were observable at 190°C. Solution treatment and water quench greatly improve the microhardness of the composite. This is particularly because the dislocation generation due to thermal expansion mismatch between aluminum matrix and Al_2O_3 reinforcement.

An accelerated aging phenomenon has been reported, which is attributed to the increase in dislocation density due to Al_2O_3 reinforcement. Transmission electron microscope (TEM) analysis of the aged samples revealed the presence of θ' and S' precipitates, which were generally quite stable at 130°C, but underwent some coarsening with a concomitant drop in hardness following aging at 190°C. The dislocation density in room-temperature tensile-tested samples was quite low, which was consistent with the low ductility at this temperature. On the other hand, the dislocation density in samples thermally soaked and tested at higher temperatures (500 and 700°F) was high. This is thought to be associated with the combined effect of ease of plastic deformation at high temperatures, coupled with differential thermal contraction of Al and Al_2O_3 on

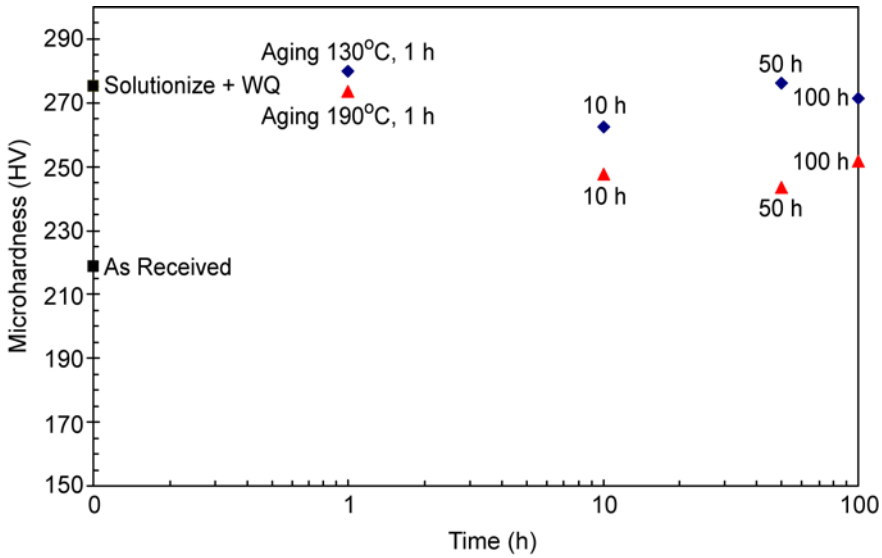

Figure 1. Variation of microhardness as a function of aging time for the 2024Al-Al2O3 composite.

cooling from the elevated temperatures of testing. Figure 2 shows TEM micrographs of the dislocation states of the 2024Al-Al_2O_3 as solutionized and water-quenched material.

2. Physical Properties

To further verify that the DSC material exhibits adequate mechanical strength to meet the operation requirements, mechanical and physical properties of DSC materials will be measured. Chesapeake Composites Corporations and PCC-AFT manufactured billets of DSC material with 1.7-in. diameter and 7.0 in. long. The DSC billets contain 40 vol % of Al_2O_3 nona-particles and were infiltrated with 1090 aluminum alloy.

Samples of a DSC material were machined for thermophysical property testing from room temperature to 400ºC. The density of the DSC material was measured to be 2.991 g/cm^3, which is about 12% heavier than that of the A354-T6 alloy (2.677 g/cm^3). The higher density needs to be taken into consideration during design because the

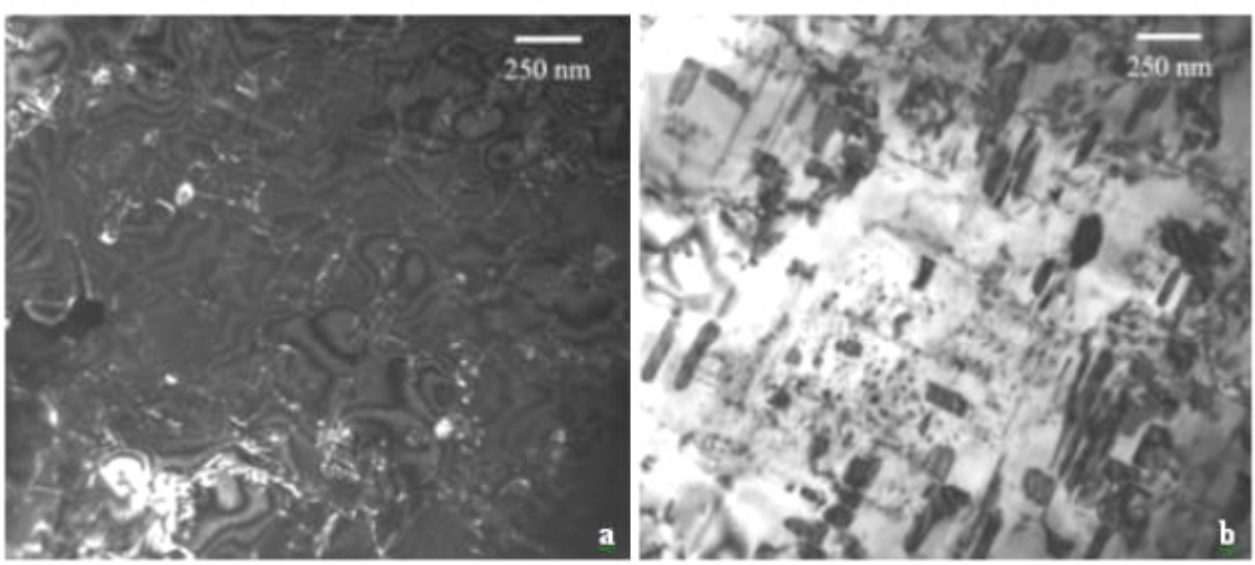

Figure 2. TEM micrographs showing the dislocation states of the 2024Al-Al_2O_3 as solutionized + water quenched material: (a) TEM DF (dark field) image; (b) TEM BF (bright field) image (precipitates).

compressor wheels made of DSC material will have higher reciprocal weight compared to those made of traditional aluminum alloy such as A354 alloy. Figure 3 displays the thermal conductivity of the DSC material as a function of temperature. Note that the thermal conductivity of the DSC material decreases as the temperature increases. This is most likely due to the presence of a high percentage of Al_2O_3 particles inside the aluminum matrix. The thermal conductivity of the DSC material was found to be much lower than that of a traditional aluminum alloy. The lower thermal conductivity in the DSC material may result in higher operating temperature. The mean CTE of the DSC material increases as the temperature increases, Figure 4. Note that the mean CTE of DSC material was significantly lower than that of a traditional aluminum alloy. The lower mean CTE was also most likely due to the presence of a high percentage of Al_2O_3 particles inside the aluminum matrix of the DSC material. The lower CTE in the DSC material may indicate smaller dimensional changes during operation.

3. Tensile Testing

Tensile samples with dimensions of 4.2-mm diameter by 18-mm gage length were prepared from the DSC billet for tensile testing at room temperature, 200ºC, 300ºC, and 400ºC without supplemental thermal soaking. Figure 5 shows the tensile strength of the DSC material as a function of temperature. The tensile strength of the DSC material tested in 2002 was also plotted for comparison. Note that the tensile strength of the DSC sample produced lately was much lower than that tested in 2002. The percent elongation and reduction of area at room temperature were almost zero. Some samples broke quickly before yielding such that no yield strength was available. The much lower tensile strength of the DSC samples manufactured in 2005 was unexpected.

4. Microstructural Characterization

To compare the microstructure of the current billets and that of the billets which exhibited much higher tensile strength, five tested tensile bars prepared from the DSC billets manufactured by Chesapeake Composites in 2002 were submitted for microstructure analysis to determine if defects were present in the material. The tensile bar samples were tested previously at varied temperatures and after a 500-h soak. Figure 6 shows the comparison between the tensile sample tested in 2002 and the billet samples manufactured in 2005. Note that the tensile sample tested in 2002 exhibited less cellular structure and much finer grain size as compared to the billet sample manufactured in 2005. Very few or no aluminum veins were observed in the tensile sample tested in 2002. The difference in the microstructure had resulted in significant difference in the tensile strength of the DSC billets.

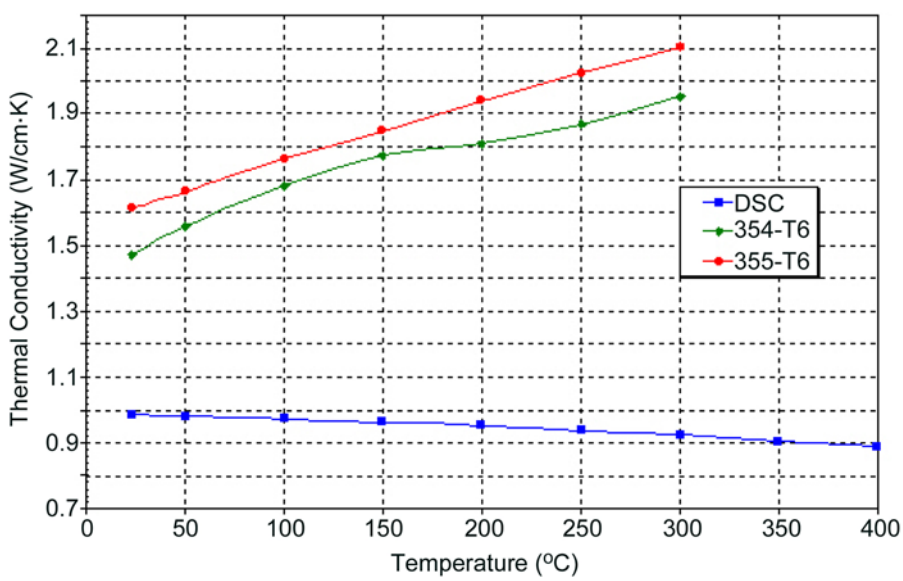

Figure 3. Thermal conductivity of the DSC material, 354-T6, and 355-T6 aluminum alloys.

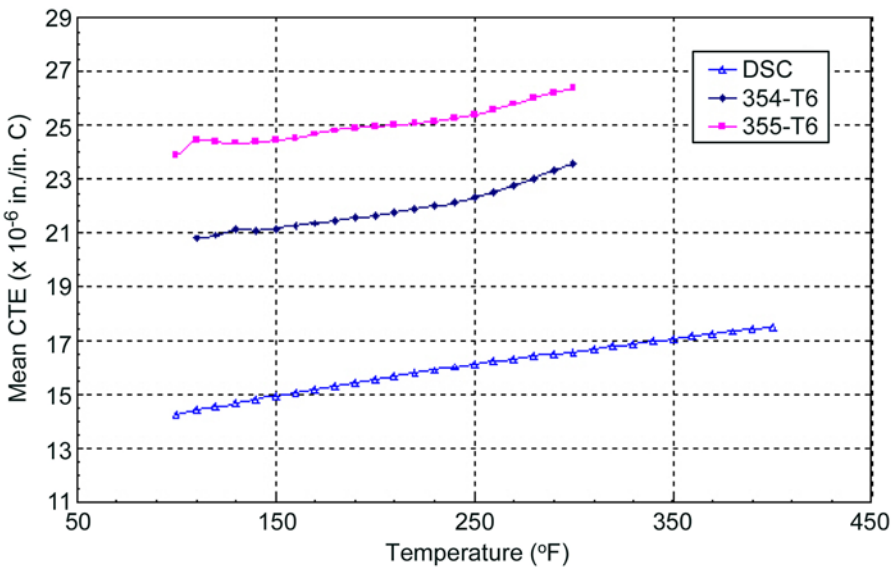

Figure 4. Mean CTE of the DSC material, 354-T6, and 355-T6.

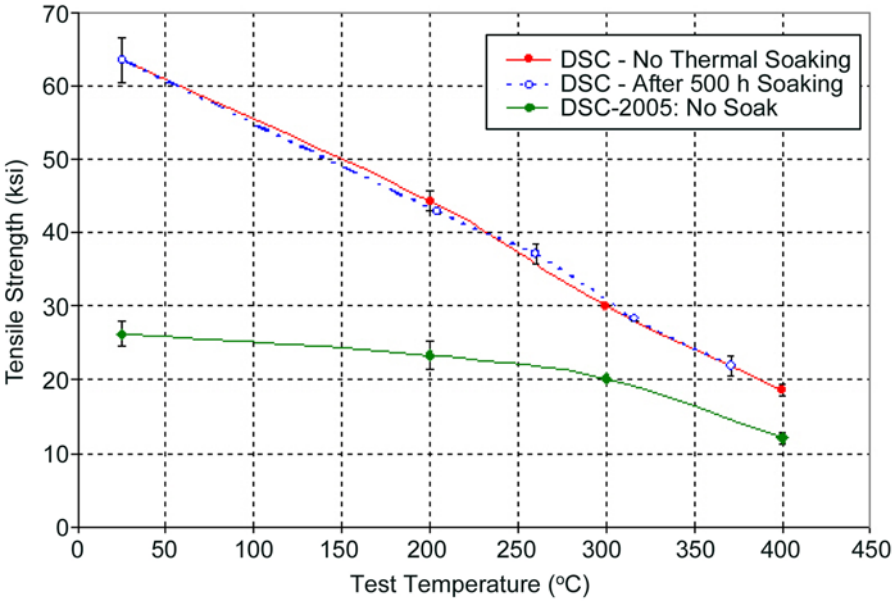

Figure 5. Elevated-temperature tensile strength of the DSC material manufactured in 2005 and DSC material manufactured in 2002.

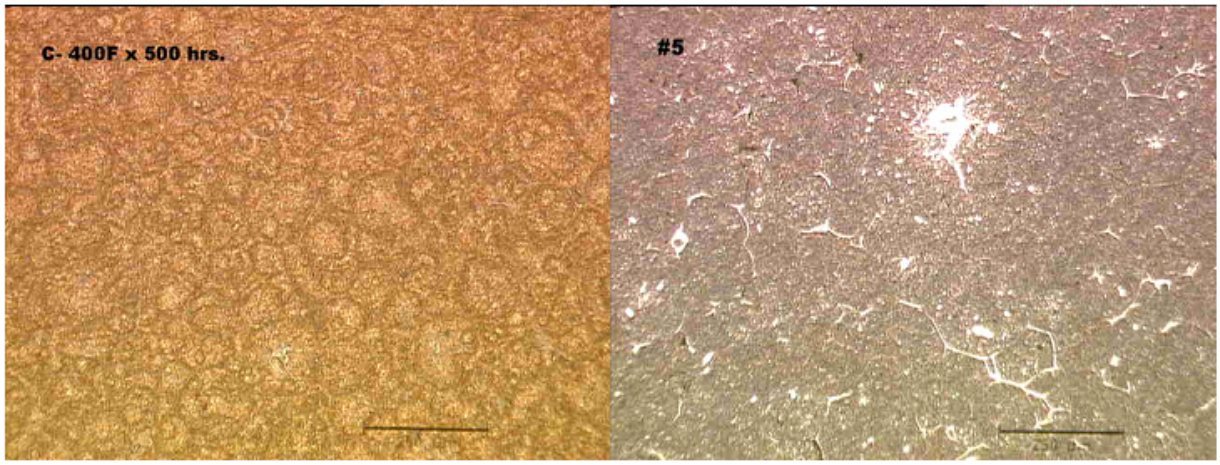

Figure 6. Comparison of the microstructure of tensile sample (left) to billet sample of different batch (right) at 100×. The microstructure of billet contains a larger number of large veins and defects.

According to the supplier, a different manufacturing process was used in making fine aluminum powders needed for making preforms. The difference in the quality of the powders had resulted in the dramatic difference in the final tensile strength. The quality of the current DSC billets was considered unsatisfactory, and further process development is needed by the supplier to get material close to past strength and quality.

5. Machinability Study

The machinability study of DSC aluminum was performed in the areas of drilling, sawing, single-point turning, and five-axis milling. The milling and drilling tools tested were selected by the Advanced Integrated Manufacturing Center, which consisted of carbide end mills from OSG Tooling and high-speed steel drills and taps.

A Daewoo Puma 240MS turret lathe, Figure 7(a), was used for the turning test. All turning parts were processed to machine the face then rough turn the outside to form two different diameters. All parts produced broken chips. There was no formation of long "springy" chips. Figure 7(b) shows excellent surface finish on both diameters. A Deckel Maho DMU50, Figure 8(a), was the five-axis machining center used for the test. The nonorthogonal fifth axis provides excellent machine stability. The part was 2-D roughed in 0.050-in. increments with the 0.375-in. two-flute end mill. The contour was finished utilizing all five axes of the machining center with the 0.250-in. ball end mill. The blade areas were finished, and the corners were removed

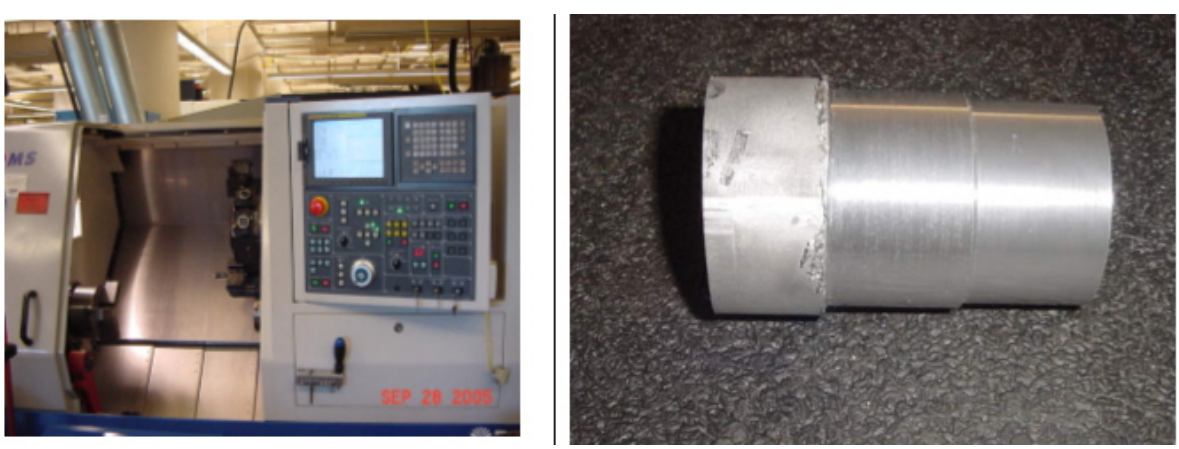

Figure 7. (a) A Daewoo Puma 240MS turret lathe was used for the turning test. (b) Excellent finish on both diameters was obtained with optimal cutting parameters.

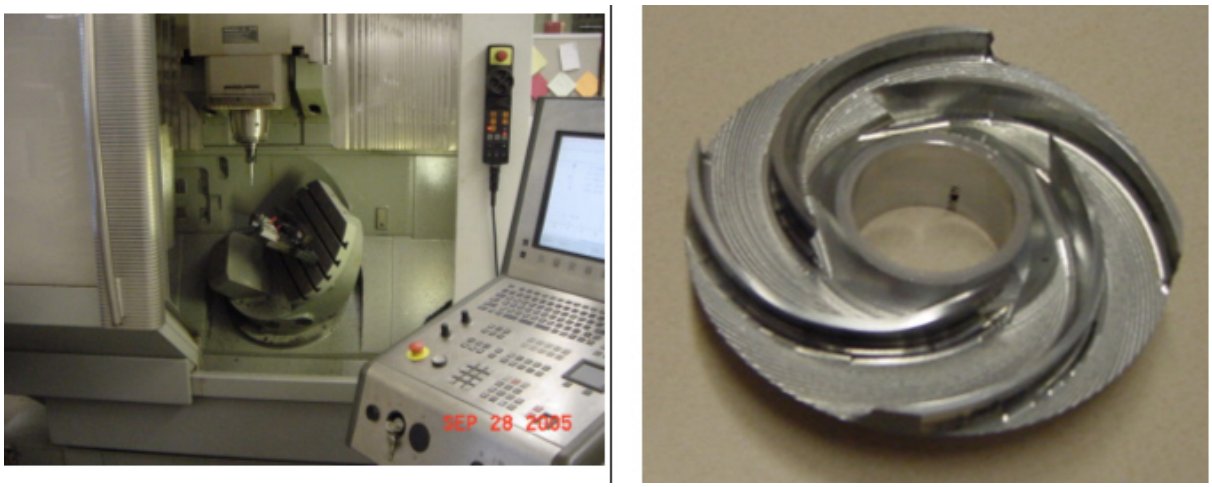

Figure 8. (a) A Deckel Maho DMU50 was the five-axis machining center used for the milling test. (b) One demonstration part was completed by the five-axis machining center.

with the 0.125-6in. ball end mill. Figure 8(b) shows one demonstration part completed by the five-axis machining center. A microscope was used to measure the tool wear. The tool wear for the study was found to be minimal, similar to the machining of 6061-T6 aluminum. No significant difference in machining the DSC was noted when compared to the machining of traditional wrought aluminum alloys.

Conclusions

Three different paths are adopted to develop and evaluate high-temperature aluminum alloys for turbocharger compressor wheel and housing applications. The versatility of the ThermoCalc software was demonstrated in the plotting of the phase diagrams. The Al-Y and Al-Yb binary-phase diagrams were generated and validated. The Al-Y-Yb ternary system will be modeled. Slight improvement in the tensile strength was only realized at test temperatures above 300ºC for the NASA 388-T5 alloy as compared to the current materials. The degree of improvement was deemed to be insignificant as compared to the further development needed for the new casting process and prototype trials. The decision was made to discontinue the evaluation work for the NASA 388-T5 alloy for turbocharger application. The DSC material exhibited very impressive high-temperature tensile and fatigue strength. Excellent thermal stability was confirmed with SEM and transmission electron microscope (TEM) studies. Physical property measurements of the DSC material were completed. The thermal conductivity of the DSC material was found to be much lower than that of a traditional aluminum alloy. The lower thermal conductivity in the DSC material may result in higher operating temperature. The mean CTE of DSC material was significantly lower than a traditional aluminum alloy. The lower CTE of the DSC material may indicate smaller dimensional changes during operation. The tensile strength of the DSC sample produced in 2005 was much lower than that of the billets tested in 2002. The inferior strength of the current DSC billets was most likely due to the presence of aluminum veins and defects inside the aluminum matrix. The quality of the current DSC billets is not satisfactory. Further process improvement is needed by the supplier. Machinability study of the DSC material was completed. No significant difference in machining the DSC was noted when compared to the machining of traditional wrought aluminum alloys.

References

1. R. J. Arsenault and R. M. Fisher, *Scripta Metall.*, **17**, 67 (1983).

O. Application of Titanium Alloys for Heavy-Duty Vehicles

P. C. Becker
Oak Ridge National Laboratory
P.O. Box 2008, MS 6066
Oak Ridge, Tennessee 37831-6068
(865) 576-4844; fax (865) 574-6098; e-mail: beckerpc@ornl.gov

DOE Technology Development Area Specialist: James J. Eberhardt
(202) 586-9837; fax: (202) 586-1600; e-mail: james.eberhardt@ee.doe.gov
ORNL Technical Advisor: D. Ray Johnson
(865) 576-6832; fax: (865) 574-6098; e-mail: johnsondr@ornl.gov

---

Contractor: Oak Ridge National Laboratory, Oak Ridge, Tennessee
Prime Contract No.: DE-AC05-00OR22725

Objectives

- Complete the final details of the finite element analysis (FEA) modeling of a diesel engine head and block where an aluminum (Al) casting alloy is used to replace gray cast iron.
- Complete the final details of the FEA modeling of a diesel engine head and block where a magnesium (Mg) casting alloy is used to replace gray cast iron.
- Try to seek funding from either a major diesel engine manufacturer or a major customer to construct and test engines with heads and blocks made from titanium (Ti), Al, or Mg alloys.
- Generate fatigue data that could indicate whether the sub-liquidus casting (SLC) process is attractive for making Al turbocharger compressor wheels with improved fatigue life.

Approach

- Use FEA modeling of a heavy-duty diesel engine head and block to determine whether it is feasible to substitute parts from Ti, Al, and Mg instead of gray cast iron.

Accomplishments

- Confirmed through FEA modeling that it is feasible to substitute Al and Mg for cast iron in the head and block of a heavy-duty diesel engine.
- Conducted a preliminary evaluation of the SLC process. Mechanical property data from A354-T6 samples were generated and compared with data of the same alloy that was permanent mold cast. The data showed that ultimate tensile strength, yield strength, and extrapolated fatigue life for the SLC cast bars was significantly higher than for the permanent mold cast bars.

Future Direction

- Make a more definitive evaluation of the SLC sample after THT Presses delivers higher-quality cast bars.

Project Description and Activities

Modeling Lightweight Alloys

In FY 2004, modeling provided by Ricardo, Inc., using FEA of temperatures and stresses showed that it was feasible to make a heavy-duty diesel engine head and block of cast Ti-6Al 4V instead of gray cast iron. The engine that was modeled was a Cummins 5.9-L B-Series engine (Figure 1). The analysis showed that the only problem was unacceptable temperatures generated in the head valve bridges; therefore, a novel means of mitigating this effect was proposed and modeled. The novel approach was to substitute for the Ti in the valve bridges a high-thermal-conductivity alloy insert of Be-Cu. The engine was again modeled, but the normal 305-hp rating used for modeling was increased by 50% to 450 hp. The model showed that this approach was viable and resulted in a 10% weight savings as well as a higher horse power. It was felt that these advantages could be attractive to the military, specifically TACOM. In FY 2005, numerous presentations were made to the diesel engine companies, to Oshkosh Truck, and to the Defense Advanced Research Projects Agency (DARPA) and TACOM to determine their level of interest.

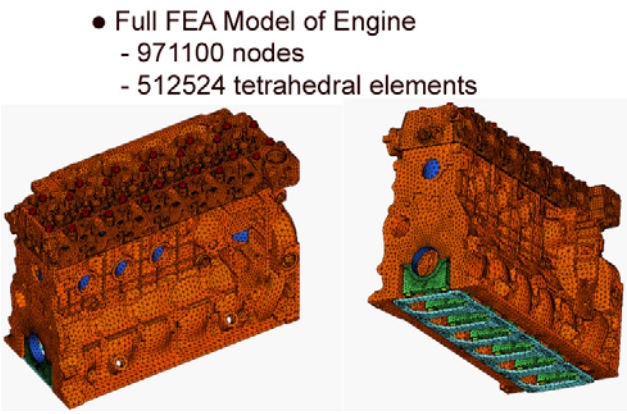

Figure 1. FEA model of the Cummins engine.

After the engine was modeled in Ti, two other lightweight materials, high-strength Al and high-strength Mg casting alloys, were modeled as replacements for cast iron in a diesel engine head and block at a normal maximum rating (305 hp). The alloys were A354-T6 AL and We-43-T6 MG. The stresses and fatigue safety factors in the block were found to be acceptable. The same was true for the head. However, the temperatures in the valve bridges were of concern based on the results of the Ti modeling. The results of the thermal FEA of the engine head are shown in Figure 2.

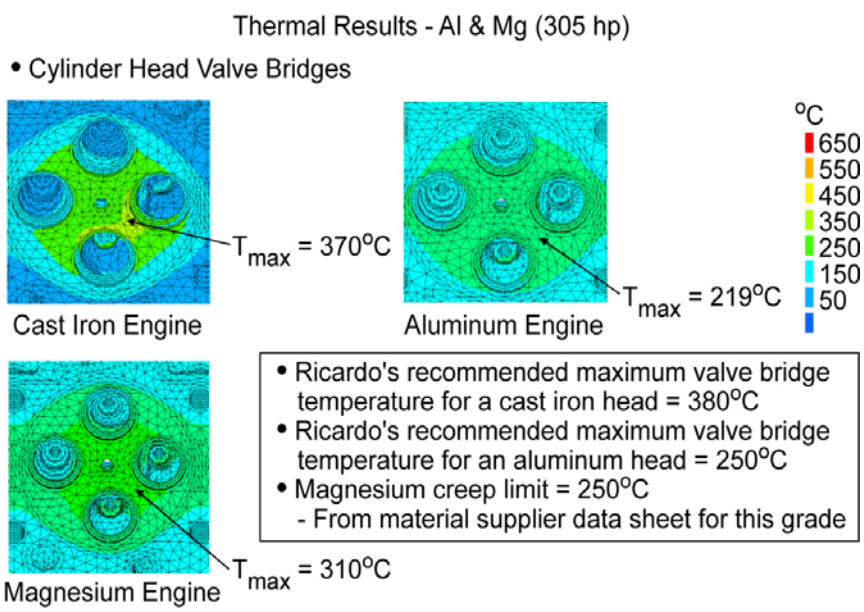

Figure 2. Thermal results comparing the valve bridge region in the head for production cast iron, Al, and Mg.

The FEA results show that the temperatures are low enough to be considered acceptable, keeping in mind that the analysis assumed that the engine was running at maximum power throughout its life, which does not mirror reality. The temperature of 310°C in the Mg head was somewhat high, but for this study it was not high enough to make the head unfeasible in this material.

The potential overall engine weight saving was 20% for Al and 33% for Mg. Most of the FEA work was done in FY 2004, but some details were completed in FY 2005. These involved calculating weight benefits and presenting the work to potential customers and manufacturers.

Since the commercial Cummins engine weighs about 1100 lb, 220 lb could saved if the head and block were made of Al and 363 lb could be saved if made from Mg. All of these data and analyses were presented to Cummins and Caterpillar as well as to TACOM in FY 2005.

SLC of Al for Turbocharger Compressor Wheels

SLC is a lower-cost approach to semi-solid forming (SSF) of Al castings. The advantage of the SSF process is that a nearly porosity-free casting can be made that results in high fatigue strengths. The process is attractive for making high-performance diesel engine turbocharger compressor wheels. Using the SLC approach solves two major problems inherent in traditional SSF processing. First, since the semi-solid charge is produced in the heating chamber of the die casting tooling, the cost to produce a part is nearly the same as for a traditional die casting. This contrasts with a 25% cost premium for parts made by traditional SSF. Second, SLC requires only about 5000 psi to force the slurry into the mold; traditional SSF requires 20–25,000 psi. Therefore, a plaster mold or some other destructible material could possibly be used to make the compressor wheels, which is a requirement. The severe curvature of the compressor wheel's vanes makes it impossible to extract a casting from hard tooling. Figure 3 is a schematic drawing of the SLC concept.

SLC cast test bars of A354 were made at THT Presses and then heat-treated to T-6. These bars were sent to Metcut Research for machining and testing. The data were then to be compared with semi-permanent mold castings made from the same alloy. Tensile test data are shown in Table 1. The table compares data from test bars cast by the SLC process to data from permanent mold test samples cast with the same alloy and heat treatment process.

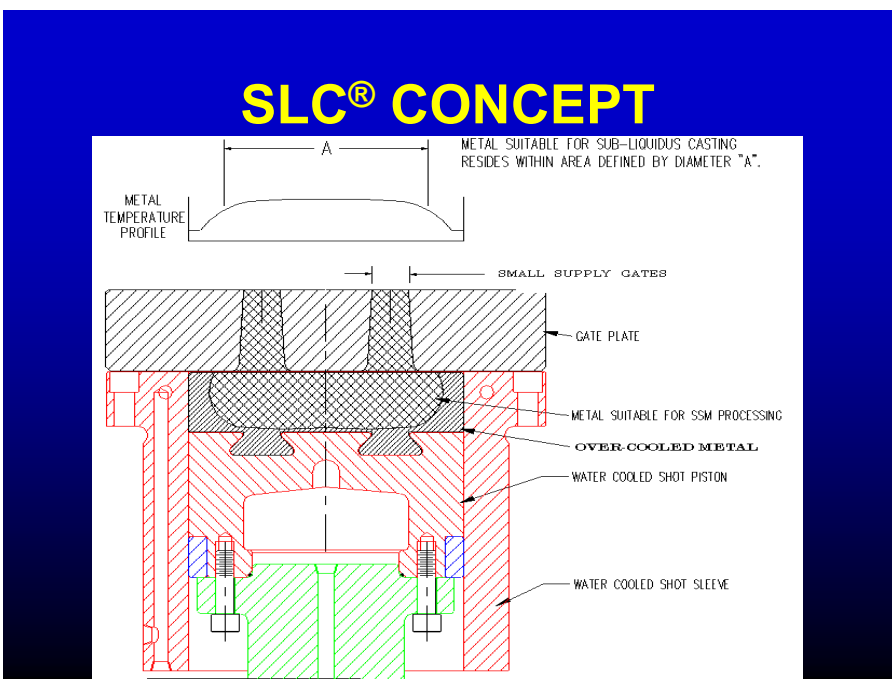

Figure 3. Schematic drawing of the SLC casting chamber.

Table 1. Comparison of permanent mold cast to SLC A354-T6

Test temp. (°C)	UTS (Ksi)	0.2% YS Ksi	Elongation (%)
Permanent mold (no chill)			
Room temp	38.5	35	0.57
150	31	30	0.37
200	29	29	0.33
260	21	20	1.1
Sub-liquidus			
Room temp.	46	40	1.8
150	42	35	3.9
200	36	34	1.7
250	26	24	3.8

UTS = ultimate tensile strength
YS = yield strength

The fatigue properties at room temperature of samples made by the SLC process were measured at Metcut Research using the rotating beam technique, and the data were compared with permanent mold data produced for Cummins in an earlier DOE-funded program. Cummins did the data analyses using its proprietary fatigue analysis software FATIGUE. The comparison is shown in Figure 4.

As can be seen from these two S/N curves, the SLC process provides a slightly higher fatigue life at cycles greater than 10^7, which is more pronounced at 5×10^7 cycles. Unfortunately, the SLC samples had higher than expected porosity, which would explain the high scatter in the data. Optical microscopy of the SLC cast bars conducted at ORNL (Figure 5) shows the porosity.

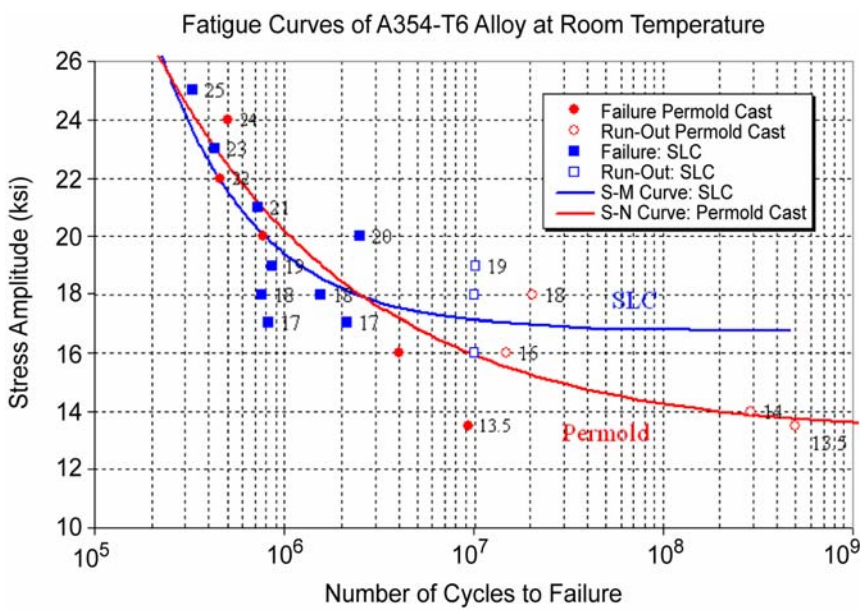

Figure 4. Comparison of rotating beam curves of permanent mold and SLC castings of A354-T6.

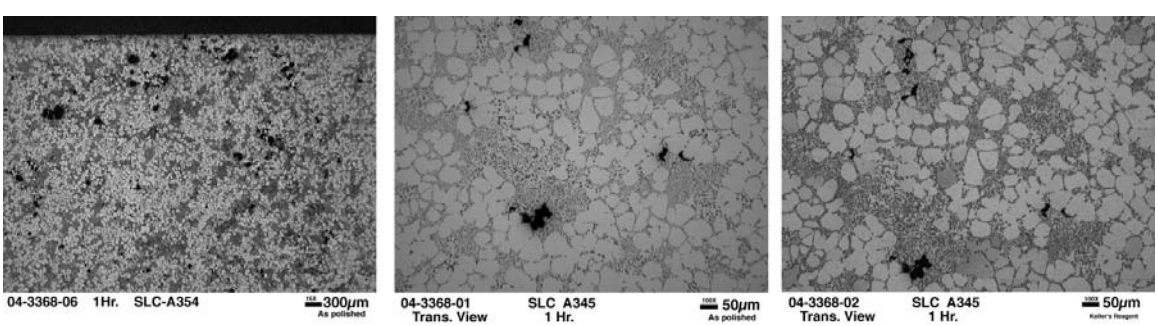

Figure 5. Micrographs of SLC samples showing the porosity from the casting process. The micrographs are from the infrared heat-treated sample.

Figure 6 shows the microstructure of the SLC cast bars. The micrograph on the left shows the conventional T-6 heat-treated microstructure, and the one on the right shows the infra-red heat-treated microstructure. In both cases, the microstructure is finer than for the permanent mold castings of the same alloy, but using infra-red provides an even finer structure and hence even higher mechanical properties. The fine microstructure explains why the cycle fatigue life of the SLC samples is higher than that of the permanent mold samples even though the SLC castings do not have optimum structure because of the high porosity.

THT Presses has promised to replace these samples with higher-quality cast bars so that a more definitive evaluation can be made.

Conclusions

- FEA modeling has confirmed that it is feasible to substitute Al and Mg for cast iron in the head and block of a heavy-duty diesel engine. This substitution can result in an overall engine weight saving of 20% for Al and 33% for Mg. Although this work and the previous work on Ti were presented numerous times to TACOM, DARPA, Cummins, and Caterpillar, none of these organizations has yet committed funding to continue the program.
- The SLC process was given a preliminary evaluation. Mechanical property data from A354-T6 samples were generated and compared with data of the same alloy that was permanent mold cast. The ultimate tensile strength at room temperature for the SLC cast bars was about 19% higher than for the permanent mold cast bars, and the yield strength was about 14% higher. The extrapolated fatigue life of the SLC process produced a 17% improvement over that of the permanent mold cast samples at 5×10^7 cycles.

If the SLC samples contained the very low porosity that the process is capable of, even higher fatigue properties should be achievable.

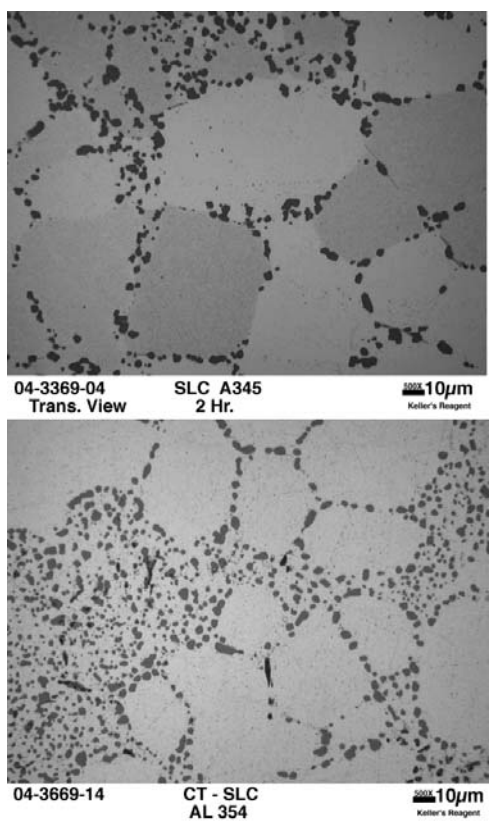

Figure 6. Microstructures of SLC samples that have undergone either conventional T-6 heat treatment or infra-red heat treatment.

Presentations

Puja B. Kadolkar, Craig A. Blue, Qingyou Han, and Paul C. Becker, "Rapid Infrared Heat Treatment of Al Cast Structures," presented to the Materials Science and Technology 2005 Conference and Exhibition, September 25–28, 2005.

P. C. Becker, presentation on Ti, Al, and Mg in diesel engines to Caterpillar, April 27, 2005.

P. C. Becker, presentations on Ti, Al, and Mg in diesel engines to Cummins, April 25, 2005.

P. C. Becker, presentation on Ti, Al, and Mg in diesel engines to TACOM, April 15, 2005.

P. Mechanical Behavior of Ceramic Materials for Heavy-Duty Diesel Engines

Andrew A. Wereszczak and Hong Wang
Ceramic Science and Technology Group (CerSaT)
Oak Ridge National Laboratory
P.O. Box 2008, MS 6068
Oak Ridge, TN 37831-6068
(865) 576-1169; fax: (865) 574-6098; e-mail: wereszczakaa@ornl.gov

DOE Technology Development Area Specialist: James J. Eberhardt
(202) 586-9837; fax: (202) 586-1600; e-mail: james.eberhardt@ee.doe.gov
ORNL Technical Advisor: D. Ray Johnson
(865) 576-6832; fax: (865) 574-6098; e-mail: johnsondr@ornl.gov

---

Contractor: Oak Ridge National Laboratory, Oak Ridge, Tennessee
Contract No.: DE-AC05-00OR22725

Objectives

- Enable the development of more wear-resistant and mechanically robust ceramic components through the systematic evaluation of contact damage in ceramics.
- Characterize rate effects on deformation processes in Si_3N_4.
- Develop supplemental models to assist in the interpretation of deformation.

Approach

- Characterize damage processes in Si_3N_4 ceramics through instrumented static and dynamic indentation and instrumented scratch testing.
- Develop criterion that can be used to rank resistance to damage.
- Evaluate relevant Si_3N_4 grades (e.g., existing commercial roller element and ball bearing compositions, standard reference materials).
- Evaluate grain size effects on damage processes through static and dynamic indentation (model Al_2O_3 ceramics used).

Accomplishments

- Established dynamic indentation and instrumented scratch testing facilities.
- Developed a new brittleness parameter that represents static and dynamic indentation responses.
- Developed a generic finite element method (FEM) that predicts the onsets of quasi-plasticity and fracture/cracking in any target material as a function of indentation load, indenter material, friction, and confinement.
- Co-developed and copyrighted μ-*FEA* software.

Future Direction

- Conduct a complete study of grain size effects on rate and deformation processes.
- Begin a new project involving reliability analysis and design optimization of piezostack fuel injectors for diesel engines.

Introduction

The application of more ceramic components in engines and transportation systems would be enabled if they could be confidently used in more wear-related applications and if they could be manufactured and machined faster (i.e., more cost-effectively). This would occur if contact-induced damage mechanisms (that limit their mechanical performance or dictate their machinability) were understood, predictable, and controlled.

This project quantifies the loads and stresses associated with the initiation of "quasi-plasticity" and fracture processes in ceramics using instrumented indentation and scratch testings. Understanding their competition and interaction is a critical part of this project as well. Traditional structural ceramics (e.g., Si_3N_4) under consideration for diesel engine components are of primary focus.

Through the quantification of the loads or stresses that initiate quasi-plasticity and fracture, contact-induced damage mechanisms in ceramics are characterized and modeled and linked to micro-structure, and ultimately to wear performance, the optimization of machining, and rolling contact fatigue. Additionally, the influence that independent parameters such as grain size, loading rate, confinement or residual stresses, temperature, field effects have on the evolution of contact-induced damage are also examined. The thorough understanding of the competition of fracture and quasi-plasticity in ceramics will enable improved and faster means of ceramic component manufacturing and surface engineering (e.g., ductile regime machining) and maximize mechanical performance when surface condition (e.g., bending) or when surface-located events (e.g., wear, impact) are service-life-limiters in engine and transportation system components.

Approach

There were four primary components to the FY 2005 work. Instrumented indentation and static indentation and instrumented scratch testing were used to characterize contact-induced damage processes in Si_3N_4. A criterion was developed that can be used to rank resistance to contact-induced damage. Several grades of Si_3N_4 were evaluated (e.g., existing roller element and ball bearing compositions as well as standard reference materials). Lastly, grain size effects (in model Al_2O_3 ceramics) on damage processes from indentation and scratch testings were examined.

Results

Static and dynamic indentation hardnesses of Ceralloy 147-31N, NBD200, SN101C, TSN-03NH, and NC132 silicon nitrides were measured as a function of load and their results are respectively shown in Figures 1–5. The rationale for testing each grade: the 147-31N grade is presently used as a cam

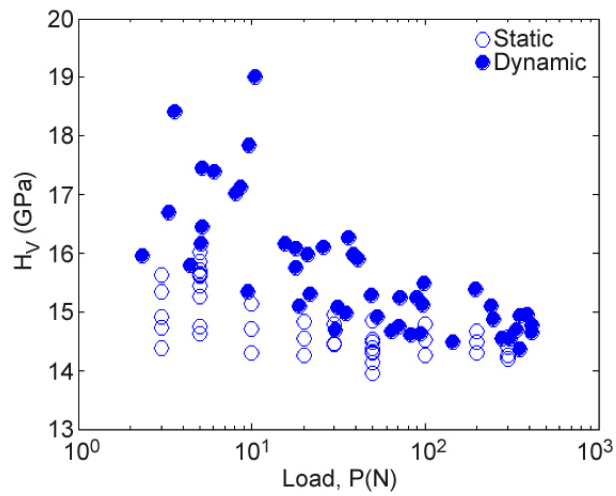

Figure 1. Vickers Hardness for Ceralloy 147-31N Si_3N_4 as a function of load for quasi-static and dynamic indentation.

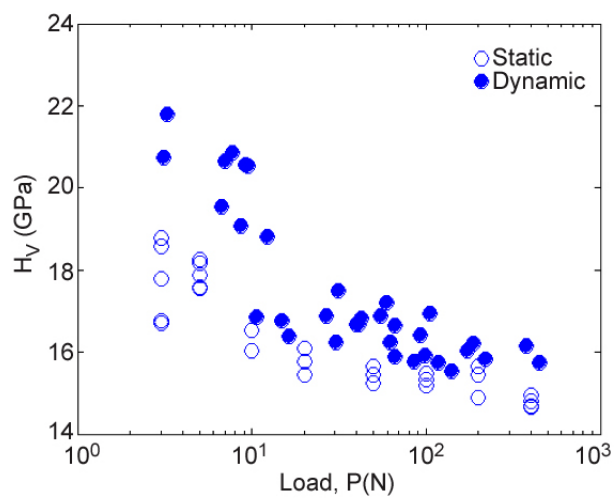

Figure 2. Vickers Hardness for NBD200 Si_3N_4 as a function of load for quasi-static and dynamic indentation.

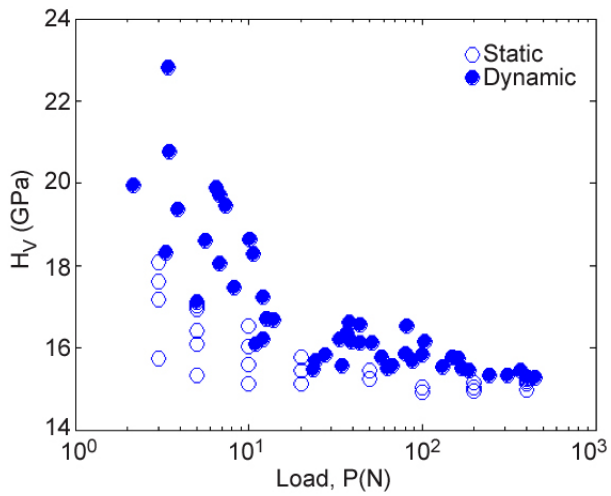

Figure 3. Vickers Hardness for SN101C Si_3N_4 as a function of load for quasi-static and dynamic indentation.

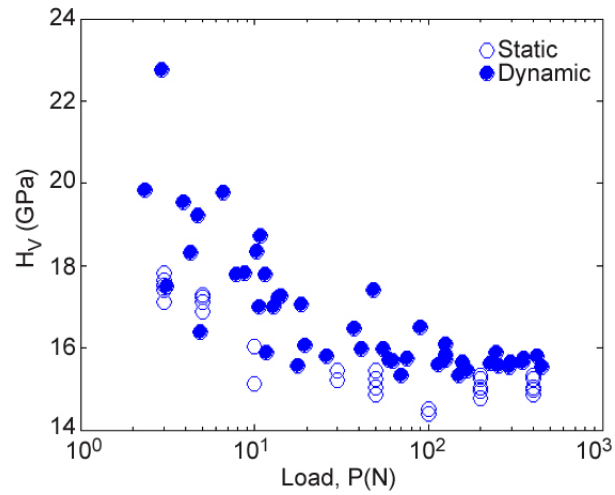

Figure 4. Vickers Hardness for TSN-03NH Si_3N_4 as a function of load for quasi-static and dynamic indentation.

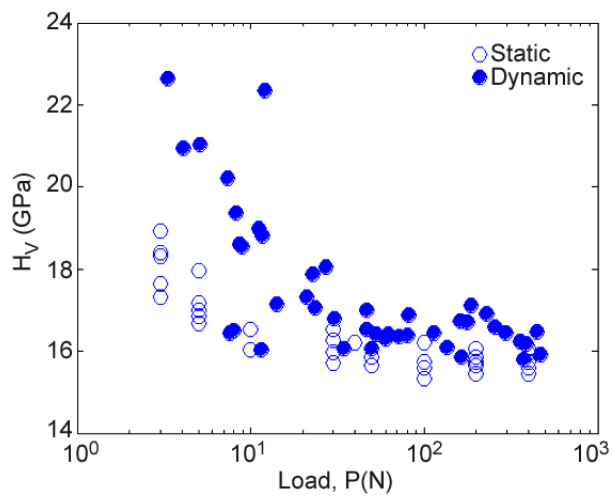

Figure 5. Vickers Hardness for NC132 Si_3N_4 as a function of load for quasi-static and dynamic indentation.

roller follower material, so interest exists to quantify its indentation and scratch responses, NBD200, SN101C, and TSN-03NH are ball bearing grades so their testing is relevant to their examination of rolling contact fatigue behavior, NBD200 is a NIST SRM for Knoop hardness, and NC132 is a NIST SRM for fracture toughness so they serve as references upon performance comparison among all the silicon nitrides. An indentation size effect (ISE) and a rate effect are exhibited by all (increased H and greater ISE with rate).

A good fit to the experimental data is often obtained using a formula that Frohlich et al.,[1] and Li and Bradt[2] attribute to Bernhardt[3]

$$P = a_1 d + a_2 d^2 \quad , \qquad (1)$$

where P is indentation load, d is indent diagonal size, and a_1 and a_2 are constants. The a_1 term is relatable to the energy consumed in creating new surfaces,[1–2] whereas the a_2 term is relatable to the volume energy of deformation.[4] The determination of those terms for each of the silicon nitrides as a function of rate is shown in Figure 6. Additionally, a new brittleness parameter was developed that involves the use of the ratio of a_2/a_1 because it can provide insight into the competition of those two mechanisms. The brittleness of the five silicon nitrides is shown in Figure 7, and the relation shows

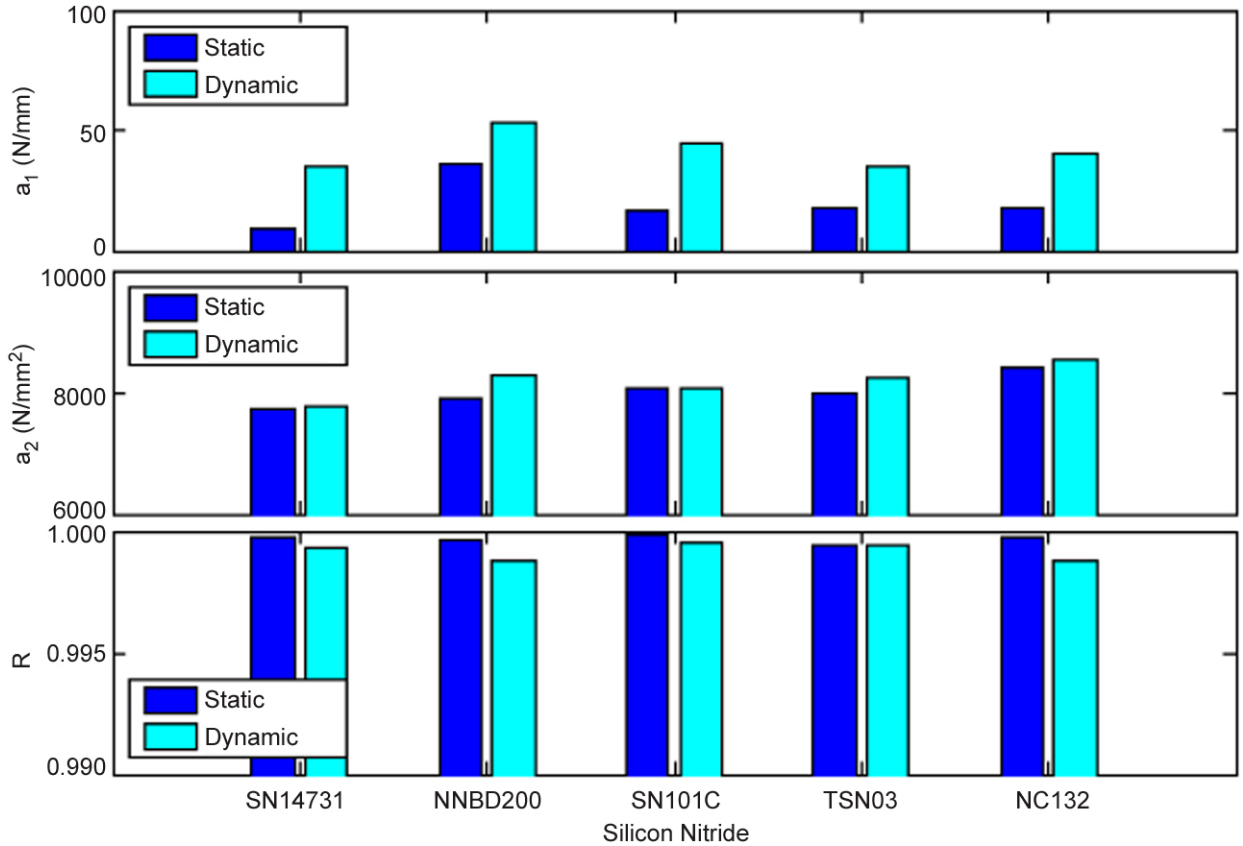

Figure 6. Comparison of a_1 and a_2 terms [see Eq. (1)] for the five silicon nitrides when indentation was performed statically and dynamically.

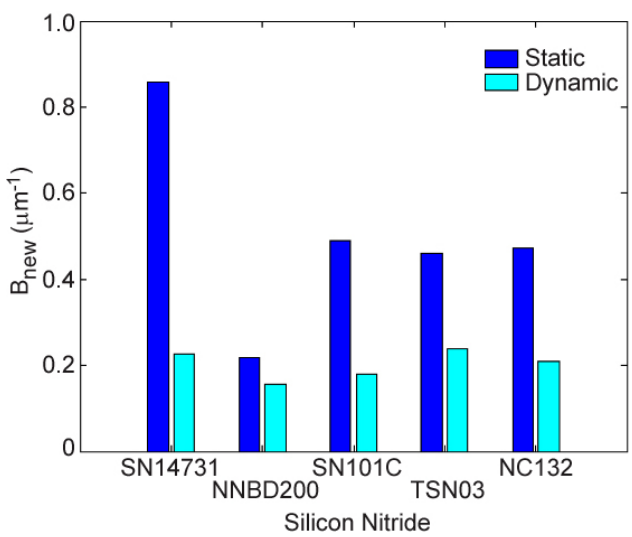

Figure 7. Comparison of a new Brittleness parameter (a_2/a_1) for the five evaluated silicon nitrides for static and dynamic loadings. The trends show that all the grades act less brittle when they were dynamically loaded.

that all five silicon nitrides respond in a less brittle fashion when they were dynamically indented.

The exploration of the effect of indentation on residual stress generation was initiated using optical fluorescence. An illustration of this is shown in Figure 8 for a 99.9% alumina that was Knoop indented at 2 kg. A maximum tensile stress of ~100 MPa is observed at the tip of the cracks that come from the Knoop indent diagonals. Quantification of these effects will enable engineering control of ceramic machining or allowable wear conditions to inhibit or avoid deleterious effects that may be more strongly linked to fracture or quasi-plastic processes or both.

An ANSYS Hertzian indentation model that was developed in FY 2004 continued to be refined in FY 2005. A three-dimensional (3-D) model was developed in FY 2005 using "concrete" elements that will enable the prescription of strength asymmetry in tension and compression. A tensile strength value will be imputable that will be associated with fracture processes, whereas a

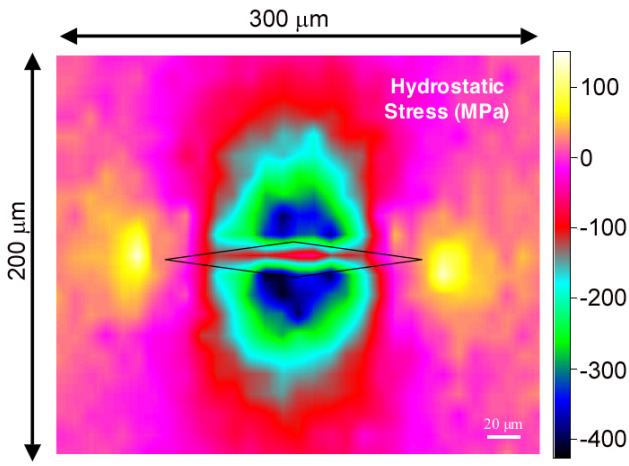

Figure 8. Hydrostatic stress map generated with optical fluorescence about a 2-kg Knoop indent in a 99.9% alumina having a ~2- to 3-µm average grain size.

compressive strength value will be imputable that will be associated with contact-induced quasi-plastic deformation mechanisms.

A substantial amount of instrumented scratch characterization occurred during the latter half of FY 2005. Testing of silicon nitride focused on the evaluation of Ceradyne's Ceralloy 147-31N, which is a reaction-bonded material used in cam roller followers. Evaluation of three 99.9% aluminas having mean sizes of 2, 15, and 25 µm (see Figure 9) also proceeded; the rationale behind the alumina testing is to evaluate scratch response as a function of controlled grain size with the same chemical composition. Additionally, the testing of alumina affords the opportunity to map out residual stresses about the contact or scratch damage using optical fluorescence. Scratch damage evolution and its quantification are being related to machining and wear performance.

The interpretation of the load histories during scratch testing with respect to microstructural examination is ongoing. Normal and tangential forces are continuously monitored during the (pendulum) scratch test. Examples of these with associated microstructural damage are shown in Figures 10–11 for Ceralloy 147-31N, and Figures 12–17, for the 2-, 15-, and 25-µm alumina, respectively. The effects of lateral crack formation on normal and tangential load histories and depth changes are illustrated in Figure 18. SEM observations show that there is an apparent grain size effect on the scratch responses; in particular,

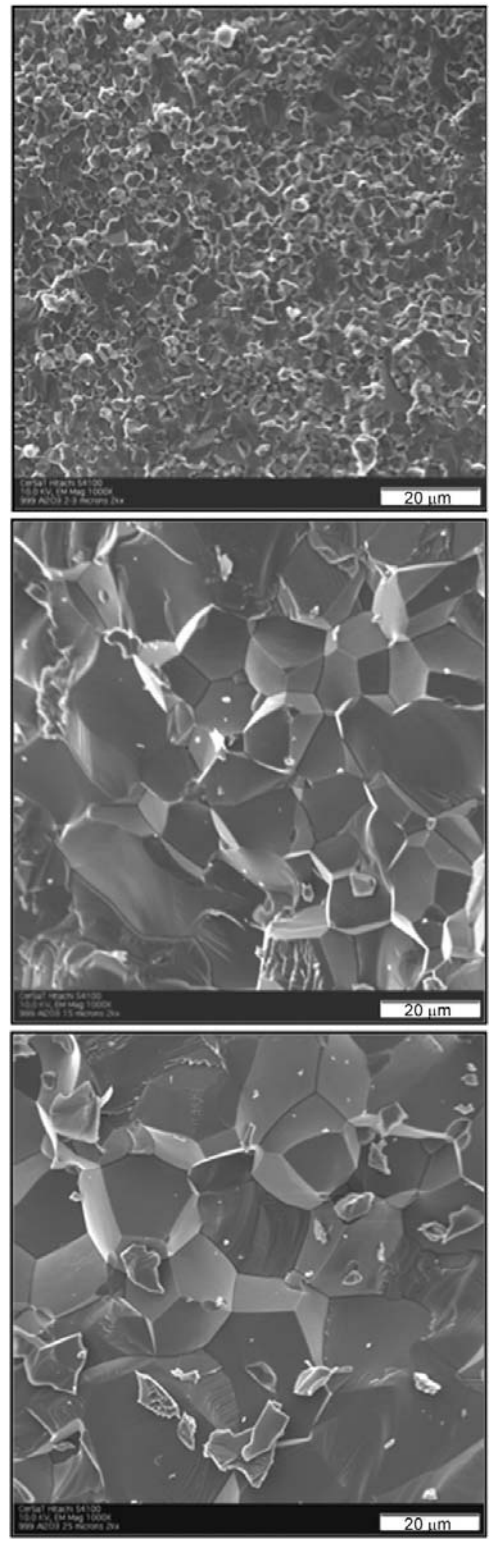

Figure 9. Microstructure of 99.9% aluminas with mean average grain size of (top) 2 µm, (middle) 15 µm, and (bottom) 25 µm.

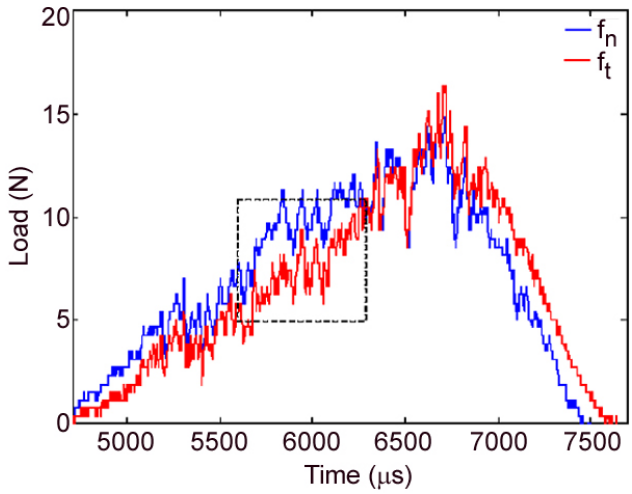

Figure 10. Example of normal (blue) and tangential (red) load histories during a Ceralloy 147-31N silicon nitride scratch test.

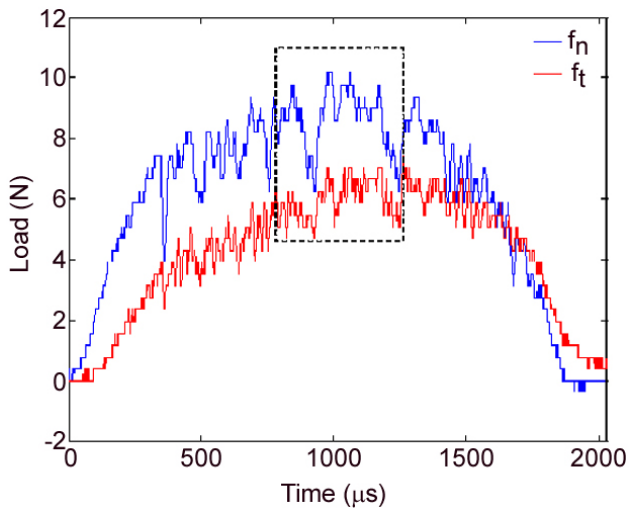

Figure 12. Example of normal (blue) and tangential (red) load histories during a 99.9% 2-μm alumina scratch test.

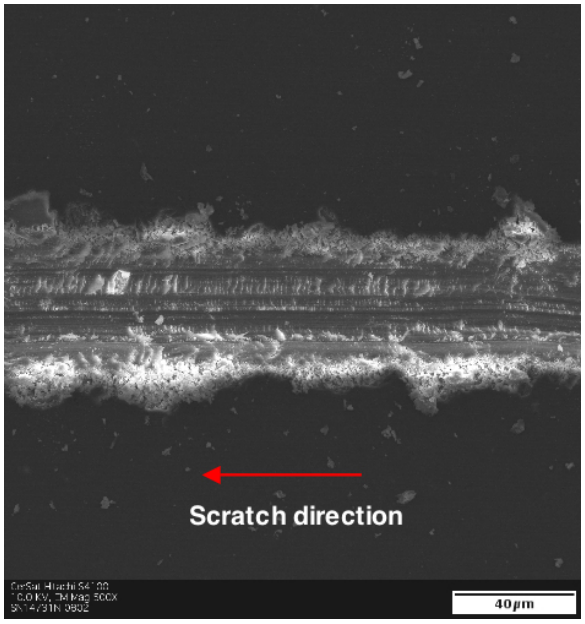

Figure 11. Scratch on Ceralloy 147-31N associated with boxed region in Figure 10.

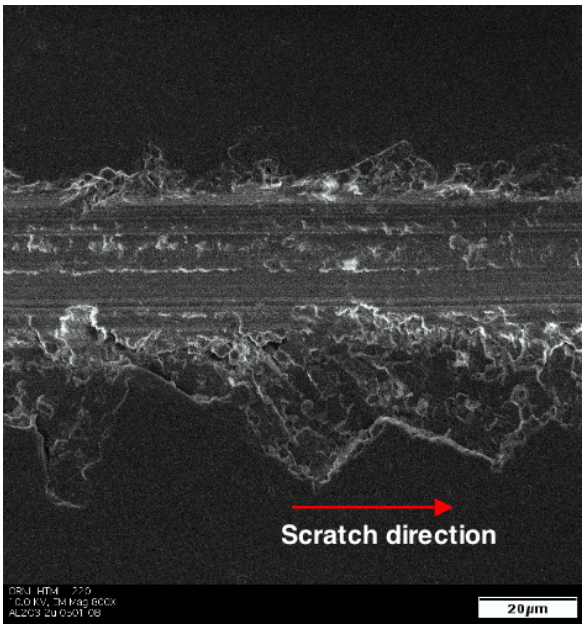

Figure 13. Scratch on 99.9% 2-μm alumina associated with boxed region in Figure 12.

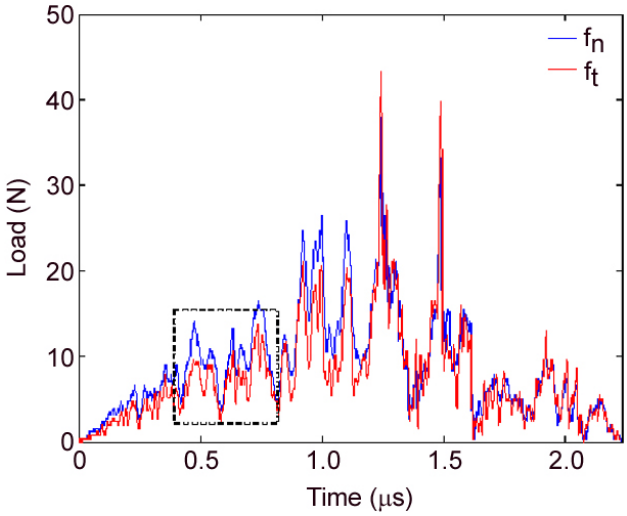

Figure 14. Example of normal (blue) and tangential (red) load histories during a 99.9% 15-μm alumina scratch test.

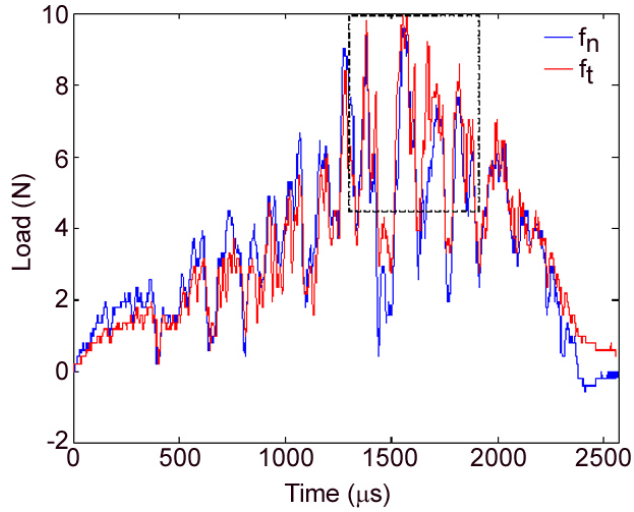

Figure 16. Example of normal (blue) and tangential (red) load histories during a 99.9% 25-μm alumina scratch test.

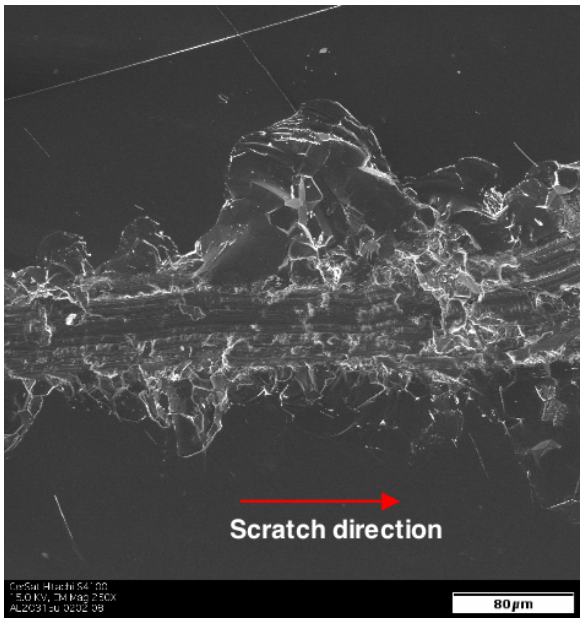

Figure 15. Scratch on 99.9% 15-μm alumina associated with boxed region in Figure 14.

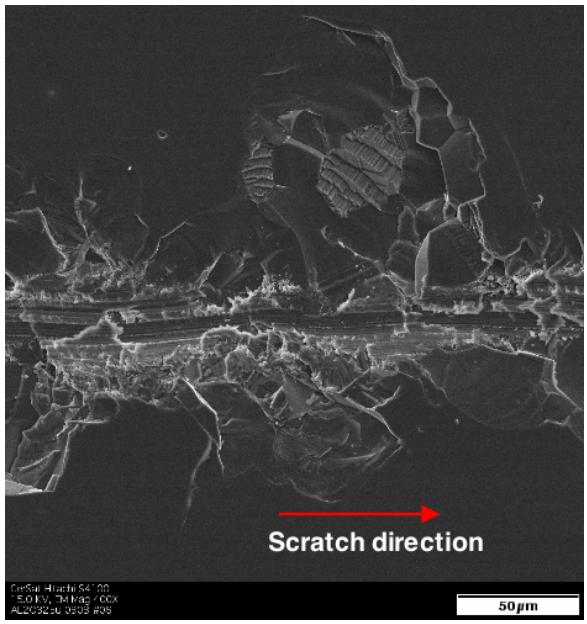

Figure 17. Scratch on 99.9% 25-μm alumina associated with boxed region in Figure 16.

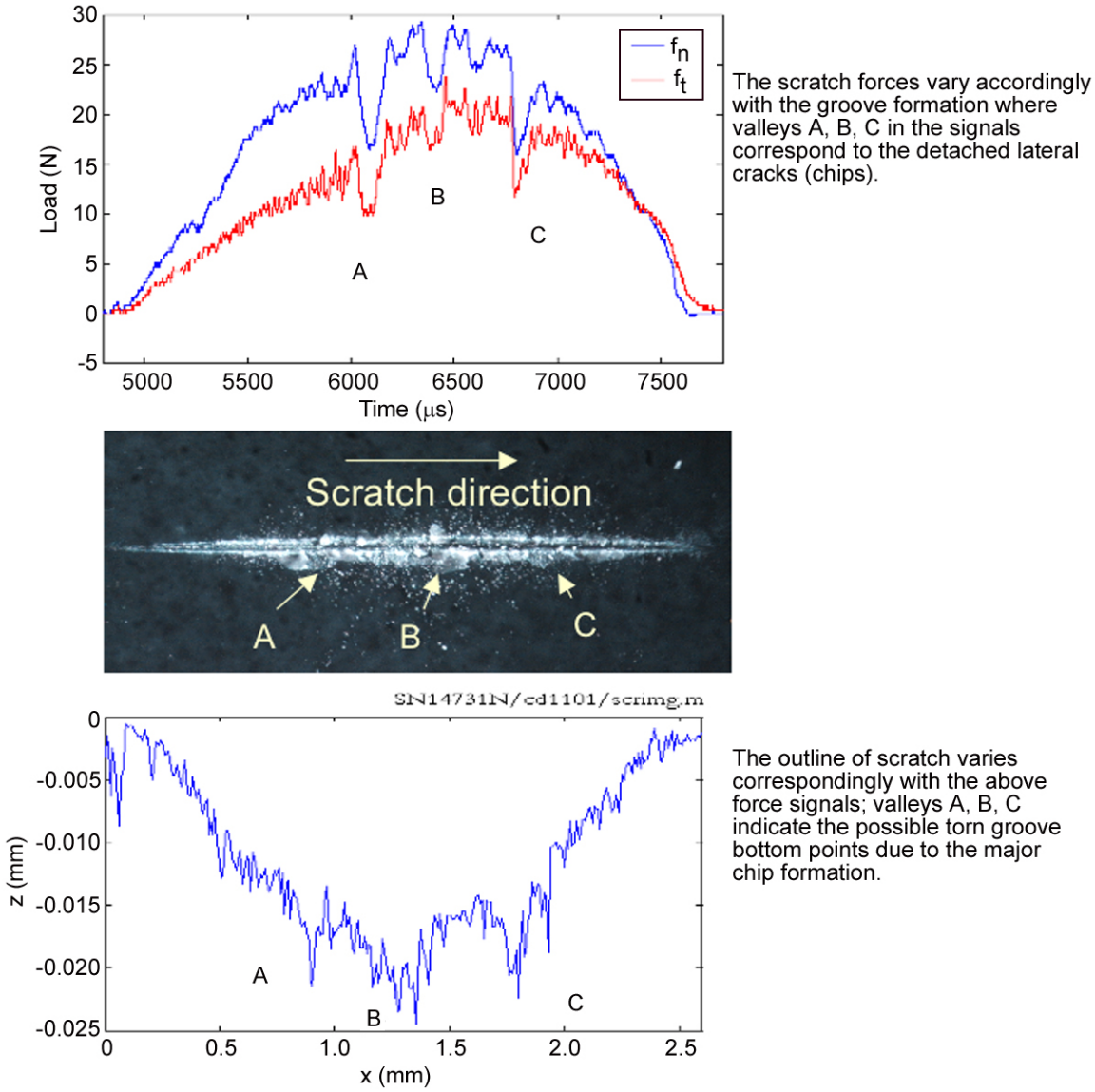

Figure 18. Evidence of lateral crack formation evident in the normal and tangential load histories (top graph) and in depth changes too (profilometry–bottom graph).

scratch forces oscillate more significantly during the scratching of larger-grained alumina corresponding to a greater amount of lateral crack formation.

μ-*FEA*, a "microstructure-based finite-element analysis" computer program, was copyrighted in FY 2005. μ-*FEA* is a graphics-user-interfaced LabVIEW executable program that serves as a pre- and post-processor to the ANSYS finite-element analysis solver and enables stress analyses of both real (e.g., imaged with SEM or OM) and simulated material microstructures. For one of its applications, μ-*FEA* is being used to study stress concentrators, deformation, and microcracking around pores and large grains and in secondary phases in materials subjected to a Hertzian contact stress gradient.

Conclusions

Static and dynamic indentation and instrumented scratch testing facilities were established to quantify the loads and stresses associated with the initiation of quasi-plasticity and fracture processes. Numerous silicon nitride ceramics were investigated, and rate effects on hardness (i.e., quasi-plasticity) were studied. A new brittleness parameter was developed that enables static and dynamic indentation responses to be ranked for different ceramics. A

generic FEM was developed that can be used to predict the onsets of quasi-plasticity and fracture/ cracking in any target material as a function of indentation load, indenter material, friction, and confinement. Lastly, microstructure-based finite-element analysis software (*μ-FEA*) was copyrighted. The software enables stress analysis characterization at the microstructural scale and to help with the interpretation of quasi-plastic and fracture processes.

References

1. F. Fröhlich, P. Grau, and W. Grellmann, *Phys. Stat. Sol. (a)*, **42**, 79–89 (1977).
2. H. Li and R. C. Bradt, *J. Non-Crystalline Solids*, **146**, 197–212 (1992).
3. V. E. O. Bernhardt, *Z. Metallkde*, **33**, 135–144 (1941).
4. H. Li, A. Ghosh, Y. H. Han, and R. C. Bradt, *J. Mat. Res.*, **8**, 1028–1032 (1993).

Presentations and Publications

A. A. Wereszczak and T. P. Kirkland, "Exclusivity of Strength-Limiting Extrinsic Surface and Hybrid Flaws," in press, *Ceramic Engineering and Science Proceedings* (2006).

H. Wang and A. A. Wereszczak, "Mechanical Responses of Silicon Nitrides Under Dynamic Indentation," *Ceramic Engineering and Science Proceedings,* **26**, 275–283 (2005).

G. Subhash, M. A. Marszalek, A. A. Wereszczak, and M. J. Lance, "Evaluation of Scratch Resistance and Residual Stresses in Machined Silicon Nitride," *Ceramic Engineering and Science Proceedings*, **26**, 285-292 (2005).

H. Wang, A. A. Wereszczak, and M. K. Ferber, "Characterization of Dynamic Indentation of Silicon Nitrides by Using Vickers Indentation," in preparation.

"Research Overview of ORNL's Ceramic Science and Technology Group," University of Alabama, Tuscaloosa, Alabama, April 20, 2005.

Special Recognitions and Awards/Patents Issued

μ-*FEA* Software, M. K. Ferber and A. A. Wereszczak, U.S. Copyright Office, Certificate of Registration No. TXu1-234–195, 25 April 2005.

Q. Powder Processing of Nanostructured Alloys Produced by Machining

S. Chandrasekar, K. P. Trumble, and W. D. Compton
College of Engineering
Purdue University, IE, GRIS
315 North Grant Street
West Lafayette, IN 47907-2023
(765) 494-3623; fax: (765) 494-5448; e-mail: chandy@purdue.edu

DOE Technology Development Area Specialist: James J. Eberhardt
(202) 586-9837; fax: (202) 586-1600; e-mail: james.eberhardt@ee.doe.gov
ORNL Technical Advisor: D. Ray Johnson
(865) 576-6832; fax: (865) 574-6098; e-mail: johnsondr@ornl.gov

---

Contractor: Oak Ridge National Laboratory, Oak Ridge, Tennessee
Prime DOE Contract No.: DE-AC05-00OR22725
Subcontractor: Purdue University, West Lafayette, Indiana

Objective

- Develop manufacturing technologies for creating advanced nanostructured alloys with enhanced mechanical properties for transportation applications.

Approach

- Create nanostructured chips by machining alloys of aluminum, titanium, and iron under controlled machining conditions.
- Characterize microstructure and determine relationships between structure and mechanical properties of the nanostructured chips.
- Develop methods for converting the nanostructured chips into particulates suitable for processing bulk forms.
- Develop low-temperature consolidation routes for creating monolithic and composite materials without significant coarsening of the nanocrystalline microstructures.
- Characterize microstructure, mechanical properties, and performance of the bulk forms.

Accomplishments

- Produced nanostructured chips of a variety of alloys and metals—including Al6061-T6, copper, iron, commercially pure titanium, stainless steel, and Inconel—by machining. The nanostructured chips are up to three times as hard as the bulk material.
- Developed low-temperature consolidation routes that limit coarsening in Al6061-T6, and steels. Achieved a high degree of interparticle bonding in room temperature powder extrusion of nanostructured Al6061-T6.
- Developed highly stable nanostructured (HSN) materials, for example, Inconel 718, Waspaloy, of high-strength through a combination of grain-size refinement by machining and creation of fine-scale precipitates by heat treatment.
- Developed a new process, extrusion-machining, to engineer bulk samples, for example, foils, filaments, with ultra-fine grained (UFG) microstructure and enhanced mechanical properties.

Future Direction

- Continue development of low-temperature consolidation routes to produce bulk monolithic and/or composite alloys with nanocrystalline microstructure.
- Characterize microstructure and properties of the bulk forms to demonstrate retention of nanostructures and enhanced mechanical properties.
- Determine tensile and wear properties of bulk forms to demonstrate integrity of the consolidated alloy samples and guide application.
- Develop (identify 1–2) applications in the transportation sector for prototype development.

Introduction

This project builds on the recent discovery of a low-cost means of producing nanostructured materials in essentially any alloy via normal machining. Comminution of the nanostructured chips enables large-scale production of nanocrystalline particulate, which can be converted into nanostructured bulk forms using powder processing methods. Particulate having controlled size and shape can also be produced by a modulated machining process. The chips and particulates also may be used as continuous or discontinuous reinforcements in metal or polymer matrices to create advanced composites.

Progress from FY 2005 in two main areas is highlighted in this report: (1) low-temperature consolidation routes, primarily of ultrafine-grained Al6061-T6 and (2) microstructure development in machining of solution-treated alloys. Modulated machining could be in there as a third, but not necessary or enough space.

Approach

Three routes for consolidation and densification of the nanostructured particulate to produce monolithic and composite materials were pursued: (1) shear-based deformation processing (e.g., powder extrusion); (2) rapid infiltration processing using low-melting metal alloys; and (3) polymer die-press bonding.

These routes are all geared toward densification and bonding of the particulate while minimizing thermal coarsening. For the powder extrusion, nanostructured Al-6061-T6 chips were converted into particulate using attrition milling. The resulting particulate was mixed with varying weight percentages of commercial gas-atomized aluminum powder; this mixture was powder extruded through steel dies at extrusion ratios of 10–60. The extruded samples were prepared in the form of cylinders up to 10 mm in diameter and 5–25 mm in length.

The polymer bonding is a new approach in which a thermosetting polymer resin is used, together with high-pressure compression molding in a steel die to yield a structure consisting of low-volume fractions of polymer bonding the nanostructured metal particles. The focus so far has been on Al-6061-T6 chip powders bonded with different epoxies. This approach is based on the observation that the cure conditions of the resin are well below the known time-temperature conditions for coarsening (and loss of hardness) of the nanostructures in the chip particles. Application for lightweight, wear-resistant components is envisioned.

Another avenue of investigation has focused on creation of high-strength, high-temperature nanostructured materials such as titanium and nickel-based alloys, with exceptional thermal stability of the microstructure. In this context, we have demonstrated a means of extending the temperature range for structural applications of nanomaterials through the introduction of a dispersion of second-phase precipitates, whose thermal stability determines the temperature at which the strength deteriorates. Precipitate-stabilized nanostructured materials synthesized from solution-treated Inconel 718 are shown to be extremely stable even after prolonged heat treatment for 500 h at temperatures as high as one-half of the melting point; we designate them as "highly-stable nanostructured (HSN) materials." The enhanced thermal stability of the material's strength results from retention of both the fine microstructure and the fine precipitate phase coexisting at the high temperatures. This novel microstructure was created by first deforming solution-treated Inconel 718 to a

large shear strain by machining, followed by thermal aging of the chip to create fine-scale precipitates.

Results

Room Temperature Powder Extrusion of Al-6061-T6 Chip Particulate

Extrusion of nanostructured Al6061-T6 chip particulate results in poor densification and bonding. However, by blending the chip particulate with pure aluminum powder, near complete densification is possible. The effect of chip powder particle size relative to the pure aluminum (Ampal, 99.9%, gas-atomized, ~60 μm) and extrusion ratio are under investigation. Figure 1 shows the extrudate and corresponding microstructure for a ~180-μm nano-chip particulate blended 50–50 with pure aluminum and extruded at room temperature with an extrusion ratio of 42. Immersion density measurements indicated a relative density of 98.7%, consistent with the small amount of porosity observed in optical microscopy. The chip particles are clearly distinguished in the micrographs and appear well—bonding with the continuous pure aluminum matrix. Tensile testing (3-mm-diam gage sections) completed late this year confirmed a significant degree of bonding. A fully sintered pure aluminum powder specimen was tested in the same manner to serve as a control sample. The detailed test results are as follows:

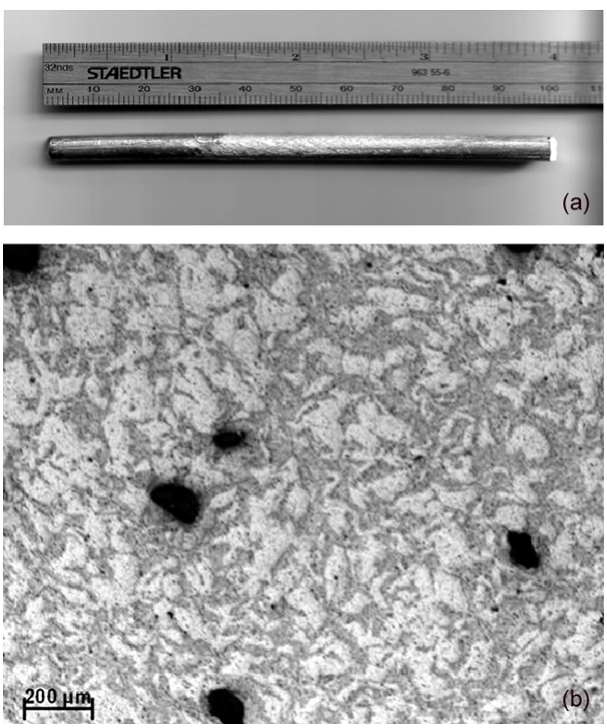

Figure 1. (a) Macrograph showing Al-6061-T6 nanochip/pure aluminum (1:1 by volume) extrudate; extrusion ratio = 42. (b) Optical micrograph of corresponding microstructure in cross-section showing small amount of residual porosity on the order of the nanochip particle size but otherwise well-bonded structure.

Material	Properties (YS/UTS/%El)
Fully sintered pure aluminum	60 MPa/75 MPa/5%
6061 nanochips + pure aluminum	170 MPa/170 MPa/nil
6061 nanochips + 601AB	200 MPa/200 MPa/nil

The measured strength values indicate significant interparticle bonding in the ambient temperature extruded materials based on machining chips. The tensile strength values furthermore support the apparent interparticle bonding revealed by metallography, as we have reported before. For comparison, sintered 601AB exhibits tensile property sets from 50 MPa/125MPa/8% to 240 MPa/250 MPa/2%, depending on the density and temper.[1] Work is ongoing to quantify the degree of bonding in terms of tensile strength, which, with such limited ductility, is also strongly dependent on the size of pores and other flaws.

Larger scale extrusions using the ORNL extrusion facilities are in progress.

Polymer-Bonded Chip Particulate Composites

Die press bonding has been used to produce bulk Al-6061-T6 samples from nanostructured chip particulate using a small amount (<10%) of epoxy as binder. Figure 2 shows a typical example. Small amounts of porosity persist, especially where larger particles were not packed uniformly, but most particle boundaries show a thin bond layer of epoxy. Epoxy and porosity volumes as low as 6% have been achieved so far, and preliminary nanohardness measurements show little or no loss of hardening imparted in producing the chips, consistent with separate measurements of coarsening-softening kinetics in this alloy.

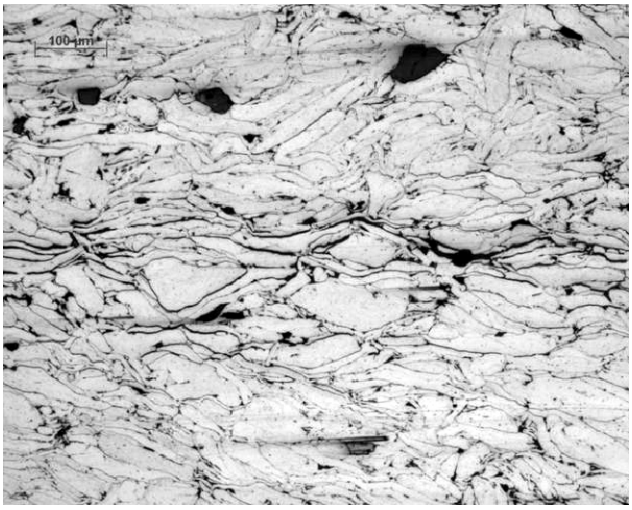

Figure 2. Optical micrograph showing epoxy-bonded Al-6061-T6 chip particulate (15–100 µm) pressed at 1000 MPa and cured at 100°C.

Work in the next year will proceed to tensile testing in order to evaluate the degree of bonding. Although high strength and ductility are not predicted, the high hardness should impart improved wear resistance together with the shaping advantages of powder processing.

Highly Stable Nanostructured Materials

Figure 3 illustrates the nanostructured material composed of grains typically 100 nm in size produced from solution-treated microcrystalline Inconel 718 (grain size ~50 µm in the initial state) due to plastic shear strains of ~6. The microstructure is composed primarily of equi-axed grains, along with some elongated structures. The diffraction pattern inset in Figure 3 indicates the presence of large angle grain boundaries in this nanostructured material. The Vickers microhardness value of this microstructure was 550 kg/mm^2 (~5.4 GPa), nearly twice that of the undeformed bulk microcrystalline solution-treated material (300 kg/mm^2).

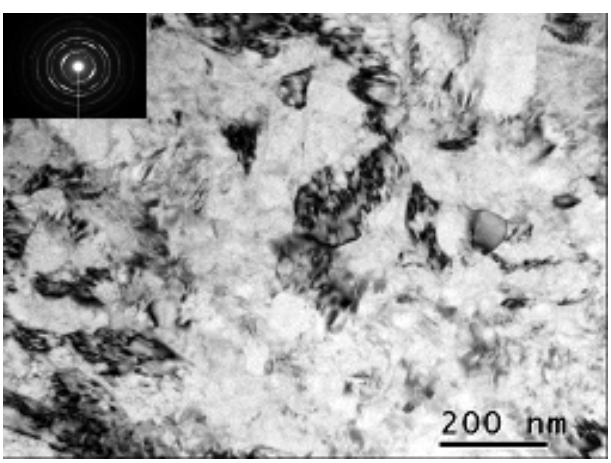

Figure 3. TEM micrograph of nanostructured Inconel 718 produced by large strain machining (shear strain ~6) from solution-treated microcrystalline Inconel 718. Average grain size is ~100 nm.

When this nanostructured material was heat treated at 600°C (~ one-half the melting point), a rapid hardening was found that can be associated with precipitation in the nanostructured solution-treated material. Figure 4 illustrates the variation in microhardness of the nanostructured Inconel 718 with temperature and the attainment of a peak hardness value of 630 kg/mm^2 (~6.2 GPa) after about 6 h of annealing. This hardness value corresponds to a tensile yield strength of ~2 GPa for this material. Figure 4 confirms the extraordinary stability of material strength (hardness) of this HSN Inconel 718 even after 30 h at 600°C (~ one-half of the melting temperature). The peak hardness of

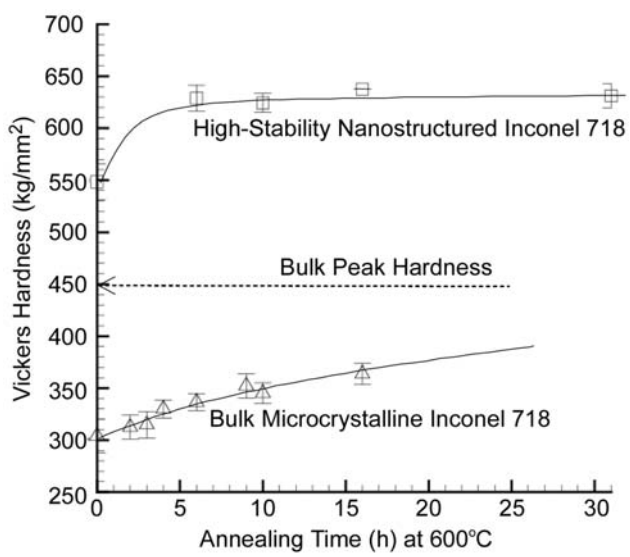

Figure 4. Variation of Vickers hardness with annealing time at 600°C for high-stability nanostructured (HSN) Inconel 718 and bulk microcrystalline Inconel 718 (undeformed bulk, grain size ~50 µm). The bulk peak hardness of 450 kg/mm^2 is that of microcrystalline Inconel 718 after prolonged double-ageing treatment and is shown for comparison. HSN Inconel 718 was also heat treated at 600°C for 500 h, and its hardness was found to remain stable at ~630 kg/mm^2.

630 kg/mm^2 is unchanged throughout this heat treatment, and this hardness value is still ~40% greater than that of peak-aged Inconel 718 (~450kg/mm^2) in the conventional microcrystalline form. We also performed annealing experiments at 600°C for 500 h on the HSN Inconel 718, and even such prolonged heat treatment was found to have a negligible effect on the stable hardness value (~630 kg/mm^2).

The materials design principle propounded above can be generalized to other precipitation-treatable materials and offer a new line of development for this important class of structural materials. Other material systems that form stable, fine precipitate phases, for example, P-series stainless steels, Waspaloy, can be expected to behave in a similar manner in the nanostructured state. Exceptional thermal stability and retention of the material strength are ensured by the stable, fine precipitate phase and the fine microstructure coexisting at high temperatures for significant lengths of time, resulting in a class of HSN materials with enormous potential for high-strength and/or high-temperature applications. These avenues will be investigated in detail in the coming year.

Nanostructured Pure Titanium by Machining

Figure 5 shows a TEM micrograph and selected area diffraction pattern of nanostructured titanium formed in machining chips. The starting grain size of the commercially pure titanium was ~50 µm, and TEM revealed a grain size range of 50 to 200 nm in the chip specimens. Correspondingly, Vickers hardness increased from 144 ± 5 to 230 ± 9 kg/mm^2, consistent with the machining response of a wide range of other pure metals and alloys.

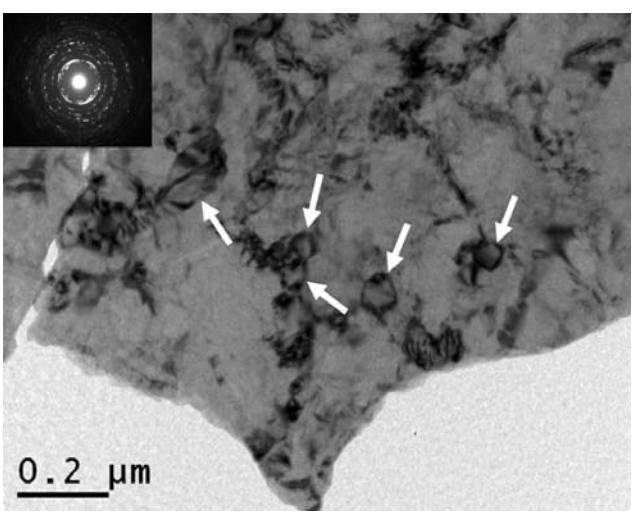

Figure 5. TEM micrograph.

References

1. *Metals Handbook*, 9th ed., Vol. **2** (1979).

Presentations and Publications

S. Swaminathan, S. Chandrasekar, W. D. Compton, K. P. Trumble, and A. H. King, "Microstructural Refinement in Single-Phase Copper Solid Solutions by Machining," in *Nanoscale Materials and Modeling-Relations Among Processing, Microstructure and Mechanical Properties, Materials Research Society (MRS) Proceedings*, **821**, p. 8.27 (2004).

S. Swaminathan, C. Swanson, T. L. Brown, R. F. Kezar, S. Chandrasekar, W. D. Compton, and K. P. Trumble, "Microstructure Refinement in Steels by Machining," in *Nanoscale Materials and Modeling—Relations Among Processing, Microstructure and Mechanical Properties, Materials Research Society (MRS) Proceedings,* **821**, p. 9.5 (2004).

S. Swaminathan, M. Ravi Shankar, S. Lee, J. Hwang, A. H. King, R. F. Kezar, B. C. Rao, T. L. Brown, S. Chandrasekar, W. D. Compton, and K. P. Trumble, "Large Strain Deformation and Ultra-Fine Grained Materials by Machining," *Materials Science and Engineering A*, **410–411**, 358–363, 2005.

M. R. Shankar, S. Chandrasekar, A. H. King, and W. D. Compton, **"**Microstructure and Stability of Nanocrystalline Aluminum Created by Large Strain Machining," *Acta Metallurgica*, **53**, 4781–4793 (2005).

M. Ravi Shankar, S. Chandrasekar, W. D. Compton, and A. H. King, "Characteristics of Aluminum 6061-T6 Deformed to Large Strains by Machining," *Materials Science and Engineering A*, **410–411**, 364–368 (2005).

M. Sevier, S. Lee, M. Ravi Shankar, H. T. Y. Yang, S. Chandrasekar, and W. D. Compton, "Deformation Mechanics Associated with Formation of Ultra-Fine Grained Chips in Machining," *Materials Science Forum*, **503–504**, 379–384 (2005).

Y. Uluca, B. C. Rao, M. Ravi Shankar, T. L. Brown, J. B. Mann, S. Chandrasekar, and W. D. Compton, "Low-Cost Ultra-Fine Grained Materials from Aerospace Machining Chips," *Proceedings*

SAE Aerotech Congress & Exhibition, *Dallas, Texas,* in press.

S. Swaminathan, S. Chandrasekar, W. D. Compton, A. H. King, and K. P. Trumble, "Large Strain Deformation of Single-Phase Solid Solutions by Plane Strain Machining," *Materials Science Forum*, **503–504**, 651–656 (2005).

S. Swaminathan, M. Ravi Shankar, B. C. Rao, S. Chandrasekar, W. D. Compton, A. H. King, and K. P. Trumble, "Nanostructured Materials by Machining," in *Proceedings of ASME IMECE*, 2005.

Patents

J. B. Mann, M. Ravi Shankar, S. Chandrasekar, W.D. Compton, and W. Moscoso, "Direct Production of Nanocrystalline Particulate by Modulated Machining," U.S. Patent Pending Ser. No. 60/677,247, May 3, 2005.

R. Deformation Processes for the Next-Generation Ceramics

P. F. Becher
Oak Ridge National Laboratory
P.O. 2008, MS 6068
Oak Ridge, Tennessee
(865) 574-5157; fax: (865) 574-6098; e-mail: becherpf@ornl.gov

DOE Technology Development Area Specialist: James J. Eberhardt
(202) 586-9837; fax: (202) 586-1600; e-mail: james.eberhardt@ee.doe.gov
ORNL Technical Advisor: D. Ray Johnson
(865) 576-6832; fax: (865) 574-6098; e-mail: johnsondr@ornl.gov

---

Contractor: Oak Ridge National Laboratory, Oak Ridge, Tennessee
Contract No.: DE-AC05-00OR22725

Objectives

- Assess the plastic deformation behavior in nanocrystalline oxide ceramics and applicability to fabrication of complex shapes.
- Characterize thermal and mechanical properties to assess influence of nanocrystalline microstructures for gaining improved performance for wear and other components.

Approach

- Collaborate with members of the Pennsylvania State University task on Synthesis of Nanocrystalline Ceramics, develop advanced colloidal technology-based processing to fabricate monolithic bodies and sintering technology to be able to fabricate dense monolithic nanocrystalline (i.e., grain sizes <100-nm) bodies.
- Characterize the potential for enhanced plasticity in ceramics resulting from reducing grain size below 100 nm and with the application of applied electric fields with regard to mechanical behavior improvements and applicability to forming and surface finishing technologies.

Accomplishments

- Expanded the fabrication of powder compacts to include granulation technology, which can readily produce larger samples and more complex geometries. The recent sintering studies of granulated compacts were sintered to >92% of theoretical density and exhibited grain sizes of 6 to 140 nm. However, these bodies contained mainly monoclinic phase, which was attributed to a loss of yttria during powder synthesis. This is now being addressed in the Pennsylvania State University task.
- Observed electric field effects on deformation to exhibit a temperature dependence that apparently is altered by the mechanism dictating the plastic flow. Above 1200°C, the reduction in yield stress increases with decrease in temperature. At 1200°C, the field effect becomes more sensitive to the strain rate, which suggests a shift from grain boundary sliding to a dislocation-related process.

Future Direction

- Develop a two-step sintering profile to be able to optimize the microstructure of large compacts produced by the granulation process. Room temperature fracture and wear properties will be examined to seek approaches for developing ceramics with greater wear resistance.

Introduction

In addition to lower specific weight, ceramics have a number of attractive properties for application as components in various heavy-vehicle systems. However, many heavy-vehicle components require ceramics with complex shapes as well as function. Furthermore the demanding service conditions necessitate improved mechanical reliability together with fracture and/or wear resistance. Underlying the performance and use of ceramics is their tendency to fail in a brittle fashion except at temperatures generally well above 1000°C. Complex shape forming processes for ceramics are relegated to approaches based on powder processing as a result of the excessive temperatures for hot forming. On the other hand, metallic alloys can be hot worked at temperatures below 1000°C to not only form the desired shape but also to enhance their properties. The ductility (>20% plastic strain) of metallic alloys at temperatures below 500°C is the source of their 10- to 100-fold greater fracture toughness as compared to that of ceramics.

In ceramic systems, one needs to combine processing to tailor microstructures with novel concepts that offer the potential to enhance deformation. One such concept that has seen considerable interest is that of superplastic deformation of submicron-grain-sized ceramics above 1000°C.[1] Recent studies suggest that reducing the microstructure to achieve grain sizes <100 nm could lead to permanent/plastic deformation in ceramics at quite modest temperatures.[2,3] Recent studies have shown that the application of electric fields can reduce the yield stress or increase the creep rates of ceramic systems.[4] To date, this has not been exploited to determine the effects on the deformation of nanocrystalline oxides. The present study seeks to examine the influence of true nanocrystalline microstructures on the mechanical properties of ceramics, as well as approaches to economically fabricate nanocrystalline ceramics monoliths.

Hardness values generally obey the Petch-Hall behavior with the hardness rising as the grain size is reduced. However, results show that when the grain size is ~20 nm, the room temperature hardness then decreases as the grain size continues to be decreased.[1,5] This behavior has two important implications for applications of interest here. One is that some permanent deformation might be achieved in ceramics with grain sizes <30 nm, and this might offer improved reliability. More likely of interest is the fact that ceramics with grain sizes below 100 nm but above the softening point will be extremely hard, and that offers substantial advantages in overcoming wear problems in rolling stock. In addition, surface roughness of as-sintered ceramics decreases as the grain size decreases. In fact, the as-sintered surfaces of alumina substrates with grain sizes <500 nm exhibit a mirror-like finish without any surface preparation. This feature should be applicable to the fabrication of low-friction components.

Approach

This project involves two major thrusts. The first is a collaborative effort with researchers in the Synthesis of Nanocrystalline Ceramics task at Pennsylvania State University in the processing and sintering of nanocrystalline ceramics. The goal being to develop the technology to form "green" (unfired) bodies of nanocrystalline particles with densities well in excess of 50% of the theoretical density to allow one to devise pressureless sintering profiles to produce dense monolithic bodies with grain sizes <100 nm (see Ref. 6 for a review of processing of nanocrystalline ceramics). This is aimed at finding approaches to produce sizeable monolithic bodies for subsequent evaluation. The second thrust focuses on the mechanical and friction and wear behavior of nanocrystalline ceramics and the influence of external parameters [e.g., stressing rate, temperature, environment (e.g., air, vacuum)], and electric fields on the plastic deformation behavior.

Synthesis, Evolution, and Stability of Nanostructures in Bulk Materials

Outstanding challenges in particle processing to form bulk, dense nanograin-sized materials include the dispersion of the nanosize particles and control of gas evolution from the very high surface area compacts during sintering. Typically, nanometer size particulates suffer from a high degree of agglomeration, which results in poor particle packing (green densities <40% of theoretical), which inhibits sintering and promotes undesirable grain growth. Two routes to obtaining well-dispersed powders include comminution and colloidal processing.[7,8] By optimizing colloidal processing approaches, one should be able to produce "green" bodies with densities in excess of 60% of theoretical

by control of interparticle forces through appropriate chemical additives to suspensions of nanoparticulates combined with filter pressing or pressure casting of the high-solids-content slurries. By controlling the packing of nanoparticulates one should be able to control the porosity to achieve the narrow size distribution necessary, which then will enhance densification.

Densification of nanocrystalline ceramics has typically involved the use of applied pressure to achieve dense sub-100-nm grain sized samples.[9] In those few cases where pressureless sintering has been employed successfully, long hold times at the sintering temperatures were required to achieve densities ≥95% of theoretical, which allows undesired grain growth to proceed.[10] Heating to a temperature sufficient to achieve densities of ≥75% of theoretical followed by rapidly lowering the temperature to a level to obtain sufficient boundary diffusion to remove pores trapped on boundaries while minimizing grain growth have been only partially successful because long hold times at the lower temperature were still required.[11] Here we seek to optimize the processing of the "green" bodies and utilize modified sintering cycles to achieve dense sub-100-nm grain size oxides.

Deformation Behavior in Nanostructured Materials: Baseline deformation data will be established through studies of high purity, dense submicron grain size zirconia ceramics in order to evaluate the influence of nanocrystalline microstructures. These studies will then be extended to <100-nm grain sized ceramics. This will include (a) nanostructured ceramics to explore for the softening effects observed in nanocrystalline metals by evaluating both the creep response over a range of temperatures and applied stresses, and the yield stress as a function of strain rate and temperature, and (b) the influence of external factors (e.g., electric fields) that have been shown to enhance deformation processes in ceramics with micrometer grain sizes. Modeling studies will be conducted to describe the deformation behavior and to address such phenomenon as space charge/solute segregation coupled with electric field effects. Additionally, the fracture, hardness, and wear response of nanocrystalline oxides will be evaluated to assess their application in wear components.

Results

Sintering

The Synthesis of Nanocrystalline Ceramics task recently expanded the powder processing method to include granulation to more readily produce large powder compacts. In the granulation step, the chemically derived particulates are dried and treated to form granules, which are basically large, soft agglomerations. These then could be pressed to form bodies of various dimensions to densities of 50 to 55% of theoretical density! The process is very amenable to commercial manufacturing. The ORNL studies have focused on exploring the densification of compacts based on the granulation process approach. Sintering trials at ORNL showed that these granulated compacts could then be densified to greater than 90% of theoretical density, while achieving grain sizes <200 nm. Subsequent characterization revealed that the sintered materials consisted of primarily monolithic zirconia rather than the tetragonal phase. The monoclinic phase is a result of the martensitic transformation from the tetragonal phase upon cooling from the sintering temperature. Transformation to the monoclinic phase involves a volume expansion of ~4%, which is quite large and the associated stress state results in extensive microcrack formation. Such microcracking leads not only to a decrease in density but also to damage and loss of structural intensity.

Earlier work demonstrated that colloidal processed ZrO_2-1.7 mol % Y_2O_3 bodies could be sintered to densities >95% of theoretical density (TD) when held at 1150°C for only 5 min. These were fully tetragonal phase and had grain sizes <100 nm. Even with 200- to 400-nm grain sizes, ZrO_2-1.7 mol % Y_2O_3 bodies were fully tetragonal. On the other hand, granulated compacts sintered at 1125°C for 5 min had densities > 90%TD but were composed of 75% monoclinic and 25% tetragonal phases even though the grain size was below 100 nm. Because the grain size is well below 200 nm, the formation of monoclinic phase must be attributed to an insufficient yttria solute content, which is added to stabilize the tetragonal phase. Current synthesis efforts are addressing steps to control and maintain the yttria levels in the as-synthesized powders.

Deformation studies

Collaborations with Prof. Hans Conrad and Dr. Kang Jung of North Carolina State University are assessing the reduction in flow stress in zirconia ceramics due to the application of an applied direct current (dc) field. In this case, the chemical/ electrochemical potential associated with vacancy flux can be altered by both an applied stress and an applied electric field:

$$\mu^* = \mu^o + Ze\phi_i - \sigma\Omega - Ze\phi_a \quad , \qquad (1)$$

where μ is the potential (superscript o for the standard state, superscript * with electric field); Z is the valence of the ion; e is the charge in coulombs; σ is the stress; Ω is the atomic volume; Φ_a is the applied electric potential (= EX_{SC}); E is the applied electric field; X_{SC} is the width of the space charge zone at the grain boundaries; and Φ_i is the local potential. Thus, one can enhance the flow of vacancies needed for material transport and dislocation motion by applying stress and an electric field. The direction of the vacancy flux is a function of the sign of the applied stress (i.e., vacancies flow to regions under compression). This applies locally to vacancy flow in the deformation of a polycrystalline ceramic where vacancies move from grain boundaries under tension to those in compression while ions/atoms move in the reverse direction. As a result, one can then reduce the applied stress required to deform the material by applying an electric field:

$$\Delta\sigma_E = ZeEx_{SC}/\Omega \quad , \qquad (2)$$

where $\Delta\sigma_E$ represents the reduction in the flow stress due to the applied field.

The width of the space charge zone is related to the Debye length of the material:

$$X_{SC} = \beta\lambda \quad , \qquad (3)$$

where it is a proportionality factor in the range of 2 to 5. Theoretical treatments show that the Debye length (δ) in ionic solids increases as both the bulk solute content and temperature are decreased.[12,13] In addition, δ must be much less than the distance between opposite space charge zones (i.e., << grain size). The influence of temperature and solute content on the Debye length in alkali halides is shown in Figure 1. The increases in the Debye length due to decreases in temperature and solute content will be reflected as increases in the space charge width [Eq. (3)]. One should then expect that the decrease in flow/yield stress brought about by application of an electric field would increase as the temperature decreases [Eq. (2)]. This is indeed the case found for polycrystalline MgO and ZrO_2-3 mol % Y_2O_3 ceramics (Figure 2).

Initial studies on the influence of an electric field on the yield stress in compression of tetragonal zirconia ceramics containing 2 and 2.5 mol % yttria with grain sizes of 350 to 400 nm were conducted at 1200°C to determine a lower temperature limit for such effects. At 1200°C, the electric field effects apparently are much more sensitive to strain rates as analysis of the results indicated the field effects increase with decrease in strain rates. Analysis of the data reveals the stress exponent at 1200°C is ~4 in the zirconia with 2 and 2.5 mol % yttria. On the other hand at ≥1400°C the stress exponent is 2 both for the zirconia containing 2 and 2.5 mol % yttria ceramics without an applied field and the zirconia-3 mol % yttria with an applied field. As a result, the field effect just begins to be indicated at strain rates of 10^{-4}/s at 1200°C, which is the limit of the test facility available for the field effect tests. Studies are now under way to examine the effects of the electric field on the yield stress of the zirconia with 2 and 2.5 mol % yttria at 1450°C. This will allow us to test the effects of solute content on the predicted space

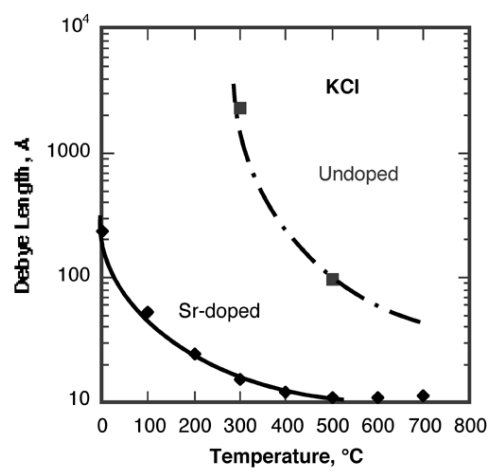

Figure 1. The Debye length is predicted to increase as either the temperature or the solute content decrease as shown for the case of potassium chloride.[12]

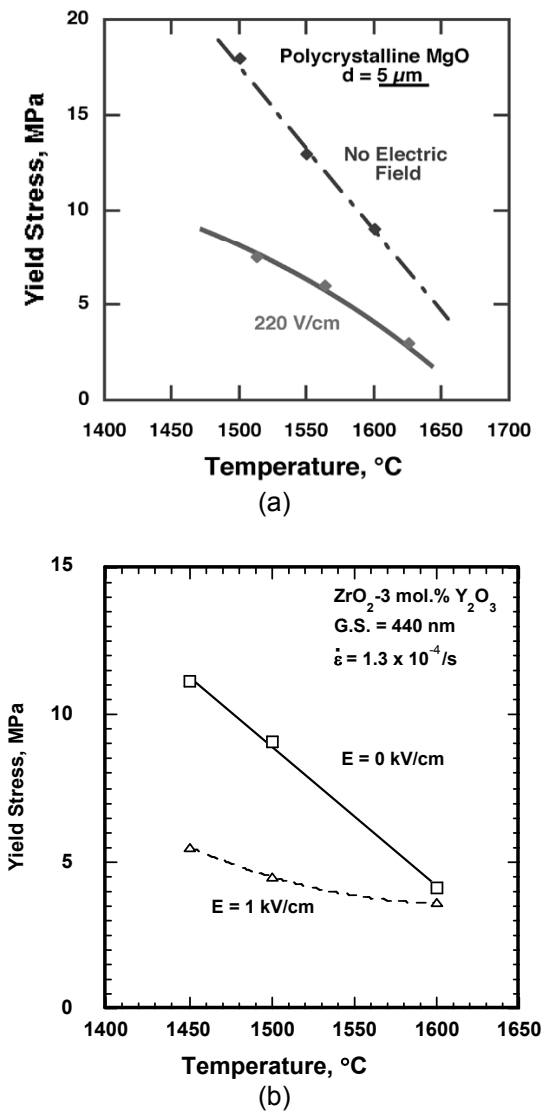

Figure 2. The effectiveness of the application of a dc electric field in decreasing the tensile yield stress increases as the temperature in the range of 1650°C to 1450°C in the case of both cubic magnesia (a)[14] and cubic zirconia containing 3 mol % yttria[15] (b) ceramics.

charge zone size and the role of the space charge zone on the yield behavior.

Conclusions

The fabrication of powder compacts was expanded to include granulation technology, which can readily produce larger samples and more complex geometries. The recent sintering studies of granulated compacts were sintered to >92% of theoretical density and exhibited grain sizes of 6 to 140 nm. However, these bodies contained mainly monoclinic phase, which was attributed to a loss of yttria during powder synthesis. This is now being addressed in the Pennsylvania State University task.

Electric field effects on deformation were observed to exhibit a temperature dependence that apparently is altered by the mechanism dictating the plastic flow. Above 1200°C, the reduction in yield stress increases with decrease in temperature. At 1200°C, the field effect becomes more sensitive to the strain rate, which suggests a shift from grain boundary sliding to a dislocation-related process.

References

1. T. G. Nieh and J. Wadsworth, "Superplastic Behavior of a Fine-Grained Yttria-Stabilized, Tetragonal Zirconia Polycrystal (Y-TZP)," *Acta Metall et Mater.*, **38**, 1121–1133 (1990).

2. H. Conrad and J. Narayan, "On the Grain Size Softening in Nanocrystalline Materials," *Script. Mater.*, **42**, 1025–30 (2000).

3. M. Yoshida, Y. Shinoda, T. Akatsu, and F. Wakai, "Deformation of Monoclinic ZrO_2 Polycrystals and Y_2O_3-Stabilized Tetragonal ZrO_2 Polycrystals below the Monoclinic-Tetragonal Transition Temperature," *J. Am. Ceram. Soc.*, **85**(11), 2834–36 (2002). Ibid, "Superplasticity-Like Deformation of Nanocrystalline Monoclinic Zirconia at Elevated Temperatures," *J. Am. Ceram. Soc.*, **87**(6), 1122–25 (2004).

4. H. Conrad, "Space Charge and the Dependence of the Flow Stress of Ceramics on an Applied Electric Field," *Scripta Mater.*, **44**, 211–16 (2001).

5. T. G. Nieh and J. Wadsworth, "Hall-Petch Relation in Nanocrystalline Solids," *Scripta Metall.*, **25**, 955–58 (1991).

6. M. J. Mayo, "Processing of Nanocrystalline Ceramics from Ultrafine Powders," *Int'l Mater. Rev.*, **41**(3), 85–115 (1996).

7. J. H. Adair et al., "Dynamic Control and Enhanced Chemical Milling of Ceramics to Submicron Particle Sizes," U.S. Patent 6,415,966 B1, July 9, 2002.

8. A. Bleier, P. F. Becher, K. B. Alexander, and C. G. Westmoreland, "The Effect of Aqueous Processing Conditions on the Microstructure and Transformation Behavior of Al_2O_3-$ZrO_2(CeO_2)$ Composites," *J. Am. Ceram. Soc.*, **75**(10), 2649–58 (1992).

9. R. Chaim and M. Hefetz, "Fabrication of Dense Nanocrystalline ZrO_2-3 wt. % Y_2O_3 by Hot-Isostatic Pressing," *J. Mater. Res.*, **13**(7), 1875–80 (1998).

10. A. Bravo-Leon, Y. Morikawa, M. Kawahara, and M. J. Mayo, "Fracture Toughness of Nanocrystalline Tetragonal Zirconia with Low Yttria Content," *Act. Mater.*, **50**, 4555–62 (2002).

11. I.-W. Chen and X.-H. Wang, "Sintering Dense Nanocrystalline Ceramics Without Final-Stage Grain Growth," *Nature*, **404**, 168–71 (2000).

12. K. L. Kliewer and J. S. Koehler, "Space Charge in Ionic Crystals. I. General Approach with Application to NaCl," *Phys. Rev. A*, **140**(4A), 1226–40 (1965).

13. M. F. Yan, R. M. Cannon, H. K. Bowen, and R. L. Coble, "Space-Charge Contribution to Grain-Boundary Diffusion," *J. Am. Ceram. Soc.*, **60**(3–4), 120–27 (1977).

14. H. Conrad and D. Yang, "Influence of an Electric Field on the Plastic Deformation of Fine-Grained MgO at High Homologous Temperatures," *Acta Mater.*, **48**, 4045–52 (2000).

15. K. Jung and H. Conrad, personal communication, 2005.

S. Development of Titanium Component Applications in Heavy-Duty Diesel Engines

Nan Yang, Jeremy Trethewey, Michael Pollard, Jesus Chapa-Cabrera, and John Grassi
Advanced Materials Technology, Caterpillar, Inc.
Tech Center 854-80 TC-E
14009 Old Galena Rd.
Mossville, IL 61552
(309) 578-0056; fax: (309) 578-2953; e-mail: Trethewey_Jeremy_S@cat.com

DOE Technology Development Area Specialist: James J. Eberhardt
(202) 586-9837; fax: (202) 586-1600; e-mail: james.eberhardt@ee.doe.gov
ORNL Technical Advisor: D. Ray Johnson
(865) 576-6832; fax: (865) 574-6098; e-mail: johnsondr@ornl.gov

---

Contractor: Oak Ridge National Laboratory, Oak Ridge, Tennessee
Contract No.: DE-AC05-00OR22725
Subcontractor: Caterpillar, Inc., Peoria, Illinois

Objectives

- Develop and demonstrate a high-strength, lightweight titanium aluminide (TiAl) turbine for a heavy-duty diesel engine. The unique material properties of TiAl will enable the next generation of turbocharger designs to have
  - improved thermal efficiency, and
  - increased transient response.

Approach

- Select the appropriate TiAl compounds and procure high-quality TiAl castings/forgings.
- Develop robust TiAl joining technology to deliver prototype TiAl turbine assemblies for engine testing.
- Demonstrate improved thermal efficiency and transient response in engine test.
- Establish a TiAl material property database to be used as a design tool and for improving next-generation TiAl turbine design.

Accomplishments

- Demonstrated joining of TiAl turbine wheel to Ti-6Al-4V shaft.
- Demonstrated joining of TiAl specimens to steel shaft material.
- Completed foreign object damage (FOD) testing.
- Evaluated physical and mechanical properties of candidate TiAl compounds.
- Assessed the commercial viability of using titanium alloys for turbocharger applications for heavy-duty diesel engines.

Future Direction

- Contract end September 30, 2005

Introduction

Turbochargers on diesel engines play an integral role in enhancing engine performance, controlling fuel economy, and meeting emission regulations. After a half century of development, the performance of a turbocharger is now greatly limited by the properties of turbine materials. Turbines in diesel engines, subjected to long-term exposure to high-temperature exhaust gases above 750°C, are traditionally made of nickel-based superalloys. These superalloys have a relatively low specific strength and large inertia due to their high density, approximately 8.0 g/cm^3. Therefore, turbines made of superalloys usually utilize a low air efficiency design and inherently have a slow transient response. A lightweight, high-strength, heat-resistant material to replace the current turbine materials is critical for further improving turbocharger performance.

Caterpillar has selected candidate TiAl intermetallic compounds to enable next-generation turbocharger designs. The candidate TiAl compounds possess a favorable combination of low-density and attractive high-temperature capabilities. Turbines made of TiAl compounds are anticipated to provide faster response (with reduced transient emissions) and better fuel economy. One of these turbine designs has already been chosen as the prime path for select Caterpillar off-highway applications in 2008. Experience with low-volume product under harsh conditions will also encourage high-volume applications aligned to Caterpillar ACERT™ engines for on-highway trucks in 2010.

Approach

The primary focus of the TiAl turbocharger project in the year 2005 is to develop technology to join TiAl turbine wheel to shaft materials. The difference between a TiAl turbocharger and a conventional one is the material used for the turbine wheel. In the 2004 budget year, Caterpillar identified two potential suppliers along with the candidate TiAl alloys and procured good quality cast TiAl wheels. Subsequently, the most important technology in manufacturing TiAl turbochargers is now the joining of the turbine wheel to its shaft.

Similar to other intermetallic compounds, limited ductility at ambient temperature of TiAl compounds intrinsically presents a great technical challenge for joining TiAl turbine to its shaft. Friction welding (FW) was selected as a prime path for the joining because of previous success in joining TiAl valves to Ti6Al4V shafts in a Department of Energy (DOE)-funded project. However, weak and cracked joints with strengths of approximately 50 MPa were produced when the welding was scaled up from valve to turbine. A parametric study to conduct FW at different conditions could not avoid cracking, which typically occurred at the later stage of FW process. Therefore, two approaches have been pursued for the joining in this year. One is to continue the effort in friction welding to solve the cracking problem and achieve acceptable joint strength. Another is to examine brazing methods.

Once the turbine wheel is successfully joined to the turbine assembly with acceptable strength, a gas stand test will be completed for preliminary turbo efficiency and reliability. Subsequently, engine and machine tests will be conducted for demonstrating improved thermal efficiency and transient response. Material property characterizations have been conducted in parallel to the turbine rig tests to establish a TiAl materials database to be used as a design tool for improving next-generation TiAl turbine designs.

Results

Successful FW was accomplished to join TiAl turbine wheels to Ti6Al4V shafts. The successful welding was achieved through extensive finite-element analysis (FEA) simulations, aimed at understanding the correlation among the welding parameters, and intensive welding trials, designed according to the input acquired from the FEA simulations and microstructure characterization. The ultimate tensile strength of the joints between TiAl turbines and Ti6Al4V shafts has achieved 570 MPa.

The FEA simulations results confirmed the extremely high thermal stresses inside the TiAl turbine near the welding interface. The FEA simulations were conducted using commercial simulation tools and customized user subroutines based on a thermal mechanical model. Welding parts geometry and welding parameters were input to the simulation. Temperature profile, stress components, and strain components (deformation) were output from the simulation (an example is shown in Figure 1). Simulations using the conditions for the early FW trials showed that the hoop stresses near the welding line were more than 1 GPa. The simulation result agreed with the failure analysis work conducted at

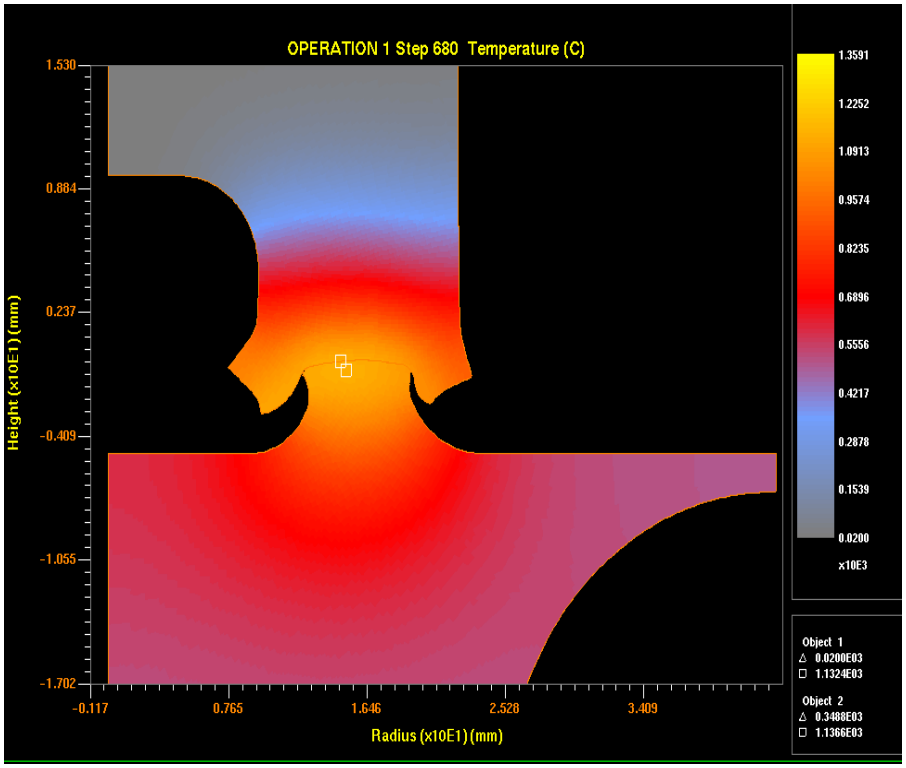

Figure 1. A temperature profile at the beginning of the forging stage obtained through simulations using a thermal mechanical model. FEA of the joining process is used to understand the sensitivity of the thermal stresses to FW control parameters. The simulations were carried out for the friction and forging stages, respectively, for the welding process.

cracked joints. Excessive thermal stresses were therefore identified as the primary cause for the joint cracking.

The critical factors determining the thermal stresses were then identified through FEA sensitivity studies. These simulations were performed using a systematic combination of the factors affecting FW process, including part geometry, rotational speed, friction and forge loads, and friction and forge times. Analyses were then conducted on the simulation results to provide a general understanding of the effect of these factors on the resulting temperature profile and thermal stresses. Among these factors, welding part geometries were relatively independent to other factors and were therefore optimized separately to minimize their effect on thermal stresses (Figure 2). Optimizing other critical factors was completed through intensive experimental trials. These experiments have been designed based on the understanding gained from the FEA simulations. Modification of the friction welding facilities has been implemented to conduct the design of experiments.

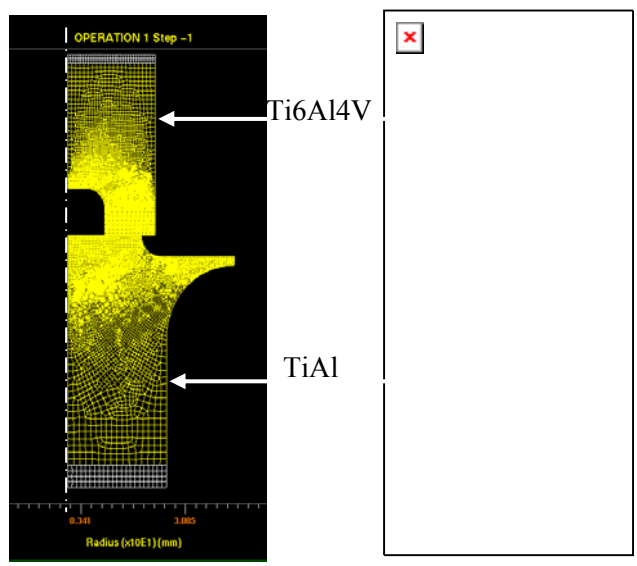

Figure 2. FEA used to study the effect of geometry constraint on the joint quality.

With the above efforts, the thermal stress cracking issue has been resolved and crack-free welding has been achieved. Figure 3 is a

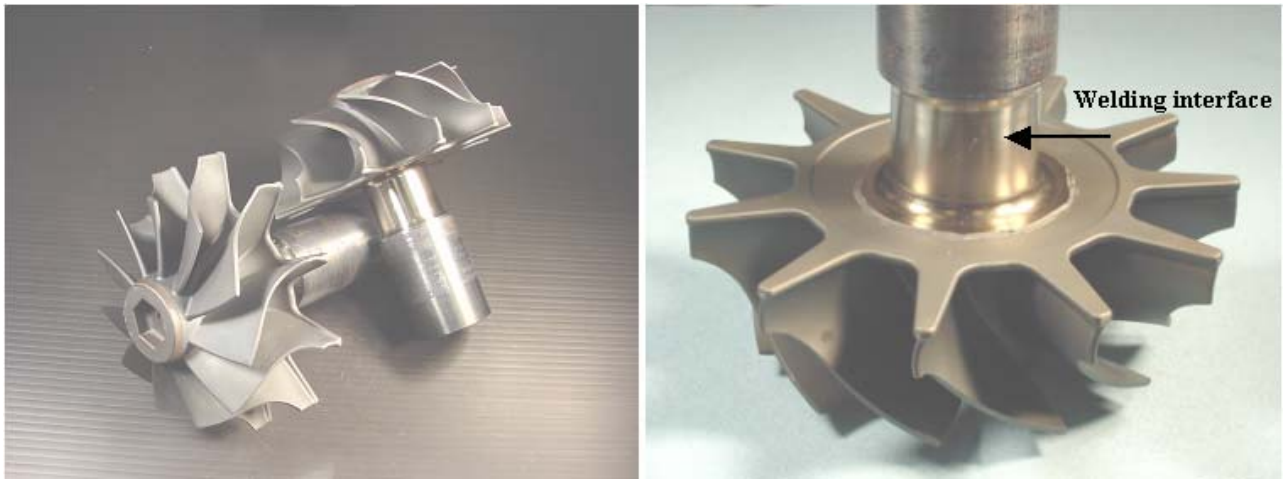

Figure 3. TiAl turbine wheels joined to Ti-6Al-4V shafts by FW.

representative photograph of these joined TiAl turbines (~1 kg). Nondestructive evaluation (NDE) techniques have been used in examining the weld joints. No crack or defect could be identified in the welding zone or heat affected zone. Figure 4 shows several representative NDE scans obtained with Eddy current and ultrasonic inspection techniques. These scans could not capture any surface/subsurface cracks or radial cracks, but rather demonstrate the uniform weld interface. Compared to the

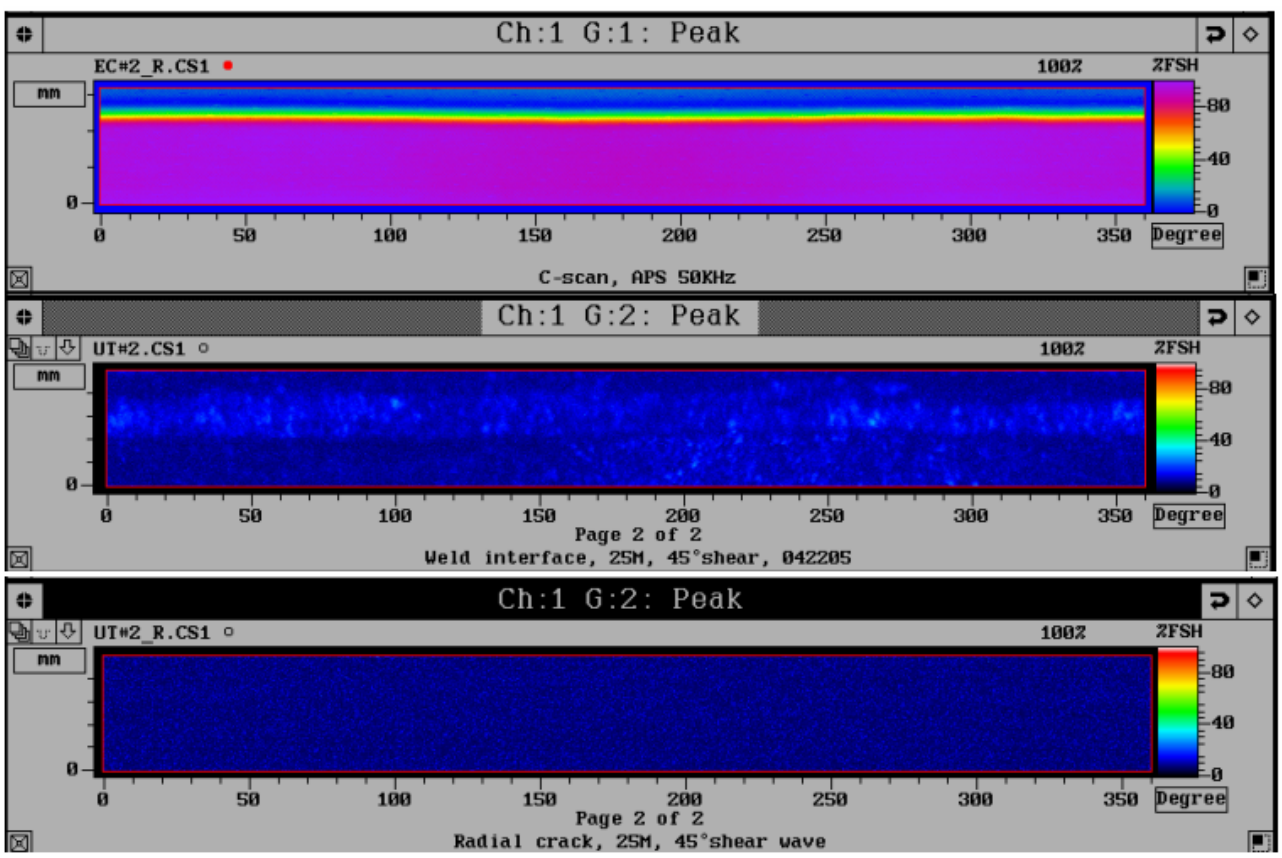

Figure 4. NDE results at the weld and heat affected zone. No surface or near surface cracks could be detected using (a) Eddy current technique, (b) ultrasonic inspections also indicate that the welding interface is uniform, and (c) free of radial cracks.

NDE results in the previous year annual report, the current NDE results indicated a significant improvement in joint quality. Tensile bars prepared from these welded joints demonstrated that the highest tensile strength was about 570 MPa. These tensile test bars usually failed several millimeters away from the welding interface in the TiAl turbine wheel side. In a full-scale tensile test on the turbine wheel, the fracture surface is about 20 mm away from the joint interface as shown in Figure 5. The joint strength has reached the strength of the TiAl alloy. The FW process has been further scaled up to larger size TiAl turbine wheels (~2 kg). Joints have been successfully produced free of any visual cracks. NDE examinations and tensile tests are yet to be completed on these joints.

Eighteen FW trials were conducted to join 50-mm-diam. Ti6Al4V bars to 37.5-mm-diam. 4140 steel bars with a goal to use steel instead of Ti6Al4V as a shaft material. Fifteen out of eighteen trials were successfully joined without any visual cracks. NDE examinations could not detect any cracks or defects in these joints. Mechanical tensile test have been conducted on tensile bars prepared from the joints. The highest tensile strength is slightly more than 300 MPa, but the joints are rather brittle.

Materials characterizations have been carried out for the TiAl materials obtained from the two suppliers to compare the properties and establish a materials database to be used as a design tool for next-generation turbine applications. Mechanical tensile tests were performed at room and elevated temperatures for the TiAl materials from both suppliers. Figure 6 shows normalized results of ultimate tensile strength and elongation at failure for the two TiAl materials. Material from Supplier B has lower strength at low temperatures than Supplier A. However the curves cross over at about 700°C, above which the TiAl material from Supplier B becomes stronger than Supplier A. In addition, the ductility of the TiAl material from Supplier B is higher than that from Supplier A. Physical properties have also been measured, and the results show that the density of the TiAl materials from Supplier A is about 2% higher than that of Supplier B. Thermophysical properties of the two TiAl materials are apparently different. As shown in Figure 7, thermal conductivity of the TiAl material from Supplier B is

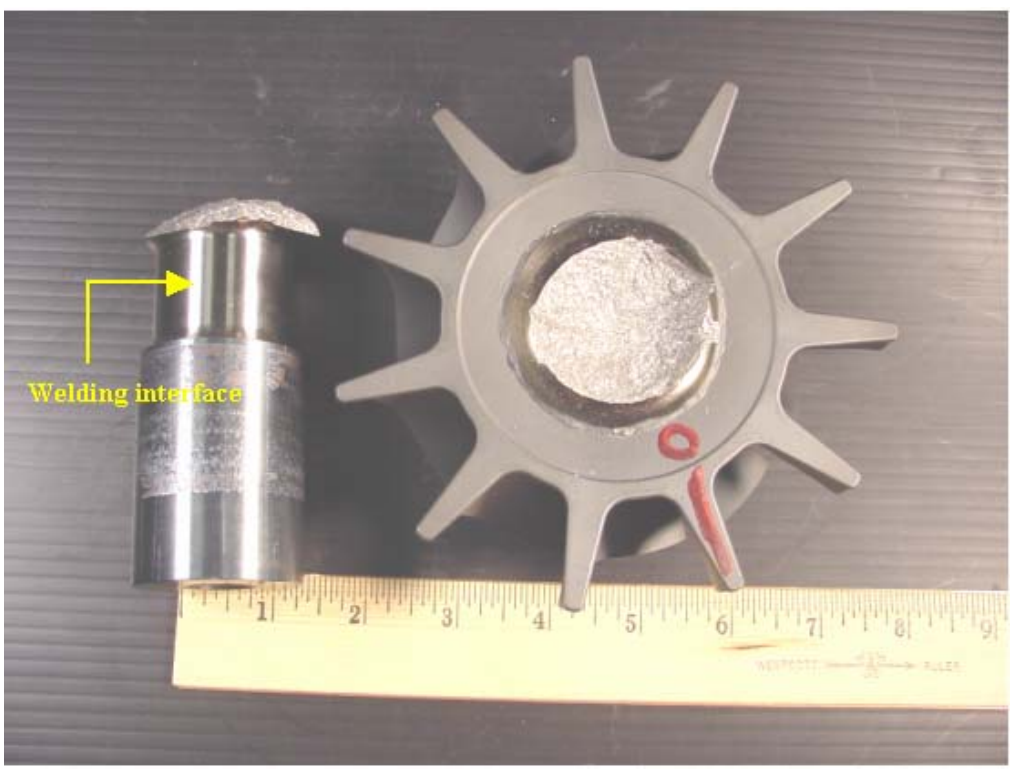

Figure 5. Friction-welded TiAl turbine wheel failed about 20 mm away from the FW interface in mechanical tensile test. The hub of TiAl turbine wheel is completely pulled out of TiAl wheel.

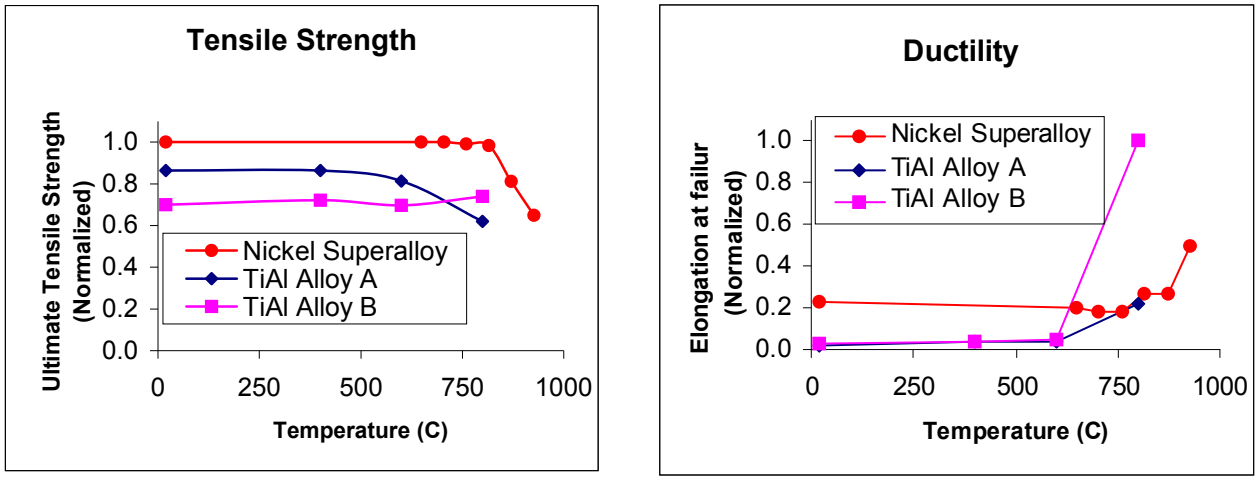

Figure 6. Comparison of tensile strength and ductility of TiAl compounds and nickel-based alloy.

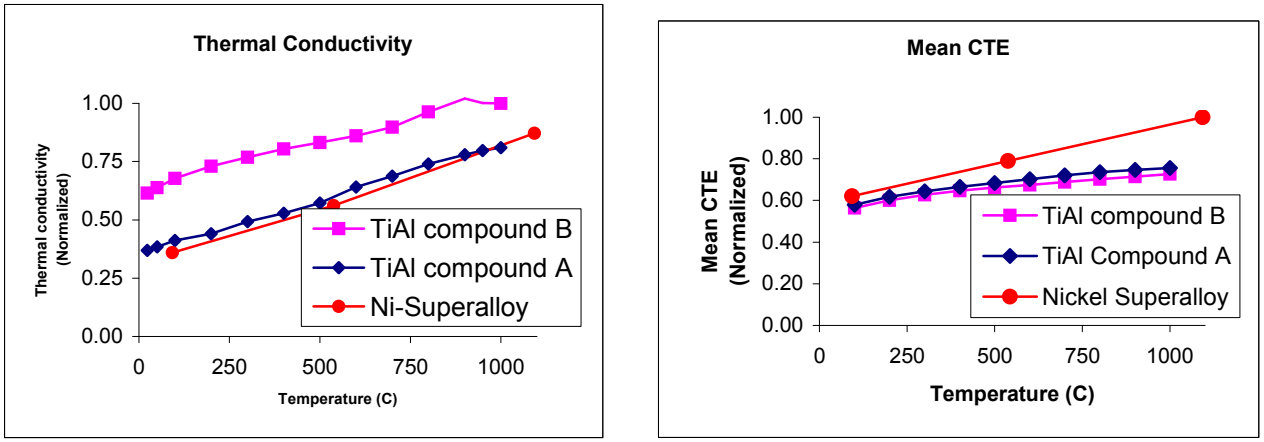

Figure 7. Comparison of thermal conductivity and coefficient of thermal expansion for TiAl compounds and nickel-based alloy.

more than 30% higher than that from Supplier A, but the coefficient of thermal expansion of the TiAl material from Supplier B is about 5% less than that of the material from Supplier A.

FEA simulations have been conducted to evaluate the effect of material property differences of the two TiAl alloys in the turbocharger applications. This involved the analysis of the strain/stress differences in the turbine at engine operating conditions based on the measured properties data. Consequently, no significant effect could be found despite the discrepancies in properties of the two TiAl materials. Creep tests are being conducted at Oak Ridge National Laboratory (ORNL) as well as an external test facility. These tests are scheduled to be completed by the end of 2005. Low-cycle fatigue (LCF) tests will start in the next quarter and be followed with full-scale thermal mechanical fatigue (TMF) tests.

Conclusions

Successful FW has been achieved in joining ~1-kg TiAl turbines to Ti6Al4V shaft. The joint tensile strength has been increased more than tenfold from ~50 MPa to 570 MPa. The FW process is yet to be fully scaled up to a ~2-kg TiAl turbine wheel. Sufficient confidence has already been gained in FW TiAl turbine wheels to Ti6Al4V shafts. Validating

the joint quality needs to be completed before a gas stand or engine test on these turbines to demonstrate improved transient response and thermal efficiency. The option of using steel shaft through FW joining is still dubious. The tensile strength of the joints produced between 4140 steel and Ti6Al4V shafts is about 300 MPa, lower than the tensile strength of TiAl material. Microstructure characterization needs to be conducted to investigate the brittleness of these joints.

Mechanical tensile tests, physical properties characterizations and FEA simulations have been carried out for the TiAl materials from the two suppliers. No significant differences in terms of turbine applications have been identified for the two TiAl materials despite some discrepancy in their mechanical and thermophysical properties. Characterizations for creep properties and thermomechanical fatigue properties of the two TiAl materials are yet to be completed.

Presentations and Publications

Presented for a DOE annual program review on April 27, 2005.

Poster for DOE Heavy Vehicle Propulsion Materials Merit Review, September 12–16, 2005.

T. High-Speed Machining of Titanium

Rahul Aphale
Third Wave Systems, Inc.
Minneapolis, MN
(952) 832-5515

DOE Technology Development Area Specialist: James J. Eberhardt
(202) 586-9837; fax: (202) 586-1600; e-mail: james.eberhardt@ee.doe.gov
ORNL Technical Advisor: D. Ray Johnson
(865) 576-6832; fax: (865) 574-6098; e-mail: johnsondr@ornl.gov

Contractor: Oak Ridge National Laboratory, Oak Ridge, Tennessee
Contract No.: DE-AC05-00OR22725
Subcontractor: Third Wave Systems, Inc., Minneapolis, MN

Objectives

- To improve the material removal rate in machining of Ti-6Al-4V by developing modeling capabilities for various machining processes.

Approach

- Develop drilling modeling capability in the finite element modeling–based tool, AdvantEdge.

Accomplishments

- Delivered and validated drilling capability for titanium workpieces.
- Validated predictions from the AdvantEdge modeling software using drilling test data generated by the University of Michigan.

Future Direction

- Continue to work on reducing computational times and improving accuracy.

Summary

Delivery and validation of drilling capability for titanium workpieces has been successfully accomplished. Third Wave Systems developed the drilling modeling capability in a finite element modeling–based tool, AdvantEdge. Drilling test data generated by the University of Michigan were used to validate predictions from the AdvantEdge modeling software. The agreement between predicted and experimental data was within 15%. Third Wave Systems continues to concentrate its efforts on reducing computational times and improving accuracy.

Task Details

Development of the drilling model was performed for two fluted twist drills via modifications to adaptive meshing and contact algorithms for improvement in overall performance and robustness.

The graphical user interface (GUI) development was performed with the implementation of parametric definition of drill geometry. Twist drills can be defined with either drill design parameters or drill grind parameters (Figure 1). The fundamental information used by the initial mesh generator are the grind parameters, since this is the information

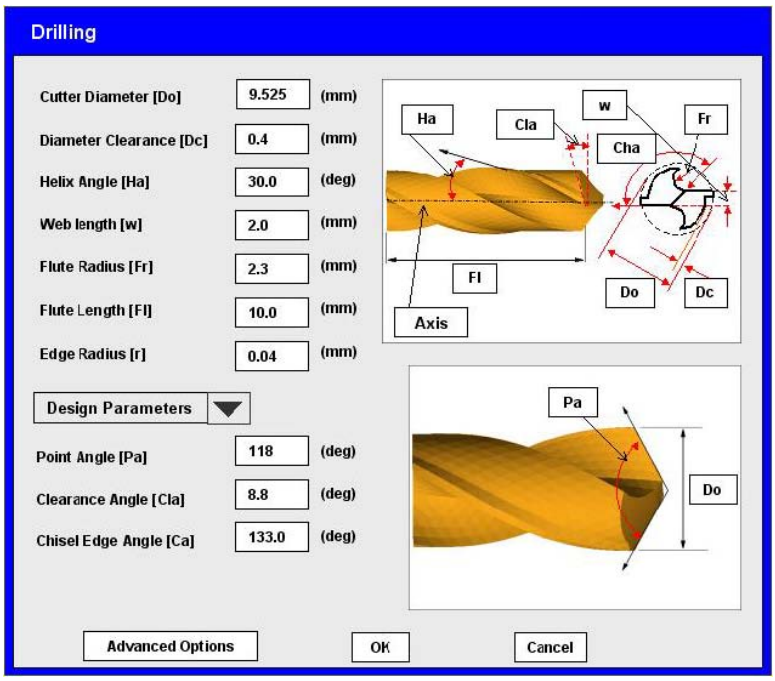

Figure 1. Inputs parameters are shown for drill geometry specification.

used in fabrication. Consequently, a nonlinear set of equations needs to be solved to determine the grind parameters if the user defines the drill geometry via design parameters. The solution of these equations is very fast, taking only a few seconds. Figure 2 shows an example of drilling modeling setup, with chips curling up along the flutes and heat being conducted into chips and deposited on the workpiece.

Additional modifications to contact and mesh adaptation algorithms allow even more chip formation development and drill break-through, . The drill is removed from the analysis, revealing the chip and workpiece with a break-through hole (Figure 3). The adaptation and contact algorithms are able to model both the cutting action of the drill flutes as well as the plowing action of the chisel edge.

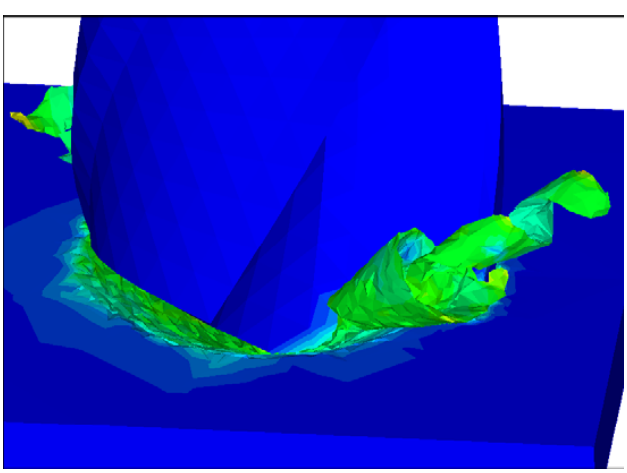

Figure 2. Chip formation for drilling of aerospace alloys. Temperature plots are shown for each chip formed by the two-fluted twist drill.

In order to model the entire hole drilling process, it is necessary to analyze the entrance, full engagement, and exit stages of the cut. To model full engagement it is necessary to have a pre-drilled hole in the workpiece. This hole has the same geometry as the drill would make in one complete revolution. The drill is then inserted into the pre-drilled hole and programmed speeds and feeds are applied. As the drill rotates it progresses deeper in the hole until it finally breaks out, Figure 4.

Modeling and simulation of indexable drills was performed. Automated initial mesh generation was performed for a number of ISO standard inserts. An example of indexable drilling modeling with rectangular inserts is shown in Figure 5. Inserts are offset from center axis of drill, so each insert experiences a different chip load and cutting speed.

Experimental thrust force and drilling torque data were generated by the University of Michigan (Figures 6–9). The drills used were 3.97 mm in

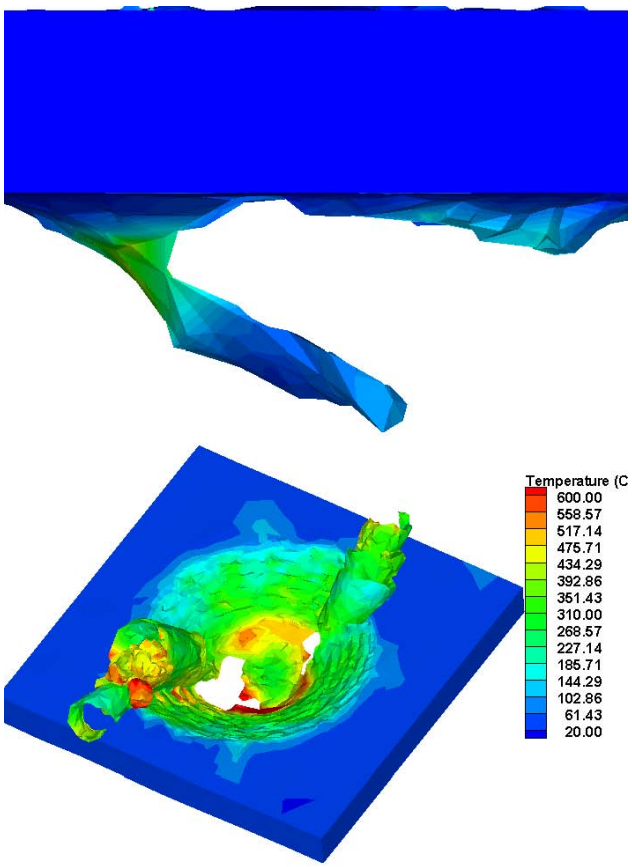

Figure 3. AdvantEdge model of drill breakout shown with drill geometry removed. Burr formation on breakout (top) and chip formation with temperature contours (bottom).

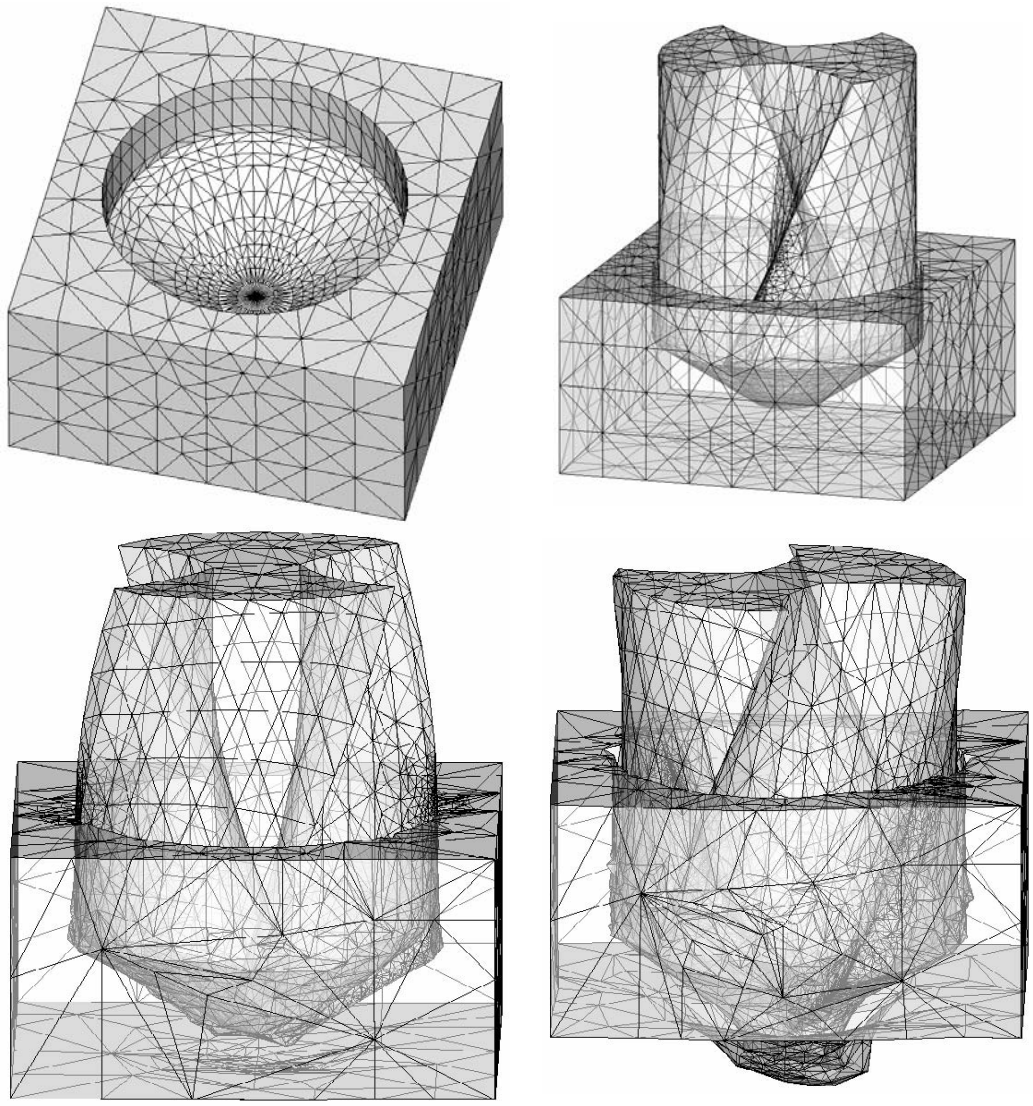

Figure 4. Different stages of drilling with pre-drilled holes are shown. (a) The initial pre-drilled hole in the workpiece; (b) the drill and workpiece combined (translucent mesh); (c) drill and workpiece after several rotations of the drill; (d) and drill break out on the bottom side of the workpiece.

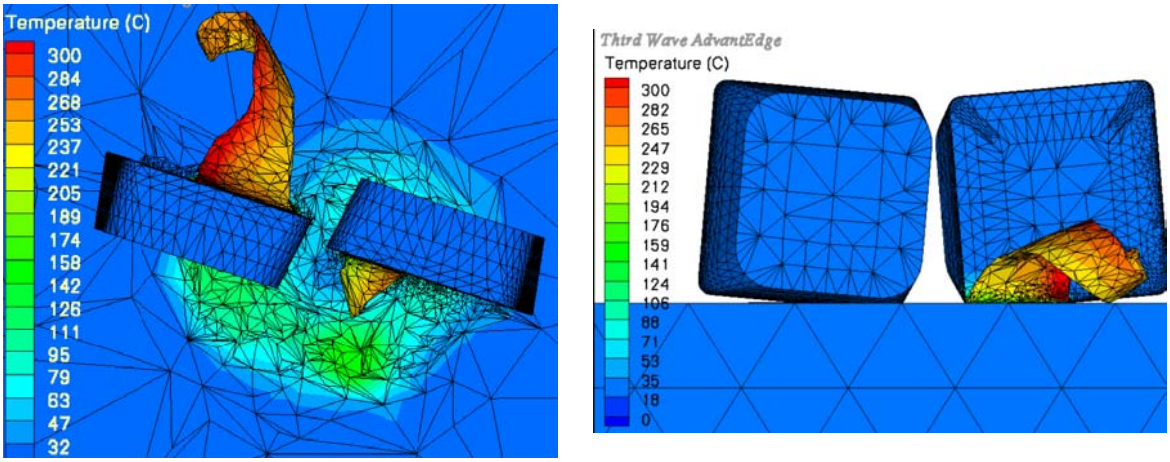

Figure 5. Modeling of indexable drilling is shown with finite element mesh and temperature contours overlaid. Chip formation is seen from the inserts which are offset from center, top view, left; side view, right**.**

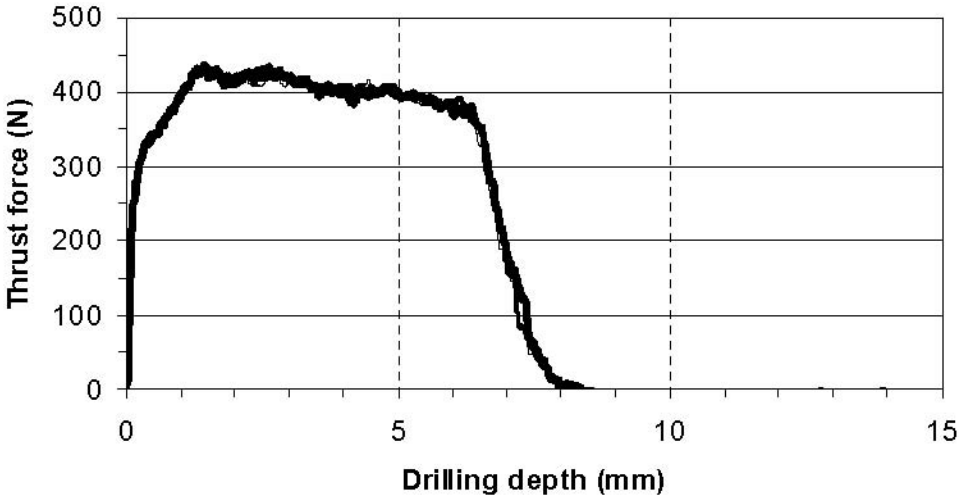

Figure 6. Experimental thrust force data from University of Michigan, for drill diameter of 3.97 mm, 734 rev/min, and 0.050 mm/rev.

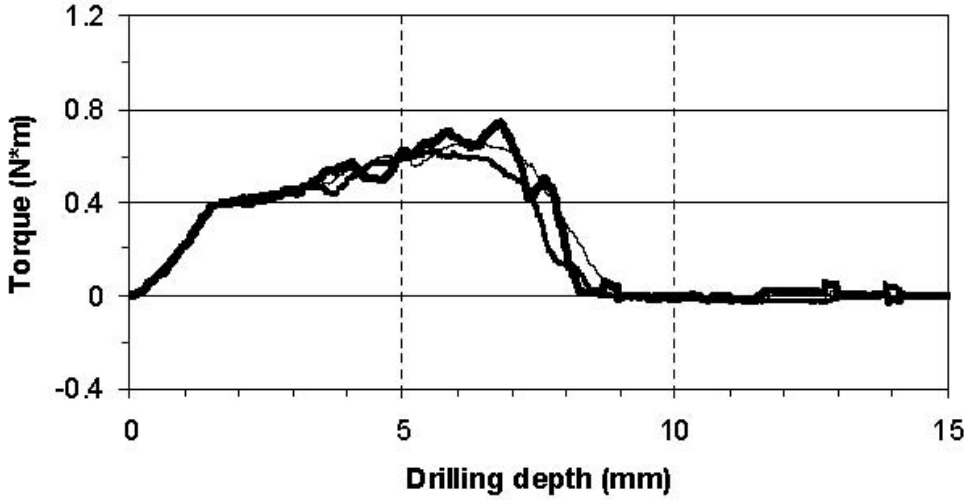

Figure 7. Experimental torque data from University of Michigan, for drill diameter of 3.97 mm, 734 rev/min, and 0.050 mm/rev.

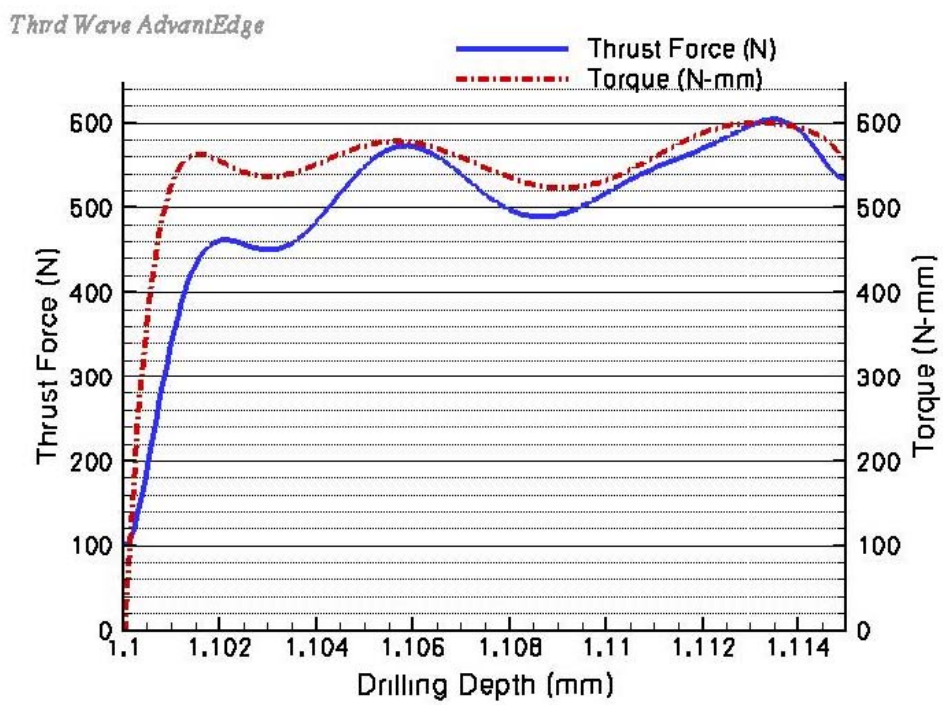

Figure 8. Model predicted torque and thrust force.

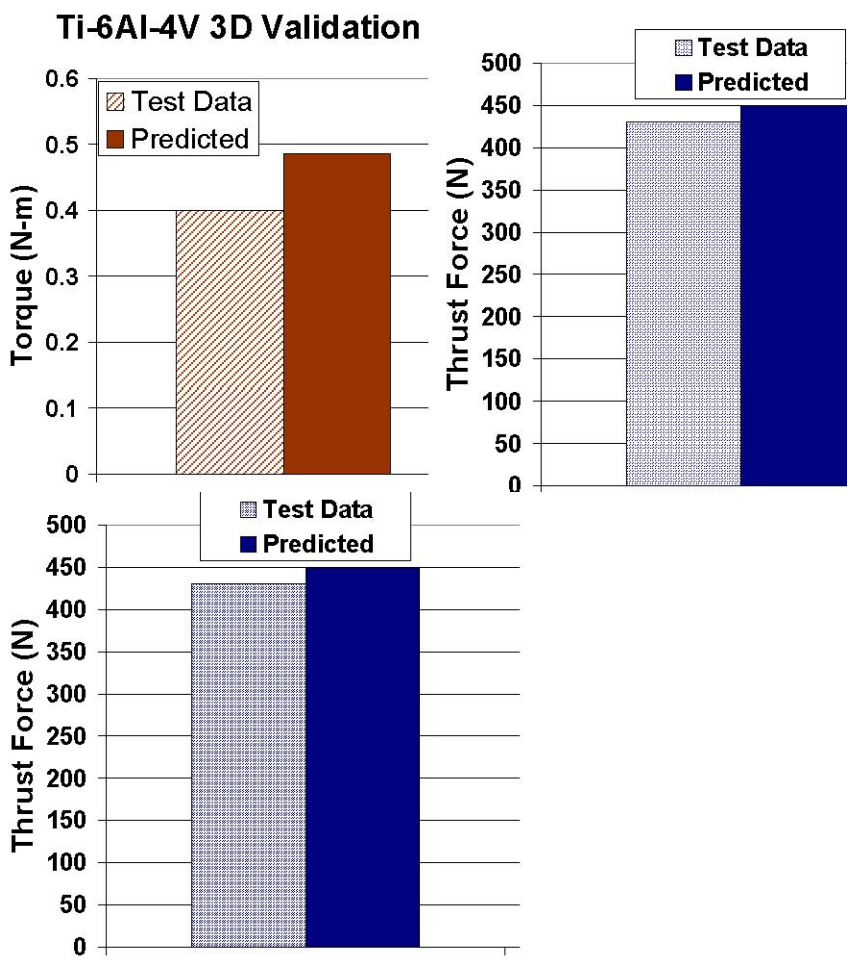

Figure 9. Validation data for drilling with 3.97-mm diameter drill, 734 rev/min, and 0.05-mm/rev feed.

diameter and tests were performed at 0.05 mm/rev feed, and 734 rev/min and 1468 rev/min spindle speeds. AdvantEdge simulations were performed by Third Wave Systems. Simulation results were analyzed and compared with the experimental test data, F. It was observed that the model prediction for thrust force was within 15% of experimental thrust force at 734 rev/min speed and within 25% at 1468 rev/min, F. Third Wave Systems continues to concentrate its efforts on significant improvements in the computational times and accuracy of the predictions.

Future Work

Third Wave Systems continues to work with University of Michigan and ORNL for completion of remaining tasks per milestone.

5. TEST AND MATERIALS STANDARDS

A. Rolling Contact Fatigue

Andrew A. Wereszczak
Ceramic Science and Technology Group (CerSaT)
Oak Ridge National Laboratory
PO Box 2008, MS 6068
Oak Ridge, TN 37831-6068
(865) 576-1169; fax: (865) 574-6098; e-mail: wereszczakaa@ornl.gov

DOE Technology Development Area Specialist: James J. Eberhardt
(202) 586-9837; fax: (202) 586-1600; e-mail: james.eberhardt@ee.doe.gov
Field Technical Manager: D. Ray Johnson
(865) 576-6832; fax: (865) 574-6098; e-mail: johnsondr@ornl.gov

---

Contractor: Oak Ridge National Laboratory, Oak Ridge, Tennessee
Prime DOE Contract Number: DE-AC05-00OR22725

Objectives

- Enable greater use of next-generation ceramic and coated-metal roller elements for diesel engines through rolling contact fatigue (RCF) and microstructural characterizations.
- Link surface and subsurface flaws to RCF response to enable microstructural engineering that will promote microstructure engineering and improved RCF performance.
- Link RCF performances measured by different internationally used RCF test techniques.

Approach

- Establish three-ball-on-rod (3BOR) RCF test facilities and collaborations with domestic and international institutions that employ different RCF test techniques and correlate test results.
- Vary machining-induced subsurface damage in a Si_3N_4 and correlate that to measured RCF performance and model hypothetical microstructures that will promote improved RCF performance.
- Develop supporting mechanical test methods that enable the study of surface and subsurface flaws in roller elements.

Accomplishments

- Established 3BOR RCF test facility at Oak Ridge National Laboratory.
- Completed summary report on RCF test methods and result interpretations used in Germany, Japan, United Kingdom, and the United States.
- Developed method to evaluate and discriminate the elastic properties of ball bearings in situ using resonance ultrasound spectroscopy (RUS).
- Conceived “c-sphere” flexure strength specimen to enable surface flaw examination.

Future Direction

- Conduct International interlaboratory study to compare 3BOR performances of a selected Si_3N_4.
- Compare RCF damage on rods and balls of a selected Si_3N_4 with the same coarse and fine grinding.
- Refine the geometry and testing of the "c-sphere" flexure strength specimen and the ability to characterize surface and subsurface damage in finished ceramic balls and link to RCF performance.
- Link surface and subsurface flaws to RCF performance.

Introduction

Technical ceramics used as materials for rolling contact bearing components show several practical advantages over traditional bearing steels. The properties of ceramics, specifically low density, high stiffness, high hardness, low coefficient of thermal expansion, and high-temperature capability are properties suited to rolling element materials. Silicon nitride (Si_3N_4) has been found to have a good combination of properties suitable for these applications. Research over the past three decades on structure, quality control, and manufacturing techniques has produced ceramic materials that are suitable alternatives to steel for rolling contact bearing design. This is especially true for hybrid ball bearings (i.e., precision angular contact ball bearings using ceramic rolling elements) that are now offered as standard components within the ball bearing manufacturing industry.

An expansion in the use of ceramic bearings necessitates guidelines for the choice of bearings or rolling elements. In light of these requirements, ASTM standard F2094-01, "Standard Specification of Silicon Nitride Bearing Balls," has been issued recently. The dimensional specifications of balls are based on those of rolling element bearing steel balls. The most remarkable thing in the standard is that the ranking of Si_3N_4's mechanical properties is provided depending on various applications of bearings. However, nothing is described about rolling contact fatigue (RCF) behavior, which is fundamental information to assess the lifetime of the material. Due to the lack of such information, some concern for the reliability of ceramic bearings still remains.

RCF is the surface damage process due to the repeated application of stresses when the surfaces of two bodies roll on each other. RCF is encountered most often in rolling element bearings and gears. The failure process of RCF involves fatigue crack initiation and propagation, which is related to the characteristics of the surface and subsurface quality or flaw population, stress distributions, and lubrication condition. Presently, surface crack defects are considered as a main factor that causes RCF failure. It is difficult to detect these surface cracks during high-volume production processes, and hence it is crucially important to understand their influence and the fundamental mechanism of the failures they cause.

To address these issues, this project characterizes the RCF performance of Si_3N_4 compositions that are under consideration for use, or that are presently used, in rolling element components (e.g., hybrid bearings—see Figure 1, cam roller followers, etc.). The study of the effects that subsurface damage and the stress state from Hertzian contact have on RCF performance is a primary component to this project. Several different test methods are used internationally to measure RCF performance, so this project also works toward reconciling their

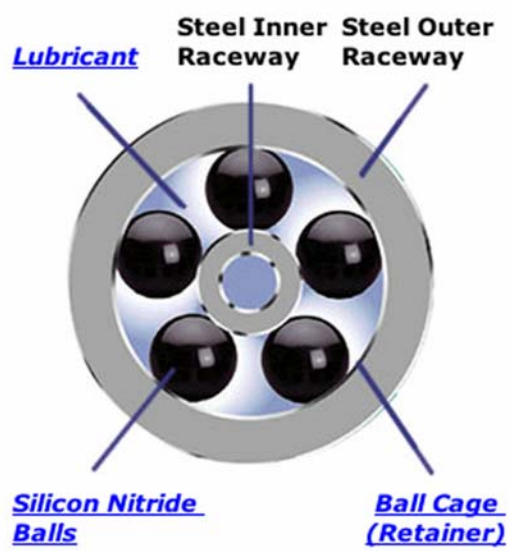

Figure 1. Schematic of a hybrid bearing system that includes silicon nitride balls. Image from Cerbec Web site (www.cerbec.com).

measured differences so that their results can be validly pooled. Based on all these findings, hypothetical microstructures that will promote improved RCF performance will be identified and shared with ceramic manufacturers.

Approach

There are three primary aspects to the project: (1) examine the effects that subsurface damage and microstructure have on RCF performance, (2) measure RCF performance and reconcile results that were generated using different RCF test techniques, and (3) iteratively work with ceramic manufacturers and communicate RCF results and interpretations that those manufacturers can then use to develop lower cost Si_3N_4 compositions or improve Si_3N_4 machinability or improve RCF performance or combinations thereof.

Results

Effects of Surface and Subsurface Damage

The "C-Sphere" flexure strength specimen was conceived and preliminarily developed to measure the strength of bearing-grade Si_3N_4 balls and to relate that property to surface-located strength-limiting flaws (e.g., machining damage) ***and to ultimately link those flaw populations to RCF performance***. A slot is machined into the balls to a set depth to produce the "C-sphere" geometry. C-sphere specimens are then diametrally compressed to produce a monotonically increasing hoop tensile stress at their surface that ultimately caused their fracture (see Figure 2). Strength is determined using the combination of failure load, C-sphere geometry, and FEA.

The stress field was used to determine C-sphere effective areas and effective volumes as a function of Weibull modulus. A quarter symmetry model for the C-sphere specimen is shown in Figure 3 with the mesh distribution that was ultimately used to evaluate its effective volume and area. Solid95 tetrahedral elements were used, and a 100-N point load was applied to the sphere's apex. The mesh contained 52703 elements and 76682 nodes. As can be seen from Figure 3, finer mesh density was used in the region where high tensile stresses would develop, gradually getting coarser toward the area where the load is applied and the overhang section. The ball from which the specimen was simulated had the dimensions of a 12.7-mm diameter and a slot width of 6.35 mm.

The issue of artificially high stress concentration within the narrow zone under the applied point load and its effect on the computed effective sizes was considered. In the virtual world of finite element analysis (FEA), the load is applied as a perfectly concentrated point load, which causes stress singularity in that region. This is an idealization of what physically takes place where distributed load acting over a narrow area is actually applied. In other words, as the mesh gets finer, the stress under the load will increase indefinitely making the model and hence the effective sizes mesh dependent.

To understand the issue of stress singularity under the point load, both nodal and element first principal stress distributions are shown in Figures 4 and 5 for the intermediate and fine mesh models, respectively. A nodal plot smoothes the stress distribution by averaging the stresses at that point in all the elements having that common node. This smoothing is masking the very high stresses taking place within the individual elements, which if not removed would yield erroneous effective size calculations. This is because when the effective size is computed, the stress distribution is normalized with respect to the maximum effective stress in the component. If this maximum effective stress were incorrect, due for example, to a localized stress concentration, as is the case for this model, then the computed value would be incorrect. To unmask the

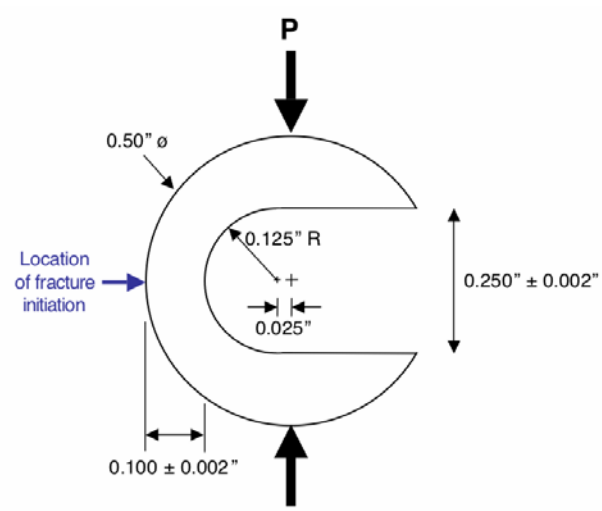

Figure 2. Schematic of the "C-Sphere" test specimen and its diametral compressive loading. Fracture will initiate at the outer surface and propagate radially inward.

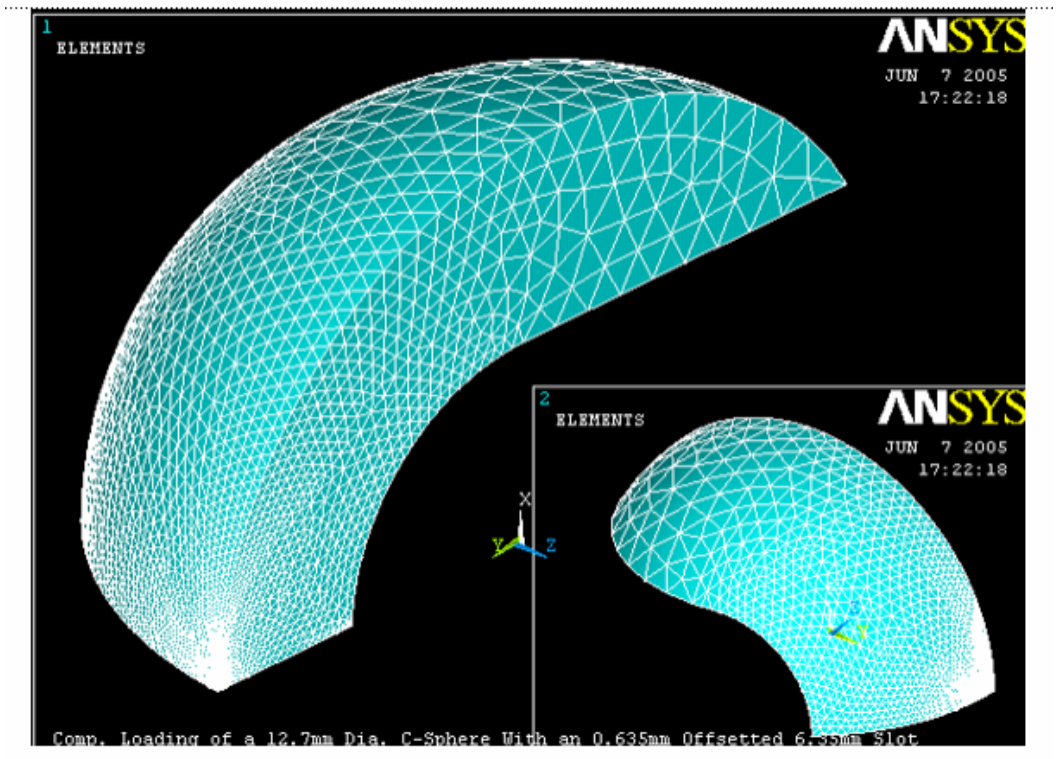

Figure 3. Mesh distribution for one-fourth symmetry model of the C-sphere specimen, having 52703 elements and 76682 nodes. Three different mesh densities were used to evaluate the specimen, and they were coarse (8497 elements), intermediate (16090 elements), and fine mesh (shown—52703 elements).

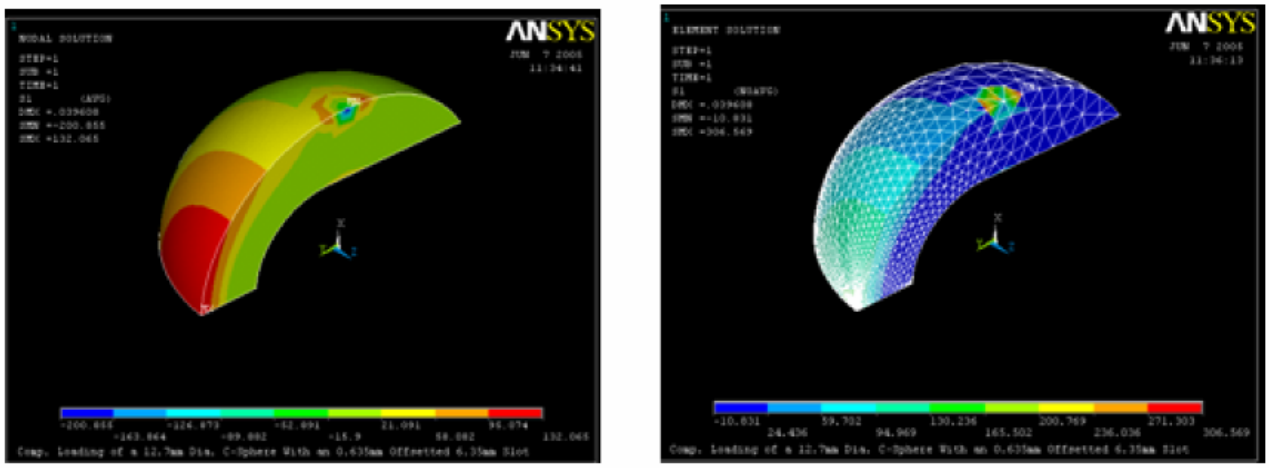

Figure 4. Nodal first principal stress distribution (left) and element first principal stress distribution (right) for the C-sphere specimen, using the intermediate mesh model.

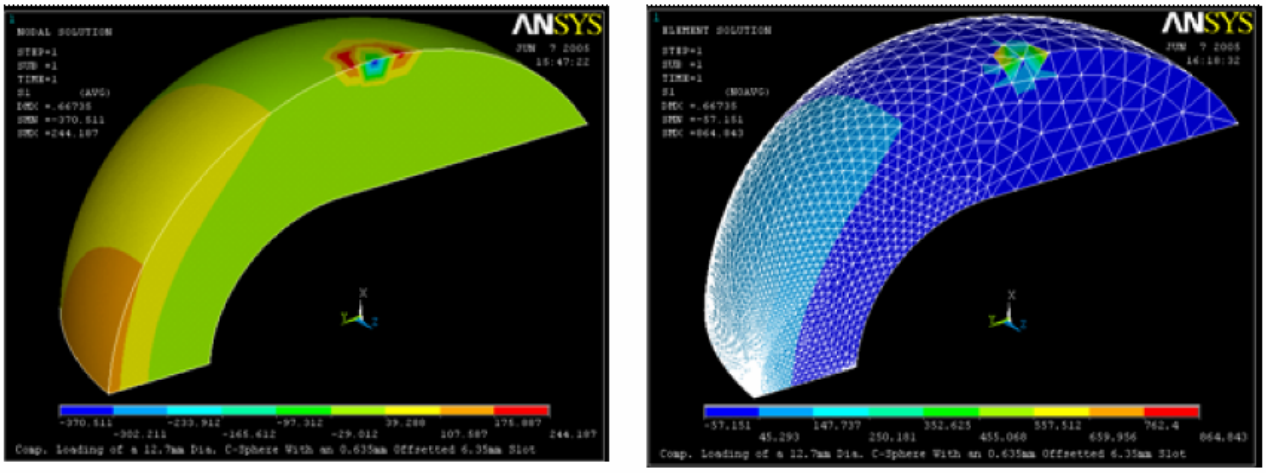

Figure 5. Nodal first principal stress distribution (left) and element first principal stress distribution (right) for the C-sphere specimen, using the fine mesh model.

high nodal stresses, element stress plots are used that display the actual nodal stresses as computed for each element.

The nodal and element first principal stress distributions for the C-sphere specimen using the intermediate mesh model are shown in Figure 4. As can be seen from the nodal plot, the maximum tensile stress is computed to be 132.1 MPa, taking place at the side of the sphere as expected. However, when the element stress plot is examined, the high tensile stress (306-MPa) region shifts to the area under the load, which is obviously an artifact of the point load effect. For the fine mesh model (Figure 5), both nodal and element stress plots show the highest tensile stress region to be under the point load, with the maximum first principal nodal and element stresses increasing to 244 MPa, and 644 MPa, respectively. Figures 4 and 5 clearly show that the stresses under the load are extremely mesh dependent and will keep changing as the mesh changes; for the rest of the specimen, the stresses have long converged even for the coarse mesh specimen model.

To take out the effect of localized stress concentration on the effective size calculations, the artificially high stressed elements under the load were removed. The remaining elements, comprising the vast majority of the specimen, were then used to assess the specimen's effective sizes. The nodal and element stress distribution plots for the C-sphere model are shown in Figure 6, with the highly stressed elements carved out. One would then observe from these plots how the maximum tensile stress of 132 MPa shifts back to the side of the specimen where it should be. The fact that both the nodal and element stress plots yield the same stress distribution indicates that the suspect elements were successfully removed and that the remaining model can now be used to compute the effective sizes. Hence, it is the model in Figure 6 that was utilized to compute the effective area and effective volume for the C-sphere specimen.

The effective area (A_e) and effective volume (V_e) as function of Weibull modulus for the C-sphere specimen are illustrated in Figures 7–8, respectively. The effective sizes were computed using the following equations:

$$A_e = \left(\frac{\sigma_0}{\sigma_e}\right)^m \ln\left(\frac{1}{1-P_f}\right),$$

$$V_e = \left(\frac{\sigma_0}{\sigma_e}\right)^m \ln\left(\frac{1}{1-P_f}\right),$$

where σ_0 is the scale parameter, m is the Weibull modulus, σ_e is the maximum effective stress (computed by CARES/Life), and P_f is the probability of failure (computed by CARES/Life). The effective sizes are independent of the scale parameter because they only vary with geometry, loading, and the Weibull modulus. Hence, the scale parameter was assigned a random value in order to carry out the reliability and effective size calculations.

To achieve familiarity with the new C-sphere geometry, approximately 30 finished Si_3N_4 spheres

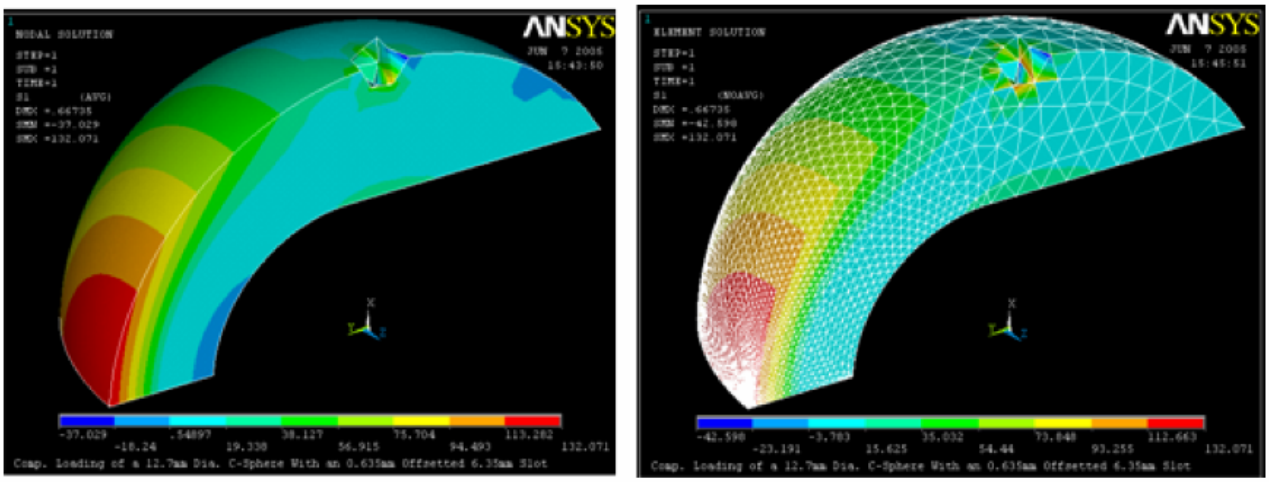

Figure 6. Nodal first principal stress distribution (left) and element first principal stress distribution (right) for the C-sphere specimen using the fine mesh model with the elements within the high stress concentration zone (under the load) carved out. This is the model used to evaluate the effective sizes whose results are shown in Figures 7–8.

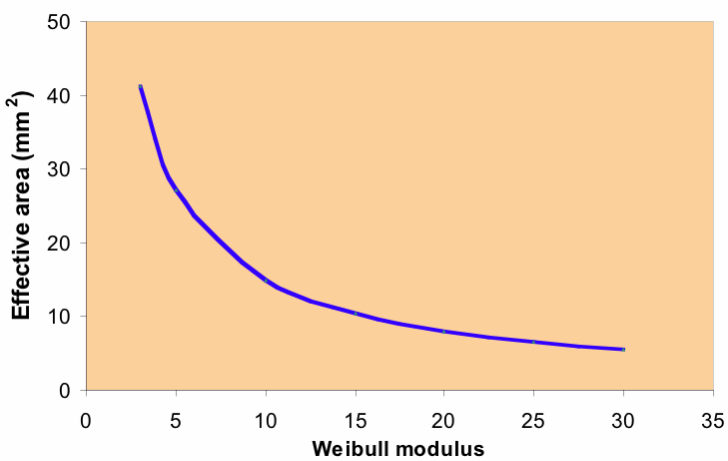

Figure 7. Effective area vs Weibull module for the C-sphere specimen.

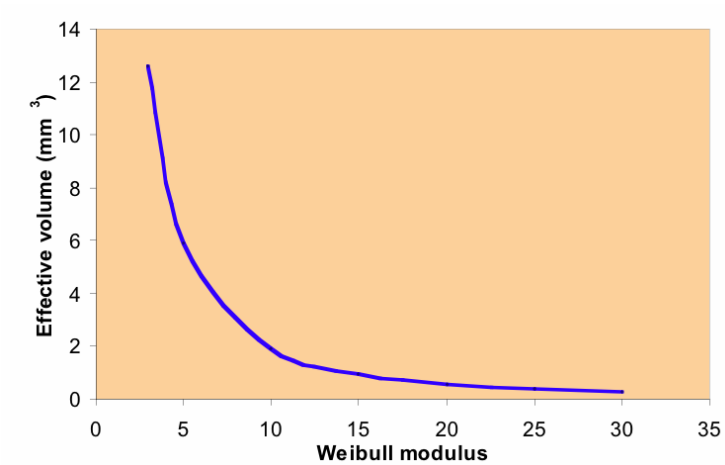

Figure 8. Effective volume vs Weibull module for the C-sphere specimen.

were machined according to Figure 2 and were strength tested. The failure loads and geometrical parameters are now being combined to calculate strength and for interpretation. Additional C-sphere specimens of NBD200, SN101C, and TSN-03NH will be machined to generate more confident Weibull statistics, and C-sphere tests from balls machined according to Table 1 will be performed too. Fractography will then be performed to link strength-limiting flaw type to strength and ultimately RCF performance.

All four machined ball sets have been received (see Table 1). Bournemouth University is using the one larger diameter set to reduce to a 12.7-mm diameter using an internally developed lapping procedure that will essentially yield a fourth (lapped) finish condition.

The utility of using resonant ultrasound spectroscopy (RUS) to quantify elastic properties of Si_3N_4 balls, to assess consistency of those properties, and (hopefully) be able to nondestructively proof test them or identify preexisting flaws is under exploration. H. Trivedi of UES (an Air Force Research Laboratory contractor) forwarded numerous Si_3N_4 balls that were damaged from their RCF testing for attempted RUS characterization and that is under way. Part of those supplied balls included pristine Toshiba TSN-03NH balls whose elastic properties were measured with the RUS and compared with those of NBD 200 and SN101C silicon nitrides. Their comparison is shown in Figure 9, and it was observed that the TSN-03NH balls showed the least amount of variability in those properties of the three Si_3N_4 compositions. The elastic properties

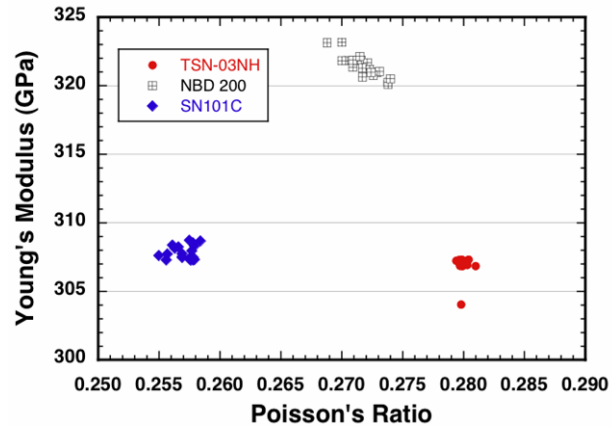

Figure 9. Elastic modulus and Poisson's ratio distributions for three bearing grade Si_3N_4 materials as measured with RUS.

of the three 12.7-mm-diameter sets listed in Table 1 were also measured with RUS, and those results are shown in Figure 10. Several of the balls showed variability, but it may be argued that close clustering of data suggest that most of the ball diameters and material density were uniform and that machining condition did not affect that.

To better understand RCF damage and its link to material microstructure, several supplemental characterization test methods are used. For example, instrumented static and dynamic indentation testing, and instrumented scratch testing of the Ceralloy 147-31N is used to explore how contact loading damage (as a function of loading rate) is affected by subsurface damage. The competition of quasi-plastic damage and cracking processes in Ceralloy 147-31N

Table 1. Grinding conditions for silicon nitride spheres

Step	Diameter & finish	Wheel	Removal (in.)	Removal per pass (in.)
12.7 mm/0.500 in.	1 (roughing)	Accepted practice		0.001
	2 (induce damage)	100 grit	0.004	0.001
Coarse	3 (finishing)	600 grit	0.0005	0.0001
13.2 mm/0.520 in.	1 (roughing)	Accepted practice		0.001
	2 (induce damage)	100 grit	0.004	0.001
Coarse	3 (finishing)	600 grit	0.0005	0.0001
12.7 mm/0.500 in.	1 (roughing)	Accepted practice		0.001
	2 (induce damage)	180 grit	0.004	0.001
Fine	3 (finishing)	600 grit	0.0005	0.0001
12.7 mm/0.500 in. RCF-conventional	"Accepted" practice for RCF test bar finishing			

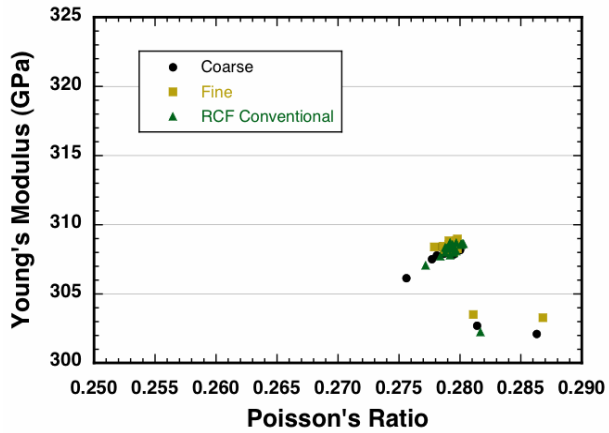

Figure 10. Elastic modulus and Poisson's ratio distributions for Ceralloy 147-31N Si_3N_4 balls as measured with RUS. The three sets were machined per the conditions in Table 1.

is being interrogated as a function of the depth of the subsurface damage and compared to polished material as well. NBD200 Si_3N_4 (NIST SRM for Knoop hardness) and NC132 Si_3N_4 (NIST SRM for fracture toughness) are also being tested; specimens of those materials are presently undergoing indentation and scratch testings whose results will serve as a performance reference for comparisons of performances of Ceralloy 147-31N and whatever additional ceramics that are ultimately tested in this program. SN101C and TSN-03NH (both bearing grades of Si_3N_4) are undergoing instrumented indentation and scratch testings as well, and their performances will be compared with those of the other listed silicon nitride compositions. Raman spectroscopy, and its ability to measure residual stresses, is being used. Preliminary results suggest that residual stresses (manifested by changes in wave number peak location in Figure 8) can indeed be quantified.

Reconciliation of RCF Test Results

A summary report was completed that describes RCF test methods used in Germany, Japan, United Kingdom, and the United States and the interpretation of their results. The report will be published as an ORNL Technical Report.

Japan's National Institute of Advanced Industrial Science and Technology (AIST) will start a 3-year standardization project of RCF testing funded by Japan's Ministry of Economy, Trade, and Industry (METI), Japan, in Quarter 4, and the present project will collaborate. AIST's W. Kanematsu invited this project participation for the purpose of performing three-ball-on-rod (3BOR) RCF testing. The UK National Physical Laboratory (NPL) and Germany (BAM) will also participate. AIST will provide materials for the testing.

Interaction with Domestic Manufacturers

Dialog with ceramic bearing manufacturers is critical to relevance being maintained in this program. Frequent communication occurs between the principal investigator and chief scientists at several domestic manufacturers (Cerbec/Saint-Gobain, Ceradyne, Enceratec, Kennametal, and Cercom) regarding this project's test matrix, plans, and progress.

Conclusions

A 3BOR RCF test facility was established in ORNL, and the evaluation of ceramic RCF performance of Si_3N_4 roller element materials is now well under way. A formal collaboration is under way with BU for three ball-on-ball (3BOB) RCF testing of ceramics, and this enables the eventual reconciliation of RCF performances measured with those two techniques. The effects of subsurface damage on RCF performance are being scrutinized with the C-sphere flexure strength specimen. A summary report was completed that describes RCF testing and result interpretations used in Germany, Japan, the United Kingdom, and the United States. A method was developed to evaluate and discriminate the elastic properties of ball bearings in situ using resonance ultrasound spectroscopy. Ultimately, the results from this project will link surface and subsurface flaws to RCF performance and enable greater use of next-generation ceramic and coated-metal roller elements for diesel engines through RCF and microstructural characterizations.

Presentations and Publications

A. A. Wereszczak, W. Wang, O. M. Jadaan, and M. J. Lance, "Strength of a C-Sphere Specimen," abstract submitted to the January 2006 Cocoa Beach conference.

Y. Wang, M. Hadfield, W. Wang, and A. A. Wereszczak, "Rolling Contact Fatigue of Ceramics," in internal review, to be published as a DOE/ORNL Technical Memorandum.

B. Implementing Agreement for a Programme of Research and Development on Advanced Materials for Transportation Applications

M. K. Ferber
Ceramic Science and Technology Group
Oak Ridge National Laboratory
P.O. Box 2008, MS: 6068
Oak Ridge, TN 37831-6068
(865) 576-0818; fax: (865) 574-6098; e-Mail: ferbermk@ornl.gov

DOE Technology Development Area Specialist: James J. Eberhardt
(202) 586-9837; fax: (202) 586-1600; e-mail: james.eberhardt@ee.doe.gov
ORNL Technical Advisor: D. Ray Johnson
(865) 576-6832; fax: (865) 574-6098; e-mail: johnsondr@ornl.gov

---

Contractor: Oak Ridge National Laboratory, Oak Ridge, Tennessee
Prime Contract No.: DE-AC05-00OR22725

Objectives

- Facilitate the integration of new technologies into the transportation sector by implementing research that validates the applicability of this technology to improve material properties while maintaining acceptable life-cycle costs.
- Promote commercialization of new materials technologies by developing standard testing and characterization methods in conjunction with national and international standards communities.

Approach

- Define and implement research under the International Energy Agency (IEA) Implementing Agreement (IA) entitled Implementing Agreement For A Programme Of Research And Development On Advanced Materials For Transportation Applications (IA-AMT).
- Conduct major research themes as annexes under the current IA:
  - Annex II: Co-Operative Program on Ceramics for Advanced Engines and Other Conservation Applications
  - Annex III: Co-operative Program on Contact Reliability of Advanced Engine Materials
  - Annex IV: A Cooperative Program on Integrated Engineered Surface Technology

Accomplishments

- Completed final work on project Annex II, "Subtask 13: Burner Rig Round Robin." The final report can be found at http://ia-amt.ornl.gov/index.html.
- Completed a final report summarizing all activities conducted under Annex II. The final report can be found at http://ia-amt.ornl.gov/index.html.
- Completed preliminary assessment of the laser spallation test for the measurement of coating adherence. The technique was capable of generating controlled spallation of both metallic and ceramic coatings. The remaining challenge is to quantify stress levels associated with the spallation event.

Future Direction

- Develop a plan for the lightweighting materials annex and present it to the Executive Committee for approval.
- Expand the scope of the implementing agreement by adding an annex on characterization/qualification of ceramic coatings for wear, thermal, and environmental protection.

Introduction

The current mission of the IA-AMT is to investigate promising new technologies for evaluating and ultimately improving the performance of materials for transportation systems. The primary motivation for this activity is the fact that new material technologies are required to increase efficiency and reduce harmful emissions in these systems. Examples of these technologies include (1) lightweighting to improve fuel efficiency; (2) surface engineering to improve the resistance to wear and contact damage; (3) development of durable coating systems for thermal, wear, and environmental management; and (4) development of revolutionary materials (structural ceramics and ceramic matrix composites) for operation at much higher temperatures and pressures. As discussed in this report, the research activities within the IA-AMT focus specifically on (1) identifying promising new technologies for improving materials performance and (2) developing specialized characterization techniques for validating the applicability of this technology to improve material properties while maintaining acceptable life-cycle costs.

Approach

In performance improvement, the current emphasis is on integrated engineered surface technology (IEST) and lightweighting of materials. IEST encompasses the synthesis, processing, characterization, and application of technologies that enhance the functionality of surfaces in contact with the environment or with the surfaces of other solids. Activities on lightweighting of materials focus on aluminum, high-strength steels, magnesium, metal and polymer composites, titanium, intermetallic alloys and other advanced materials. Current topics under consideration include (1) data on production and resource availability; (2) life cycle data on environmental impacts associated with production, processing and use of lightweight materials; (3) recycling information, including regulatory frameworks; (4) data on crashworthiness, design, and testing methodologies, (5) data on base material costs; (6) data on energy impacts of lightweight materials; and (7) shared information on research programs on lightweight materials.

In terms of performance evaluation, the primary focus is on techniques for (1) assessing environmental degradation of structural (non-oxide) ceramics; (2) evaluating time-dependent degradation of mechanical performance of structural ceramics; (3) quantifying key properties of coatings for wear, thermal, and environmental protection of current transportation materials; and (4) developing techniques for the measurement of key properties (topography, chemistry, subsurface damage) of engineered surfaces. Items 1 and 2 are motivated by the need to address key barriers to the use of this important class of material. For example, given the recent concern over environmental degradation of non-oxide ceramics in combustion environments, cost-effective techniques are required to simulate these effects as well as to assess the effectiveness of environmental barrier coatings. The IA-AMT is currently evaluating a variety of techniques ranging from complex high-pressure burner rig tests to a simple cost-effective steam injection system. Ceramic coatings hold considerable promise for (1) improving wear resistance, (2) providing thermal protection, and (3) reducing environmental degradation of critical metallic components used in internal combustion engines. Unfortunately techniques for assessing key properties particularly with respect the interface are unproven. Item 3 addresses this limitation. In a similar fashion, as surface modification technologies mature, proven characterization techniques will also be required to validate their performance (Item 4).

Results

A major result this year was the completion of Annex II. The Annex II subtasks primarily focused on addressing key technology barriers to the use of structural ceramics in both automotive and land-based gas turbines. The motivating factors for

ceramic gas turbine development were the (1) desire to dramatically improve efficiency through higher turbine inlet temperatures, (2) potential for reducing the dependency on strategic metals, and (3) lowering of harmful emissions. Structural ceramics were considered for use as combustors, transition sections, hot gas ducts, turbine vanes and shrouds, turbine blades, and integrally bladed rotors (blisks). High-performance SiN and SiC ceramics were considered as leading candidates for use in these applications.[1–10] These materials offered the following advantages over their metallic counterparts: (1) low density, (2) refractoriness, (3) adequate short-term strength, and (4) good oxidation resistance at ambient pressures. The technical barriers to the implementation of ceramic technology in gas turbines included maturation of powder processing methodologies for component fabrication; establishment of proven methodologies to assess key mechanical properties (required for the development of design database); and optimization of the machining process used in the final stages of component manufacturing (related to cost optimization). Given these barriers, Annex II focused on (1) characterization of powder properties, (2) quantification of the green-state characteristics, (3) evaluation of mechanical performance (strength and thermal shock), (4) machining, and (5) evaluation of environmental degradation of non-oxide ceramics (see Table 1). An extensive set of results was generated from the work

Table 1. Summary of all subtasks implemented under Annex II

Subtask	Title (final report)	Started	Completed	Countries
1	Information Exchange	1985	2004	Germany, Japan, Sweden, United States
2	Characterization of Ceramic Powders: Data and Analyses	1985	Final Report—March 1990	Germany, Sweden, United States
3	Characterization of Sintered Silicon Nitride and Silicon Carbide Structural Ceramics	1985	Final Report—October 1989	Germany, Sweden, United States
4	(1) Fractography Analysis of Silicon Nitride and Silicon Carbide Structural Ceramics, (2) Statistical Analysis of Flexure Strength Data, and (3) Analysis of Error Sources in Four Point Flexure Strength Measurements of Structural Ceramics	1985	Final Reports—June 1989 (1 and 2) December 1989 (3)	Germany, Sweden, United States
5	Study of the Flexure and Tensile Strength of a United States Silicon Nitride	1990	Final Report—September 1993	Germany, Japan, Sweden, United States
6	Development and Testing of Procedures for Characterization of Ceramic Powders	1990	Final Report—September 1993	Germany, Japan, Sweden, United States
7	Effect of Machining Conditions on the Strength of Silicon Nitride	1993	Final Report—March 1998	Germany, Japan, Sweden, United States
8	Development and Testing of Primary and Secondary Properties of Ceramic Powders	1993	Final Report—December 1996	Belgium, Germany, Japan, Sweden, United States
9	Thermal Shock Testing of Advanced Ceramics	1996	Final Report—March 2000	Belgium, Germany, Japan, Sweden, United States
10	Assessment of Powder Characterization Methods for Advanced Ceramics	1996	Final Report—February 2000	Belgium, Germany, Japan, Sweden, United States
11	Techniques for the Measurement of Thermal and Mechanical Fatigue	2000	Final Report—March 2004	Germany, Japan, Sweden, United States
12	Characterization of Ceramic Powders and Green Bodies	2000	Final Report—September 2001	Belgium, Germany, Japan, Sweden, United States
13	Burner Rig Round Robin	2003	Final Report—March 2005	Germany, Japan, United States

conducted in Annex II. The major reports summarizing most of the subtasks can be downloaded from http://ia-amt.ornl.gov/index.html.

The results from Annex II were subsequently used in the establishment of standards [via American Society for Testing and Materials (ASTM), Japan Industrial Standards (JIS), Committee for European Normalization (CEN), International Organization for Standardization (ISO), and National Institute of Standards and Technology (NIST) guidelines (see the publications list). Table 2 summarizes some the existing standards that benefited from this work. In the case of room-temperature flexural strength, the standard, ASTM C1161, was revised to reflect lessons learned about fixturing and test specimen configurations. ISO 14704 evolved from several standards (ASTM C1161, CEN EN843-1 and JIS R1601) and lessons learned from the IA-AMT work. The high-temperature flexural strength standard, ASTM C1211, evolved about the time of the IEA round robin and included lessons learned from C1161 and the IEA work. ISO DIS 17565 (not yet a standard) has evolved from several standards (ASTM C1211, CEN prEN820-1, JIS R1604) and lessons learned from the IA-AMT subtask. The room-temperature tensile strength standard, ASTM C1273, was developed as the IA-AMT results were being reviewed and analyzed and included many lessons learned. ISO 15490 evolved from two standards (ASTM C1273 and JIS1606), and the ISO round robin results were instrumental in establishing test specimen configurations, gripping arrangements, allowable bending, and test rates. The thermal shock standard, ASTM C1525, was developed after the IA-AMT subtask on thermal shock was completed. Although this standard follows a more conventional approach to thermal shock by using water and standard MOR bars, insights garnered from the IA-AMT work are used in providing guidance to users in notes and discussions.

Thirteen subtasks were ultimately conducted under Annex II. Technical experts in the field defined the work scope for each subtask, with final approval given by the executive committee members during the annual meetings. Once the subtask was approved, each country was responsible for selecting technical task leaders; the executive committee appointed an overall subtask coordinator. Working group meetings were used to monitor the progress of the effort and provide a venue for technical data exchange by the task leaders. Once a subtask was completed, the coordinator was responsible for collecting and analyzing the data and preparing the final reports. Many of the reports are available on the IA-AMT web site: http://ia-amt.ornl.gov/index.html.

Table 2. Standards that have benefited from the IA subtasks

Property	JIS	ASTM	CEN	ISO
Flexural strength: RT	R1601-95	C1161-96	EN 843-1:95	14704:2000
Flexural strength: HT	R1604-95	C1211-98	prEN 820-1	DIS 17565
Statistical analysis	R1625-96	C1239-95	ENV 843-5:97	CD 20501
Fractography		C1322-96	prENV843-6	
Tensile strength	R1606-95	C1273-95		15490:2000
Sample preparation for the determination of particle size distribution of ceramic powders	R1619:95	C1282-94	EN 725-5:96	14703:2000
Surface area	R1626-96	C1274-95	EN 725-6:96	DIS 18757
Particle size distribution of powder by laser diffraction method	R1629:97			TC206 NP02
Thermal shock	R1615-93	C1100	prEN 820-3	
Flowability	R1639-4:99			TC206 WI93
Size distribution of granules	R1639-1:99			
Binder content of granules				
Drying loss of granules	R1639-3:99			
Bending fatigue: RT	R1621:95			TC206 PWI 07
Bending fatigue: HT	R16xx:01			

RT = room temperature; HT = high temperature.

As shown in Table 1, the 13 subtasks included an ongoing information exchange (subtask 1), which occurred in conjunction with the annual executive committee meeting, and specific research activities (subtasks 2–13), which consisted of task sharing collaborations between the participating national organizations. Most of these subtasks included extensive industry participation. Because the more recent subtasks involved fairly specialized hardware (thermal shock facilities for the centrally heated disk specimen—subtask 9, burner rig facilities—subtask 13), industrial participation was limited. Throughout Annex II, the industrial participants provided (1) expertise in the development of experimental research plans, (2) materials and facilities required for the implementation of those plans, and (3) personnel to actively participate in the research activities. In this approach, each country benefited from the experience and work of the other countries by gaining access to a larger quantity of data required to substantiate the standard methods under development. This approach also minimized the effort required to transition standards from the national to international level. As a result the structure of the IA led to considerable cost savings.

The motivation for subtask 13, the last task implemented under Annex II, was the need to develop a reliable method to assess the environmental attack on non-oxide ceramics arising from the global removal of the normally protective silica scale via reaction with water vapor present in the combustion gases. In stagnant environments, oxidation of both SiN and SiC is increased by (1) the replacement of oxygen by water vapor and (2) an increase in the pressure of the oxidant. In addition, the high velocities and presence of water in the environment can lead to the volatilization of the normally protective silica layer. The resulting recession of non-oxide ceramics such as SiC and SiN ultimately leads to excessive material loss, which increases the stress levels arising from both thermal and mechanical loading (Figure 1).

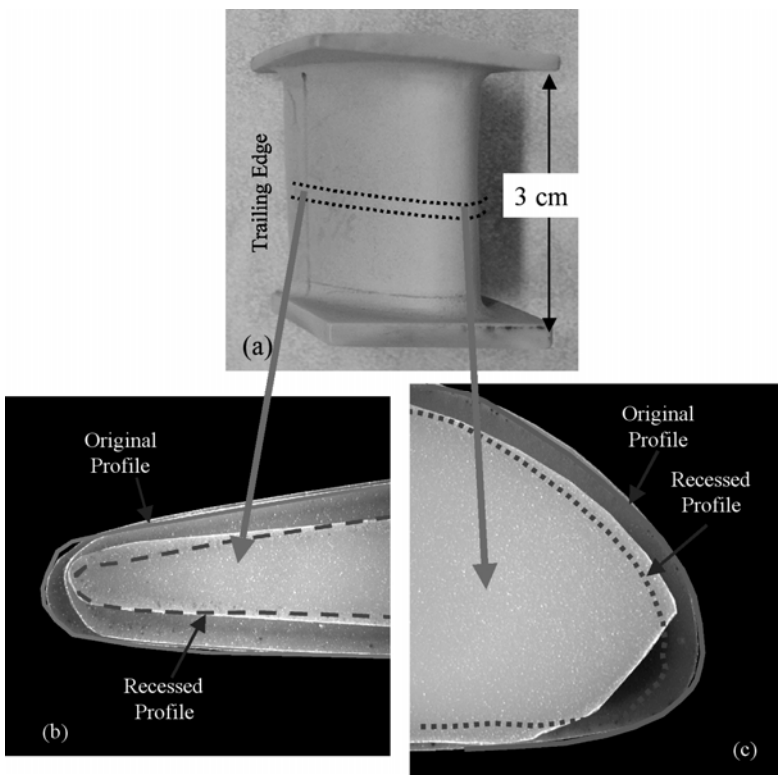

Figure 1. Photograph of uncoated AS800 prior to field testing (a). The dotted lines show the sections that were machined for subsequent polishing and evaluation by scanning electron microscopy. Typical sections for an as-received vane and a vane exposed for 815 h are compared in (b) trail edge and (c) leading edge. The dotted lines are predicted recession profiles.

Because of this recession problem, considerable emphasis has been placed on the development of environmental barrier coatings (EBCs) to act as diffusion barriers to water vapor. The effectiveness of EBC systems is defined by their (1) ability to isolate the non-oxide ceramic from the water vapor and (2) phase stability in the gas turbine environment. Both aspects can be evaluated from burner rig studies. Unfortunately, the results obtained from a given burner rig system depend upon a number of factors, including specimen geometries, gas flow/specimen configuration, temperature uniformity, and burner stability. The goal of this subtask was to implement a round robin in which a selected SiN material was evaluated in burner rig facilities located in Japan and the United States.

In subtask 13, three techniques were used to evaluate the recession behavior of the SN282 material. The first method consisted of exposing rectangular specimens for 400, 600, and 1000 hours in a high-pressure, high-velocity burner rig located at General Electric Global Research Center. This rig, which was used extensively used in the Continuous Fiber Ceramic Composite program,[11] runs largely unattended with extensive computer control, data acquisition, and safety monitoring. The second technique considered involved the development of a system for injecting steam onto a small region of the SiN specimen using an alumina or SiC tube. As shown in Figure 2, this method was quite effective at inducing localized recession in the injection area. The final technique involved exposing prismatic bars in an atmospheric burner rig. A detailed comparison of the resulting recession data[12] indicated that all three techniques gave comparable values of the recession rates (Figure 3).

Conclusions

The IA-AMT has made significant progress in expanding its scope, as evidenced by the addition of two new annexes, IV and V. Both annexes are expected to generate new members. Given this progress, a formal request has made to the IEA to extend the IA-AMT for a period of 3–5 years.

Presentations and Publications

M. K. Ferber, *Burner Rig Round Robin—Subtask 13: Final Report*, March 2005. Available at http://ia-amt.ornl.gov/index.html.

M. K. Ferber, *Annex II: Co-Operative Program on Ceramics for Advanced Engines and Other Conservation Applications—Final Report*, September 2005, available at http://ia-amt.ornl.gov/index.html.

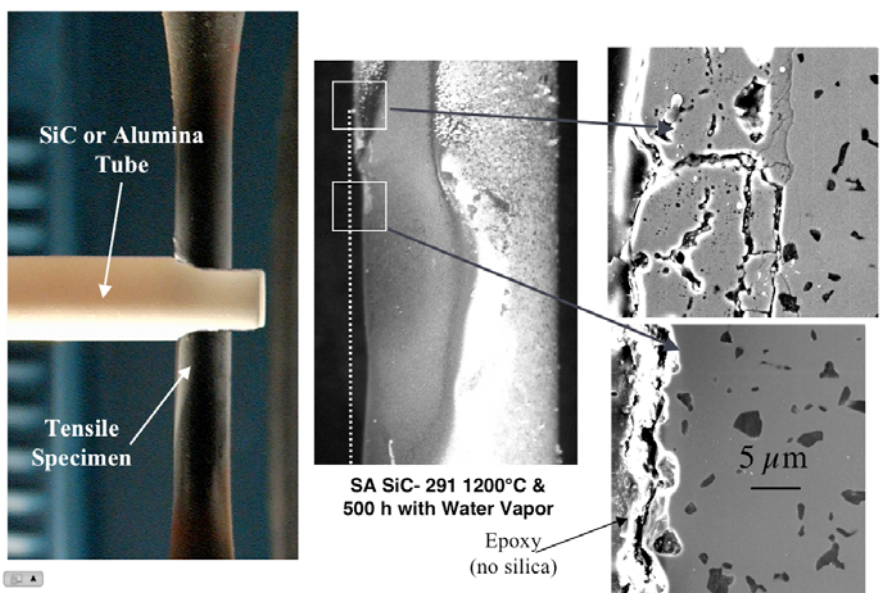

Figure 2. Sintered alpha SiC tensile specimen after 500 h exposure to a saturated water vapor environment at 1200°C. The white dotted line on the right shows the position of the original surface prior to testing.

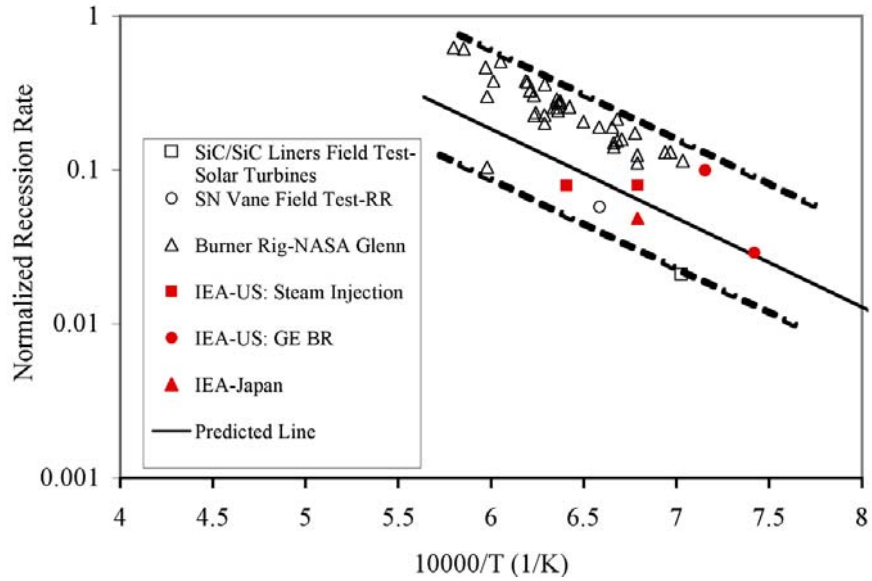

Figure 3. Comparison of normalized recession rate versus 1/T data obtained in present study with similar data reported in the literature.

References

1. D. Anson, K. S. Ramesh, and M. DeCorso, Application of Ceramics To Industrial Gas Turbines, DOE/CE/40878-1&2, Volume 1—Technology Background and Volume 2—Economics, Market Analysis and R&D Plan, Battelle Columbus, Ohio, March 1991.

2. H. E. Helms, R. A. Johnson, and L. E. Groseclose, "AGT 100-Advanced Gas Turbine Technology Development Project," pp. 137–155 in Proceedings of the Twenty-Third Automotive Technology Development Contractor' Coordination Meeting, P-165, Society of Automotive Engineers, Warrendale, Pennsylvania, March 1986.

3. M. van Roode, "Ceramic Retrofit Program," pp. 77–93 in Proceedings of the Joint Contractors Meeting: FE/EE Advanced Turbine Systems Conference—FE Fuel Cells and Coal-Fired Heat Engines Conference, DOE/METC-93/6132, August 1993.

4. D. Carruthers and L. Lindberg, "Critical Issues for Ceramics for Gas Turbines," pp. 1258–72 in Third International Symposium on Ceramic Components and Materials for Engines, V. J. Tennery, ed., American Ceramic Society, Westerville, Ohio, 1988.

5. P. J. Haley, R. L. Holtman, L. E. Groseclose, S. J. Hilpisch, and A. H. Bell III, "Advanced Turbine Technology Applications Project (ATTAP)," pp. 19–29 in Proceedings of the Twenty-Ninth Automotive Technology Development Contractors' Coordination Meeting, Society of Automotive Engineers, Warrendale, Pennsylvania, June 1992.

6. Ceramic Technology for Advanced Heat Engines Program Plan 1983–1993, ORNL/M-1248, Oak Ridge National Laboratory, July 1990.

7. A. Nagahiro, Present Status of the National Project of R and D of Fine Ceramics, FC Annual Report, 1986, pp. 61–66.

8. J. I. Mueller, "Handicapping the World's Derby for Advanced Ceramics," *Am. Ceram. Soc. Bull.*, **61**(5), 588–591 (1982).

9. S. O. Kronogård and L. Malmrup, "Ceramic Engine Research and Development in Sweden," in pp. 51–80 in Ceramics for High-Performance Applications III Reliability, E. M. Lenoe, R. N. Katz, and J. J. Burke, eds., Plenum Press, New York, 1983.

10. W. Bunk, E. Gugel, and P. Walzer, "Overview of the German Ceramic Gas Turbine Program," pp. 29–50 in Ceramics for High-Performance Applications III Reliability, E. M. Lenoe, R. N. Katz, and J. J. Burke, eds., Plenum Press, New York, 1983.

11. G. S. Corman, A. J. Dean, S. Brabetz, M. K. Brun, and K. L. Luthra, "Rig and Engine Testing of Melt Infiltrated Ceramic Composites for Combustor and Shroud Applications," in Proceedings of ASME

Turbo Expo 2000, May 8–11, 2000, Munich, Germany, *Journal of Engineering for Gas Turbines and Power*, **124**(3) (July 2002), pp. 459–464.

12. M. K. Ferber, Burner Rig Round Robin—Subtask 13: Final Report, March 2005.

C. Mechanical Property Test Development

George D. Quinn
National Institute for Standards and Technology
Ceramics Division, Stop 8529
Gaithersburg, MD 20899
(201) 975-5765; fax: (301) 975-5334; e-mail: geoq@nist.gov

DOE Technology Development Area Specialist: James J. Eberhardt
(202) 586-9837; fax: (202) 586-1600; e-mail: james.eberhardt@ee.doe.gov
ORNL Technical Advisor: D. Ray Johnson
(865) 576-6832; fax: (865) 574-6098; e-mail: johnsondr@ornl.gov

---

Contractor: Oak Ridge National Laboratory, Oak Ridge, Tennessee
Contract No.: DE-AC05-00OR22725
Subcontractor: National Institute for Standards and Technology, Gaithersburg, Maryland

---

Objective

- Develop mechanical test method standards in support of the Propulsion Systems Materials Program. New methods and sound engineering data will facilitate adoption of new materials in heavy vehicle propulsion systems.

Approach

- Conduct pre-standardization research on test methods that need refinements, or develop new methods.
- Develop draft recommendations for practices or procedures based upon the needs identified by the research.
- Conduct round robins as necessary.
- Standardize procedures in the American Society for Testing and Materials (ASTM) and/or the International Organization for Standards (ISO).

Accomplishments

- Conducted new experiments on zirconia split cylinder flexural strength test specimens using the latest generation material and compared results with full rod flexural strength test results. Conducted extensive fractographic analysis to find the strength-limiting flaws in this commercially important material.
- Neared completion of the comprehensive Guide to Practical Fractography for Ceramics and Glasses.
- Completed a set of papers and made presentations.
- Revised, refined, and improved several current ASTM and ISO standards.

Future Direction

- Finish the split cylinder flexural strength test work and write a paper on the method. Show how a simple modification of ordinary bend fixtures for rectangular bars can do double duty and also work with split cylinders.
- Finish the comprehensive Guide to Fractography.
- Complete prestandardization work on flexure testing of rods and write the first draft of an ASTM standard.

- Resume pre-standardization evaluation of diametral compression strength testing for small round-shaped specimens

---

Introduction

This project creates new test methods that will facilitate the use of advanced materials in heavy-weight propulsion systems. Much of the work is for brittle materials such as ceramics, for which classical metal mechanical test methods are not suitable. For example, tension strength test specimens of many ceramic materials made in short, stubby cylindrical shapes (e.g., diesel engine fuel injector pins, timing plungers, valves) and classical dog bone shapes are impractical (Figure 1). Our goal is to adapt or refine existing methods or invent new ones that will allow engineers and researchers to measure mechanical properties with good accuracy and precision. They then will be able to construct their own databases with greater confidence. Formal test method standards are our primary objective. Sound test methods and high-quality databases will enhance the credibility of new materials and encourage engineers to use them in advanced heat engines. This purpose of this project is to develop the test methods.

Figure 1. Round ceramic engine components.

Approach

Over the course of this program, we have formulated or contributed to the development of 17 ASTM and ISO standards. We currently are working aggressively on three more:

- Flexural strength of cylindrical rods
- Flexural strength of split cylinders
- Fractographic measurement of fracture mirror sizes

We also plan to tackle the diametral compression strength test method when those three standards are completed in FY 2006.

The standards adopted so far include methods for ceramics such as flexural strength, elastic modulus, Weibull statistical analysis, fractographic analysis, and fracture toughness. As a direct result of this work, there has been a dramatic improvement in test data quality and reliability in the structural ceramics field. We have also contributed to a ceramic material specification for silicon nitride ball bearings. The specification uses several of the test method standards developed in this program. The test method standards have been sufficiently generic that they have even been used in to the biomedical field for materials specifications for ceramic surgical implants.

Considerable energy was put into finishing a Guide to Practice for Fractography of Ceramics and Glasses this year. This is a large document that has been written with a strong practical slant. It will complement the ASTM standard practice for fractography, and it is intended to help engineers and scientists find flaws and fracture origins and help them do their jobs better. The goal is to make fractographic analysis less an art and more an engineering practice.

Results

Flexural Strength of Split Cylinders

Splitting a rod and testing the halves is one way of evaluating the strength of short, stubby cylindrical parts that otherwise might be difficult to test correctly. The break forces for solid full rods are very high and fixtures may be damaged, or high contact stresses could cause Hertzian cracking in the specimen. Splitting the rods makes them much easier to test, as shown in Figure 2. Our goal is to refine this simple procedure and make it available to engineers and scientists as an optional test configuration.

We did a thorough fractographic analysis of the split Coors zirconia rods that we had previously broken. Our goal was to identify the strength-limiting flaws and ascertain whether the new fixture

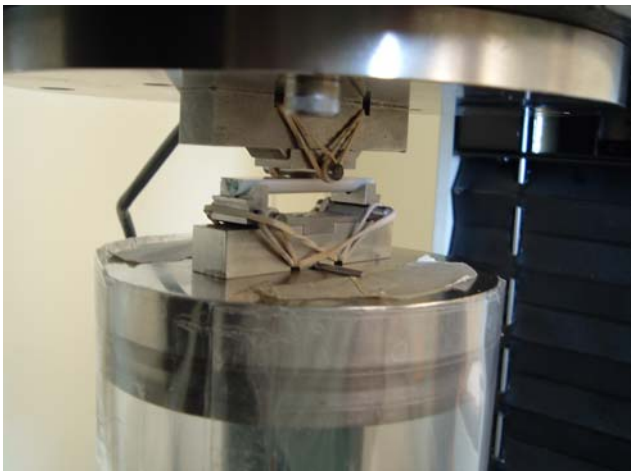

Figure 2. Split zirconia fuel injector pin in the NIST bend fixture for split rods.

scheme produced legitimate test results and breakage patterns. Fractography was very difficult in this material because of its coarse microstructure, but we found that flaw pockets (local clusters of tiny defects), as shown in Figure 3, and grain boundary faults were the origins. A paper on this work is in preparation.

We did additional split cylinder testing to fill in a gap in our results. We previously had tested split rods made from the Coors zirconia, but we did not have any solid rod strengths with which to directly compare our results. To get a better sense of whether the split cylinders were giving data comparable to or different from those for solid rods, we obtained a new set of solid zirconia pins from Cummins. These were from a set of Carpenter zirconia rods that had been set aside. Some of these were split into two halves and each half was tested, as shown in Figure 2. The 4-point testing was with effective spans of 20 × 40 mm. The 3-point testing was with a 40-mm span. The strength outcomes are shown in Figure 4. Three-point strength numbers for the same batch of material that were obtained by Cummins are also shown for comparison. The good news is that the 3-point strengths of the split rods are nearly identical to those of the full rods. The 4-point strengths are less, and the shift was in perfect accordance with Weibull size effects.

The fracture origins these specimens were also thoroughly analyzed. An interesting outcome was that most specimens failed from a flaw type not detected in the Coors batch. The Carpenter specimens had lovely fracture surfaces with distinct mirrors and broke from transformed grains right on the outer ground surfaces, as shown in Figure 5. Evidently improved processing in the Carpenter material has eliminated many of the grain boundary and flaw pocket faults that controlled properties in the earlier-generation Coors material.

A remarkable finding was that although the split cylinders had the usual strength variability associated with ceramics, the strengths of the two halves of a particular rod were remarkably consistent. That suggests that the strength-limiting flaws are very consistent within any given rod.

Our work is converging on a very simple solution for this test method. An ordinary bend fixture designed for rectangular specimens may be easily adapted by using simple cradles with alignment parts that enable it to instantly convert to test split cylinders. Engineering drawings of the new single-piece cradles are being prepared.

Flexural Strength of Solid Cylindrical Rods

Work resumed in conjunction with the split cylinder testing described in the next paragraph. As

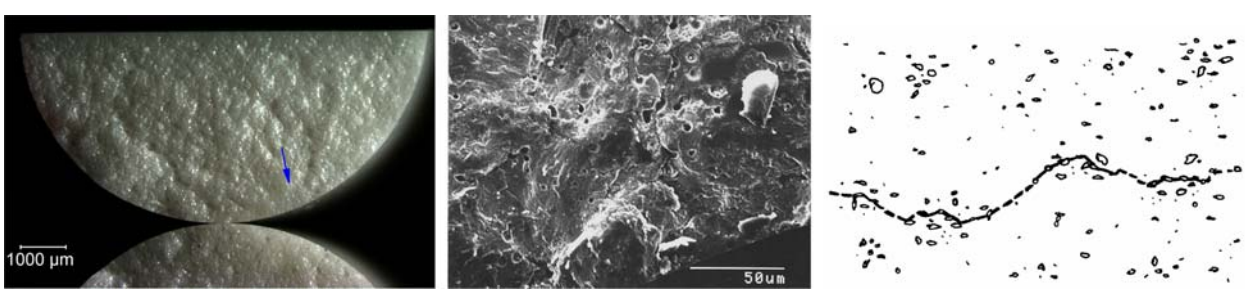

Figure 3. Fracture surface of a Coors zirconia slit cylinder specimen showing the very rough surface. The origin was a region of locally greater porosity coupled with grain boundary faults. The schematic suggests how these pockets could control strength.

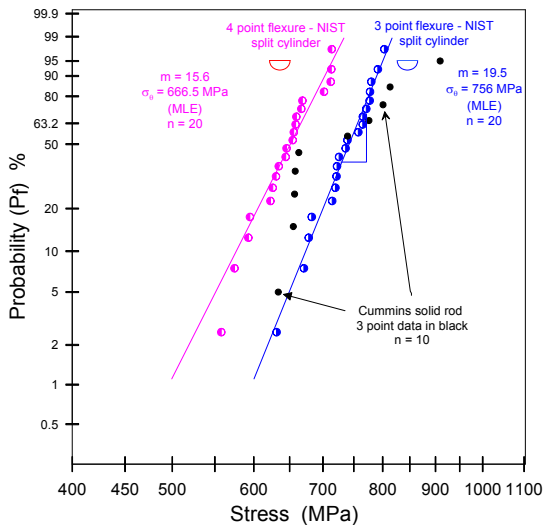

Figure 4. Flexural strengths of split zirconia rods tested measured at NIST. Cummins 3-point data for solid rods is shown in black. Weibull parameter estimates are noted. The 3- and 4-point distributions are simply shifted in accordance with the customary Weibull size effect.

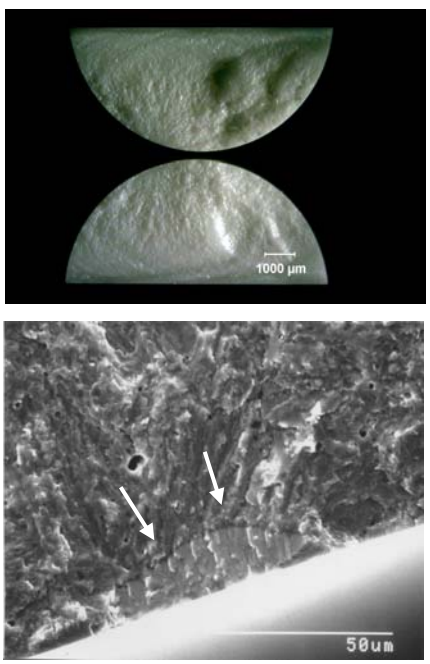

Figure 5. Fracture surface and origin of a Carpenter zirconia split rod specimen. The microstructure is less rough than in Figure 3, and there is a fracture mirror. The second photo shows a typical origin: a transformed grain on the ground surface.

part of our fixture design work, we tested one oversized steel dowel rod in our flexure fixture that has special cradles to hold round specimens (Figure 6). We did this to ascertain whether minor yielding in the steel cradles (which had been detected after doing some ceramic tests) was due to fixture overload or an artifact of a transient load pulse when the ceramic specimens fractured. The yielding was only on a tiny portion of an edge of the cradles, but we decided to investigate the source of the deformation to possibly refine our new fixture design. The fixture and hardened steel dowel were loaded to static loads well above those used in the ceramic strength tests and then unloaded for inspection. No deformation whatever was detected in the steel fixture parts or the hardened steel dowel rod. This tends to confirm the notion that a shock–pulse in the fixture when the ceramic test pieces broke was the cause of the observed small deformations.

We have resumed our error analyses work for flexure testing of round specimens. This will be the cornerstone of the standard. Once we have analytical estimates of errors for different specimen and fixture geometries, then we will be able to intelligently select an optimum configuration and set ranges of acceptable configurations and close practical engineering tolerances. The error analysis builds upon similar work for rectangular specimens done by Francis Baratta and Quinn in the early 1980s.

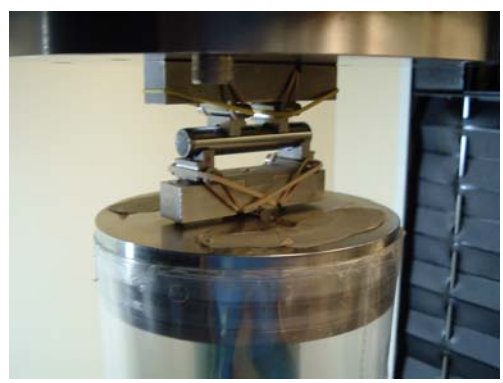

Figure 6. Steel dummy specimen in the same 4-point bend fixtures that were used to test split cylinder specimens. Special cradles hold the round specimens in the fixtures that are normally used to test rectangular bend specimens. Deformations on the cradle edges were observed after ceramic strength tests.

Nuances pertaining to rod shapes must be considered, however, before the analysis can be directly applied to the rod. Most errors are similar or identical, but contact point tangency shift with the new cradles, errors from severe contact loadings from crossed rollers, and wedging stresses are different for rods and rectangular bars. So, for example, in October 2005 we completed a new, simpler analysis for contact point tangency shift for beams in flexure. This error occurs when the specimen deflects and its point of contact with the loading rollers shifts. This in turn affects the moment that is applied to the specimen and alters the stress in the beam. The error is minimal (< 1%) in the standardized rectangular bend bars so long as loading roller sizes are kept small. A similar effect is expected for rods, except that if cradles are used, the error could get as large as 5% or more. The original Baratta analysis of 1982 was cumbersome and required an iterative analysis to solve for a particular geometry. The newer, simpler analysis we derived gives virtually identical error estimates and is far simpler to use. Our goal is to finish the complete error analysis by December 2005, so that we can use the analysis to set reasonable testing limits for an ASTM draft standard.

Guide to Fractography

Work continued on a NIST user-friendly Guide to Best Practice for fractographic analysis. This pamphlet-style document will be about 400 pages long with hundreds of figures illustrating key fractographic markings in ceramics and brittle materials. It will complement ASTM standard C 1322, Standard Practice for Fractography and Characterization of Fracture Origins in Advanced Ceramics.

Small revisions to five flaw definitions in ASTM C 1322, Standard Practice for Fractography, were balloted. Two negatives were obtained. These negatives were discussed at the Reno, Nevada, meeting of ASTM Committee C-28, Advanced Ceramics, on May 16, 2005, and were found to be unpersuasive. The final revised version 2005b of C1322 was reviewed and has been sent to press. This concludes all our planned revisions to this standard for the time being.

One important byproduct of the Guide to Best Practice is a new set of guidelines for how to measure fracture mirrors. The guidelines are one step away from a formal standard. They will be shown to ASTM Committee C-28 in January 2006 for review and consideration. Fracture mirrors are relatively smooth surrounding a fracture origin in a brittle material, such as is shown in Figure 7. Mirrors are formed when the crack radiates outward from the origin and initially generates a smooth surface, but then creates a rough surface once the crack reaches terminal velocity. A remarkable characteristic of fracture mirrors is that their size is inversely related to the square of stress in the part at the instant of fracture. Thus mirrors may be used to estimate the breakage stress in failed components, even if the engineer has no idea how the parts were loaded or stressed. Mirrors are discussed in the ASTM fractography standard C 1322, which focused on how to characterize fracture origins, but there was no guidance on how to measure them. There are wide variations in how these fractures are currently measured. We are ready to rectify this now with a new standalone standard if the ASTM Committee concurs.

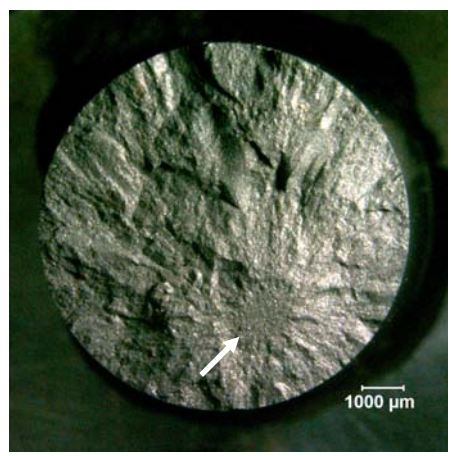

Figure 7. Fracture mirror in a ceramic. The fracture stress can be estimated fairly accurately from the size of the relatively smooth circular fracture mirror.

Other

A review paper, "Design and Reliability of Ceramics: Do Modelers, Designers, and Fractographers See the Same World?" was presented at the American Ceramic Society conference in January. One of the case studies cited in the paper was the excellent work done by the Ford Motor Company in the early 1980s on a model silicon

nitride gas turbine rotor that was spun to failure in a hot test rig (Figure 8).

Figure 8. The Ford model turbine rotor was a featured example in a review paper on design and reliability.

Although a high-quality ASTM standard for fracture toughness evaluation has been on the books for 8 years, and although NIST has a Standard Reference Material (SRM) 2100 to support it, people are still using the defective Vickers indentation crack length method to evaluate fracture toughness. Therefore, we have begun some Vickers indentation crack length measurements to estimate the "indentation fracture resistance" of the NIST SRM 2100 in order to demonstrate the shortcomings of the method and the errors that can result. Our goal is to get these findings into the literature as soon as possible before the adoption of indentation crack length methodologies gets codified too far. We advocate the use of genuine fracture mechanics tests for evaluating fracture toughness. The Vickers indentation crack length method evaluates a particular measure of fracture resistance, which crudely approximates fracture toughness. The indentation crack length method may have some utility, but data from it ought to be deemed "indentation fracture resistance" and not "fracture toughness."

We helped to update and refine some existing ASTM and ISO standards. We are continuing to work with W. Mandler of Enceratec/Cummins and B. Mikijelj of Ceradyne as the silicon nitride ball bearing material specification F2094 evolves. Some corrections to data specifications were reviewed and balloted this year. The ASTM specification is also being converted into an ISO international standard. There is some controversy about some of the procedures, and we are working with the stakeholders to ensure that a technically sound specification is prepared. Another example is the new static fatigue test method draft standard that we helped review. Quinn reviewed the history of Committee C-28's awards and furnished a summary report to the current award subcommittee leader. Quinn also reviewed the history of the development of two ASTM powder characterization standards, C 1282 and C 1274, and two nondestructive evaluation standards, C 1212 and C 1336, and sent a summary report to Steve Gonczy, the C-28 chairman. Gonczy wanted to know the backgrounds so that plans could be made to upgrade, refine, or drop these standards as appropriate.

Conclusions

Step by step, we are building a national and international standards infrastructure to facilitate the commercial utilization of new advanced materials in engine applications. The generic test method standards developed to date have proved to be so practical, reliable, and versatile that they are now being used to support a wide range of applications, including surgical implants in humans and even ceramic military body armor.

Publications/Presentations

G. D. Quinn, L. K, Ives, and S. Jahanmir, "On the Nature of Machining Cracks in Ground Ceramics: Part I: SRBSN Strengths and Fractographic Analysis," *Machining Science and Technology*, **9**, 169–210 (2005).

G. D. Quinn, L. K, Ives, and S. Jahanmir, "On the Nature of Machining Cracks in Ground Ceramics: Part II: Comparison to Other Silicon Nitrides and Damage Maps," *Machining Science and Technology*, **9** 211–237 (2005).

G. D. Quinn, L. K. Ives, and S. Jahanmir, "Machining Cracks in Finished Ceramics," pp. 1–14 in Fractography of Advanced Ceramics, II, ed. J. Dusza, R. Danzer, and R. Morrell, TransTech Publ., Zurich, 2005.

G. D. Quinn, "Design and Reliability of Ceramics: Do Modelers, Designers and Fractographers See the Same World?" presented at the Cocoa Beach Ceramic Society Conference, January 2005, to be published in Ceramic Engineering and Science Proceedings.

G. D. Quinn, "Indentation Size Effects for Glasses: Yes, There is a Fracture Contribution," pp. 149–172 in Fracture Mechanics of Glasses and Ceramics, Vol. 14, eds. R. C. Bradt, D. Munz, M. Sakai, and K. W. White, Klewer/Plenum, New York, 2005.

G. D. Quinn, K. Xu, J. A, Salem, and J. J. Swab, "SRM 2100: the World's First Fracture Toughness Reference Material," pp. 499–530 in Fracture Mechanics of Glasses and Ceramics, Vol. 14, eds. R. C. Bradt, D. Munz, M. Sakai, and K. W. White, Klewer/Plenum, New York, 2005.

J. A. Salem, G. D. Quinn, and M. G. Jenkins, "Measuring the Real Fracture Toughness of Ceramics—ASTM C 1421," pp. 531–554 in Fracture Mechanics of Glasses and Ceramics, Vol. 14, eds. R. C. Bradt, D. Munz, M. Sakai, and K. W. White, Klewer/Plenum, New York, 2005.

G. D. Quinn, R. J. Gettings, and L. K. Ives, "A Standard Reference Materials for Vickers Hardness of Ceramics and Hardmetals," pp. 121–128 in Proceedings of HARDMEKO 2004, Hardness Measurements Theory and Application in Laboratories and Industries, IMEKO Technical Committee 5 Hardness Conference, Washington, D.C., November 11–12, 2004, ed., S. Low.

D. An Integrated Surface Modification of Engineering Materials for Heavy Vehicle Applications

Stephen Hsu
National Institute of Standards and Technology
100 Bureau Drive, Gaithersburg, MD 20899
301-975-6120; fax: 301-975-5995; e-mail: stephen.hsu@nist.gov

Xaiolei Wang, Lewis K. Ives, Huan Zhang, Yanan Liang, Charles Ying
National Institute of Standards and Technology

DOE Technology Development Area Specialist: James J. Eberhardt
(202) 586-9837; fax: (202) 586-1600; e-mail: james.eberhardt@ee.doe.gov
ORNL Technical Advisor: D. Ray Johnson
(865) 576-6832; fax: (865) 574-6098; e-mail: johnsondr@ornl.gov

---

Contractor: Oak Ridge National Laboratory, Oak Ridge, Tennessee
Contract No.: DE-AC05-00OR22725
Subcontractor: National Institute of Standards and Technology, Gaithersburg, Maryland

---

Objectives

- Organize an international cooperative research program on an integrated surface modification technology under the auspices of the International Energy Agency (IEA).
- Design and identify surface features and patterns that can achieve friction reduction and enhanced durability for heavy-duty diesel engine components.
- Develop understanding and appropriate models to explain the effects of texturing on frictional characteristics. Develop appropriate thin films and coatings to achieve synergistic and complementary relationship with texturing to enhance performance.
- Discover and develop surface chemistry for protecting the films and coatings that work in synergy with the coatings.

Approach

- Determine the effects of the size, shape, pitch, and patterns of surface textural features on friction under (1) a high-speed, low-load regime; (2) a high-load, high-speed regime; and (3) a high-load, low-speed regime.
- Develop cost-effective fabrication technologies for creating surface textural features on various surfaces, including metals, ceramics, and coatings.
- Develop a test methodology to measure the effects of the textures on friction.
- Conduct research to develop an integrated system approach to combine the best practices in thin films, coatings, and surface chemistry for performances unrealizable by individual approaches alone.
- Concurrently, organize an international cooperative research program under the auspices of the IEA to pool resources and share this energy conservation technology worldwide.

Accomplishments

- Attended the IEA End Use Working Party meeting in Paris 2005 and presented the Implementing Agreement on Advanced Materials for Transportation (IA-AMT) end-of-term report. Based on input from the meeting, numerous revisions were made to incorporate new activities and future emphases.
- Won a 3-year extension of the IEA work from the Committee on Energy Research and Technology (CERT).
- Contacted potential participants in China, Australia, Finland, Japan, the United Kingdom, and Belgium to ask them to participate and to attend the Executive Committee meeting to be held in Porto, Portugal.
- Participated in a Special Symposium on Surface Texture in Porto in conjunction with the COST 532 conference.
- Demonstrated the geometric effects of various surface features under high-speed, low-load conditions and achieved significant friction reduction.
- Developed a new design principle incorporating a hydrodynamic wedge geometry inside the surface feature and achieved success in friction reduction, first on steel on soft metals (because of limitations of fabrication techniques).
- Overcame the fabrication limitation and demonstrated for the first time bearing steel on bearing steel under high-load, low-speed conditions (boundary lubrication conditions). Such surface texturing would yield a 30% reduction in friction in bench testing.
- Completed the initial development effort on an enhanced selective electrochemical etching technique in combination with photolithography on steel surfaces.
- Successfully demonstrated that cavitation played a role under high-speed, high-load conditions in a single dimple observation apparatus.
- Initiated an elasto-plastic lubrication model development effort to describe the friction reduction mechanism of surface textures under boundary lubrication conditions.

Future Direction

- Continue parametric study of the size, pattern, density, and L/D ratio in this uncharted territory.

Introduction

Frictional losses are inherent in most practical mechanical systems. The ability to control friction offers many opportunities to achieve energy conservation. Over the years, materials, lubricants, and surface modifications have been used to reduce friction in automotive and diesel engine applications to promote energy efficiency. However, in recent years, progress in friction reduction technology has slowed because much obvious inefficiency has been eliminated. A new avenue is needed.

Recently, laser-ablated dimples on surfaces have shown friction reduction properties and have been demonstrated successfully in conformal contacts, such as seals, where the speed is high and the load is low. The friction reduction mechanism in this regime appears to depend on the size, patterns, and density of dimples in the contact. The success of dimples in reducing friction has opened a new avenue for friction control for engine applications.

The objective of this project, therefore, is to explore the feasibility of surface texture designs to reduce frictional losses in energy transmission components, cylinder liner ring contacts, cam and lifters, and overhead bearing components. To ensure that the durability criteria are met, the texture patterns must be protected by thin films/coatings and appropriate lubricating chemistry over a broad range of operating conditions. The final outcome of the project will be to develop design principles and guidelines for various engine components under a wide range of operating conditions. To achieve maximum energy conservation, this technology should be implemented worldwide through international avenues for cooperation such as the IEA IA-AMT. Therefore, concomitant international cooperative research under IEA auspices is being

conducted to pool resources from various countries to accelerate this technology development. Toward this end, the United Kingdom, China, Australia, Finland, Sweden, Israel, and Japan have agreed to participate under IEA annex IV on surface technology.

Approach

Previously, experiments were conducted to examine various surface textures on steel surfaces using photolithography and chemical etching. Using the same area coverage (percentage of area occupied by the surface textural features), surface features such as grooves, triangles, ellipses, and circles were compared under high-speed, low-load conditions similar to the operating conditions for seals. Results suggested that (1) surface texture size and shape had significant influence on friction, (2) orientation of the surface features with respect to the sliding direction changed the friction; and (3) the primary effect of surface textures is to accelerate the transition into a hydrodynamic lubrication regime. What is the fundamental friction reduction mechanism in this regime is still not clearly understood.

From an energy conservation point of view, most parasitic losses take place under high-load, medium- to low-speed conditions. Therefore, we need to extend this concept to increasingly severe contact conditions. However, when we ran the same surface texture patterns under boundary lubrication conditions, friction increased. A collaborative effort with Northwestern University using a sophisticated elastohydrodynamic friction model confirmed our experimental observations. Basically, under boundary lubricated conditions (high-load, low-speed), the edge stresses around the dimple increase frictional losses as if the surface is much rougher. So there is a trade-off in this regime.

Technical Highlights

During the past year, we developed a new surface textural feature with an inclined plane at the bottom of the feature to artificially generate a hydrodynamic wedge effect under plastic deformation loading; we called this the elasto-plastic lubrication model. Experiments conducted demonstrated significant friction reductions for steel on brass, aluminum, copper, and steel under boundary lubricated conditions.

When we used hard metals such as 52100 steel, the initial high contact pressure caused severe wear, damaging the surface textures; and the friction reduction results were erratic. To overcome this issue, we developed a wear-in procedure to create a smooth crater surface approximately 0.5 mm in diameter and then carved the texture onto the surface inside the crater with a diamond tip on the triboindenter. This way, a controlled interface was created to avoid severe wear-in and destruction of the surface features. We demonstrated that friction in a 52100 steel/52100 steel contact could be reduced significantly from 0.09 to 0.06.

We also focused on developing a low-cost, rapid fabrication method and conducted tests to verify the friction reduction characteristics of the new fabrication technique. We used a microlithography/chemical etching process previously to fabricate dimples with depths ranging from 3 to 10 μm. For shallow dimples, we needed to control the etching process precisely. Numerous factors could affect the electrochemical etching process, including the kind of electrolyte, the voltage, and the composition of the material. Since electricity always passed through the high-conductivity points, an inhomogeneous oxidation rate on a heterogeneous work piece will make the etching process selective. This was critical when a shallow depth was needed. A special electrolyte composed with acids was used for this purpose. Acid was effective in removing the oxidant on the surface so that etching could start quickly and uniformly. A circular dimple pattern was produced by this technique. A four-ball wear tester was used to carry out the friction tests using a ball-on-three flat configuration. The results showed that friction reduction of up to 32% has been achieved by the texture generated by this fabrication technique. Compared with previous textures generated by nanoscratching with sloped bottoms, the friction reduction was not as high (40–80%).

L/D Ratio and Size Effects

One of the critical issues in fabricating the new surface features was the effect of the slope at the bottom of the feature. In bearing applications, this typically was called the L/D ratio (bearing length over radius of the bearing) to estimate the lift force. We borrowed this concept and applied it to our design in terms of the length over the depth of the slope fabricated at the bottom of the surface features.

Another important factor was the size of the surface feature over the contact area. In boundary lubrication conditions, the edges of the surface features served as rough spots, increasing the friction; therefore, the optimum number of the features might be much smaller than for the high-speed, low-load regime. So we decided to conduct a series of experiments to investigate this effect.

We fabricated several surface features by varying the L/D ratios and the sizes of the surface features. We ended with three patterns, A3, B2, and C4. The micrographs are shown in Figure 1. The densities of the three patterns are kept at 5%. Pattern A has a reversed wedge; pattern B has a symmetrical wedge, and pattern C has the classic wedge design orientation.

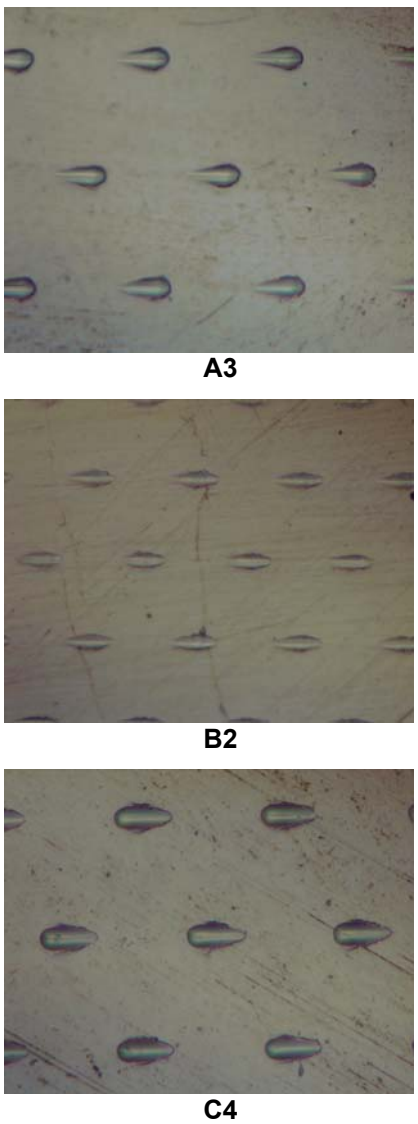

Figure. 1. Three wedge orientation patterns for testing.

Figure 2 shows that the classical wedge orientation has the highest friction reduction capacity, reducing the average friction coefficient of the untextured pattern (UNT) from 0.09 to about 0.05, a 44% decrease in a 52100 bearing steel on 52100 bearing steel contact. Another significant point is that the friction starts at 0.09, which is at the low end of the boundary lubrication regime; the surface texturing features lower it to the hydrodynamic lubrication regime even though the contact is still operating at the boundary lubrication regime, as evidenced by the wear of the contact.

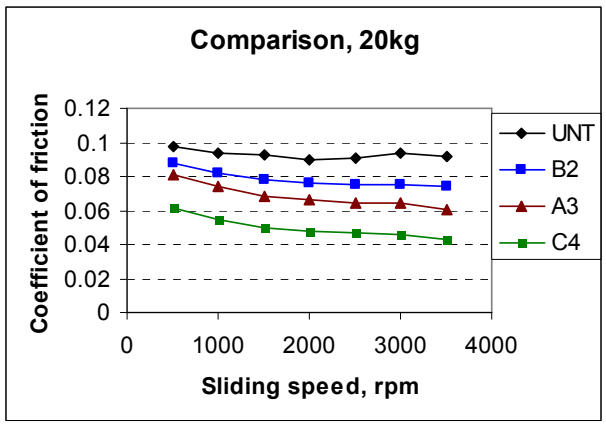

Figure 2. Comparison of friction coefficients of the three patterns under boundary lubrication conditions.

IEA Highlights

We attended the IEA End-Use Working Party (EUWP) meeting in Paris on April 18–19, 2005, and presented the IA-AMT end-of-term report. Based on input from the meeting, numerous revisions were made to incorporate new activities and future emphases. The EUWP voted to recommend a 4-year extension of the IEA work to CERT. CERT voted in June to give tentative approval for a 3-year extension, but it was noted that CERT wishes to see rapid progress on implementing the changes.

Potential participants in China, Australia, Finland, Japan, the United Kingdom, and Belgium were contacted to ask them to participate and to attend the IEA Executive Committee meeting to be held in Porto, Portugal, in conjunction with the COST 532 (European Cooperative Research Consortium on Triboscience and Tribotechnology)

technical conference. The Executive Committee was successfully convened in Porto with delegates from China, the United Kingdom, Australia, Finland, Japan, Belgium, Portugal, and the United States. Annex 2 was successfully concluded; annexes 3 and 4 are continuing. We discussed two new activities in coatings and nanomaterials. The delegates will take the information and seek their governments' approval for formal participation in IA-AMT. The next meeting was scheduled for Calgary, Canada, for May 7–12, 2006, in conjunction with the Society of Tribologists and Lubrication Engineers (STLE)) meeting.

A Special Symposium on Surface Texture was held in Porto in conjunction with the COST 532 conference on October 12–15, 2005. The symposium featured speakers from eight countries—representing academia, industry, and government laboratories—who described their latest results in surface texturing in controlling friction.

Future Direction

We will continue our parametric study of size, pattern, density, and L/D ratio in this uncharted territory. Until we understand the basic operating mechanism and the effects of the operating parameters on the mechanism, we will not be able to develop design guidelines.

Presentations and Publications

S. M. Hsu, "Surface Texturing under Boundary Lubrication for Friction Control," Society of Tribologists and Lubrication Engineers annual meeting, Toronto, Canada, May 17–20, 2004.

Jorn Larson Basse, X. Wang, L. Ives, and S. M. Hsu, "Some Friction Experiments with Dimpled Surface Texture," Fourth China International Symposium on Tribology, Xian, China, November 8–11, 2004.

S. M. Hsu, "An Integrated Surface Texture Technology for Friction Control in Engine Components," DOE DEER Conference, San Diego, August 30–September 2, 2004.

S. M. Hsu, "Surface Texturing to Reduce Friction in Engine Components and IEA Program," COST 532 management meeting, Ghent, Belgium, October 17, 2004.

S. M. Hsu, "An Integrated Surface Modification Technique to Control Friction: A New Paradigm," Keynote speech at the Fourth China International Symposium on Tribology, Xian, China, November 8–11, 2004.

Y. Chae, X. Wang, and S. M. Hsu, "The Size Effect of Surface Texture on Lubricated Friction," First International Conference on Advanced Tribology, Singapore, December 1–3, 2004.

Jorn Larson Basse, Lew Ives, and S. M. Hsu, "Lubricated Friction Experiments with Coarse Groove Texture," Society of Tribologists and Lubrication Engineers annual meeting, Las Vegas, May 15–19, 2005.

S. M. Hsu and Xiaoli Wang," Surface Texturing for Friction Control," Society of Tribologists and Lubrication Engineers annual meeting, Las Vegas, May 15–19, 2005.

S. M. Hsu, "Surface Texturing: A New Design Principle for Friction Control under Boundary Lubricated Conditions," International Tribology Congress, Kobe, Japan, May 29–June 2, 2005.

S. M. Hsu, "Surface Texturing: Comparison of Various Geometric Shapes on Friction under High-speed Low-load Conditions," International Tribology Congress, Kobe, Japan, May 29–June 2, 2005.

S. M. Hsu, "An Integrated Surface Modification Technology: Project Review," DOE project review, Oak Ridge National Laboratory, Oak Ridge, Tennessee, September 13–15, 2005.

S. M. Hsu, "Integrated Surface Modification Technology: A Progress Report," COST 532 Symposium on Surface Textures, Porto, Portugal, October 12, 2005.

Jorn Larson Basse, X. Wang, L. Ives, and S. M. Hsu, "Some Friction Experiments with Textured Surfaces," in *Proceedings of Nordic Symposium on Tribology*, Troms, Norway, June 2004.

X. Wang, S. M. Hsu, "An Integrated Surface Modification Technique to Control Friction: A New Paradigm," in *Proceedings of the Fourth China International Symposium on Tribology*, Xian, China, November 8–11, 2004.

X. Wang and S. M. Hsu, "Surface Texturing: Comparison of Various Geometric Shapes on Friction under High-Speed Low-Load Conditions," in *Proceedings of the International Tribology Conference*, Kobe, Japan, May 29–June 2, 2005

X. Wang and S. M. Hsu, "Surface Texturing: A New Design Principle for Friction Reduction Under Boundary Lubrication Conditions," in *Proceedings of the International Tribology Conference*, Kobe, Japan, May 29–June 2, 2005.

Appendix A. ACRONYMS AND ABBREVIATIONS

2-D	two-dimensional
3BOB	three ball-on-ball
3BOR	three ball-on-rod
3-D	three-dimensional
ACEM	aberration-corrected electron microscope
ACERT	Advanced Combustion Emissions Reduction Technology
ADF	annular dark-field
AE	acoustic emission
AFM	atomic force microscope
AFRL	Air Force Research Laboratory (Wright-Patterson Air Force Base, Dayton, Ohio)
AIST	(National Institute of) Advanced Industrial Science and Technology (Nagoya, Japan)
Al	aluminum
AMCL	Advanced Materials Characterization Laboratory
ANL	Argonne National Laboratory
ANSYS	commercial finite-element analysis software
ASM	American Society for Metals
ASME	American Society of Mechanical Engineers
ASTM	American Society for Testing and Materials
Ba	barium
BAM	Bundesanstalt für Materilforschung und - prüfung (Berlin, Germany)
BET	Brunauer-Emmett-Teller theory
BMOs	Base metal oxides
BU	Bournemouth University (United Kingdom)
CARES	Ceramics Analysis and Reliability Evaluation of Structures
CC	current collector
CCVD	combustion chemical vapor deposition
CDF	cumulative distribution function
CEN	Committee for European Normalization
CerSaT	Ceramic Science and Technology
CERT	Committee on Energy Research and Technology
CHIP	cold + hot isostatic pressing
CIM	chemically interactive material
CMM	coordinate measuring machine
CP	commercially pure
CRADA	cooperative research and development agreement
CRT	continuously regenerating technology
CTE	coefficient of thermal expansion
CVD	chemical vapor deposition
CWRU	Case Western Reserve University
DDC	Detroit Diesel Corporation
DISI	direct-injection spark-ignition
DITS	dynamic indentation test system
DOE	U.S. Department of Energy

DPF	diesel particulate filter
DRIFT	diffuse reflectance infrared Fourier transform spectroscopy
DSC	dispersion-strengthened composite
DT	deformation twin
DTA	differential thermal analyzer
EDM	electro-discharge machining
EDS	energy-dispersive spectroscopy
EERE	Office of Energy Efficiency and Renewable Energy
EGR	engine gas recirculation
EPA	U.S. Environmental Protection Agency
EPMA	electron probe microanalysis
EVD	electrochemical vapor deposition
FCVT	FreedomCAR and Vehicle Technologies
FEA	finite element analysis
FEM	finite element method
FEM	finite element method/finite element modeling
FTIR	Fourier transform infrared spectroscopy
FY	fiscal year
GPa	gigapascals
HA-ADF	high-angle annular dark-field
HA-ADG	high-angle annular dark field
HC	hydrocarbons
HDI	high-density infrared
HFIR	High Flux Isotope Reactor
HIP	hot isostatic pressing
HIPed	hot isostatically pressed
HS	high stress
HSWR	High-Strength Weight-Reduction Materials Program
HTML	High Temperature Materials Laboratory
HVOF	high velocity oxygen-fuel
IA	implementing agreement
IA-AMT	Implementing Agreement for a Programme of Research and Development on Advanced Materials for Transportation Applications
IEA	International Energy Agency
IEST	integrated engineered surface technology
IITS	instrumented indentation test system
INL	Idaho National Engineering and Environmental Laboratory
ISO	International Organization for Standards
JIS	Japan Industrial Standards

LabVIEW	Programming software made by National Instruments
LANL	Los Alamos National Laboratory
LBNL	Lawrence Berkeley National Laboratory
LNT	lean NO_x trap
LS	low stress
LST	laser surface texturing
METI	Ministry of Economy, Trade and Industry (Japan; formerly MITI)
Mg	magnesium
MMC	metal matrix composite
NASA	National Aeronautics and Space Administration
NDE	nondestructive evaluation
NiAl	nickel aluminide
NiCr	nickel chromium
NiCrFe	nickel chromium iron
NIST	National Institute for Standards and Technology
NIST	National Institute of Standards and Technology
NO_x	oxides of nitrogen; nitrites/nitrates species
NPD	neutron powder diffraction
NPL	National Physical Laboratory (UK)
NSF	National Science Foundation
NSR	NO_x stoichiometric ratio
NTN	NTN Bower
NTRC	National Transportation Research Center
OBD	on-board diagnostic
OFCVT	Office of FreedomCAR and Vehicle Technologies
OFHC	oxygen-free high-conductivity
OM	optical microscopy
ORNL	Oak Ridge National Laboratory
PBC	phosphate-bonded composite
PCA	principal component analysis
PDS	probabilistic design system
PI	principal investigator
PM	particulate matter
PMT	photomultiplier tube
PNNL	Pacific Northwest National Laboratory
PoT	pin-on-twin oscillating wear test
Pt	platinum
PZT	lead zirconate titanate
RBS	rotary bend strength
RCF	rolling contact fatigue
RE	reference electrode

SAcM	scanning acoustic microscopy
SAM	scanning auger microprobe
SAXS	small angle x-ray scattering
SCG	slow crack growth
SCR	selective catalytic reduction
SE	sensing electrode
SEM	scanning electron microscopy
Si_3N_4	silicon nitride
SiC	silicon carbide
SIDI	spark-ignition direct-injection
SIUC	Southern Illinois University–Carbondale
SMPS	scanning mobility particle sizer
SOFC	solid oxide fuel cell
SO_x	sulfur and oxygen containing compounds
SpaciMS	spacially resolved mass spectrometer
SRBSN	sintered reaction-bonded silicon nitride
SRM	standard reference material
SS	stainless steel
STEM	scanning transmission electron microscopy
TBCs	thermal barrier coatings
TEM	transmission electron microscopy
TFS	through focal series
TGA	thermal gravimetric analysis (or analyzer)
Ti	titanium
TiAl	titanium aluminide
TiC	titanium carbide
TTBCs	thick thermal barrier coatings
TTZ	transformation-toughened zirconia
TWC	three-way catalyst
TWS	Third-Wave Systems
UHMW-PE	ultra-high molecular weight polyethylene
UHR-TEM	ultra-high resolution TEM
UTBM	University of Technology at Belfort-Montbeliard
WBDF	weak beam dark field
WC	tungsten carbide
XPS	X-ray photoelectron spectroscopy
XRD	X-ray diffraction/X-ray powder diffraction
YSZ	yttria-stabilized zirconia